Study on the accuracy of rock surface roughness data using close range photogrammetry

Mr Dong-Hyun Kim

BSc, MEng

Griffith School of Engineering

Griffith Sciences

Griffith University

Submitted in fulfilment of the requirements of the degree of

Doctor of Philosophy

June 2016

ABSTRACTS

In civil and mining engineering areas, close range photogrammetry (CRP) has been used in recent years to investigate various aspects of rock faces such as geological structures, weathering, and crack propagations. The 3D models of CRP are efficiently used for the mapping and characterization of rock slopes on the cost-effective and less labor-intensive advantages of digital photogrammetry. The recent development of high-end equipment for remote sensing surveys in the field of digital cameras and photographing technology has also encouraged the spread of CRP to obtain accurate geomorphological data from the photogrammetric 3D images.

The roughness of rock joint planes is a crucial factor to investigate the shear strength and the groundwater infiltration characteristics along the joint planes. In geological and geotechnical purposes, the degree of roughness is identified by roughness parameters and the values are obtained from observations using large and small scale profiles in laboratory and field conditions. As a representative parameter, the rock joint roughness coefficient (JRC) has been widely employed combined with its strength characteristics. In order to measure the surface roughness, manual measurements using a profile gauge have been traditionally taken in both laboratory and field investigations. This mapping process is quite labourious and involves risks during field work. For this reason, close range photogrammetry has advantages over the traditional mapping methods in reducing surveying time and minimizing possible risks involved in field work.

Despite the advantages of photogrammetry, its application to date represents less than half of this technology's potential. The applicability of photogrammetry for estimating the roughness parameters has not been sufficiently researched. Current photogrammetric techniques have a potential to provide roughness profiles which have the same or much smaller measurement intervals compared to manual measurement. In practice, the accuracy and precision of the photogrammetric roughness data could depend on several adjustable factors such as the resolutions of the images, the camera distance to the objects and the camera oblique angles facing to the object in photogrammetry setups.

This research focuses on studying the accuracy of photogrammetry for the estimation of the two dimensional roughness parameter, JRC values based on laboratory and site

photogrammetric experiments. In this study, roughness profiles are collected from various natural rock surfaces. The ranges of the JRCs obtained from each photogrammetry survey are used for back analyses by using various numerical analysis tools for the specific rock engineering issue of each site. This case study intends to show that the level of reliability of the results can be interpreted by the level of accuracy of the photogrammetric JRC data employed.

Another key performance of this research is the development of a CRP error model for JRC estimation based on the specific data distributions obtained from the laboratory photogrammetry tests varying the focal length of lenses. The developed model can be a guideline to verify the photogrammetric JRC values based on the accuracy of the employed focal length of lenses in an ideal photographic setup. This model also suggests the assessment of the allowable distances for the camera setups associated with the employed focal lengths. Finally, the suggested error model is used to verify the roughness data obtained from the field surveys which have various conditions of camera-to-object distances and focal length of lenses. Based on the data analysis using the field data, the ranges of preferred camera oblique angles are also proposed in this study.

This research contributes to the field of site investigation in both rock mechanics and photogrammetry areas. The level of accuracy of JRC values obtained from CRP can be interpreted by the photogrammetry setup using the developed error models. This methodology encourages the use of photogrammetry in rock engineering based on experimental approaches.

STATEMENT OF ORIGINALITY

This work has not previously been submitted for a degree or diploma in any university. To the best of my knowledge and belief, the thesis contains no material previously published or written by another person except where due reference is made in the thesis itself.

(Signed)_____

Dong-Hyun Kim

TABLE OF CONTENTS

iv

ACKNOWLEDGEMENT

ACKNOWLEDGEMENT OF PAPERS INCLUDED IN THIS THESIS

Included in this thesis are papers published in leading international journals which are co-authored with my supervisors and other researchers. I would like to express my appreciation to the co-authors for their invaluable helps for this research. The bibliographic details for these papers including all authors are:

1. Chapter 4, Section 4.4:

D.H. Kim, I. Gratchev, G.V. Poropat (2013) The determination of joint roughness coefficient using three-dimensional models for slope stability analysis. Proceeding of Australian Centre for Geomechanics, Slope Stability 2013, Brisbane, pp. 281-289.

2. Chapter 5:

D.H. Kim, G.V. Poropat, I. Gratchev, A.S. Balasubramaniam (2015) Improvement of photogrammetric JRC data distributions based on parabolic error models. International Journal of Rock Mechanics and Mining Sciences, 80; 19-30.

3. Chapter 6:

D.H. Kim, G.V. Poropat, I. Gratchev, A.S. Balasubramaniam (2016) Assessment of the accuracy of close distance photogrammetric JRC data. Rock Mechanics and Rock Engineering; doi: 10.1007/s00603-016-1042-9

4. Chapter 7, Section 7.2:

D.H. Kim, I. Gratchev, A.S. Balasubramaniam (2013) Determination of joint roughness coefficient (JRC) for slope stability analysis: a case study from the Gold Coast area. Landslides, 10; 657-664.

5. Chapter 7, Section 7.3:

D.H. Kim, I. Gratchev, A.S. Balasubramaniam (2015) A photogrammetric approach for stability analysis of weathered rock slopes. Geotechnical and Geological Engineering, 33; 443-454.

6. Chapter 7, Section 7.4:

D.H. Kim, I. Gratchev, A.S. Balasubramaniam (2014) Back analysis of a natural jointed rock slope based on the photogrammetry method. Landslides, 12; 147-154.

7. Chapter 7, Section 7.5:

D.H. Kim, I. Gratchev, G. Berends, A.S. Balasubramaniam (2015) Calibration of restitution coefficients using rockfall simulations based on 3D photogrammetry model: a case study, Natural Hazards, 78; 1931-1946.

8. Chapter 7, Section 7.6:

D.H. Kim, I. Gratchev, E. Oh, A.S. Balasubramaniam (2016) Assessment of rock slope weathering based on the alteration of photogrammetric roughness data. Proceedings of the 19th Southeast Asian Geotechnical Conference & 2nd AGSSEA Conference (19SEAGC & 2AGSSEA), Kuala Lumpur, pp. 901-906.

Appropriate acknowledgements of those who contributed to the research but did not qualify as authors are included in each paper.

LIST OF FIGURES

xv

xviii

LIST OF TABLES

1 INTRODUCTION

1.1 Research background

In the investigation of rock joint roughness, the measurement of the degree of asperities is usually associated with the shear strength of the rock joints. Since Barton and Choubey (1977) and ISRM (1978) introduced the rock joint roughness coefficient (JRC), the shapes of the typical roughness profiles have been regarded as a model in many ways. These typical profiles, with their coefficients, have been popularly applied to investigate various engineering issues, especially in which the behaviour along joints is dominant in the rock mass. Therefore, as an important parameter in rock engineering, JRC values are quantified by engineers both in site and laboratory conditions.

JRC values can be roughly estimated based on the differences between the visual observations of the measured roughness profiles and the typical profiles. However, rock engineers are often confronted with the problem that the determination of JRCs by observation is quite subjective. This has led to investigation of appropriate mathematical methods to quantify JRC values to overcome the subjectivity. In order to quantify JRC values from irregular roughness profiles, the roughness parameters which are correlated with JRC have been introduced. The parameters are mathematically obtained by means of the values which express the shapes of roughness, such as the asperity heights or the angles of each tooth of the profiles. For example, Tse and Cruden (1979) proposed to estimate JRC values using a roughness parameter Z_2, which is a discrete form using the differences of asperity heights. Similarly, Maerz et al., (1990) investigated a relationship between JRC values and a parameter R_P which is related to the inclination angles of the teeth of a sawtooth surface. These mathematical approaches have provided a background for employing the coordinates of 3D surfaces surveyed by remote sensing methods.

Remote sensing techniques such as laser scanning and photogrammetry have been employed to obtain 3D rock surface models (Bistacchi et al., 2011; Brideau et al., 2011; Ferrero et al., 2011a; Firpo et al., 2011; Sturzenegger & Stead, 2009). Actually, the 3D meshes of the surfaces constructed by using the 3D point clouds are able to provide the asperity distances and heights of profiles to obtain the roughness parameters in every

direction through appropriate geo-referencing procedures. Using high density 3D rock surface models, the quantification of JRC has been studied by many researchers (e.g. Grasselli et al., 2002; Hong et al., 2006; Haneberg, 2007; Fardin, 2008; Poropat, 2008; Guo et al., 2011). In these studies, JRC values have been investigated in 2D and 3D conditions due to the capability of digital 3D models.

Terrestrial laser scanning (TLS) has been selected as a remote survey tools more often than terrestrial digital photogrammetry (TDS), because laser scanning can generally provide high density 3D images which are preferable for investigating detailed roughness data. However, although it is generally recognized that TLS produces higher resolution images than TDP, it is difficult to disregard the significant advantages of photogrammetry, which are portability, economic feasibility and convenience. The development of photogrammetry, which is associated with photography methods as well as camera devices, has led to an increase in the applicability of close range photogrammetry for the estimation of JRC values. In practice, recent close range photography has not been limited by the location of investigations. For example, quality images can be taken by using remote controlled unmanned aerial vehicles (UAV) (Niethammer et al., 2012; Ryan et al., 2015).

The feasibility of JRC estimation from digital photogrammetric data was reported by Lee and Ahn (2004), Haneberg (2007) and Poropat (2008). The results showed that higher resolution images are required to obtain reliable JRC values from photogrammetry and the resolution of images. The extent of the accuracy of JRC values, and the image resolution can be controlled by the hardware of photogrammetry such as the sensor size of the camera, and the focal length of the lens. Also, this can be controlled photography factors such as the camera-to-object distance, the base-to-distance ratio and the camera oblique angles. According to the required accuracy of the images in the investigations, the extent of using photogrammetry and photography can be managed. However, relevant studies on these factors have not been sufficiently reported to date.

It is recognized that close range photogrammetry can create surface roughness profiles with at least the same accuracy as the traditional measurements based on well planned photogrammetry surveys. From a practical point of view, the use of CRP for JRC estimation requires further investigations to optimize the methodology of CRP for obtaining surface roughness data with better accuracy. The limitations for the accuracy of the photogrammetry should be also sufficiently investigated with regard to a guideline of CRP.

This study investigates the accuracy of CRP for the photogrammetric JRC values based on various experimental works.

1.2 Research objectives

This study aims to investigate the level of accuracy of photogrammetric JRC values focussing on the practical use of CRP in various survey conditions. This study aims to develop a photogrammetric JRC error model which can be served as guidelines for the JRC data estimated from photogrammetric 3D models. This research focuses on the influence of the factors mentioned above on the accuracy of photogrammetric roughness data. The developed error model is then verified by means of the collected roughness data and the results of numerical analyses on the field issues.

The principal objectives of this research are:

(1) To critically review previous studies related to:

- identification of discontinuities exposed on rock masses.

- joint roughness coefficient (JRC) and the estimation methods.

- roughness parameters related to JRC estimation.

- application of remote sensing methods for JRC estimation.

- measurement of directional roughness profiles.

- extraction of roughness profiles using photogrammetric 3D models.

- limitation and error factors of photogrammetry.

(2) To validate the photogrammetric JRC values collected from various field conditions using:

- field photogrammetry surveys performed on various rock slopes.

- analytical and numerical analyses the obtained roughness data for the specific site issues. The results of this indicate the influence of the estimated JRC ranges on the safety of the rock slope in various rock engineering issues.

▪ case studies which show the use of the photogrammetric data for practical applications in rock mechanics.

(3) To develop a methodology framework which will include:

▪ a set of photogrammetry laboratory tests is performed in this stage.

▪ statistical analyses using the results of the laboratory tests. This stage of the study suggests quadratic error functions associated with the employed focal lengths.

▪ guidelines to use the focal lengths to obtain more accurate results.

▪ the developed parabolic error curves which can be used as a guideline for photogrammetric JRC surveys.

(4) To validate the newly-developed error model by:

▪ collecting and analysing field photogrammetric data on surface roughness.

▪ comparing the data from field investigations and lab tests. Data deviations are then analysed based on the data analysis, and a guideline of CRP for the estimation of JRC values is established.

1.3 Layout of thesis

The first two chapters of this thesis give a general introduction including the background of this study and literature review.

Chapter 3 describes the state of the art in the methodology of photogrammetry from creating 3D models to extracting surface roughness profiles. The factors, which affect the accuracy of 3D models such as the variation of image resolutions and the measurement errors, are presented in terms of the fundamentals of photogrammetry and the photographic setup. This chapter also presents the methodology of profile extraction from 3D coordinates including the reviews of previous approaches. This methodology demonstrates a detailed way to obtain profile coordinates for the measurement of the designated directions.

Chapter 4 introduces field photogrammetry investigations performed in this study. The photogrammetry surveys are performed on the Gold Coast and in Brisbane area, Australia. The 3D models and roughness data obtained from the photogrammetry surveys are used for

the various rock slope issues which are discussed later in Chapter 7. This chapter also describes the equipment employed in this photogrammetry survey and for the measurement of roughness of rock surfaces. A part of this chapter is included in the proceedings of an ACG conference (Australian Centre for Geomechanics) as a peer-refereed conference paper.

Chapter 5 describes the procedure and test data from a series of photogrammetry laboratory tests. These tests were designed to investigate the influence of image resolutions to produce roughness parameters and estimate JRC values. The laboratory tests performed at a close range (< 7m) are intended to identify the effect of resolution on JRC values in the same or smaller scale of roughness profiles with manual measurements. This chapter suggests a parabolic error model which depends on the focal length of lenses. This model can be used for reassessing the obtained JRC data from photogrammetric 3D models. The data reconciliation using the error model is for the improvement of the original data distributions in their accuracy and precision. A part of this chapter has been published in "International Journal of Rock Mechanics and Mining Science".

In Chapter 6, the roughness profiles and JRC values from the previous field surveys are statistically analysed and the newly-developed error models are verified. Through the analysis, three important factors are considered: camera-to-object distance, focal length and the angles of incidence between the line of sight of camera and the profiles of interest. This chapter also discusses the accuracy of the collected data and also demonstrates how the accuracy of close range photogrammetry can be improved based on the newly-developed guidelines. A part of this chapter has been published in "Rock Mechanics and Rock Engineering" journal.

Chapter 7 deals with the slope stability issues at five different sites and the each rock slope is reviewed using the obtained photogrammetric roughness data at various points. The photogrammetric setups are planned to fit the purpose, and to be suitable for each site condition. This chapter describes detailed field investigations on the characterization of joint roughness profiles and their roughness coefficients through several case studies. The first four cases discuss the feasibility of photogrammetric 3D models in various rock engineering aspects. The last case study discusses the accuracy of roughness profiles focussing on the influences of planning errors on photogrammetric roughness data. The five case studies in this chapter have been published in international journals: Landslides,

Geotechnical and Geological Engineering, Natural Hazards and are included in the proceedings of a 19SEAGC & 2AGSSEA conference as a peer-refereed conference paper.

Chapter 8 discusses the feasibility of photogrammetry for JRC estimation and recommends guidelines for CRP to create reliable roughness profiles and estimate JRC values. The work discusses the methods and strategies to obtain reliable JRC values through photogrammetry surveys in the field. Finally, Conclusions together with recommendations for future research are included in this chapter.

Appendix 1, in table format, summarizes the photogrammetry survey data used for geo-referencing. The roughness profiles extracted from 3D models and from manual measurements are demonstrated in detail in Appendix 2. The profile incidence angles with line of sight are presented using stereo graphs in Appendix 3. Lastly, the results of strength tests performed in laboratory and fields are summarized in table format in Appendix 4.

2 LITERATURE REVIEW

2.1 Introduction

This literature review is related to following four conceptual areas. The first part of the review (Section 2.2) discusses the discontinuities of rock structures which can be visually identified from exposed rock cuts. The geological structures of rocks are studied for the use of visual information observed from excavated or natural rock cuts. The second part (Section 2.3 ~ 2.5) deals with the research on joint roughness coefficient (JRC) which can be used to quantify the rock surface asperity using a mathematical approach. With respect to the methodology to quantify rock surface asperity, JRC estimation is reviewed in terms of both mathematical and empirical ways. In the third part (Section 2.6 & 2.7), photogrammetry methods are discussed focussing on the application for the estimation of rock joint roughness in laboratory and field conditions. The fourth part (Section 2.8) is concerned with relevant error factors in close range photogrammetry, which are discussed to clarify the causes of field data deviations.

2.2 Discontinuities on rock masses

2.2.1 Identification of discontinuities

The knowledge of the dimensions and frequencies of the discontinuity sets which are obtained from exposed rock slopes is important to understand the rock masses. Discontinuity is a general term for any mechanical break of rock mass, which includes joints, fractures, fissures, weak bedding and faults (Priest & Hudson, 1981). In any types of discontinuities, the geometric characteristics of the discontinuities such as orientations, spacing and persistence can be primary factors to be investigated for understanding the behaviour of rock slopes and underground openings.

The geometric characteristics are generally identified by observing from exposed rock cuts. The relative parameters to visual observation and measuring from rock surfaces are schematically presented in Figure 2.1 (Hudson & Harrison, 1997) and can be described using ISRM (1978) as follows:

7

- Orientation: The angular position of a discontinuity in space. In geology, the orientation of a discontinuity is described by the dip of the line of steepest direction of the discontinuity plane and the dip direction of the plane.
- Spacing: The perpendicular distances between adjacent discontinuities
- Persistence: The discontinuity trace lengths or the areal extent of a discontinuity
- Roughness: The inherent surface unevenness and waviness of a discontinuity relative to its mean plane
- Aperture: The perpendicular distance separating the adjacent rock walls
- Filling: The material in the rock discontinuities

The quantification of the parameters is associated with various rock engineering issues from the initial stage of rock mass classification to the stability of rock mass. It has been known that there are practical difficulties to characterize the discontinuities, which are caused by the physical limitation of the observation areas based on the confined nature of rock masses (Pahl, 1981). The characterization of discontinuity depends on the limited information appeared as traces on exposed surfaces which may represent hidden space within rock masses. Thus, the discontinuity measurements can be affected by the uncertainty.
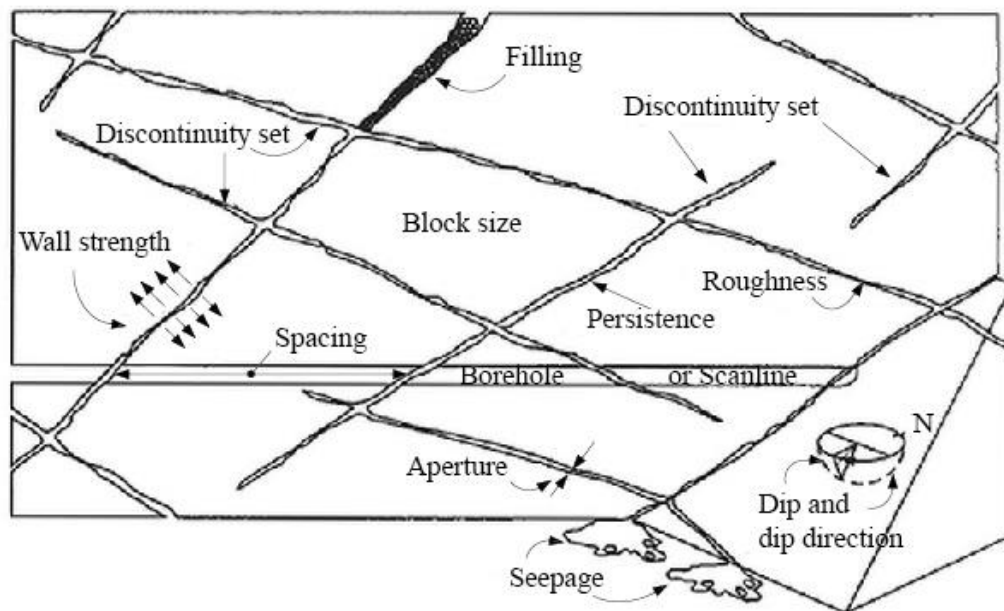
Fig. 2.1 Discontinuities in rock mass (Hudson & Harrison, 1997)

To address this problem, many studies suggested mapping techniques to sample more reliable information about the size, spacing and orientation of discontinuity sets. For

example, scanline and window mapping techniques have applied to investigate the size and spacing of the exposed discontinuities (Priest & Hudson, 1981; Priest, 1993). In order to minimize the orientation bias, a correction factor was suggested to account for the perpendicular values to the scanline or windows under-represented discontinuity sets (Terzaghi, 1965; Priest, 1993). Similarly, several mathematical approaches, which are associated with the length of discontinuity traces (Pahl, 1981; Lyman, 2003), the trace density (Zhang & Einstein, 2000; Mauldon et al., 2001) have been proposed to estimate and trace discontinuities with more reliable methods.

Compared to the basic geometric properties, the measurement of roughness could not been determined by alternative mapping methods. The measurement of roughness properties requires direct measurement with high accuracy. In the failure behaviour of a blocky rock mass, the roughness properties are significantly influenced by the measurement directions in relation to the failure behaviour of the rock mass. It can be thus recognized that biased values in surface roughness are directly associated with the safety of rock masses when the failure is governed by sliding behaviour. If the surface roughness is measured from an exposed rock discontinuity plane, the representative of the plane for a rock mass of interest requires a decision in a geological point of view. In many cases, site investigations may be needed in the large areas for the deterministic characterization.

For the all proposed methods, quantifications demand accurate and abundant data from the area for investigation. For this reason, manual measurement of the properties may be difficult for large sites such as mining and underground excavations. It is mainly because that there is lack of appropriate ways to cover the large scale site investigations. Due to the practical difficulties, the collection of data has mostly been performed by photographing and analysing subsequent processing of the photographs (Haneberg et al., 2006; Vita et al., 2012) than manual measurements. Thus, the quantified values of discontinuities, which are obtained from the image analysis, are strongly dependent on the accuracy and precision of the remote investigation techniques.

2.2.2 Roughness of discontinuity

The roughness of a discontinuity surface has a crucial effect on its shear strength. Between the walls of discontinuities, the gaps can be filled and unfilled (clean) conditions. In consideration of the geometric characteristics of discontinuity, the surface roughness of

discontinuities can be more important feature when the discontinuity sets are interlocked with unfilled joint sets. The importance of the roughness of the discontinuity can be reduced with increasing the size of aperture and filling thickness (Zhang, 2005). Thus, the roughness of discontinuity has been usually defined for the roughness of joint planes in rock engineering.

Rock joint roughness is scale dependent. If the wavelength of a laboratory scale is less than 100 mm, the referred roughness is of small scale. Priest (1993) defined roughness as surface irregularities with a wavelength less than 100 mm which can be expressed by Barton's JRC values. A large scale wavelength, which is larger around 100 mm, was referred to as curvature. Curvature can be quantified by measuring offsets in 100 mm intervals along a straight line. Similarly, Palmström (2001) expressed the scales of joint roughness as both the large scale undulations (waviness) and the small scale smoothness of the joint surface.

In rock engineering, following methods have been typically employed to quantify the degree of roughness. Large scale roughness is assessed by measuring the degree of waviness using a compass fitted with a back plate ranging in diameter from 50 to 200 mm as demonstrated in Figure 2.2 (ISRM, 1978). This method can identify the variations of the undulation angle (i) of a joint plane in large scale. As a similar method to find the degree of undulation, Piteau (1970) described the straight edge method, which measures the maximum amplitude of a directional roughness profile using a 0.9 m long straight edge.

Small scale roughness can be simply classified by touching the surface of joint planes. For the small scale (several centimetres) and the intermediate scale (several metres) roughness, ISRM (1978) suggested a classification of discontinuity roughness and typical roughness profiles as shown in Table 2-1. The method of measurements for joint wall waviness is well demonstrated in the literature of Milne et al. (1992).

The small scale roughness has been widely investigated by comparing with typical roughness profiles and their joint roughness coefficient (JRC) values as defined by Barton (1976). The suggested JRC values combined with the shear strength criterion have been studied by many researchers. In this thesis, the measured roughness in laboratory and site conditions is investigated by using the Barton's typical roughness profiles and the JRC values. The overview of the Barton's JRC is reviewed into more detail in the next section.
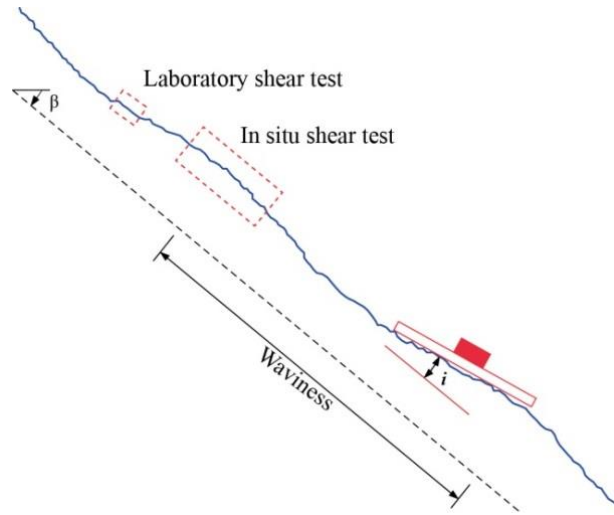
Fig. 2.2 Schematic description of discontinuity scales and comparison of roughness scales according to the types of tests (ISRM, 1978)

Table 2-1. Classification of discontinuity roughness (ISRM, 1978)

Class	Description
I	Rough or irregular, stepped
II	Smooth, stepped
III	Slickensided, stepped
IV	Rough or irregular, undulating
V	Smooth, undulating
VI	Slickensided, undulating
VII	Rough or irregular, planar
VIII	Smooth, planar
IX	Slickensided, planar

In an engineering point of view, joint roughness has been involved in rock mass rating in various forms. Q-system (NGI, 2013) considers joint conditions to the rock mass classification in great detail as shown in Table 2-2. The joint roughness term, J_r which ranges from 0.5 to 4.0 directly influences the Q-values as shown in Eq. (2-1).

$$Q = \frac{RQD}{J_n} \times \frac{J_r}{J_a} \times \frac{J_w}{SRF} \qquad (2\text{-}1)$$

where, RQD is degree of jointing; J_n is number of joint sets; J_r is joint roughness number; J_a is joint alteration number; J_w is joint water reduction factor; SRF is joint water reduction factor.

Palmström (1995, 2001) categorized the roughness of rock joints into both the small scale asperities (j_s, smoothness) and the large scale planarity (j_w, waviness) of a joint plane. Based on the Q system, it was suggested that the joint roughness factor (jR) can be identified as the product of j_s and j_w. This is similar to the J_r of the Q system. j_s is surface smoothness factor which is obtained by touch as an empirical factor and j_w is joint waviness factor. The descriptions of the parameters are presented in Table 2-3 and 2-4. In the large scale planarity, the undulation (u) can be calculated by the ratio of the maximum amplitude (a) to the measured length along the joint (L).

Table 2-2. Joint roughness number (J_r) (NGI, 2013)

Class	Description	J_r
	a) Rock-wall contact, and	
	b) Rock-wall contact before 10 cm of shear movement	
A	Discontinuous joints	4
B	Rough or irregular, undulating	3
C	Smooth, undulating	2
D	Slickensided, undulating	1.5
E	Rough, irregular, planar	1.5
F	Smooth, planar	1
G	Slickensided, planar	0.5
	Note 1) Description refers to small scale features and intermediate scale features in that order	
H	c) No rock-wall contact when sheared	1
	Zone containing clay minerals thick enough to prevent rock-wall contact when sheared	
	Note 1) Add 1 if the mean spacing of the relevant joint set is greater than 3 m (dependent on the size of the underground opening)	
	Note 2) $J_r = 0.5$ can be used for planar slickensided joints having lineations, provided the lineations are oriented in the estimated sliding direction	

Table 2-3. The ratings of the joint waviness factor (j_w) (Palmström, 1995)

Term for waviness	Undulation, u	Rating of j_w
Interlocking (large scale)		3
Stepped		2.5
Large undulation	u > 3%	2
Small-moderate undulation	u = 0.3 ~3%	1.5
Planar	u < 0.3%	1

Table 2-4. The ratings of the smoothness factor (j_s) (Palmström, 1995)

Term	Description	Rating of j^s
Very rough	Near vertical steps and ridges occur with interlocking effect	3
Rough	on the joint surface	2
	Some ridge and side-angle are evident; asperities are clearly	
Slightly rough	visible; discontinuity surface feels very abrasive (like sandpaper grade approx.<30)	1.5
Smooth	Asperities on the discontinuity surfaces are distinguishable and can be felt (like sandpaper grad approx. 30 ~ 300)	1
Polished	Surface appear smooth and feels so to the touch (smoother than sandpaper grade approx.. 300)	0.75
Slickensided	Visual evidence of polishing exists, or very smooth surface as is often seen in coating of chlorite and specially talc	0.6 ~ 1.5
	Polished and often striated surface that results from friction along a fault surface or other movement surface	

2.3 Roughness of discontinuity in rock engineering issues

2.3.1 Joint roughness coefficients (JRC)

The joint roughness coefficient (JRC) classification has been largely introduced to evaluate rock mass stability problems since the JRCs were developed to investigate the rock joint shear behaviours. The ranges of JRC values, which represent the degree of joint surface roughness, have been empirically determined by comparisons with the typical roughness profiles (Barton and Choubey, 1977; ISRM, 1978). A commonly used guideline of the

typical profile shapes was developed by Barton and Choubey (1977) as shown in Figure 2.3. The value of JRC varies from 0 to 20 according to the geometry of the wall surfaces of joints and the values are generally obtained by a comparison between joint geometries and these standard profiles. The JRC values were ranged by using the laboratory test results of 130 weathered rock samples, and the obtained standard profiles were originated from the ten different types of rocks. In the rock joint shear strength criterion, JRC values are directly proportional to the shear strength of joints as presented in Eq. (2-2).

$$\tau_p = \sigma_n \tan[JRC \, log_{10}\left(\frac{JCS}{\sigma_n}\right) + \phi_r] \qquad (2\text{-}2)$$

where, τ_p is the shear strength of joints; σ_n is normal stress; JCS is joint compressive strength; ϕ_r is the residual friction angle. As discussed by ISRM (1978), the range of JRC suggested by the Barton's work can be however used as an example, because the profile shapes only cover the shapes and scales of the profiles which are associated with the laboratory tests. The classification of ISRM (1978) suggested the ranges of JRC values according to the categorized joint types as shown in Figure 2.4. The degree of profiles is firstly classified by the most distinct feature of the profile in large scale as stepped, undulating and planar shapes. The classification of roughness degree is followed by the observation of the asperity in small scale. The classification also recommends that the scale effect should be considered to determine JRC values according to the length of the profiles.

In field investigations, the length of the joints can be several meters or more. In this case, the suggested profiles are not properly compared to the site conditions. In order to extend the applicability of JRC values to field conditions, a chart has been investigated to consider the appropriate scales of profiles for JRC estimation using the simple straight edge method (Barton, 1981; Palmström, 1995). This chart was originally suggested based on a number of tests (Barton and Choubey, 1977; Barton and Bandis, 1980). Palmström (1995) characterized the joint planarity and refined the Barton's chart including the boundary conditions of the undulation (u), as presented in Figure 2.5.

The measurement scales of rock joints are important factors to determine the rock mass strength for the joint investigations. Generally, JRC values decrease with the lengths of the measured profiles. Bandis et al. (1981) showed that the peak shear strength of rock joints is strongly dependent on its scale and that JRC values for the joint sets also reduce

considerably with increasing joint lengths. According to the Barton's shear strength criterion, the shear strength includes three components: the residual or basic friction component; the geometrical component; and the asperity failure component. The previous research indicated that the geometrical and the asperity failure components are highly scale dependent. Therefore, in order to obtain a JRC, Bandis et al. (1981) suggested that JRC values should be determined through performing a set of simple tilt tests, pulling tests or push tests. This procedure can also avoid the subjectivity of the visual observation. The JRC values can be back calculated from the tests using Eq. (2-3).

$$\text{JRC} = \frac{\alpha - \phi_r}{log_{10}(\frac{JCS}{\sigma_{no}})} \qquad (2-3)$$

where, α is the tilt angle in the tilt test; JCS is joint compressive strength; ϕ_r is residual friction angle and σ_{no} is normal stress when sliding occurs. JCS values can be obtained from performing Schmidt hammer tests on the joint surfaces. The typical JRC profile standards (Barton and Choubey, 1977; ISRM, 1978) allow to estimate a range of JRCs even though the procedure require shear tests to verify the values obtained from visual observations. The accuracy of JRC estimation is crucial when the behaviour of rock mass is governed by the roughness between the joint sets. Thus, in engineering practice, shear tests such as direct shear tests, tilt tests and/or pulling tests are utilized to complement the visual evaluation.
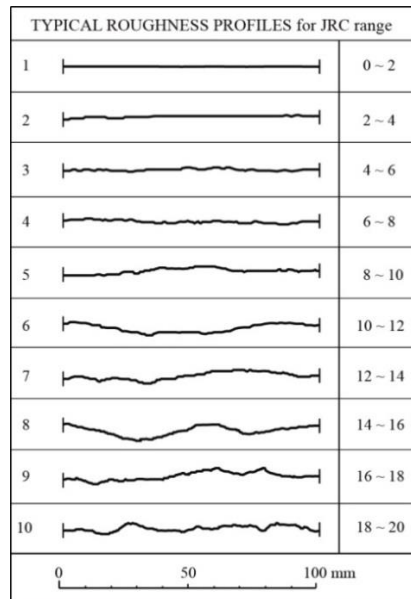
Fig. 2.3 Roughness profiles and corresponding JRC values (Barton and Choubey, 1977)

Fig. 2.4 Typical roughness profiles and corresponding JRC values (ISRM, 1978)
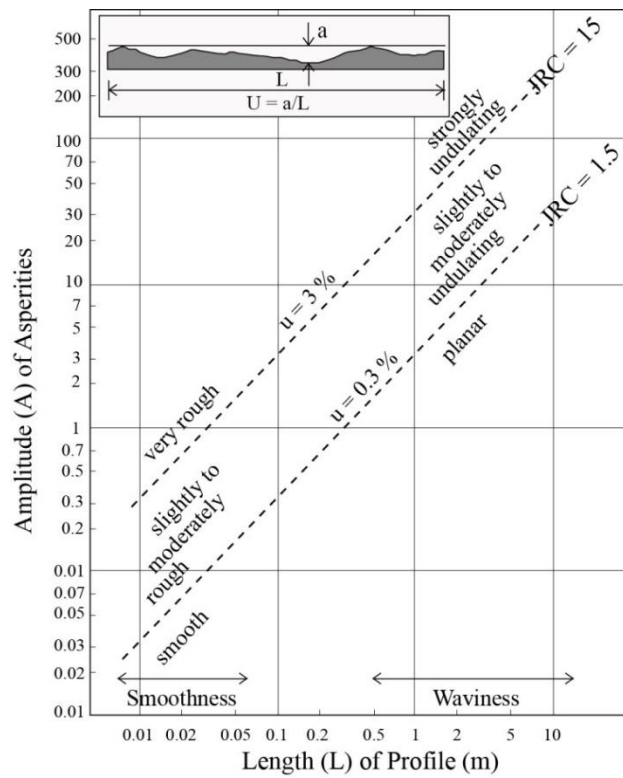
Fig. 2.5 JRC estimation chart (Palmström, 2001)

2.3.2 Block theory and rock joint roughness

In regularly bedded rock masses, the most likely pattern of slope failure and its safety factor can be determined by kinematic analyses. In the case of failure under gravity, there are considerable possibilities for block movement along weak planes. In this case, the friction between the planes of rock discontinuities has a crucial effect on its movement of discrete blocks. If the discontinuity of interest has an angle of friction, slip will occur only if the direction of applied compression makes an angle greater than the friction angle with the normal to the layers (Goodman, 1989). As a well-known analytical solutions for block behaviour, the block theory developed by Goodman and Shi (1985), presents successfully the safety of blocks according to their friction angles.

The block theory provides a three-dimensional graphical presentation of the problem, assists to identify removable (key) blocks, and find the applicable failure modes. In many practical slope stability issues, the block theory has been successfully used for various rock engineering issues in slope stability and tunnelling (Goodman and Shi, 1985; Mauldon and Goodman, 1996; Hatzor and Goodman., 1997; Tonon, 1998; Lee and Park, 2000; Huang et al., 2003; Hatzor and Feintuch, 2005; Strouth and Eberhardt, 2009; Kulatilake et al., 2011; Qingyan and Helin, 2011). The results from the stereographic projection method of the block theory are sensitive according to the friction angle of joints. However, most studies have insufficiently discussed about the friction data applied to the analyses. This can be explained by the fact that there are limitations for obtaining the friction data from site investigation and experiments.

As the roughness of rock joints is a useful information for the estimation of its friction angle, the friction angle of rock joints has been estimated by the roughness parameters of rock joints. Barton (1973) showed a direct proportional relationship between JRC values and friction angles. Therefore, the roughness data obtained from exposed rock joints can be used to estimate friction angles for the application of the block theory. In this study, the feasibility of this methodology has been investigated by through a case study. The basic principle of the block theory and the relationship between JRC values and friction angles will be discussed in Section 7.4, Chapter 7.

2.3.3 Rock fall behaviour and rock surface roughness

A rock fall event can experience various types of motion along its path combined with free fall, rolling, bouncing and sliding. During interaction of the falling body with a slope surface, the motion is usually governed by the geometry and mechanical characteristics of the material exposed on the slope surface and the falling body. Friction between the falling body and the slope surface is also a significant factor to determine the type of motion of a body (Basson, 2012).

In the relationship between rock fall behaviour and JRC values, Wang and Lee (2010) showed that the rockfall velocity reduced and bounce height increased as JRC values increased. Based on the results of a set of rockfall simulations, their study showed that the maximum velocity and average movement velocity decreased as JRC increased. Similarly, the influence of JRC values on the evaluation of restitution coefficients was reported by an experimental study using small rock blocks (Saeidi et al., 2015). Considering the scale of rock blocks, therefore, JRC values obtained from rock surfaces can be used to investigate rockfall behaviour relating to the dynamic frictions of rock slopes.

In rockfall simulations, slope roughness values are estimated from observations for the slope material which depends on its geological setting. For example, in a Rockfall (Rocscience Inc., 2003) simulation, slope roughness can be determined from the material specified for the model segment in large scale. However, the determination of the slope roughness in simulation can be ambiguous and questionable. Massey et al. (2006) reported the sensitivity of rockfall trajectories and impact energies derived from a Rocfall two dimensional analysis according to different slope roughness conditions. In a three dimensional condition, Haramy et al. (2013) also performed a series of back-calculation using different slope roughness parameters using a CRSP-3D program. Therefore, in many cases, field tests are recommended to verify the relevant parameters for the rockfall simulations.

As rockfall simulations require the friction data of the slope surface and JRC can be utilized to estimate the friction angles, the roughness data obtained from slope surface can be used for rockfall simulations. In this study, the feasibility of JRC data to rockfall simulation are investigated using a case study combined with a field rockfall test. This topic will be discussed in Section 7.5.

2.4 Roughness parameters to estimate JRCs

2.4.1 Two dimensional roughness parameters

The estimation of JRC values is typically done by using mathematical methods. Many researchers have developed the relationships between JRC values and roughness parameters in order to estimate JRC values using digitized roughness profiles. The studies were to overcome the subjectivity of the visual observation.

Tse and Cruden (1979) established empirical equations to estimate JRC values using two dimensional roughness parameters, Z_2 and SF. The equations were developed using the digitized data of 2D roughness profiles based on the Barton's typical roughness profiles. Z_2 and SF are the root mean square and the mean square of the first derivative of the profiles, respectively. The regressions were obtained from statistical analysis using two hundred discrete amplitude measurements for every profile. The correlated functions with JRC values are defined as Eqs. (2-5) and (2-6). As shown in Figure 2.6, as a representative roughness parameter, Z_2 shows better correlation with JRC values than SF. The function of Z_2 is presented in Eq (2-4).

$$JRC = 32.2 + 32.47 \log Z_2 \qquad\qquad (2\text{-}4)$$

$$JRC = 37.28 + 16.58 \log SF \qquad\qquad (2\text{-}5)$$

$$Z_2 = \left[\frac{1}{M(D_x)^2} \sum_{i=1}^{M} (y_{i+1} - y_i)^2 \right]^{1/2} \qquad\qquad (2\text{-}6)$$

where M is the number of intervals, D_x is a constant distance lag. The sum of the squares in adjacent y-coordinates is divided by the product of the number of intervals. This regression was then improved by Yu and Vayssade (1991). They studied the applicability of several roughness parameters to estimate JRC values. It was shown from this research that four roughness parameters, which are Z_2, SF, SD_i, and RL_i, showed strong correlation with JRC values. As given in Eq. (2-7), SD_i is a standard deviation of the asperity angles (i). RL_i is defined as a real profile length as presented in Eq. (2-8). It was concluded that SF was much more sensitive for sampling intervals; however, SD_i and RL_i behave almost the same as JRC.

19

$$SD_i = tan^{-1} \left[\frac{1}{L} \int_{x=0}^{x=L} \left(\frac{dy}{dx} - tan \; i_{ave} \right)^2 dx \right]^{1/2} \quad (2\text{-}7)$$

$$RL = \frac{\sum \left(\Delta x_i^2 + \Delta y_i^2 \right)^{1/2}}{L} \qquad\qquad (2\text{-}8)$$

$$RL_i = RL - 1 \qquad\qquad\qquad (2\text{-}9)$$

where, Δx_i and Δy_i are the increments of x and y directions of the profile, L is the length of the profile along abscissa. Following different ranges of equations using Z_2, Eqs. (2-10~12) were proposed to take measurement scales into account.

$$JRC = 60.32 \; Z_2 - 4.51 \qquad \text{(for sample interval = 0.25 mm)} \qquad (2\text{-}10)$$

$$JRC = 61.79 \; Z_2 - 3.47 \qquad \text{(for sample interval = 0.5 mm)} \qquad (2\text{-}11)$$

$$JRC = 64.22 \; Z_2 - 2.31 \qquad \text{(for sample interval = 1.0 mm)} \qquad (2\text{-}12)$$
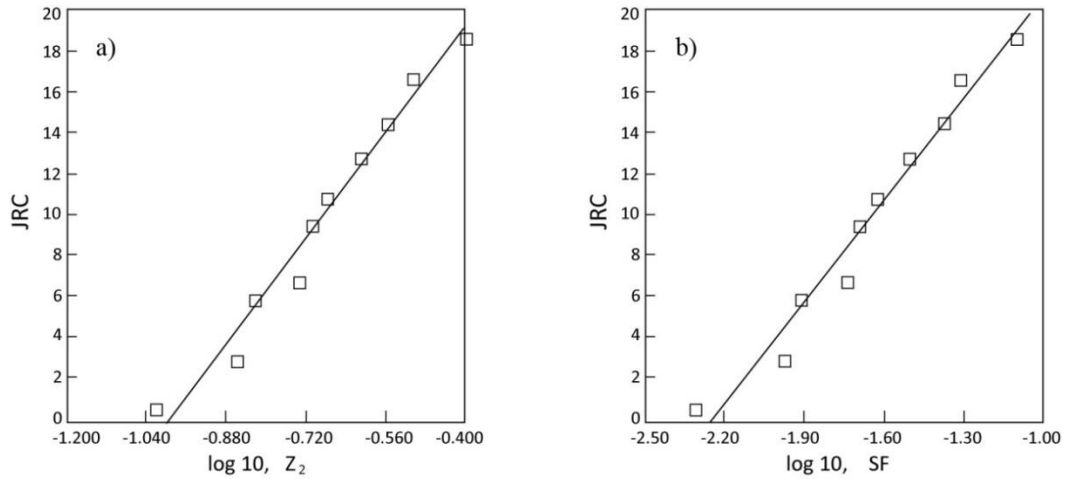
Fig. 2.6 Relationship between the JRC and parameters, Z_2 (a) and SF (b) (Tse & Cruden, 1979)

After the Tse and Cruden's work, a number of studies on the regressions of JRC values were performed using a fractal dimension (D) by many researchers (Turk et al., 1987; Carr and Warriner, 1989; Lee et al., 1990; Wakabayashi and Fukushige, 1992). The concept of their studies was based on the theory of fractal geometry (Mandelbrot, 1982). The results of these studies were compared with the back-calculated values by Hsiung et al. (1993). A set of tilt tests and shear tests using natural tuff joint sets were performed to verify the

regressions. The following equations were developed from the works of Carr and Warriner (1989), Wakabayashi and Fukushieg (1992), Turk et al. (1987) and Lee et al. (1990).

$$JRC = -1022.55 + 1023.92D \text{ (Carr and Warriner, 1989)} \qquad (2\text{-}13)$$

$$JRC = SQRT[(D-1)/0.00004413] \quad \text{(Wakabayashi and Fukushieg, 1992)} \quad (2\text{-}14)$$

$$JRC = -1138.6 + 1141.6D \quad \text{(Turk et al., 1987)} \qquad (2\text{-}15)$$

$$JRC = -0.87804 + 37.7844 \left(\frac{D-1}{0.015}\right) - 16.9304 \left(\frac{D-1}{0.015}\right)^2 \text{(Lee et al., 1990)} \qquad (2\text{-}16)$$

For these equations, D is a fractal dimension. The important finding from this comparison is that the functions used in this study underestimates the JRC values compared with the back-calculated results obtained from shear tests based on Barton's shear strength criterion. However, these studies also suggested that fractal dimension values are proportional to surface roughness so the fractal dimensions were successfully correlated with the JRC values.

Yang et al. (2001) reconstructed Barton's typical roughness profiles by digitizing the profiles into 500 data points. The coefficients obtained from Fourier series functions were adopted to describe the amplitudes of the profiles. Using the newly calculated Z_2 parameter, linear regression formulas were obtained and given as Eq. (2-17) and Eq. (2-18). It is reported in this research that these formulas produce larger values than the original functions suggested by Tse and Cruden (1979).

$$JRC = 32.69 + 32.98 \log Z_2 \qquad (2\text{-}17)$$

$$JRC = 37.63 + 16.5 \log SF \qquad (2\text{-}18)$$

where the roughness parameters, Z_2 and SF are the same as the parameters which are used in the Tse and Cruden's research.

Using the shadow profile technique, Maerz et al. (1990) suggested a method to estimate JRC values by a regression equation which explains the relationship between JRC values and the roughness profile index, R_p. This parameter is defined as the ratio of the true length of a fracture surface trace to its projected length in fracture planes. Figure 2.7 describes the

plot of JRC versus R_p. Eq. (2-19) and Eq. (2-20) were found by the linear regressions of Figure 2.7 (a) and (b), respectively.

$$JRC = 411(R_p - 1) \qquad (2\text{-}19)$$

$$JRC = 401(R_p - 1) \qquad (2\text{-}20)$$

where, the roughness profile index, R_p, is related to the asperity angle (i) which is based on the Patton's shear strength model (Patton, 1966). Turk and Dearman (1985) suggested Eq. (2-21) to estimate R_p values. Maerz et al. (1990) developed a method of photo analysis to measure (i) angles. The micro-average (i_m) was also introduced to obtain (i) value as defined by Eq. (2-22).

$$i = cos^{-1}\left[\frac{1}{R_p}\right] \qquad (2\text{-}21)$$

$$i_m = \frac{1}{n}\Sigma_{j=1}^{n}|I_j| \qquad (2\text{-}22)$$

where, n is the number of evenly spaced sampling points; i is the value of inclination angles between adjacent points along the sampling line.
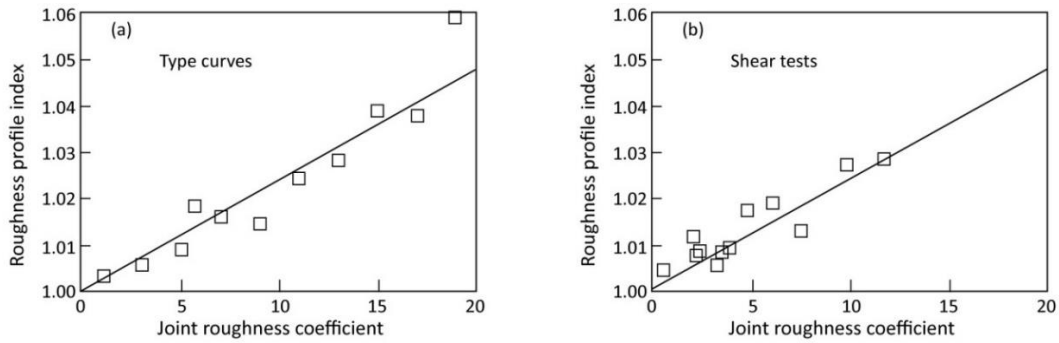
Fig. 2.7 Correlation between R_p and JRC: obtained by photo analysis of the type-profiles based on the typical profile (Barton & Choubey, 1977) (a) and determined from laboratory tilt and direct shear tests on samples of schist from the Hemlo Mine (Maerz et al., 1990)

2.4.2 Three dimensional roughness parameters

With the development of the methods to obtain rock surface data, roughness parameters have been investigated in three dimensional condition. Recently, remote sensing methods such as laser scanning technology and digital photogrammetry allow to create 3D surface models. The joint roughness data is obtained by digitized coordinates of 3D surface models. 3D roughness parameters have been developed to correlate with traditional JRC ranges or with new rock joint shear strength models. As the rapid development of the technology, 3D surface roughness parameters have more emphasis in the rock engineering area than 2D roughness parameters (Grasselli & Egger, 2003; Tatone & Grasselli, 2009). However, the majority of rock joint roughness analyses have employed linear profiles rather than 3D roughness parameters. This can be explained by the fact that the shear strength criteria of rock joints have been mainly developed in two dimensional conditions. Further, the shear strength of joints strongly relies on the roughness profiles in the shear directions. Thus, the study using two dimensional roughness parameters are primary and still valid.

In this research, the roughness data obtained by 3D photogrammetry models employ two dimensional roughness parameters focussing on the maximum asperity heights and the Barton's JRC values. It is mainly because this research aims to use the photogrammetry method as an alternative way to manual measurements of roughness profiles.

In order to understand 3D roughness parameters, representative 3D roughness parameters are discussed in this section. The studies have been performed by using laser scanners in laboratory conditions. Grasselli and Egger (2003) suggested a 3D roughness coefficient in their experimental study. In their research, replica joint sets were sheared in laboratory conditions and the surfaces of the sheared joints were analysed using an ATS optical scanner. As a result, a regression model using the parameters of contact areas, apparent dip angles and roughness was developed as shown in Eq. (2-23).

$$A_{\theta^*} = A_0 \left(\frac{\theta^*_{max} - \theta^*}{\theta^*_{max}}\right)^C \qquad (2\text{-}23)$$

where A_0 is the maximum possible contact area in the shear direction; θ^*_{max} is the maximum apparent dip angle in the shear direction; C is a roughness parameter. This equation was based on the triangulated surface data of 3D models and θ is the angle

between the shear plane and the triangles. This research was performed using high density images. The accuracy of the point clouds was in $\pm$ 50 μm.

Based on the fractal theory, Feng et al. (2003) and Fardin et al. (2004) investigated the scale dependency of rock surface roughness using a total station (TS) and a 3D laser scanner (LARA). Using scanned 3D images from replicas and from a natural rock slope, fractal parameters were calculated by the roughness-length method (RL). The RL method, which was originally suggested by Malinverno (1990), has been updated to apply the method for 3D fracture surfaces as follows:

$$S\,(w) = Aw^H \qquad\qquad (2\text{-}24)$$

where S (w) is the standard deviation of residual surface heights; w is the sampling window size; H is the Hurst exponent and A is a proportional constant. In addition, the fractal dimension (D) as well as the amplitude parameter (A) can be obtained from the correlation between S (w) and w. An important finding of this study is that both the parameters, A and D are dependent on sampling sizes.

Kulatilake et al. (2006) recommended that a combined parameter with a scale dependant fractal parameter, K_v, can be more effective for quantifying JRC values rather than solely using the normal fractal dimension (D). In this study, the linear profiles of rock joint surfaces were digitized with 0.33 mm intervals using a laser profilometer. The parameter, $D_{rld} \times K_v$, could be used to quantify the roughness of rock joints. In this combined function, D_{rld} is the mean value of fractal dimensions and K_v is a measure of amplitude of the profiles. As a simple empirical method, an asperity-amplitude relationship has been employed to estimate JRC values based on the Barton chart (Barton, 1981). Eq. (2-25) was suggested for JRC estimation in large scale profiles by Oppikofer et al. (2011) and is shown in Eq. (2-25).

$$JRC = A \cdot \sqrt{0.2 \cdot L^{-\log 80}} \qquad\qquad (2\text{-}25)$$

where, A is the maximum asperity height in millimetres and L is the profile length in metres.

2.5 Measurement of directional roughness profiles

2.5.1 Background

As discussed in Section 2.4.2, the research trend on rock joint roughness is currently towards the use of three dimensional surfaces focussing on the anisotropic features of joint planes (Jing et al., 1992; Kulatilake et al., 1995; Aydan et al., 1996; Grasselli et al., 2002; Jiang et al., 2006; Belem et al., 2007). However, in spite of the limitation of 2D roughness parameters caused by the irregularities of the asperities on joint planes, directional roughness profiles have been investigated by many researchers combining the roughness features with joint shear strength criteria or with measurement methods (Patton, 1966; Barton, 1973; Weissbach, 1978; Swan & Zongqi, 1985; Aydan et al., 1996; Xia et al., 2003; Shigui et al., 2009; Rasouli & Harrison, 2010; Bae et al., 2011).

The roughness profiles of the dip directions on the joint planes of interest are more important from an engineering perspective than that of the other directions. This is because the dip directions indicate the steepest angles which have the most potential of sliding behaviour. In site investigations, the roughness profiles of joint sets are thus preferably measured for the dip directions along the exposed joint surfaces relating to their shear behaviour. Recently, this priority of directional profiles for measurements is found in the studies of remote sensing methods. For example, a photogrammetry computer code, Sirovision (CSIRO, 2012) enables to extract roughness profiles for the steepest angle of a selected plane.

In the use of spatial coordinates, the roughness profiles of objects in any direction can be extracted by controlling object positions. However, there is a concern how the coordinates of a profile for a specific direction can be easily obtained from 3D surface models. Haneberg (2008) suggested a rotation procedure using a mathematical code for 3D rock joint surface models. In this case, a MATLAB script can be used to visualize and rotate the 3D surface models, which also consider the extraction of roughness profiles from the reoriented 3D models. The following section reviews the use of directional roughness profiles in rock engineering and the methods of profile measurements are also discussed.

2.5.2 Measurement of directional roughness profiles in rock engineering

The roughness of joints has been approached from a two dimensional viewpoint for decades. Patton (1966) presented a rock joint shear model, which quantified the roughness of joints by using the dilation angle i, of a sawtooth shape profile. Based on the criterion suggested by Barton and Choubey (1977), Bandis et al. (1983) presented the shear deformation characteristics of rock joints through considerable numbers of shear tests with various two dimensional roughness profiles. As these approaches require the accurate measurements of roughness profiles, there have been thus various attempts to obtain more accurate roughness profiles. Normal profile gauges have 0.5 to 1.0 mm step sizes and the sizes range from 100 mm to more 1 m lengths. The normal types of profile gauges are commonly used in both laboratory and field conditions. To increase the accuracy of measurements, Weissbach (1978) developed an instrument for measuring two dimensional profiles of rock surfaces. This device was able to draw the roughness profiles by using horizontal tracer steps ranging from 0.03 to 0.5 mm and the maximum sample lengths was 600 mm. The horizontal and vertical displacements are measured by transducers and plotted on the X-Y recorder as shown in Figure 2.8.

With the consideration of anisotropy, rock joint profiles were measured by a profilometer varying measurement directions. Aydan et al. (1996) presented a procedure to estimate the roughness characteristics of rock surfaces through measurements of joint profiles for rock samples. The measured profiles were digitized with a sampling interval of 2 mm and compared with those of the different directions. This research found that the length of profile varying with the measurement directions can affect the estimated roughness parameter as well as the sampling intervals.

Regarding the anisotropy of joint roughness, the roughness profiles of a large cylindrical natural rock sample (about 153 mm in diameter) were measured in different directions by a laser profilometer (Kulatilake et al., 1999). Measurements were performed in six different radial directions at every 30° interval on the sample surface. The surface height of a measured profile was recorded up to an accuracy of 0.124 mm. Based on their previous study (Kulatilake & Um, 1999), two fractal parameters (D and A) were then used to quantify the roughness of the model.

Using a LVDT (linear vertical displacement transducer), the surface topography of rock joints was measured with a profilometer with an automatic data acquisition system (Xia et al., 2003). This profilometer can control sampling intervals from 0.1 to 2.0 mm. The measured profiles were then used to identify the waviness and unevenness of the joint profiles with a proposed mathematical method in the study.
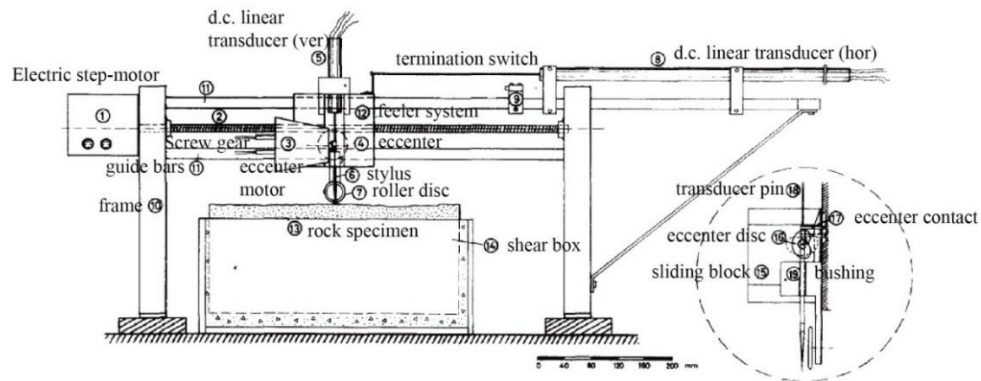
Fig. 2.8 Schematic diagram of a profilometer (Weissbach, 1978)

2.6 Remote sensing methods for rock joint roughness estimation

In field conditions, the surface roughness of rock joints is investigated in various ways. The roughness information is usually investigated by visual observation, touching and measuring with profile gauges. It has been normally accepted that the traditional methods are subjective and the quantification of roughness is a role for experts. In visual observation for the estimation of rock joints, rock joint roughness profiles are normally obtained by profile gauges with 1 mm or 0.5 mm step sizes. The profiles are then visually compared with typical standard profiles to quantify JRC values. Considering the limitations of human vision, the step sizes of 1 mm or 0.5 mm are acceptable as the standard point interval of the digitized profiles which can be obtained from photogrammetric 3D models. Recently, there have been attempts to employ laser scanning to capture the roughness of rock joints, and photogrammetry has also been employed to obtain roughness data.

2.6.1 Laser scanning methods in roughness investigation

To achieve more reliable JRC values than traditional methods, remote sensing techniques such as Terrestrial Laser Scanning (TLS) and Terrestrial Digital Photogrammetry (TDP) have been employed in both laboratory and site investigations. TLS has become more common to investigate JRC values by many researchers (Grasselli et al., 2002; Feng et al., 2003; Hong et al., 2006; Rahman et al., 2006; Fardin, 2008; Fekete et al., 2010; Tatone & Grasselli, 2010; Khoshelham et al., 2011; Mah et al., 2013) compared to TDP. This is due to the general understanding that TLS can produce a higher accuracy image with regular point intervals than TDP. However, it is difficult to ignore the significant advantages of photogrammetric methods which are portability, economic feasibility, legibility and convenience. Furthermore, photogrammetric 3D surface models can provide clear structural images to identify related geological issues from the exposed joint surfaces. In this section, representative studies on the rock surface roughness using scanning methods (laser, optical and structured light projection) are discussed.

A total station, as a type of point sensor laser scanner, was used for measuring rock joint surface roughness. Feng et al. (2003) measured a natural joint surface using a non-reflector TS, Leica TCRM 1102, which produces constant point intervals with minimum intervals of 1 mm. The TS system device was positioned at a distance of about 7 m from the rock cut, and scanned a small window (20 × 20 cm) at 5 mm point intervals. The results showed satisfactory accuracy for the large scale roughness, but not for the secondary roughness fractures due to the low resolution data points.

Grasselli (2001) reported the advantages of the ATS system (Advanced Topometric Sensor). The ATS, which is an optical measurement system and creates high density point clouds approximately 400,000 pixels per an image, was used for this study. In this system, two digital cameras are integrated into the measurement head at different angles, as shown in Figure 2.9. The accuracy of the point clouds obtained from ATS was reported as ± 50 μm for the measurement set-up chosen. The ATS in this study provided satisfactory precisions in laboratory conditions as well as convenient measurement controls. Recently, camera based scanning systems similar to the ATS have become popular to investigate rock joint roughness.

Using the camera based scanning system, Hong et al. (2006) studied the influence of the inclination of waviness for scanning directions on the estimation of roughness parameters. Laboratory tests were performed using a camera type scanner, ATOS II system. The created 3D models were analysed using the specific roughness parameters in two dimensions (SR_L) and three dimensions (SR_S). The experiments showed that the ATOS II produced relatively accurate roughness parameters thus reducing the influence of the dead zone which is caused by the inclination of waviness. Table 2-5 presents the specifications of the ATOS II.

A number of sets of two dimensional roughness profiles were investigated and acquired from triangulated irregular network (TIN) models by Tatone and Grasselli (2010). As an extension of their previous research, this study more focussed on the verification of the developed 3D roughness parameter than the feasibility of the employed remote sensing methods. This previous study was performed based on high resolution images obtained from close range laser scanning.
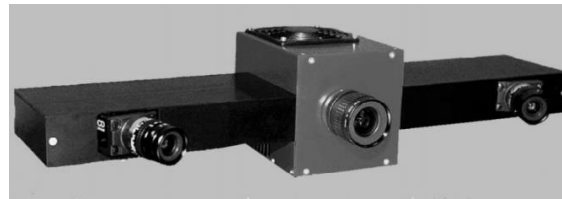
Fig. 2.9 Measuring head of the ATS (Grasselli, 2001)

Table 2-5. Specification of ATOS II (Hong et al., 2006)

Item	Specifications
Measuring volume	$100 \times 80 \times 80$ mm^3 – $1200 \times 960 \times 960$ mm^3 / measurement
Measuring distance	750 mm – 1600 mm
Camera resolution	1280×1024 pixel 12 bit (digit)
Measuring time	Approximately 8 s
Measuring point distance	0.04 – 1 mm
Measuring noise	0.002 – 0.02 mm

Using small scale roughness profiles, the influence of measurement noise in laser scanning was investigated by Khoshelham et al. (2011). The section of a natural rock slope was scanned with a Faro LS880 terrestrial laser scanner with a point spacing of 1 mm on average. The presence of noise led to an overestimation of the values of fractal dimensions and the amplitude of roughness profiles. In this previous study, the wavelet de-noising

method was suggested to estimate more realistic roughness values using laser scanning methods.

At a large scale, the accuracy of digital 3D models was discussed by Oppikofer et al. (2011). Using a large scale basalt sliding surface, the shapes of linear roughness profiles were investigated using digital elevation models (DEM). Oppikofer et al. (2011) reported the results of directional JRC estimation, which were obtained from large scale ALS-DEM models. Roughness values were estimated using the asperity-amplitude method mentioned by Barton (1981). The mean values of point cloud intervals ranged from 35 mm to 68 cm and the profile lengths ranged from 4.67 m to 72.9 m. The results also showed the importance of large scale roughness rather than centimetre-scale roughness for practical purposes.

In recent years, studies into JRC estimation for underground space have become popular. As an example, JRC values were estimated using a laser scanning method for a section of the Bankal tunnel in Oslo. Fekete et al. (2010) acquired consistent 3D roughness profiles from the section using a Lidar system, Leica Geosystems HDS6000. Similarly, Mah et al. (2013) reported the results of a laser scanning survey in an underground field. The amplitude values and the JRC values of selected roughness profiles were obtained from 3D models and compared with the result of manual measurements. The field survey was performed at a distance of 3 m from the rock surface of a nickel mine located in Thompson, Canada (Fig. 2.10). The results of the surveys showed that even though there were measurement errors arising from both manual measurements and laser scanning methods, the discrepancy of the JRC values was not significant.

In summary, the development of various scanning methods has enabled us to use the techniques for obtaining rock surface data in two and three dimensional conditions. It has been revealed that the scanning methods can produce roughness data forming a rock surface into point clouds with reliable accuracy in both laboratory and field conditions in close distance.
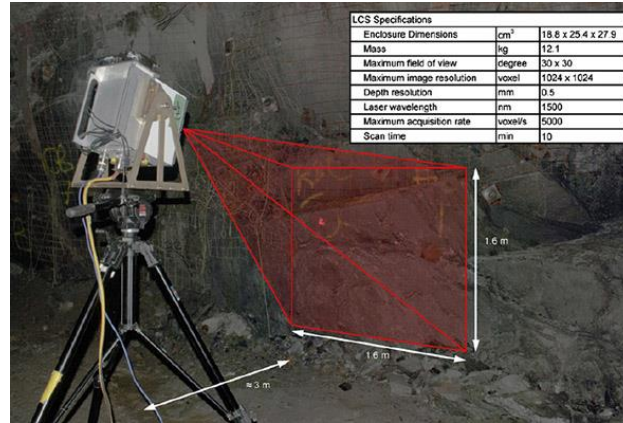
Fig. 2.10 Laser scanner in an underground situation (Mah et al., 2013)

2.6.2 Photogrammetry to investigate the rock surface roughness

Based on the advantages of various visual information obtained from images and the feasibility of photogrammetry for creating 3D surface models, many researchers used photogrammetry for characterizing surface roughness (Wickens & Barton, 1971; Jessell et al., 1995; Cravero et al., 2001; Lee & Ahn, 2004; Unal et al., 2004; Bistacchi et al., 2011; Sturzenegger & Stead, 2009; Nilsson et al., 2012). The applications of photogrammetry have been also found in wide ranges from archaeological to scientific purposes. However, the feasibility of photogrammetry for the roughness investigation has been insufficiently investigated in engineering purposes. Recent studies just covered basic issues for the applicability of photogrammetry to estimate JRC values (Haneberg, 2007; Baker et al., 2008; Poropat, 2008; Poropat, 2009).

Wickens and Barton (1971) investigated the possibility to obtain roughness profiles using a classic photogrammetry method. In the laboratory condition, the joint surfaces of rock samples were photographed using a stereometric camera, 'the Officine Galileo Santoni'. Roughness profiles were then plotted using a plotting device, The Thompson Watts Model 2, coupled to an automatic tape punch. The obtained profiles are superimposed on the rock joint samples, as presented in Figure 2.11. Using the plotting method, the spot heights of the profiles were observed at around 1 mm intervals for both lines on each joint surface image. This study showed the potential to measure the roughness using photogrammetry methods.

A new technique of photoanalysis was introduced by Franklin et al. (1988) and Maerz et al. (1990). This method uses shadows of asperities to reveal rock joint roughness clearly on the photographs. Through a set of laboratory tests, the shadow profiles, which were 325 mm length with 4.79 mm coordinate intervals, were obtained from a granite sample. The profiles were also measured by a mechanical profilometer. Comparison of both profiles from the experiments showed that the roughness parameters (R_p) of the mechanically measured profiles were similar to the values obtained from the shadow profiles.

Jessell et al. (1995) investigated the feasibility of photogrammetry to characterize rock surface roughness. Considerable sets of photogrammetric experiments were performed using stereo photographs, and a photogrammetry algorithm was developed.
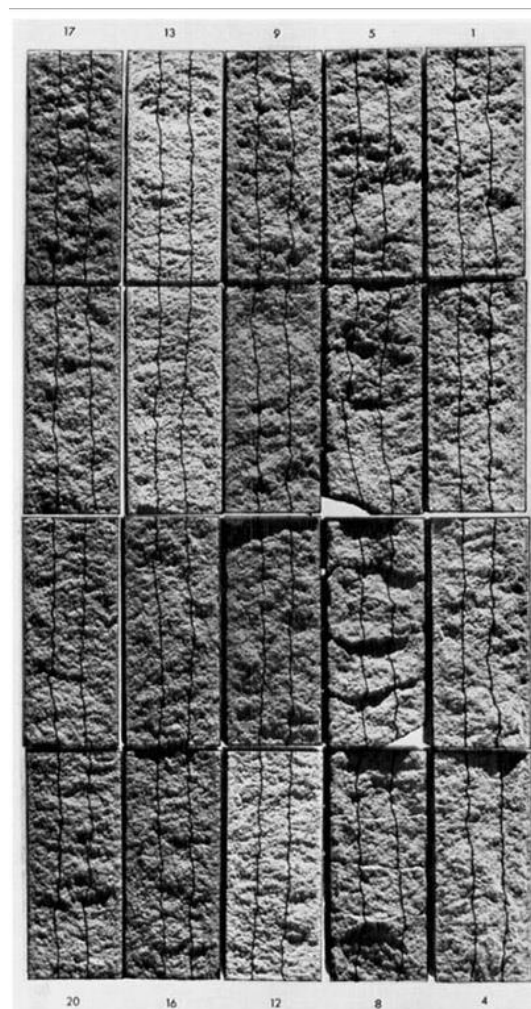
Fig. 2.11 Rock surface roughness profiles obtained from a classic photogrammetric method (Wickens & Barton, 1971)

In this study, negative format images were taken at a distance of 30 cm from the sample and the images were converted to digital formats by a scanning method, with a resolution of 75 pixels per inch. Using the prototype of photogrammetry algorithm, the 3D coordinates of the sample area were obtained. The analysed coordinates were compared with the manually measured data using a profilometry. The results showed that the photogrammetry algorithm generated a matching accuracy of 1 pixel for more than 90 % of the data.

As a similar study in geomorphology, Butler et al. (1998) used a digital elevation model (DEM) for characterizing the surface roughness of a natural gravel river bed. Close range digital photogrammetry was employed to capture the images of a specific area. Using an 80 mm Hasselblad ELX 500 camera, stereo image pairs were taken at a camera-to-object distance of approximately 2.2 m, and the base-to-distance ratio was kept at 1: 6. Stereomatching of the obtained images was carried out using the OrthoMAX module of Erdas Imagine software. The pixel size of the obtained images was approximately 0.6 mm in the object space. From this study, more precise 3D images were achieved as the quantified precision of the image matching was around 0.1 pixel (0.06 mm).

Under laboratory conditions, Unal et al. (2004) successfully measured rock surface roughness using a digital photogrammetric method. Stereo photographs were taken at a distance of 25 cm from the rock sample using a half-metric camera, Polaroid PDC 2000/40. The sample size was 7.75 cm × 7.75 cm, and a 3D roughness map was acquired using PICTRAN software. The acquired 3D surface model was exported with 0.25 cm point intervals by a graphic program called "SURFER".

Haneberg (2007) demonstrated that directional roughness profiles can be extracted from photogrammetric or laser scanning point clouds. In this research, linear roughness profiles were extracted from 3D photogrammetric models in desired directions relative to the dip directions of the joint planes, as shown in Figure 2.12. The procedure, which produces roughness profiles from 3D data, clearly showed a method to estimate JRC values based on the linear coordinates in alignment with the possible shear directions (dip directions).
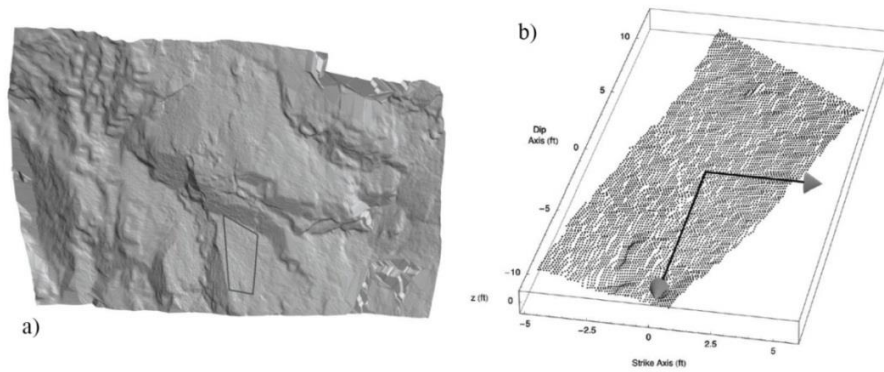
Fig. 2.12 Rock surface model obtained from Sirovision (a); Points after rotation of the coordinate to desired direction (b) (Haneberg, 2007)

Data noise from high resolution photogrammetric 3D models has been discussed by Poropat (2008). His study focused on the measurement errors induced by data noise when using small pixel sizes. JRC values were estimated from several digitized profiles. The simulated profiles were generated using 1000 data points. Compared with the general profile gauges for JRC surveys, which ranged from 0.5 to 1.0 mm comb intervals, the study investigated high density images. Against noise influence, which may result in overestimation, JRC values could be properly estimated using filtering algorithms when the noise is significant in relation to the sample spacing. Poropat (2009) also noted the JRC estimation using low resolution images with 2.5 mm pixel sizes at 100 m distances to objects. However, the applicability of this low level of image resolution to estimate JRC values has not been verified yet.

Through field photogrammetry surveys, Sturzenegger & Stead (2009) reported two methods for describing and quantifying rock joint roughness and curvature using 3D surface models. The first method is used to calculate the orthogonal distances between the average plane and the topography of a 3D model. The second method is carried out to identify the degree of curvature by selecting windows with increasing sizes to measure the orientations at many locations. As an example of the quantification of the curvature of joints on the Murrin Lake and Mount Seymour rock cuts, the linear roughness profiles and the curvatures of a 3D surface model are well reported in the literature (Sturzenegger & Stead, 2009).

Similarly, as an example of large scale roughness, close range photogrammetry was employed to survey a part of the Gole Larghe fault zone in Italy. High resolution 3D images, which were composed of spatial points with intervals ranging from 0.15 to 0.2 mm, were created using a Nikon D700 camera with a 28 mm focal length lens by Bistacchi et al.

(2011). The each frame of high density images was then reconstructed by a mosaic technique in the software Gocad® for the entire lengths of the fault zone as shown in Figure 2.15. Large scale roughness along the fault trace was effectively surveyed by the combined photogrammetry 3D model with the 3D data obtained by a Lidar system.

With comparisons between the photogrammetry data terrain model (DTM) and the laser scanned coordinates of a sample joint surface, Nilsson et al. (2012) verified the use of close range photogrammetry to create rock joint surface roughness. The images of a sandstone joint sample were taken at 0.5 m distance from the sample using a Canon EOS 5D mark II digital camera. 3D images were then generated by the commercial grade software 3DM Analyst (Adam Technology). The accuracy of the photogrammetric 3D models was verified based on the results of a series of laser scans which had an accuracy of up to 16 microns. This study showed how photogrammetry can be employed to create rock joint surface models with an accuracy of less than 1 mm intervals.

The literature review in this section indicates that the previous studies focussed on the applicability of photogrammetry with regard to surface roughness to create high resolution images. With the instinct advantage of photographs to deliver accessible information of objects, the motives of the previous studies can be explained as follows: Firstly, photographs possess a potential to express the roughness of an object by means of its shadow. The scales are also estimated by the relationships between the focal length and camera-to-object distances. Secondly, both the hardware and software of photogrammetry have considerably developed to produce the 3D models with satisfactory accuracy since the early 2000s. In third, it is difficult to ignore that the benefits of visual information of the original images in association with the created 3D models such as geological information.

For practical application, photogrammetry has not been sufficiently reviewed for the investigation of rock surface roughness. Especially, more research on the limitation and the accuracy of photogrammetric data is required to be discussed to establish the guidelines of photogrammetry for the investigation of rock surfaces. These issues are reviewed in the following sections.

2.7 Directional roughness profiles in 3D models

Since TLS (Terrestrial Laser Scanning) and TDP (Terrestrial Digital Photogrammetry) were employed to study rock joint surfaces, directional roughness profiles have been extracted from 3D surface models in laboratory conditions. A non-contact profilometer, the "rock profiler" was used for measuring roughness profiles of tuff joint sets for a set of dynamic direct shear tests (Hsiung et al., 1994). A laser profilometer was then employed to obtain digitized roughness profiles to create the 3D model of a natural rock sample (Kulatilake et al., 1999). The 3D model was composed of 400 parallel lines with 3.81 mm intervals.

In the early 2000s, the use of optical measurements has been widely reported in the rock engineering area. Grasselli and Egger (2000) quantified rock joint roughness by using an ATS system, which produces high resolution 3D images with approximately 400,000 pixels per image. Using a similar apparatus, Hong et al. (2006) obtained roughness profiles from the point clouds of 3D models by the following procedure; 1) The point clouds obtained from a laser scanner were firstly exported to ASCII format. 2) The 3D meshes are then generated to triangulated irregular networks (TIN). 3) 2D roughness profiles are finally extracted by image processing software. In his research, as the point intervals of the originally extracted profiles from the 3D scanner were not constant, a MATLAB code was employed to reconstruct the data with a constant interval as demonstrated in Figure 2.13.
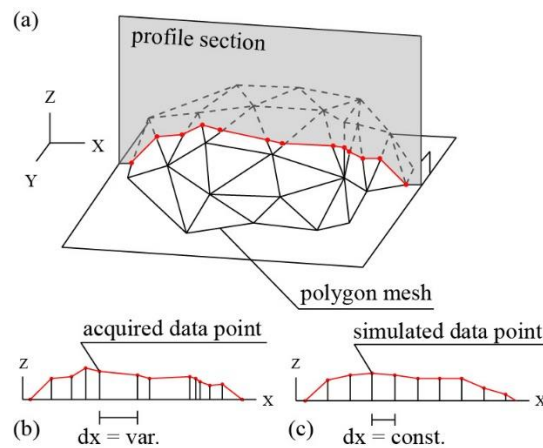
Fig. 2.13 2D profiles: (a) sectioning, (b) acquired 2D profile, (c) simulated 2D profile
(Hong et al., 2008)

Tatone and Grasselli (2009) investigated the roughness anisotropy under both laboratory and site conditions. 2D roughness profiles were measured in different directions. However,

the methodology for the rotation of the obtained point clouds was not presented in the research. This can be explained by their laboratory set up. The directions of the 3D data could be easily controlled by adjusting sample directions. The data extraction concept is demonstrated in Figure 2.14.

Large scale roughness profiles, obtained from a combined LIDAR application and photogrammetry, were analysed using a MATLAB® script by Bistacchi et al. (2011). In their study, the fault profiles were traced using RiSCAN PRO software and the 3D points along the fault traces were exported as ASCII format files for further analysis. The combined model produced roughness data in small scale (1 m to 1 mm) allowing for the estimation of roughness parameters along the range of the large fault zone.

More detailed procedure to obtain roughness profiles from 3D models was given by Mah et al. (2013). The investigators discussed that the difference between manual measurement and 3D laser scanning may cause unmatched joint orientation resulting in a difference in JRC estimation. In their study, from 3D surface models, two dimensional roughness profiles were generated by binning the points along the length of the profiles and calculating the average offset of all points falling within each bin. JRC values were then estimated by using Barton's empirical chart for the straightedge method (Barton and Choubey, 1977).
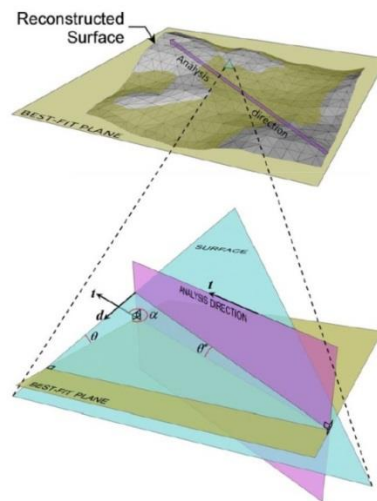
Fig. 2.14 Schematic diagram illustrating the geometric definition of azimuth, dip and apparent dip in relation to the selected analysis direction (Tatone and Grasselli, 2009)

The methodology of the point cloud rotation was described by Haneberg (2007). Focussing on the importance of the dip directions of rock joints, Haneberg (2007) established a method to produce directional rock surface profiles from photogrammetric 3D models and

laser scanner point clouds. Using an example of large size rock surface 3D models, the dip line of the surface can be identified in the first stage. Then, the 3D coordinates could be rotated into alignment with the dip line using a 3D rotation matrix. Thus, linear profiles could be extracted in any direction followed by interpolation of a regularly gridded surface. An example of the data rotation and aligned profiles is presented in Figure 2.15.

Sirovision (CSIRO, 2012) provides a tool to extract a roughness profile and roughness parameters for the steepest descent for the selected area. The dip and dip direction of the selected area are calculated and the JRC values for the line of steepest descent are estimated by the functions of Tse and Cruden (1979) and Maerz et al. (1990). This computer program also allows to obtain JRC values for different bearing angles for the same area.
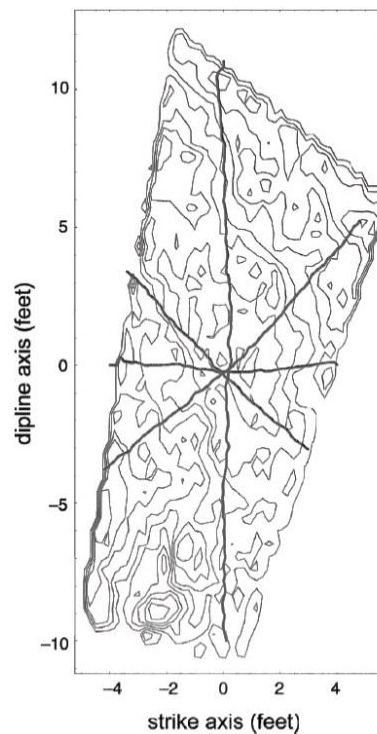
Fig. 2.15 Graphical depiction of surface roughness after rotation using roughness profiles (dark grey) superimposed on contours (light grey). Contour interval is 0.02 feet (0.6 cm). Units of length are feet (Haneberg, 2007)

2.8 Influencing factors of photogrammetric errors

It is generally accepted that photogrammetry surveys often require the use of high-end cameras and longer focal length lenses to keep high spatial resolution in order to obtain reliable JRC data from photogrammetry. However, the uncertainty of the accuracy and

precision of photogrammetric roughness data is derived from various factors as well as from the limitation of camera equipment. The influencing factors associated with the photogrammetric 3D models have been widely discussed by many researchers (Fraser, 1984, 1992; Butler et al., 1998; Poropat, 2008; Dai & Lu, 2010; Dai et al., 2014; Fooladgar et al., 2013) and summarized by Dai et al. (2014) in Table 2-6. In this section, the influencing factors are discussed by two categories: camera systematic errors and planning errors.

Table 2-6. Behaviours of photogrammetric modelling (Dai et al., 2014)

Factor	Behaviour
Distance	Farther distance, lower accuracy (40 m: 6~10 cm)
no. of overlapped images	The larger number of overlapping photos, the better accuracy
Intersection angle	The closer to 90°, the better accuracy
Angle of incidence	The closer to 0°, the better quality of images, so the better accuracy
Camera model	Higher end, higher accuracy
Resolution	Strong correlation with accuracy (raise by 1.6% per 1 MB increase)
Features (texture)	More features, higher accuracy; higher accuracy by colourful texture than grey/plain texture
Focal length	Longer focal length, higher accuracy; set to obtain optimum coverage
Camera lens	Less distortion, higher accuracy

2.8.1 Camera systematic errors

The measurement errors related to photogrammetry can be categorized by the following two aspects: one is due to camera systems and the other is attributed to bad planning of camera network geometry (Dai et al., 2014). The systematic errors can be identified as a deviation that occurs consistently due to the inaccurate factors of camera systems. The examples of the camera factors are lens distortion, principal distances and image resolutions. The resolution limit of photographs is the most essential factor in investigating the rock surface roughness. The pixel size of images is dominantly governed by the sensor size of cameras and the focal length of lenses in the same camera-to-object distances. The combinations between sensor sizes and focal lengths can theoretically count the measurement scale. However, the estimations should be carefully interpreted. Focussing on the measurement of the point distances along a roughness profile, Poropat (2008) reported the importance of post processing algorithms to obtain reliable point intervals for both laser scanning and photogrammetry.

The density of photographs can be estimated using the camera distances and the dimensions of camera devices which are the sensor size of cameras and the focal length of the employed lenses. Photogrammetric methods provide spatial points at every pixel and the accuracy of the image can be quantified using the pixel sizes. A well planned photogrammetry setting, which is the combinations of the camera, lens and survey distances, is essential to obtain the required pixel size to cover a given area by using the combinations of the factors. The scale of digital images is estimated by the ratio between the size of a pixel on the image sensor and the size of a pixel on the real object as presented in Eq. (2-26). This ratio varies with the focal length of the lens and the camera distance from the object.

$$\text{Ground pixel size (GPS)} = \frac{d}{f} \times \text{Sensor pixel size (SPS)} \qquad (2\text{-}26)$$

where d is a camera distance and f is a lens focal length. For example, using a DSLR camera Nikon D7000, GPS values are depicted with camera distances using three different focal lengths in Figure 2.16. If the required pixel size is 1 mm, photograph distances are varied with the employed focal lengths. A shorter focal length, 24 mm lens, requires a closer photographing distance (5.6 m) than a 85 mm lens (17.8 m).
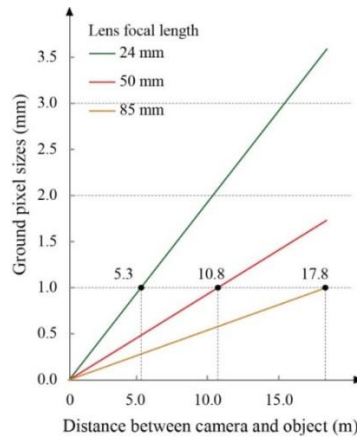
Fig. 2.16 Ground pixel sizes paired with three different focal lengths

However, it is important to note that the point intervals of 3D images are different from GPS values. The obtained pixel sizes of 3D models depend on the algorithms of employed photogrammetry codes. The acquired point data from remote sensing methods is formed as 3D point clouds. An interpolation process is required in the next stage to create a regular grid which forms a surface topography. The details of the photogrammetry processes are well covered in the literature (Poropat, 2008; CSIRO, 2012; Birch, 2006). Thus, in the

40

photogrammetry process, range measurement resolutions may be not linearly proportional to the variations of the combination of sensor sizes and focal lengths. Poropat (2008) reported that 3D point cloud data, which are randomly scattered, are linked to form a triangulated network resulting in a regular grid through some forms of photogrammetric processing. The image resolution of 3D models is a kind of camera factors which lead to image based errors. The influence of the image resolutions are in-depth discussed in this study.

Lens distortion is one of the most significant factors that can lead to systematic errors and needs to be taken into account for any photogrammetric application (Dai & Lu, 2010). The lens distortion is composed of two types of distortions, which are the radial distortion and the decentering distortion (Fraser, 1996). The decentering distortion occurs when the set of lenses of a photogrammetry setup are not collinear. In case of the radial distortion of a single optical lens, the distortion effect is magnified along the radial direction of the lens; thereby the sizes of the errors are dependent on the distance from the centre of the images. The influences of the lens distortions and principal distances can be reduced by adjusting the relative parameters through a camera calibration procedure. Currently, three representative commercial-grade digital photogrammetry packages 'Sirovision' (CAE), '3DM Analyst' (ADAM Technology) and 'ShapeMetrix3D' (3G Software and Measurement) require periodic calibration of the employed lens and camera combination or support for the calibration in the camera and lens data (Haneberg, 2008).

The photogrammetry packages mentioned above provide a function to calibrate for the employed lenses. ShapeMetriX3D provides a tool for camera calibrations using targets containing a regular pattern of dots (Gaich et al., 2006). 3DM Analyst employs 11 camera parameters to calibrate lenses with an accuracy of from 0.1 to 0.2 pixels (Birch, 2006). A window shot of the calibration procedure is demonstrated in Figure 2.17. Siro3D (CSIRO) also operates modules to calibrate the employed lenses. The module uses either a set of lens generic calibration or custom calibration data. The generic calibration is accurate to approximately 1:2,000.

In the case of the custom calibrations, the specific employed cameras and lenses can be calibrated using appropriate camera calibrator software such as 'iWitness® (Photometrix)'. The calibration files saved using these programs supply the '.iwp' format files which can be read by 'Siro3D'. The calibration data can also be input manually. 'Siro3D' provides

facilities to add the distortion data to an image. Adding calibration to an image can be performed by simply selecting a set of images. After selecting the image files, the custom calibration files (<name>.ccf) for the particular focal length are then selected. If any custom file is not available, a generic calibration is then possible.

The principal distance of a camera is defined as the distance of the perpendicular line from the centre of the lens employed to the projected plane of the camera. This distance can also cause a systematic error of the 3D images. The errors can be reduced when the object is positioned along the optical axis.
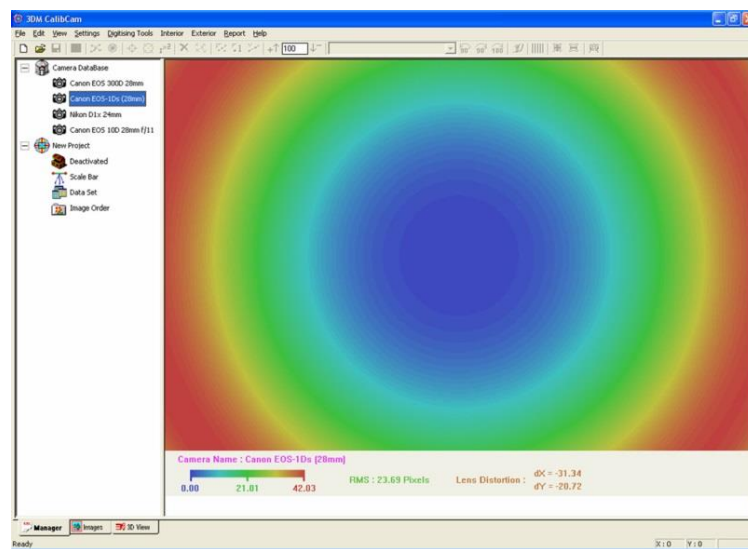
Fig. 2.17 Colour-coded lens distortions of a 28 mm lens (Birch, 2006)

2.8.2 Planning errors

In photogrammetry surveys, planning factors such as baseline distances, photograph overlaps, angles of incidence and camera intersection angles represent camera network geometry influences on the accuracy of 3D models. The camera networks, which indicate the positions of cameras and objects, are decided by the purpose of the survey in the planning stage. The camera positions and the angles of photographs according to the survey purposes have influence on the all relevant factors mentioned above. In order to create accurate 3D images, the camera networks should be properly controlled based on the understanding of following the recommendations in the survey planning stage.

Depth accuracy is a term to explain the accuracy of the view direction compared to the plan view. The depth accuracy of 3D images depends on the base-to-distance ratio. It is known from Eq. (2-27) (Birch, 2006) that the depth accuracy is improved when the baseline length is increased. However, photogrammetry software suggests an effective range of the ratio for creating the best matching 3D models. In addition, in a general photogrammetry setup for rock slope surveys, the large base distances of the stereo photographs result in two different views. This may lead to difficulty in recognizing common points in the matching process of photogrammetry (Birch, 2006).

$$\text{Depth accuracy} = \text{Planimetric accuracy} \times \frac{\text{Distance}}{\text{Baseline}} \qquad (2\text{-}27)$$

Practically, photogrammetry programs recommend a desirable range of base-to-distance ratio ranging from 1:10 to 1:2 (CSIRO, 2012; Birch, 2006) for rock slope surveys. However, the idea of baseline distance ratio may not look as simple when the camera positions are not equidistant from the rock slope cuts being imaged (CSIRO, 2012). This can be more influential if the images are taken at close distances. This means that the baseline distances can influence differently according to the positions of targets in the same image.

The numbers of overlapped images and their overlapping percentages also influence the accuracies of 3D models (Dai and Lu, 2010). To obtain accurate 3D images, it is important to strike a balance between the levels of image density needed, completely covering the area with overlapping stereo images and photogrammetry processing time (Matthews, 2008). The overlapping percentage to obtain the best stereophoto pairs is also related to the employed photogrammetric algorithms. The recommended stereophoto pairs generally have an overlap of more than 60 % (CSIRO, 2012; Matthews, 2008).

The angle of incidence is the angle between the optical axis of the lens on a surface and the line perpendicular to the surface. It should be noted that this angle should be reduced to obtain accurate 3D models. Orthogonal photographs are thus desirable for minimizing the image base errors. However, in a close camera distance to an object surface, the incidence angles can be different for the areas of interest due to the irregular shapes of the surface to the camera axis. This is a reason why the accuracy and precision of 3D images can be different in accordance with the positions of objects on a 3D model.

Occlusion and orientation bias, which result in shadow zones or missing spatial parts in the 3D models, are major limitations of remote sensing methods (Sturzenegger, 2010). These errors are caused by missing data when protruding parts hide a part of the rock surfaces or when the surface orientations are parallel to the angle of the line of view as shown in Figure 2.18. The camera positions should be planned to avoid or minimize the influences of both errors through careful observations of the rock cuts of interests.

In photogrammetry applications, many uncertainties in the field such as environmental conditions including lighting directions and view angles make independent error assessment difficult. In this study, the influence of camera incidence angles and camera intersection angles are discussed by comparison of test results between a set of laboratory test and considerable field test results in Chapters 5 and 6.
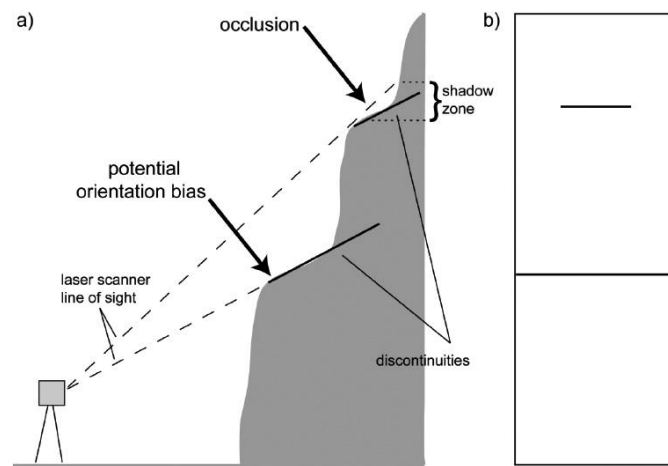
Fig. 2.18 Illustration of occlusion and vertical orientation bias, Side view (a), Front view (b), Rock cut view from the camera/scanner perspective, showing discontinuity traces (Sturzenegger and Stead, 2009)

2.9 Conclusions

This chapter reviewed literatures on relevant conceptual areas in relation to the investigation of rock joint roughness using photogrammetry. The main ideas are presented in the following four categories.

Firstly, this study focuses on the roughness data of exposed joint planes among the information obtained from the surfaces of exposed rock masses. The literature review covered the practical application of rock joint roughness data from the evaluation of the

roughness to the use of the roughness in engineering practice. Typical roughness profiles have been used as a standard for the quantification of roughness. The investigation methods in sites and laboratory conditions were discussed in detail. The level of accuracy for the measured roughness data depends on the measurement device such as profilometres and profile gauges. In manual measurement, the traditional profile gauges (0.5 ~ 1.0 mm intervals) have been widely used as a standard for the level of accuracy of roughness in rock engineering.

Secondly, this study reviewed roughness parameters in relation to the rock surface investigations. Recently, the studies on roughness characteristics obtained from remote sensing techniques have been preferably discussed using three dimensional parameters. However, with consideration for the usability of manual measurement and for survey techniques, two dimensional roughness parameters can be more appropriate to investigate the extent of accuracy of photogrammetric 3D models. The typical JRC ranges introduced by Barton et al. (1977) and ISRM (1978) have been largely employed for the joint roughness investigations. To establish the best combination with the JRC ranges, many researchers have tried to apply different roughness parameters to the regression functions. These mathematical approaches, which involve the limitations of the mathematical representation to define the JRC ranges, however have offered the possibility to be used for the quantification of JRC values by using 3D surface models.

Thirdly, this study discusses the feasibility of photogrammetry as a tool for roughness investigations. 3D surface models, which are obtained by applying close-range photogrammetry, can provide information on the roughness of the object surfaces. The availability of survey technique including digital cameras and the increasing capability of computer programs have expanded the feasibility of photogrammetry technique to an alternative way of the traditional profilometers. However, the extent of accuracy has not been sufficiently investigated. It is because that photogrammetry has been used for analyses focusing on large scale models. As photogrammetric survey methods are developing, the level of accuracy for roughness investigations should be established to the best advantage of this technique.

Fourthly, the accuracy of photogrammetric roughness data has been an important issue. However, relevant studies have been insufficiently discussed due to a number of influential factors. The relevant errors can be induced by both the camera factors and the planning

factors. The optical limitations which directly govern the resolution of images can be estimated by using the combinations of the equipment employed. However, the most uncertainties by external factors derived from the irregularity of objects and the changes of camera networks. The extent of accuracy for the obtained roughness from photogrammetry has not been appropriately established.

As reviewed in this chapter, the research scope is focussing on the accuracy of photogrammetric roughness data in two dimensional conditions. This has been achieved by experimental studies based on photogrammetry surveys and laboratory tests throughout this PhD study. The following chapter contains the fundamentals of stereo photogrammetry and the methods of profile extraction from 3D images to assist field surveys and post processing for successful data collections planed in this study.

3 METHODOLOGY

3.1 Introduction

This chapter reviews the process of the study. The research methodology is classified by the following three main categories. The first phase of this study is to collect roughness data by performing photogrammetry in various site surveys. In this phase, the obtained JRC data are applied to practical engineering issues as a parameter and the results can derive the limitations and problems of the JRC values obtained from photogrammetric method. Secondly, the main aim of this phase is to develop a model which can estimate global photogrammetric errors for JRC estimation in an ideal laboratory condition. A set of photogrammetry laboratory tests is conducted and the data is statistically analysed. In the third phase, the feasibility of the developed model is verified by a statistical analysis using collected JRC data obtained from the site surveys in the first phase. The process of this study is briefly demonstrated in Figure 3.1.

This chapter presents the methodology of the first phase. This includes overall photogrammetry methodology employed in this study from the planning to the procedures of post-process. This also summarizes the photogrammetry site surveys and the equipment employed. The methodology of the second phase and the third phase of this study are discussed in detail in Chapter 5 and Chapter 6 respectively to enable streamlined discussions related to the subjects.
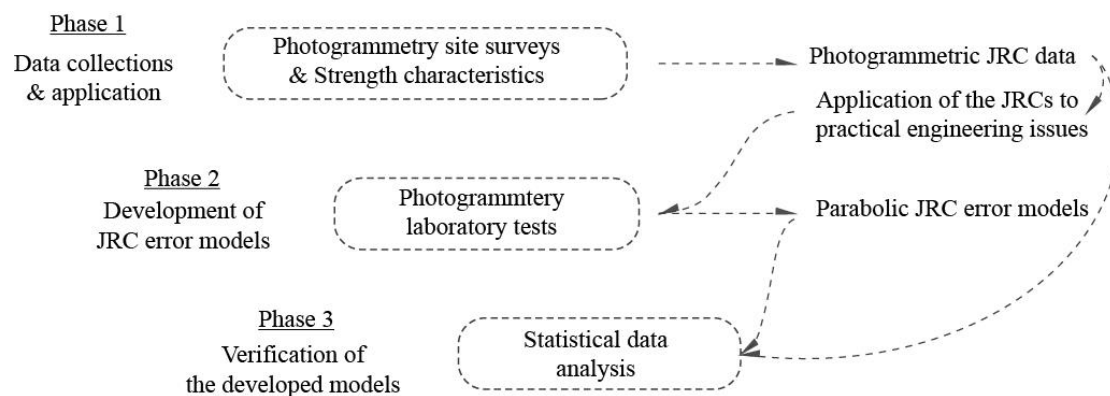
Fig. 3.1 Research methodology flowchart

3.2 Data collection

3.2.1 Digital photogrammetry

The methods of photogrammetry have been developing for over a century, while digital photogrammetry only began to be used in early 1990's (Baltsavias, 1999). Close range digital photogrammetry has developed in rock slope engineering, especially in situations where manual investigations may be dangerous and impractical. Even though the use of laser scanning has strongly increased to investigate rock slopes, photogrammetry has advantages over terrestrial laser scanners in terms of cost, convenience and a variety of other factors. Further, close range photogrammetry, which takes images at relatively small distances from tens to hundreds of metres, allows the use of DSLR cameras rather than more expensive devices for long range photographs.

The mounted higher resolution sensors on readily available DSLR cameras have enabled photogrammetry to produce high density 3D images. In the case of a 10 megapixel DSLR camera, high density images from 800,000 to 900,000 points, can be created to make 3D images (Haneberg, 2008). There are three main parameters which control average point spacings: camera sensor size, lens focal length and camera-to-object distance. These parameters should be mutually adjusted in photogrammetry surveys to obtain the desired resolutions from 3D images.
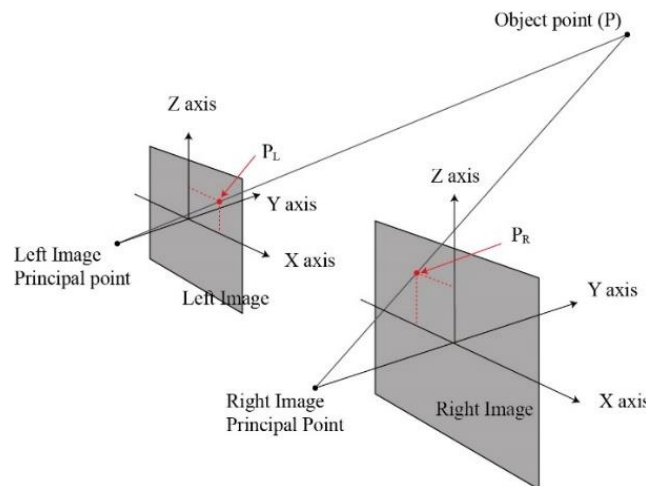
Fig. 3.2 Geometry for the determination of the position of a point in object space using photogrammetry (Poropat, 2006)

The principle of photogrammetry can be explained by the calculation of 3D coordinates based on the coordinates of images, employed camera parameters and ground control points (Wolf and Dewitt, 2000). In the pair of images, the stereoscopic parallax, which is the position change of an object with respect to the changed camera locations, demonstrates the principle of photogrammetry as shown in Figure 3.2. In the 3D coordinate system, the x coordinates of the point P on both images are located in different positions as P_L and P_R. Accordingly, the 3D position of point P is identified using relationships between the relative positions obtained from the images and the camera perspective centre. In practice, this extensive calculation is generally performed by photogrammetry algorithms.

Photogrammetric methods create 3D images using two or more images. Stereoscopic images are produced by taking two images from two different camera positions. 3D models are achieved from the overlapped area of both images (see Fig. 3.3). For example, a slope surface can be photographed and the 3D image of the overlapped area is generated by a photogrammetry program. To obtain better 3D images, after the size and area of interest is established, the most effective photo layout for the area should be determined. It is important to mention that the overlapped portion should be more than 25 % of the image area when taking photographs (CSIRO, 2012) and the best stereo image pairs have an overlap range of 50 to 60 %.
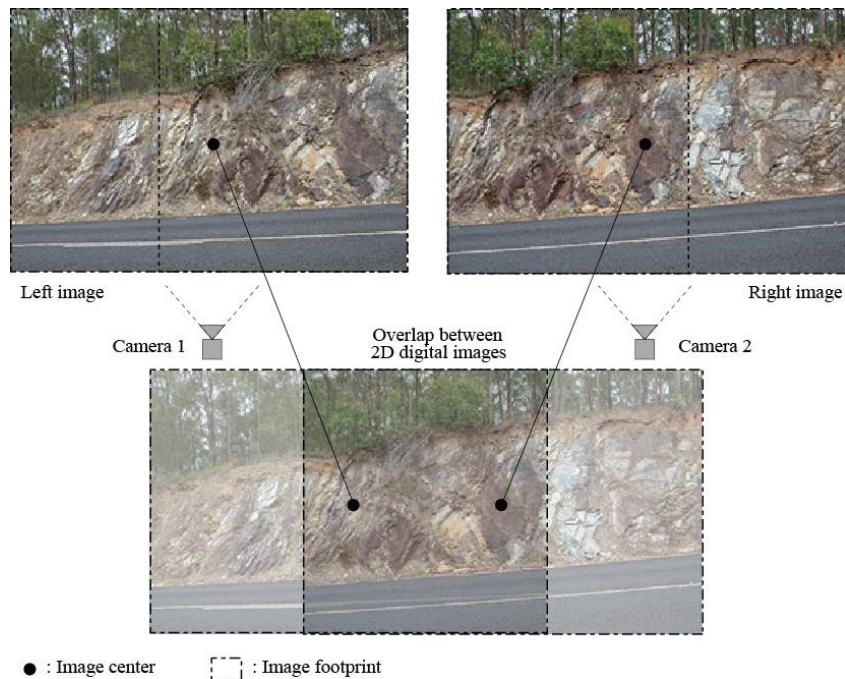
Fig. 3.3 An example of image capture setup for 3D model

Based on the principle of stereo photogrammetry, various photogrammetry programs have been developed for creating 3D models. Autodesk 1, 2, 3 (Autodesk) is a representative freeware at present, which enables anyone to create 3D models. For specialized purposes, several commercial grade photogrammetry programs have been developed and used in various industries. The programs provide functions which allow practitioners to identify the orientation of discontinuities and to extract roughness profiles from the 3D models.

There are three major photogrammetry software packages. The first code is Sirovision (CAE) which was developed by the 'CSIRO Mining and Exploration Division' in Australia. Secondly, ShapeMetrix3D was developed by '3G Software and Measurement' in Austria. The third is 3DM Analyst from 'ADAM Technology' in Australia. In terms of the procedure for creating 3D models, the three packages are the same in principle and have similarities in their procedures (Haneberg, 2008). This study uses 'Sirovision' as a photogrammetry code. Thus, the details of methodology described above refer to the procedures from Sirovision (CSIRO, 2012). Differences in the details of field procedure with Sirovision are described in the papers by Gaich et al. (2006) and Birch (2006).
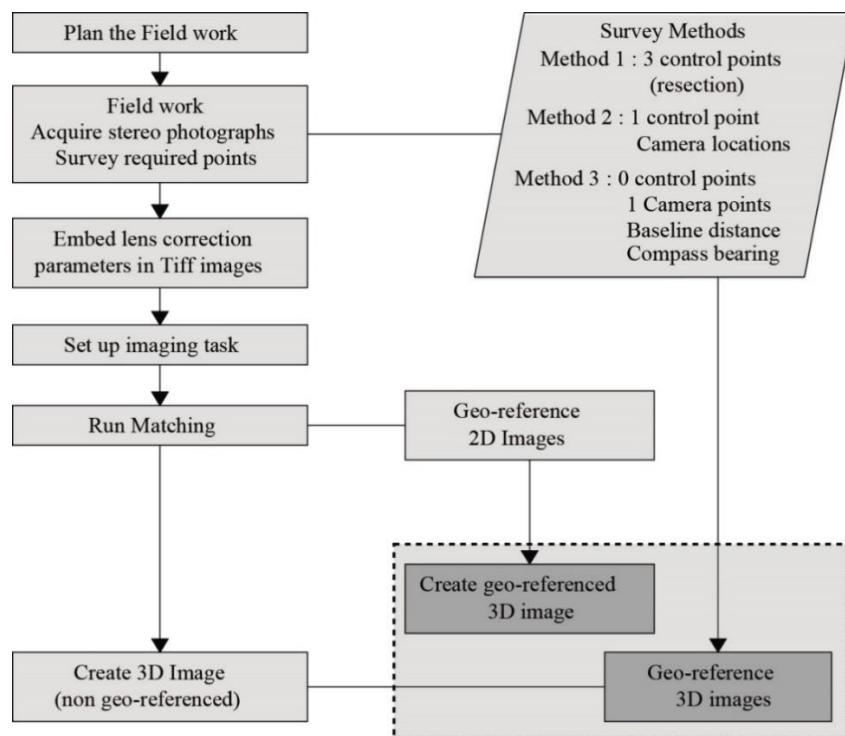
Fig. 3.4 Description of the work flow for 3D image generation (CSIRO, 2012)

Captured images produce arbitrarily scaled data through an automated coordinates matching process to find corresponding image points on pairs of images. The 3D models are then

oriented and scaled appropriately through a geo-referencing procedure. The surveyed locations of the cameras and target points during photogrammetry investigations are required for the orientation and scaling of the 3D image. It enables the 3D models to have exact bearing angles and dimensions. Figure 3.4 shows a procedure for the generation of 3D images from photogrammetric methods based on 'Sirovision'.

As discussed in Section 2.8.1, the density of the produced 3D images is not simply predicted due to various field conditions. For engineering purposes, the roughness of a rock surface has not been sufficiently investigated using photogrammetry, so the appropriate scales of 3D images for roughness estimation can be an issue. The pixel sizes of 3D images can be roughly predicted by both a brief estimation of the pixel size and a guideline supported by previous studies (ADAM technology, 2008).

Alternatively, another photogrammetry process, the structure from motion (SfM), has been also used for a wider variety of purposes, as it provides a high level of flexibility in terms of availability in both planning and equipment. SfM has been developed to be more user-friendly by determining internal camera geometry and camera position and orientation automatically and by using consumer-grade cameras. The applications of SfM have been used for various geoscience applications, from topographic landscapes to small scale objects. The advantages of the SfM technique over traditional digital photogrammetry methods have been reported by many researchers (James & Robson, 2012; Westoby et al., 2012; Fonstad et al., 2013; Bemis et al., 2014; Micheletti et al., 2015). This method requires multiple photographs with large overlap collected from different positions and directions. For this technique, a variety of cameras and software can be used to obtain the photographs to be used in the processing, including cameras built into UAVs and kites (Niethammer et al., 2012; Vasuki et al., 2014; Bemis et al., 2014; James & Robson, 2014; Ryan et al., 2015).

3.2.2 Camera and control points positions

The next consideration when designing the stereo photogrammetry layout is the camera positions that are required for establishing appropriate camera distances from the targets (S) and between the two camera positions (d). The camera distances (S) are normally

determined by the required size of the footprint of images, and the distances (S) can be approximately measured by a laser rangefinder.
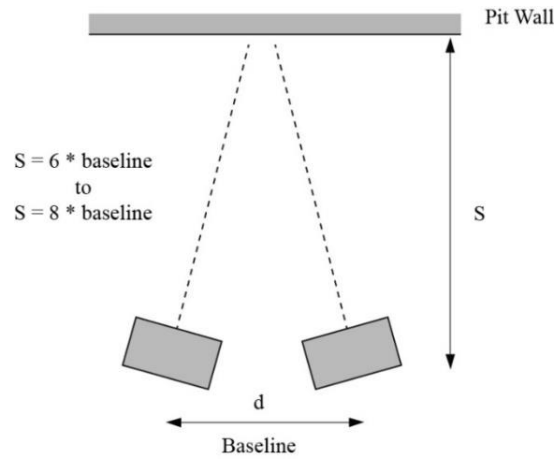
Fig. 3.5 General layout for camera positions (CSIRO, 2012)

The baseline length (d) is the distance between two camera positions. This value should also be approximately determined to obtain an effective photograph layout. Based on the camera-to-object distance, 1/6 ~ 1/8 of the target distance is recommended as an appropriate baseline length (CSIRO, 2012) (See Fig. 3.5). The suggested baseline-to-distance ratio varies with the photogrammetry algorithms employed. The camera locations can be marked by nails or flags and then surveyed using a GPS device or a survey instruments such as a total station.

However, it is worth mentioning that the preferable baseline-to-distance ratio can be varied with the employed focal length of lenses when the same camera axis is used. Considering the most effective photograph overlap layout (60 %), the overlap areas, which are taken at the same camera positions, are varied with the focal lengths (See Fig. 3.6). The view direction should be considered in relation to the planning error factor of the incidence angle of cameras as presented in Section 2.8.2.

The usual arrange of the camera setup is that the base of the stereo camera setup is parallel to the plane of the object view, and the line of sight from the camera intersects the object plane orthogonally as demonstrated in Figure 3.6. Interestingly, Dai and Lu (2008) presented that an oblique angle between both stereo cameras can minimize the systematic error caused by lens distortion. The influence of camera position is well demonstrated using the relationships between the point locations in their study.

52
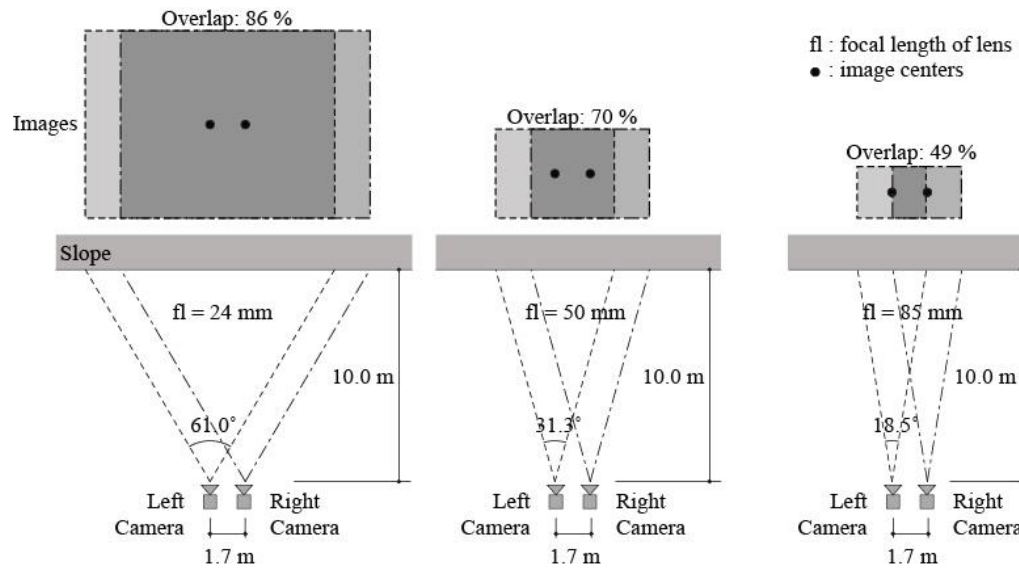
Fig. 3.6 Stereo pairs taken at the same camera positions according to the focal lengths

This means that if the angle between the optical axes of the stereo cameras is close to a right angle (90˚), the errors due to the incidence angles are reduced. However, orthogonal photographing of objects is normally recommended to achieve the best result for 3D modelling. In this study, photographs are taken in an orthogonal direction to the object in the laboratory tests, and the slopes in the field photogrammetry surveys. The orientation of the line of sight is specified by a bearing angle of cameras to the north.

The photogrammetry programs support several different procedures to determine the positions and orientations of cameras. As a process of the data setup, the positions and orientations of cameras can be determined by importing the survey data. The camera locations are normally recorded by reading a GPS device. Then, the surveyed geographic coordinates of the cameras and control point positions are requested to complete the geo-referencing procedure for creating 3D models. The original coordinates are expressed by the geographic latitude and longitude system. The ellipsoidal coordinates can then be translated to the Cartesian coordinates by mathematical calculations. The calculations are carried out using the GRS80 ellipsoid in this study. The GRS80 ellipsoid is used for Australia's new coordinate system. The conversion procedure is well presented in Geoscience Australia (www.ga.gov.au). The geographic Cartesian coordinates, easting, northing and the elevations of the positions are used for the surveying information. Table 3-1 presents an example of the survey data of the Bethania slope which is one of the survey sites performed in this study.

53

The format of survey data is a standard ASCII text file with either 3 or 4 columns of survey data. Generally, photogrammetry for large scale 3D models requires that surveyed control points should be placed with a preferred arrangement. Figure 3.7 demonstrates an example of a control point marked on a large mining site. The ground control point is a position that has been surveyed and marked for use as a spatial reference. However, in close range photogrammetry, surveyed ground control points are not always required. It depends on the purposes of the survey. For a geo-referencing of a small scale object, by placing an object of known length, such as a scale bar, an accurate scale 3D model can be created. Current photogrammetry codes also provide various options to achieve geo-referencing for the cases when the survey supports are not available.

Table 3-1. An example of survey data (Bethania, Brisbane)

Positions	Geographic coordinates		
	Easting	Northing	Elevation
Camera #1	515789.297	6935706.919	125
Camera #2	515784.325	6935707.444	126
Control point #1	515763.245	6935723.345	128
Control point #2	515734.675	6935745.645	129
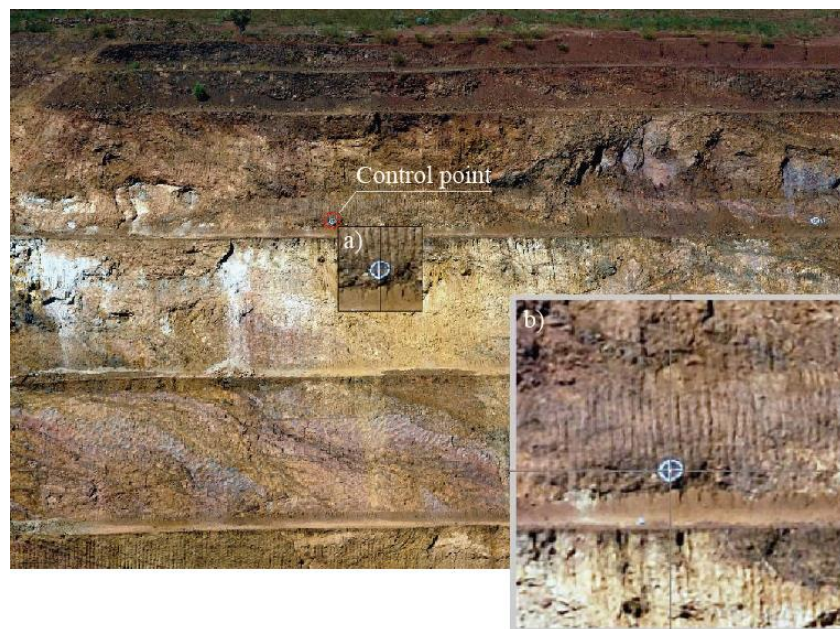
Fig. 3.7 An example of ground control points; selecting a ground control point (a), zoom window of the control point (b) (CSIRO, 2012)

3.2.3 3D model creation

The conditions of image acquisition largely depend on a variety of camera options. Essential recommendations in the use of digital cameras will be thus highlighted in this section. First of all, the preferable image format for image acquisition is the 'RAW' format, which is the highest resolution and contains the original information of the images. 3DM Analyst (ADAM Technology, 2002; Matthew, 2008) and Sirovision (CSIRO, 2012) recommend using 'RAW' format images and converting the original images into 'TIFF' format. JPEG images are not suitable for post processing.

Secondly, in the case of camera modes, it is also recommended that aperture priority exposure mode (A or Av), which uses a specific aperture value, is preferable to control lighting and the depth of field. It is recommended that an aperture of f/8 provides a good depth of field resulting in easy focus (CSIRO, 2012; Matthew, 2008). In terms of focus setting, the manual focussing mode can help to keep the same focal distances for both images in the stereo sequence, although autofocus is also available. Matthew (2008) proposed that a shutter speed of at least 1/200th of a second is normally required for handheld photography without a tripod to support the camera. However, the use of a tripod is necessary, not only for obtaining better quality images in terms of the accuracy of 3D models, but also for the accurate operation of the camera axis. This is especially important when photographs are taken at close distance from the objects.

Using captured images in stereo photography, 3D models are created by using a photogrammetry code. In this study, topographical information of selected rock slopes are analysed using a software package 'Sirovision' (http://www.sirovision.com/). The Sirovision package includes two different modules which are 'Siro3D' and 'Sirojoint'. 'Siro3D' creates 3D models from captured digital images and 'Sirojoint' analyses the 3D images for the structural characterization of joint sets. Figure 3.8 demonstrates a 3D model which was obtained from two digital images taken at a cut slope in Bethania. This excavated rock cut has a height of around 20 m height and the stereo images were taken at 33 m distances.
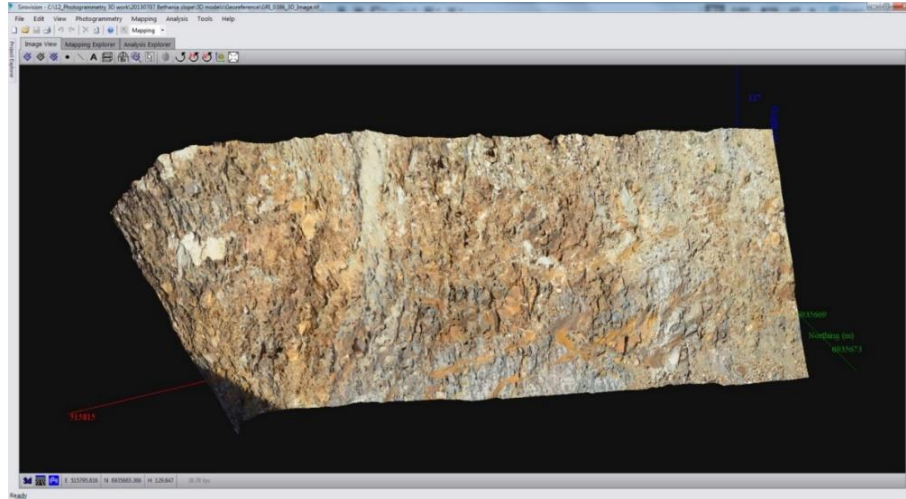
Fig. 3.8 A 3D image of Bethania slope which was generated by 'Siro3D'

In order to create a 3D image, the following stages are required:

① Processing the images to correct the effects of lens distortion: lens calibration

② Selecting an area to be overlapped from which a 3D model is to be made

③ Matching the image data for the two images being used to create the 3D model

④ Determining the orientations of the left and right 2D images: geo-referencing

Details of each stage will be described in the following section.

3.2.4 Camera and lens calibration

To remove the errors induced by the camera and lens distortions, calibration of the camera and lenses is required prior to the 3D model creation procedure. Sirovision provides two options for the calibration procedure. Firstly, generic calibration data can be used for the combination of the employed camera model and the lenses. Figure 3.9 demonstrates the list of supported cameras and corresponding lenses in the use of Sirovision. Secondly, the camera/lens combinations can be specifically calibrated using the camera calibrators supported by the photogrammetry program distributors or alternatively using the widespread calibrator, iWitness® using a custom calibration option. The images are usually recorded as TIFF format files. The data in the TIFF images identify the camera model and the nominal focal length of the lens. However, the data is not enough to build accurate 3D images. In this study the generic calibration option is used because the employed camera and lenses are fully supported by Sirovision.
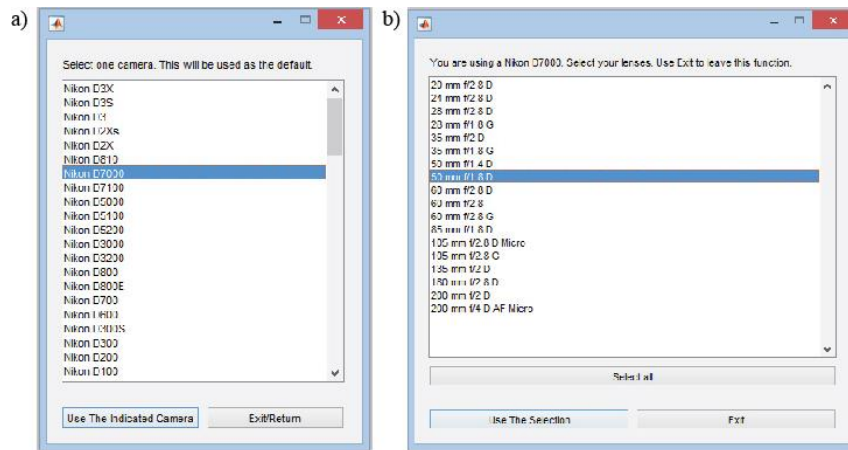
Fig. 3.9 List of supported equipment by Sirovision; cameras (a), lenses (b)

3.2.5 Selecting an area and matching data

The next step is selecting a stereo image pair. The process of selection is performed by selecting four corner points on both images. The points should be fixed at the same positions on the left and right images. The matching process can then be performed automatically using the left and right images. The process is done by searching an area in the second image to find points that are the best matches for points in the first image. In this process, matching is not for every pixel in the images, but users can define the number of necessary pixels in the task setup. The matching results, indicated by a black and white area, are displayed as the routine progresses over the selected area. The white area indicates good matching as shown in Figure 3.10. If a matching success is greater than 95%, the results are generally good. However, if matching results are less than 85%, the results can be considered as poor (CSIRO, 2012).
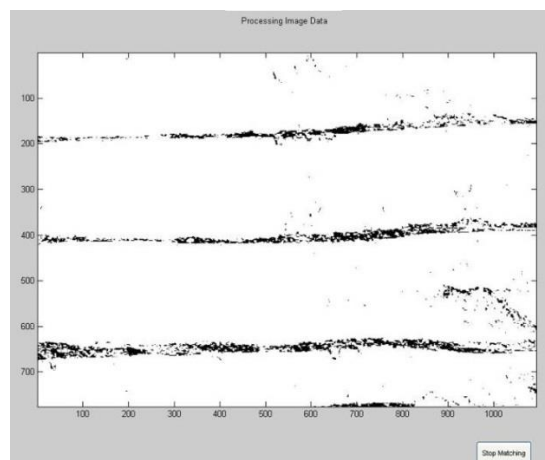
Fig. 3.10 Window showing a matching result (CSIRO, 2012)

57

3.2.6 Geo-referencing

Geo-referencing is the process to establish the coordinates of a sing 2D image, stereo pairs of 2D images, a single 3D image and a mosaic of 3D images. Photogrammetry codes provide various options for this process, so that the 3D images are correctly located and scaled in the required coordinate system. For large scale objects, the ground control points should be placed so that at least three control points can have a relative position to each other, thus forming a triangle arrangement. In small scale objects, small targets or scale bars can be used as the ground control points. The accuracy of geo-referencing is proportional to the accuracy of the roughness data obtained from the 3D images. As the JRC of rock joints is sensitive to minor variations in the profile dimensions, it can be subject to a large range of errors according to the accuracy of the geo-referencing. In most cases, it is difficult to apply conventional geo-referencing methods to the high resolution 3D images because the spatial extent of the images is limited to surveyed control points in the images. Hence, a technique which uses virtual ground points from the lower resolution 3D images was developed by Guo et al. (2011).

The terms, azimuth, elevation and tilt are used to describe the line of sight of the camera. Bearing which is referenced from north or south and the angle to the east or west from the north-south meridian is also a useful term. Azimuth is the direction of the line of sight relative to north in a horizontal plane as shown in Figure 3.11. Elevation is the angle between the line of sight and the horizontal plane. Tilt is the angle between bottom line of the camera and the horizontal plane.
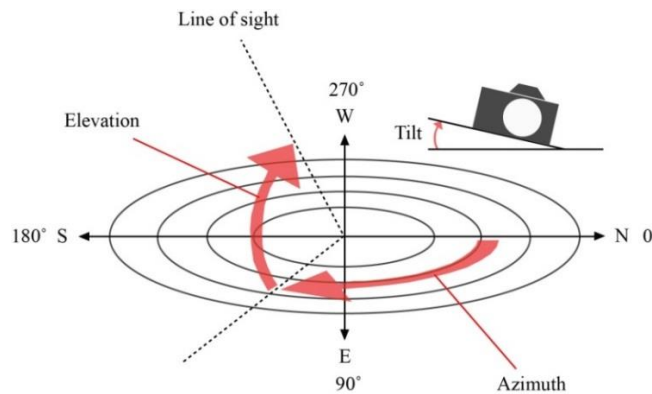
Fig. 3.11 Definition of azimuth, elevation and tilt for camera orientation

The survey data, which is mentioned in Section 3.3.3, is imported as an ASCII text file. The survey data can be edited according to the results of the geo-referencing. During geo-referencing, the camera positions and orientation can also be checked by the prompted displayed information following each input stage. Generally, the geo-referencing procedure requires following input of field measurement (CSIRO, 2012).

① Left camera position: easting, northing, height

② Bearing from left camera to the centre of the image

③ Elevation from the left camera to the centre of the image

④ Tilt of the left camera (usually "0" if the camera has been levelled using a levelling plate

3.3 Analysis of directional roughness profiles

3.3.1 Use of 3D models

The extraction of directional roughness profiles from 3D surface models is a distinct procedure for roughness analyses. Section 2.7.2 briefly indicates that in laboratory conditions, the roughness profiles of objects in any direction can be extracted by controlling the object positions. The use of data transformation to create roughness profiles for a specific direction has been well documented in the literature (Baker et. al., 2008; Haneberg, 2007, 2008). As discussed in their studies, a rotation procedure for the 3D model is generally required in order to obtain the coordinates of a profile for a specific direction from a 3D surface model of real slopes. In practice, with the function of profile extraction from a surface model, the creation of profiles at positions of interest may be a complicated procedure and the selection of an area for positioning of profiles on the surface model can also therefore be inaccurate.

Haneberg (2007) presented a useful method to produce roughness profiles in any direction by using a rotation and interpolation matrix from 3D images. This interpolation is performed by rotations based on the correlation between the azimuth of the dip-line of planes and the directions of the profiles. Similarly, using the large scale roughness of discontinuities, to extract the undulation of the profiles, a MATLAB® code was recently investigated by Markovaara-Koivisto and Laine (2012). For practical

application of 3D models for directional investigations, these applications are useful to obtain and analyse roughness profiles in specific directions for the exposed joint surfaces of interest in relation to the geological important directions such as dip and dip directions.

In this study, the roughness profiles obtained from 3D photogrammetric models are compared with the results of manual measurements. In terms of the accuracy of the positions of the profiles, the coordinates of the profiles on the 3D models can be directly extracted from the 3D coordinates. This process uses a simplified method to extract roughness profiles from regularly gridded surface models by using point distances of roughness profiles from a guide line. This chapter reviews the methods of the extraction of directional roughness profiles for both methodologies: a rotation methodology using MATLAB$^{®}$ codes and a simplified method using point distances of the profiles.

3.3.2 Data rotation and extraction using MATLAB$^{®}$

MATLAB$^{®}$ (The Mathworks Inc.) has been used as the main code to rotate 3D point clouds and extract roughness profiles. In photogrammetry analysis codes, their algorithms have been improved by developing better codes to produce an accurate simulation of objects and a user-friendly graphic interface (Madeira et al., 2010; CSIRO, 2012). MATLAB$^{®}$ is a well-suited platform for analysing 3D data using powerful matrix calculation tools. Further, this code provides effective functions to visualize 3D images. This advantage enables researchers to approach the analyses of rock joint structures in both 2D and 3D conditions. As an example, Markovaara-Koivisto and Laine (2012) recently presented a MATLAB code for visualising the results from scanline surveys as traces in 2D and 3D conditions.

This study presents a MATLAB code to change the orientations of a 3D joint plane to match the orientations of the measured profiles. The methodology for extracting roughness profiles from 3D images can be divided into three main steps. The first procedure is the acquisition of the coordinates of 3D photogrammetry models. Secondly, the obtained 3D data are rotated to match the orientation of the profiles of interest along manually measured profiles. Lastly, the coordinates of the roughness profiles are extracted in ASCII data format to estimate JRC values.

The coordinates of 3D point clouds are exported from 3D photogrammetric models. Generally, the photogrammetry codes provide a function to save a text file containing the coordinates into two different forms of X, Y, Z arrays. These data consist of Easting (X), Northing (Y) and Elevation (Z). Using the coordinates, 3D point clouds can also be imported and plotted to various visualization programs such as AutoCAD (Autodesk), Meshlab (Visual Computing Laboratory), AutoCAD civil 3D (Autodesk) and MATLAB®. The rotated coordinates of point clouds are then calculated with an orientation matrix.

As the first procedure, the dip directions and dip angles of the geo-referenced joints should be defined. As shown in Figure 3.12, if we are considering a plane surface, which is composed of N points and passes through the centroid of the point clouds, the joint surface can be described by a unit normal vector, $n = \{n_x, n_y, n_z\}$. In this space, it can be assumed that the positive x-axis corresponds to east, the positive y-axis corresponds to north and the positive z-axis represents elevation. The azimuth (θ) of the dip direction of the plane can be expressed as Eq. (3-1) and the dip angle (δ) of the plane can be calculated by Eq. (3-2).

$$\theta = arctan\left[sgn(n_z)\frac{n_x}{n_y}\right] \qquad (3\text{-}1)$$

$$\delta = -arctan\left[\frac{n_z sgn(n_z)}{\sqrt{n_x^2+n_y^2}}\right] + 90° \qquad (3\text{-}2)$$

When n_z is larger than 0, sgn (n_z) is + 1. If n_z is less than 0 sgn (n_z) is − 1.
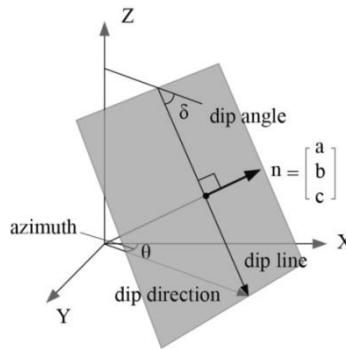
Fig. 3.12 The unit vector, n, shown perpendicular to the joint plane

The rotated coordinates of point clouds are calculated with an orientation matrix. Haneberg (2007) presented a three dimensional rotation matrix (Eq. 3-3). Using this matrix, data rotation can be performed subsequently using the methodology of data rotation.

$$\begin{Bmatrix} x' \\ y' \\ z' \end{Bmatrix} = \begin{bmatrix} -cos\theta & sin\theta & 0 \\ -cos\delta\ sin\theta & -cos\delta\ cos\theta & -sin\delta \\ -sin\delta\ sin\theta & -cos\theta\ sin\delta & cos\delta \end{bmatrix} \begin{Bmatrix} x \\ y \\ z \end{Bmatrix} \qquad (3\text{-}3)$$

After the dip direction and dip angle are defined, the rotation procedure can be performed and divided into three stages based on the axes parallel and perpendicular to the dip line. The first rotation is about the z axis, as shown in Figure 3.13 (a), so that the dip direction is parallel to the x and y axis. The second and third rotations of the plane are into the x and y axes. As an example, an upward rotation is schematically presented in Figure 3.13 (b).

Using a MATLAB® program, the point clouds are rotated to match the measured profiles, which are the roughness profiles of interest, to the dip lines of the planes. This study introduced a MATLAB® script for the application of the orientation matrix to rotate the imported coordinates of the point clouds. The rotations in 3D space have 3 different matrices for the x, y and z axes. Consequently, using the angles of rotation about each of the axes, the final positions of point clouds can be obtained by multiplying the three matrices. The rotation angles about the axes are determined by subtracting the values based on the dip direction and the dip angle of the joint plane of interest.
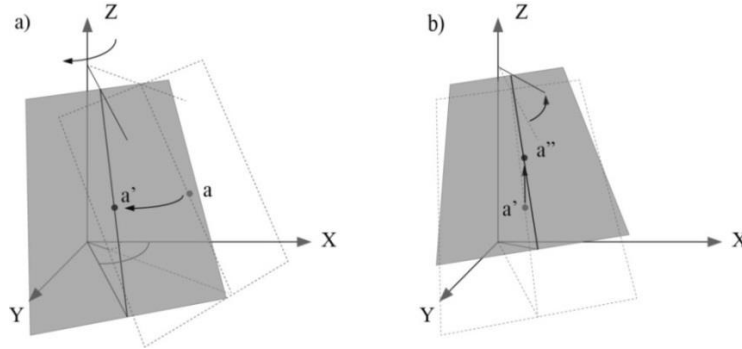
Fig. 3.13 Data rotation by orientation matrix; z axis rotation (a), x and y axis rotation (b)

According to Euler's theorem, the rotation of a point in 3D space can be described using three angles which are about the x, y and z axes. If the rotations are described by matrix forms, the rotation matrix can be written as follows;

$$R = \begin{bmatrix} a_{11} & a_{12} & a_{13} \\ a_{21} & a_{22} & a_{23} \\ a_{31} & a_{32} & a_{33} \end{bmatrix} \qquad (3\text{-}4)$$

The rotation using matrix R can be divided into three stages. If the three angles are defined as ϕ for z axis, θ for x axis and ψ for y axis as shown in Figure 3.14, the rotation of a point is performed by combining individual rotations about each axis using the following orders.

First, the rotation about the z axis is calculated by applying matrix Z. Then, the rotation about the x axis is applied using matrix X. Finally, the rotation about the y axis is performed using matrix Y. Thus, as a result, the rotation matrix R is given as R = ZXY. The rotation matrices can be written as follows:

$$Z = \begin{bmatrix} \cos\phi & \sin\phi & 0 \\ -\sin\phi & \cos\phi & 0 \\ 0 & 0 & 1 \end{bmatrix} \quad (3\text{-}5)$$

$$X = \begin{bmatrix} 1 & 0 & 0 \\ 0 & \cos\theta & \sin\theta \\ 0 & -\sin\theta & \cos\theta \end{bmatrix} \quad (3\text{-}6)$$

$$Y = \begin{bmatrix} \cos\psi & \sin\psi & 0 \\ -\sin\psi & \cos\psi & 0 \\ 0 & 0 & 1 \end{bmatrix} \quad (3\text{-}7)$$

Therefore, each element of matrix R is calculated as follows:

$$R = \begin{bmatrix} \cos\psi\cos\phi - \cos\theta\sin\phi\sin\psi & \cos\psi\sin\phi + \cos\theta\cos\phi\sin\psi & \sin\psi\sin\theta \\ -\sin\psi\cos\phi - \cos\theta\sin\phi\cos\psi & -\sin\psi\sin\phi + \cos\theta\cos\phi\cos\psi & \cos\psi\sin\theta \\ \sin\theta\sin\phi & -\sin\theta\cos\phi & \cos\theta \end{bmatrix} \quad (3\text{-}8)$$

The rotate function in MATLAB® rotates objects in 3D space. In order to rotate an object about a specified origin and direction, the script can be written as follows;

- rotate (h, direction, alpha)

- rotate (…, origin)

The 'rotate (h, direction, alpha)' script performs data rotation by alpha degrees. Using this script, the 'direction' is two or three element vectors which describe the axis of rotation in conjunction with the origin of the axis of rotation. Positive alpha angle value is defined by the right hand rule, about the direction vector as it extends from the origin of rotation. The command 'rotate (…, origin)' specifies the origin of the axis of rotation as a three-element vector $[x\theta, y\theta, z\theta]$. For example, if the data of a surface is plotted in 3D space and rotated 25 degrees about the x axis, the MATLAB® script can be written as follows;

63

- hSurface = surf (peaks(20));

- direction = [1 0 0];

- rotate (hSurface, direction, 25)
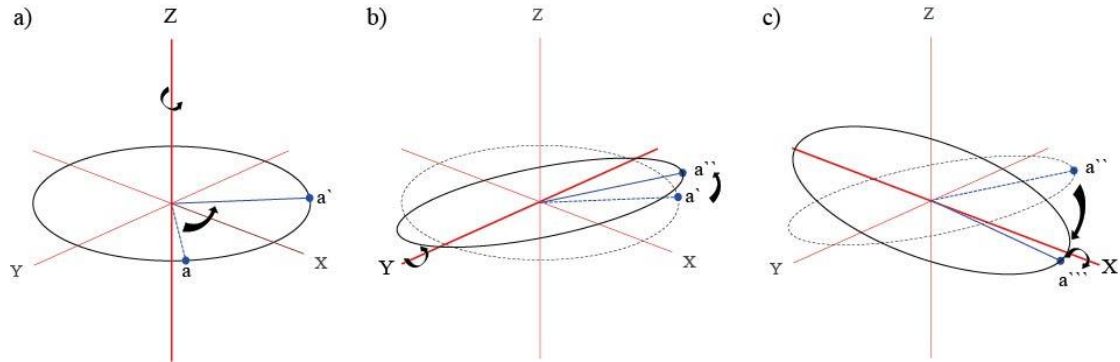
Fig. 3.14 Data rotation about z axis (a), x axis (b), y axis (c)

This rotation transformation modifies the object's data. Thus, 'rotate' changes the values of the X data, Y data and Z data properties to rotate graphic objects. If the rotation axis is around x axis and y axis, the second script line is described as 'direction = [1 1 0];'. If the data of a surface is rotated along z axis about 45 degrees centred by its centre, the script can be written as follows;

- h = surf (peaks(20));

- zdir = [0 0 1];

- center = [10 10 0];

- rotate (h, zdir, 45, center)

Based on these scripts, a MATLAB® code can be developed to rotate the coordinates of data. After this re-orientation procedure, the 3D model is arranged along an axis to extract the 2D profiles which are located along the same position as the measurement profiles.

3.3.3 Extraction of roughness profiles and points

Focussing on the convenience of the comparisons between manually measured profiles and the corresponding profiles of 3D images, this study uses a simplified method to extract roughness profiles from regularly gridded surface models by using point distances of roughness profiles from a guide line. It is assumed that the roughness profile is referenced

by an imaginary line which links between the lowest two points of the line. The line lies on a more precise location of interest for the comparison of profiles. In the correlated locations between the roughness profile and the imaginary line, the roughness profile is defined by the shortest distances from the imaginary line as demonstrated in Figure 3.15. The shortest distances from the points to the guide line is estimated by Eq. (3-9) ~ (3-11). These equations and the general matrix form of point-line distance in three dimension space are well demonstrated by Weisstein (2002).

In Figure 3.15, p_0 and p_1, the vector along the line specified by two points is identified by Eq. (3-9) using their coordinates.

$$v = \begin{bmatrix} x_0 + (x_1 - x_0)t \\ y_0 + (x_1 - x_0)t \\ z_0 + (x_1 - x_0)t \end{bmatrix} \qquad (3\text{-}9)$$

The variable t, which is satisfied with shortest distance of each point, is solved by Eq. (3-10):

$$t = -\frac{(p_0 - p_n)\cdot(p_1 - p_0)}{|p_1 - p_0|^2} \qquad (3\text{-}10)$$

The shortest distances of points to the imaginary line between p_0 and p_1 are estimated by Eq. (3-11).

$$d^2 = [(x_0 - x_n) + (x_1 - x_0)t]^2 + [(y_0 - y_n) + (y_1 - y_0)t]^2 + [(z_0 - z_n) + (z_1 - z_0)t]^2 \quad (3\text{-}11)$$

Visual comparisons between the measured profiles and the photogrammetric profiles are carried out using AutoCAD Civil 3D ver. 2015 (Autodesk).
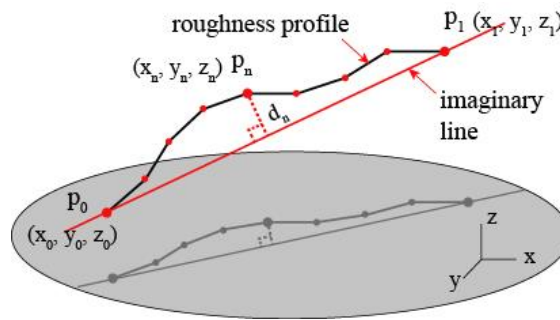
Fig. 3.15 Coordinates of a roughness profile in three dimensional space

3.4 Conclusions

The methodology of this study is presented in this chapter. The process of this study is composed of the three major categories; site photogrammetry surveys, the development of JRC error model and the verification of the developed model. This chapter firstly discusses essential methods of the photogrammetry setup and the post processing for obtaining roughness profiles from the 3D images considering better levels of accuracy. In the first phase of this study, various site investigations are carried out based on the guidelines of the recommended photogrammetry setups mentioned in this chapter. Stereo images are taken considering the various influential factors; image resolutions, baseline distance, geo-referencing and appropriate camera factors.

Secondly, this chapter presents the methods of the profile extraction from 3D models with emphasis. The MATLAB® scripts for data reorientation are presented in this section. The scripts can be used to visualize and rotate the 3D surface models and the codes also take into account the extraction of specific roughness profiles from the reoriented 3D models. The coordinates of the extracted roughness profiles are used for JRC estimation using the results of photogrammetric surveys. A simplified method to extract roughness profiles is also suggested in this section. This method can compare the photogrammetric profiles in the accurate positions with the measured lines. In this study, the photogrammetric roughness data are acquired using this simplified method to ensure matching the positions.

In the second phase of this study, a set of laboratory tests is performed based on the guidelines of the photogrammetry method in this chapter. Using the roughness data obtained from the laboratory tests, a photogrammetric JRC error model is developed by analysing in statistical analyses. The developed error model is verified by applying the collected data from the site investigations. The relevant methodologies are discussed in Chapter 5 and Chapter 6 in detail.

4 PHOTOGRAMMETRY SURVEYS

4.1 Introduction

This chapter describes the conditions of field photogrammetry surveys for the estimation of JRC values in this study. Firstly, this chapter summarizes the characteristics of the study areas and also introduces the equipment employed in the surveys. The purpose of the field study is to obtain rock surface roughness profiles and JRC values using the photogrammetric 3D models in order to assess the stability of slopes and related phenomenon. Thus, the obtained roughness data are used for investigating the engineering issues by using various engineering principles. The relevant case studies will be discussed in Chapter 7 in detail. These individual issues have been peer reviewed and published to journal articles and conference papers.

To investigate the accuracy of the obtained roughness profiles, the photogrammetric JRC values and roughness profiles of the studied areas are also compared with the results of manual measurements. In the second part of this chapter, the overall accuracy of the collected photogrammetric roughness profiles is discussed. The collected data from these study areas are also used to verify the parabolic error models which will be discussed in Chapters 5 and 6.

4.2 Study areas

The field investigations were performed at six different sites, where are natural or cut slopes on the Gold Coast and in Brisbane, Australia. The slopes are clearly fractured jointed rock slopes so that the joint planes can be identified from the areas of the exposed rock surfaces. In the surveys, close range stereo photogrammetry created the 3D models of the areas of interest. For the selected sample areas, roughness profiles are extracted from the 3D images and JRC values are estimated using the digitized coordinates of the roughness profiles.

As previously mentioned in Chapter 2, the roughness information of rock joints can be used for analysing the rock joint shear behaviour. In this study, according to the conditions of the slope, the collected JRC values are attempted to be employed to analyse the issues of the rock slopes. For example, for a weathered rock slope, the JRC values obtained from the 3D

surface model are employed to analyse the stability using a relevant strength criterion. These applications are performed to verify the JRC values using the slope features through various analysis tools. The details of the field works are summarised in Table 4-1.

Table 4-1. Summary of field works

Sites	Locations and overview	Slope conditions and focussed issues
1	Beaudesert- Nerang road, Gold Coast	Slope stability related to weathering - Sandstone and argillite - Partially failed slope due to rainfall - Slope height ≈ 8 m
2	Beaudesert- Nerang road, Gold Coast	JRC estimation with different camera distances - Shale - Slope height ≈ 5 m
3	Henri Robert Drive, Gold Coast	Block failure analysis - Greywacke - Partially failed rock blocks due to rainfall - Slope height ≈ 25 m
4	Bethania, Brisbane	Rock fall simulation - Meta-sandstone and meta-siltstone - Cut slope - Protection from rock fall hazard - Slope height ≈ 20 m
5	Nerang-Murwillumbah road, Gold Coast	JRC estimation with different camera distances and focal lengths - Sandstone - Slope height ≈ 2 ~ 7 m
6	Engineering road, Griffith University, Gold Coast	JRC estimation with different camera distances and focal lengths - Sandstone

4.3 Equipment

A Nikon D7000 SLR camera was used to capture digital images of the rock slopes. The employed lenses are 24 mm, 50 mm and 85 mm focal length lenses and the selection of lenses are dependent on the ranges and survey conditions of the sites. The details and specifications of the camera and lenses will be presented in Table 5-3 and 5-4 in Chapter 5. Some photogrammetry software companies suggest that a tripod is not necessary for photogrammetry field works. However, a tripod and a release shutter can be a preferable practice for photographing to create high quality images (Haneberg, 2008). In this study, a tripod (Manfrotto) with spirit bubbles is used for setting for the camera being used and a release shutter with 1.5 metre wire and a remote shutter are employed to minimise the influence of vibration.

A geological compass (Breighaupt, Gekom) is used to measure dip and dip directions of the discontinuities of the joints of interests. Considering an error from the irregularity of rock surface, the back base plate was used on the dipping plane. A profile gauge (L=30 cm) with 1 mm step sizes is used to measure roughness profiles on rock joint surfaces. A handheld GPS, GPSMAP 78 (GARMIN), which the accuracy is typically less than 3 meters, was used to identify the camera and control point positions. In order to enhance the accuracy of the coordinates of camera positions and control points, the measured coordinates can be corrected on the basis of a reference point and manually measured length between the points. In order to check the all point locations, based on a measured point by the GPS device, other points are checked by a comparison procedure using the measured distances of the points each other. A laser rangefinder, Forestry Pro (Nikon) was used to measure horizontal distances to the rock faces and the elevation angles to control points. This device is useful when the manual measurements using line measuring tapes are not available. A daytime laser pointer is also used to make a target point on the slope surface of interests. This device should be fixed on a tripod to keep a light point at the same positions during the stereo photogrammetry. The used equipment is shown in Figure 4.1.

a)

Nikon D7000

FL = 24 mm   FL = 50 mm   FL = 85 mm

b)

Remote shutter

Tripod   Release shutter

c)

Scale bars   Targets   Laser pointer

Handheld GPS

Laser range finder

d)

Geological compass

e)

Profile gauge (L = 30 cm)

Schmidt hammer (L type)   Schmidt hammer (N type)

Fig. 4.1 Field equipment; Camera & Lenses (a), Tripod & Shutters (b), Targets & Measurement devices (distances, locations) (c), Geological compasses (d), Measurement devices (roughness profiles, rock joint strengths) (e)

4.4 Field surveys for collection of rock surface roughness data

A part of this section which was published and included in the proceedings of ACG conference as follows:

Dong Hyun Kim, Ivan Gratchev, George Poropat (2013) The determination of joint roughness coefficient using three-dimensional models for slope stability analysis. In Proc. Slope Stability 2013, Australian Centre for Geomechanics, Brisbane, Australia: 281-289.

4.4.1 Introduction

The main objective of this section of the thesis is to investigate the influence of camera-to-object distances and the focal length of lenses on the roughness profiles and the JRC values obtained from the photogrammetric 3D models in various field conditions. In the field photogrammetry surveys, pictures were taken at different photogrammetry conditions. The orientations and the positions of the selected planes were different in the photographs and the surveys were performed varying camera-to-object distances with varying focal lengths of lenses. The created photogrammetric profiles are compared with the manual data and the results of the accuracy of photogrammetric JRCs are discussed in this section.

The results showed that the shape agreement of the photogrammetric profiles with the true profiles was varied in accordance with the data intervals. The resolution of images was the most influential factor which governs the extent of accuracy of photogrammetric profiles. There are various other factors which affect the accuracy of photogrammetry models. Through the photogrammetry surveys, it was found that the data intervals can be strongly influenced by the complexity of the object surface and the relationship between the orientations of the surface and the camera axis. Also, the extracted profiles, which were corrupted by data noise, tended to overestimate the JRC values. This section discusses the accuracy of photogrammetric profiles based on the different photograph conditions.

4.4.2 Site overview and photogrammetry surveys

1) Beaudesert Nerang road

Photogrammetry surveys were performed at natural rock slopes. The first study slope is located in Beaudesert Nerang road, Gold Coast. The rock type of the slope is composed of

71

weathered shale and the geological condition will be presented in Section 7.2.2 and 7.3.4 in detail. Figure 4.2 demonstrates an example of photogrammetry setups along the section of Beaudesert Nerang road.

Photographs were taken at three different camera-to-object (c-to-o) distances: 2 m, 5 m and 10 m. The baselines between the two camera positions are approximately adjusted by the ratio of 1: 7 for the given distances to the rock cut. Because the study slope was located on the corner of a drive way to a house, the photographing was able to be done in the range of test distances. The study section, which shows a clean joint surface, was selected to carry out photogrammetry tests as shown in Figure 4.3. The height of the selected section of the study area, which was around 50 cm from the ground, was relatively low compared to the camera heights. The section of interest was marked using two circular targets located 20 cm from each other. In the close distance (c-to-c = 2.0 m), the camera heights were adjusted to locate the targets in the foot print of each stereo image.

Fig. 4.2 An example of camera setup along Beaudesert-Nerang road

Figure 4.3 also demonstrates the differences of the image size obtained from the different camera-to-object distances. The widths of the captured image size are determined by the focal length of the lens (FL = 24 mm) and the widths are almost the same as the camera-to-object distances. In order to compare the roughness profiles obtained from the photogrammetric 3D images, two profiles in the section marked by the two targets were measured by a Barton's comb (L = 30 cm). The measured profiles were then digitized by importing the coordinates of the drawn profiles with 1 mm step sizes. The pixel sizes of the 2D images can be calculated by the equation (Eq. 2-26). The obtained ground pixel sizes represent the resolutions of the images taken at the different distances from the slope. The obtained pixel sizes of 3D images are presented in Table 4-2.
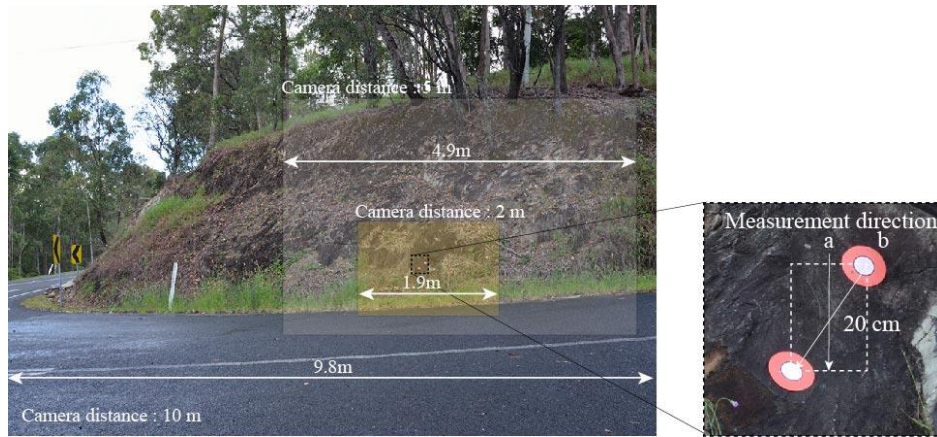
Fig. 4.3 Study slope and measurement section (Site #1. Beaudesert Nerang road)

Table 4-2 Photogrammetry survey conditions

Site		No. profiles	Focal length (mm)	Distances (m)		3D models grid size (mm)
				Camera-to-object	Baseline	
#1. Beaudesert Nerang road	1	2	24	2	0.3	1.2
				5	0.7	4.2
				10	1.5	3.2
	2	1	50	12.8	1.6	2.3
			85	12.8	1.6	1.4
#2. Nerang-Murwillumbah road	1	1	24	14.0	2.0	2.9
			50			1.6
			85			1.0
		2	24	14.8	2.0	3.7 ~ 5.7
			50			3.7 ~ 5.7
			85			3.7 ~ 5.7
	2	1	24	11.8	1.7	3.7
			50			1.7
			85			1.3
		2	24	12.0	1.7	2.5 ~ 2.9
			50			-
			85			1.0 ~ 1.3
#3. Engineering road		12	24	2	0.3	0.5 ~ 1.0
				5	0.7	0.8 ~ 2.4
				10	1.5	2.5 ~ 5.4
			50	2	0.3	0.3 ~ 0.7
				5	0.7	0.6 ~ 1.0
				10	1.5	1.2 ~ 2.2
			85	2	0.3	0.3 ~ 0.5
				5	0.7	0.4 ~ 1.1
				10	1.5	0.7 ~ 1.3

2) Nerang-Murwillumbah road

The second survey was performed for two natural rock slopes on Nerang-Murwillumbah road, Gold Coast. The rock type of the study slope is composed of a weathered sandstone. In each slope location, two clean and flat surfaces were selected as study sections. A total of six roughness profiles were investigated. Photographs were taken at the opposite space along the road facing toward the slopes (Figure 4.4). The positions of the profile section of interest were marked by small rectangular targets (width: 15 mm) and scale bars (length: 300 mm, width: 200 mm) were also installed near the targets for geo-referencing as shown in Figures 4.5 and 4.6.

Due to the limitation of space for photographing, the camera-to-object distances were fixed within the margin widths of the road varied from 14.0 to 14.8 metres. The heights of the targeted area was around from 1.0 to 1.4 metres, and the faces of the targeted areas were nearly orthogonal for the optical axis of cameras as shown in Figures 4.5 and 4.6. The roughness profiles in the section marked by the two targets were measured by a profile gauge (L = 30 cm) along the measurement directions. The measured profiles were digitized by importing the coordinates of the drawn profiles with 1 mm step sizes. In this field study, three different focal length lenses were used for creating different resolution images in the same camera-to-object distances. The conditions of the photogrammetry surveys and the obtained spatial density of 3D images are summarized in Table 4-2.

Fig. 4.4 A photogrammetry setup along Nerang-Murwillumbah road
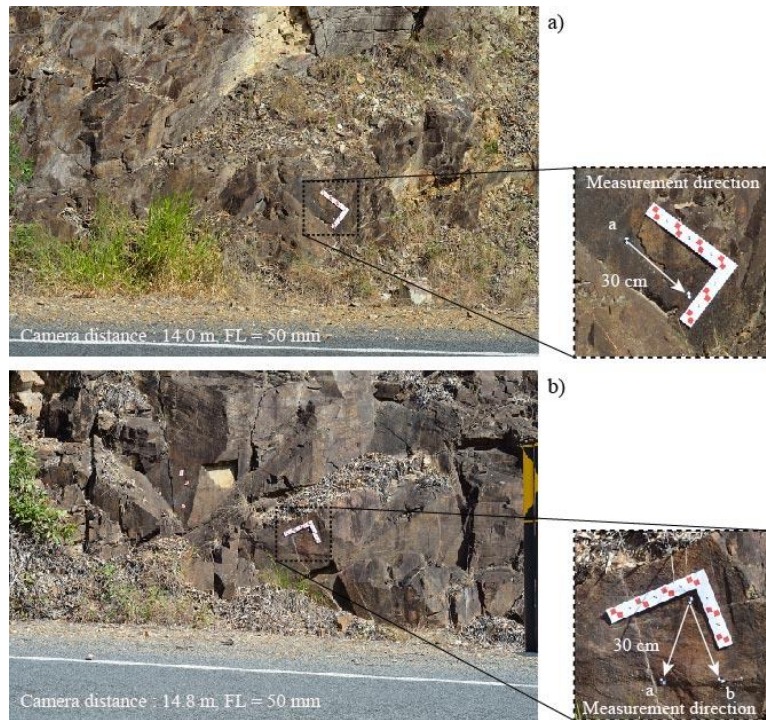
Fig. 4.5 Study slope and measurement section; section a (a), section b (b) (Site #2. Nerang-Murwillumbah road 1)
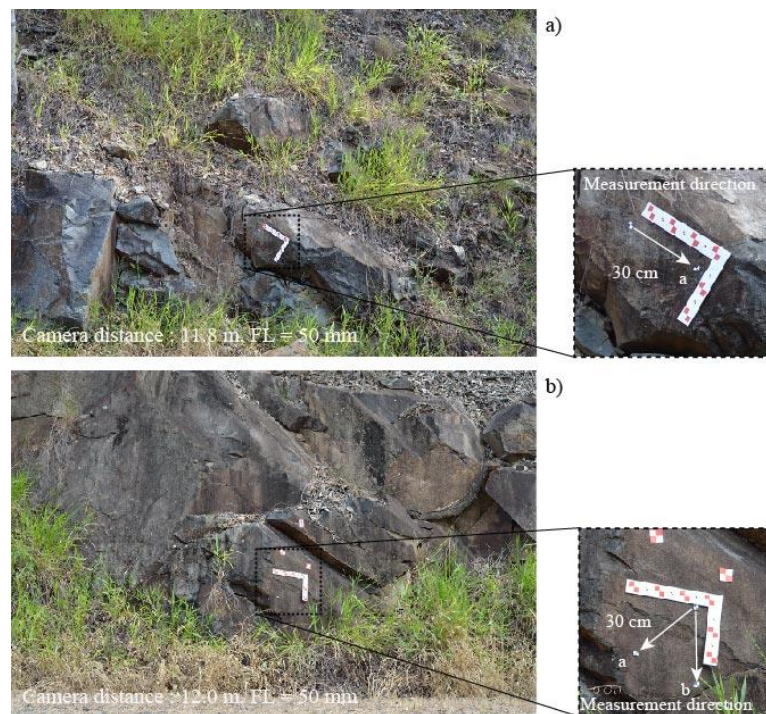
Fig. 4.6 Study slope and measurement section; section a (a), section b (b) (site #2. Nerang-Murwillumbah road 2)

3) Engineering road in Griffith University

In the third survey, photogrammetry was performed for a group of rock blocks located in Engineering road in the Gold Coast campus of Griffith University. A total of 12 roughness profiles were marked with rectangular targets (1 cm $\times$ 1 cm) and the distance between the targets is 300 mm for all profiles as shown in Figure 4.7. The directions of the 12 profiles form different orientations against the camera axis. Thus, this survey was to investigate the accuracy of 3D models focussing on the influence of the profile orientations on the accuracy of photogrammetric JRC values.

Fig. 4.7 Study slope and measurement section (site #3. Engineering road in Griffith University Gold Coast campus)

To place the object on the centre of the images, the heights of tripod were adjusted to the heights of the objects during the photogrammetry tests. As shown in Figure 4.7, the sandstone rock blocks are located line abreast for landscaping. When the pictures are taken

at a far distance and using a short focal length, the horizontal distances from the camera for each block can influence the accuracy of the 3D models. Thus, the photograph of each block was individually taken to be faced to the camera optical axis at the centre of the image to minimize the influence of the object locations.

4.4.3 Comparison of roughness profiles

Figure 4.8 illustrates the extracted 3D meshes of the site #1 that were used to obtain the roughness profiles along the measurement directions. The point cloud intervals of the 3D images represent the measurement scales for the roughness profiles. As shown in Figure 4.8, closer camera-to-object (c-to-o) distances create denser surface models than far c-to-o distances. Some areas corrupted by image noise are found in the edges of the 3D model which are taken at 10 m distances (Fig. 4.8 (c)). This corruption in 3D images may be caused by following two reasons; one is the insufficient resolution of 3D images and the other is the complexity on the periphery of the area of interest (e.g. the effects of plants and the discontinuous environment between rock cuts and surrounded environment).

The pixel sizes of the 3D meshes ranged from 1.6 mm to 12.6 mm. It was found that the extracted profiles were mostly corrupted with noise. This corruption may be related to the location of the measurement section in the entire 3D model. The location of the interested section is near the edge of the 3D model as shown in Figure 4.9. In many cases, data noise can be easily occurred at the edges of the 3D models during the 3D model creations. Also, it was found that the corrupted data could be attributed to the use of the large size targets (D = 60 mm). The attached targets affected the formation of the triangulate points in both sides of the profile. The influence of the target size on the accuracy of photogrammetry models has also been mentioned by Dold (1996).
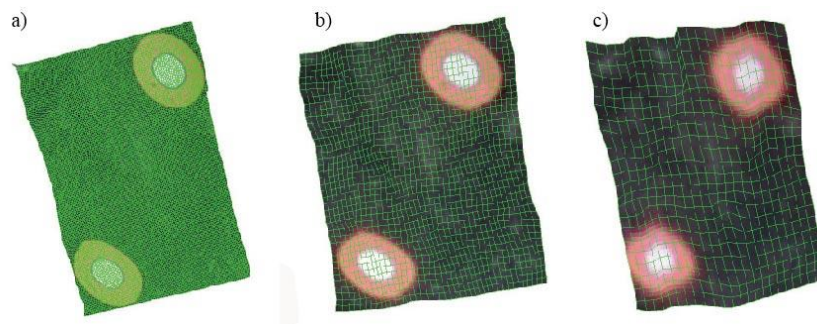
Fig. 4.8 3D surface models and 3D wireframe, D = 2.0 m (a), 5.0 m (b), 10.0 m (c)
(Beaudesert Nerang road 1)
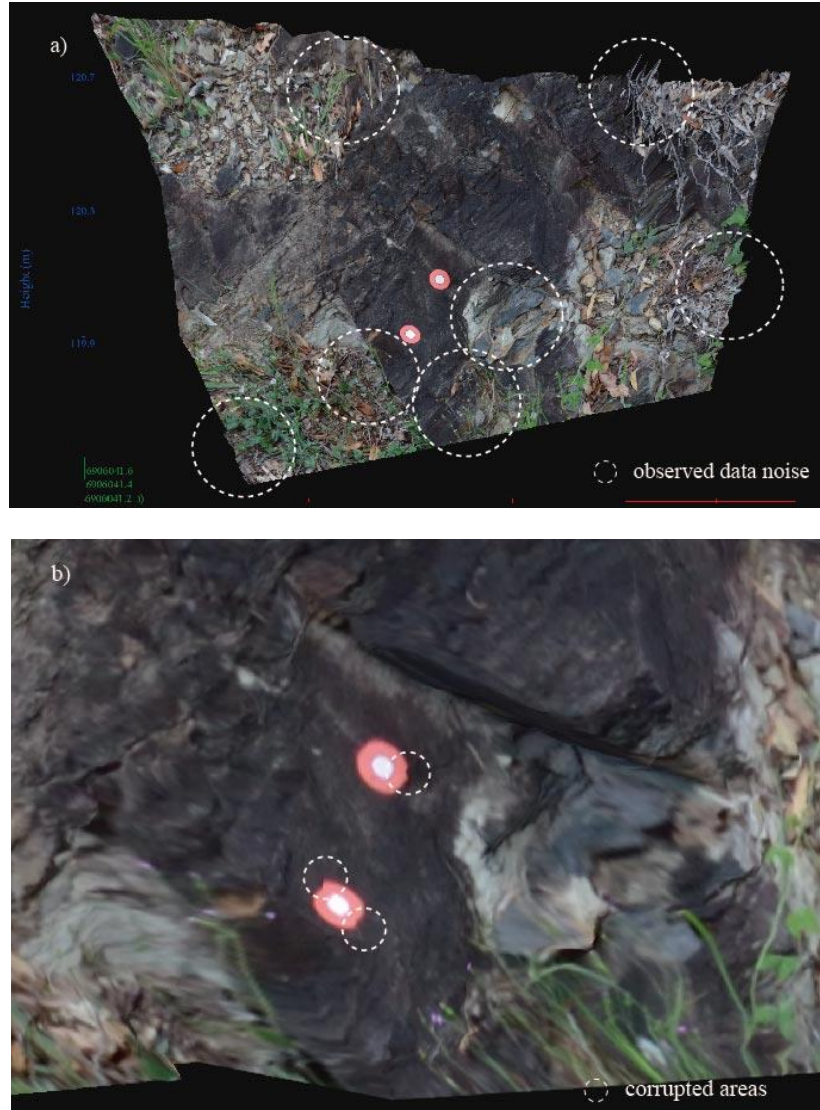
Fig. 4.9 3D photogrammetric models, noise at edges in 2m distances (a), influence of attached target in 5m distances (b)

The roughness profiles were obtained from 3D images through the procedure mentioned in Section 3.3 in Chapter 3. The extracted roughness profiles are compared to the measured profiles. The comparisons are demonstrated in Figures 4.10 ~ 4.17. The results clearly show that the profiles generated from higher resolution images are more consistent with the true profile shapes than others. In the case of Beaudesert Nerang road (Fig. 4.10), at 2 metres of camera-to-object distance, the shapes of roughness profiles are relatively well matched with the measured profile in both large scale (waviness) and small scale roughness component (unevenness). On the other hand, there are discrepancies between the 3D models and the true profiles even in the large scale roughness component at the distances of 5 m and 10 m.

As demonstrated in Figure 4.10 (c), the photogrammetric profile shows considerably distorted shape in the case of 10 metres of camera-to-distance. This is due to the insufficient point cloud data with an interval of 12.6 mm in average and also caused by the discontinuous objects on the periphery such as surrounding plants. Similarly, Figure 4.11 demonstrates the comparison of the photogrammetric profiles using 50 mm and 85 mm focal length lenses. The difference of image resolutions is also achieved by changing the focal lengths of lenses. The distortion of the photogrammetric profiles is also found in the section b.
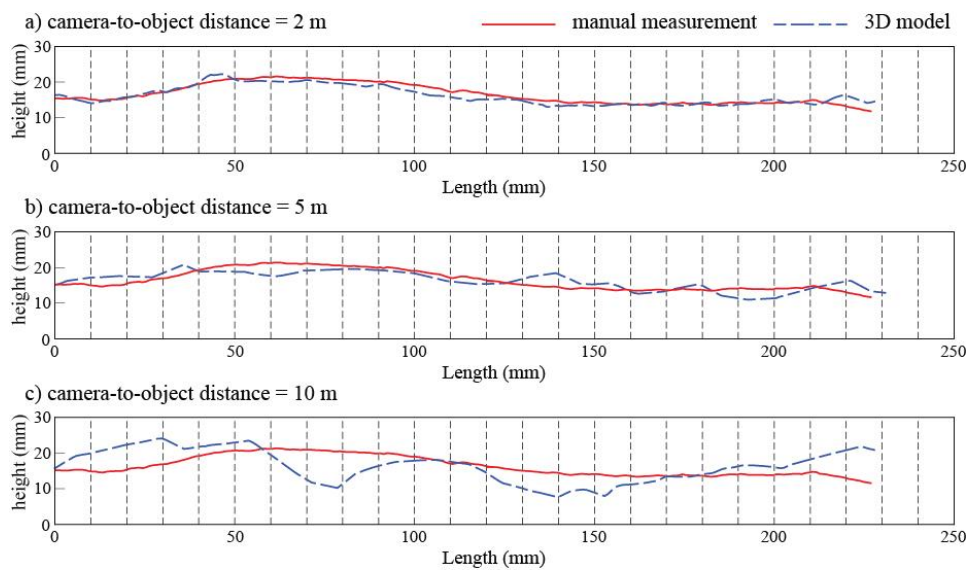
Fig. 4.10 Comparisons of photogrammetric roughness profiles with true profiles, c-to-o object = 2 m (a), 5 m (b), 10 m (c) (section a, Beaudesert Nerang road 1)
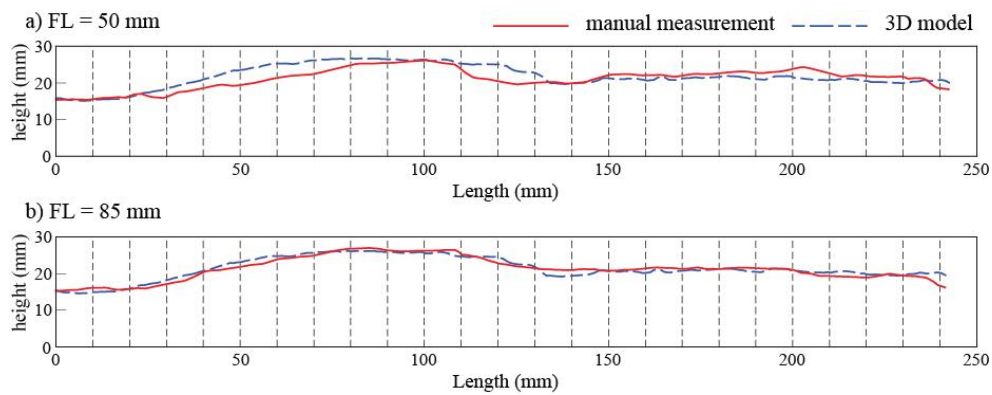
Fig. 4.11 Comparisons of photogrammetric roughness profiles with true profiles, c-to-o object = 12.8 m, FL= 50 mm (a), FL = 85 mm (section b, Beaudesert Nerang road 2)

The trend of the correspondence between photogrammetric and manually measured profiles is also found from the results of Nerang-Murwillumbah road surveys. The accuracy of the extracted profiles from 3D models is proportional to the focal length of lenses as shown in Figure 4.12. In large scale, the roughness profile created by the 85 mm lens is well matched with the manual measurement. Different from the previous case, this model was not significantly influenced by data noise. This ideal outcome can be explained by the following two factors: firstly, the sections of interest were nearly orthogonally faced to the optical axis of cameras. Secondly, there was no interruption of plants on the periphery of the sections of interest which cause corruptions of the 3D model. The comparisons of the other profiles are presented in Appendix 2.
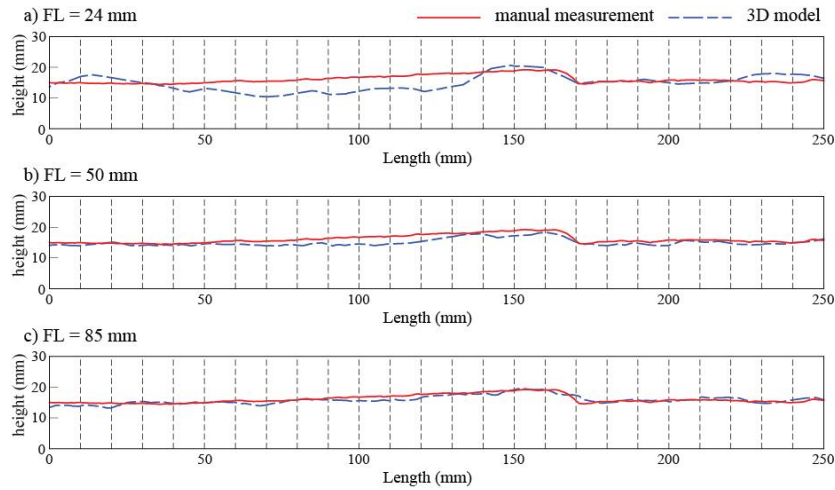
Fig. 4.12 Comparisons of photogrammetric roughness profiles with true profiles, section 1, FL = 24 mm (a), FL = 50 mm (b), FL = 85 mm (c) (Nerang-Murwillumbah road 1)
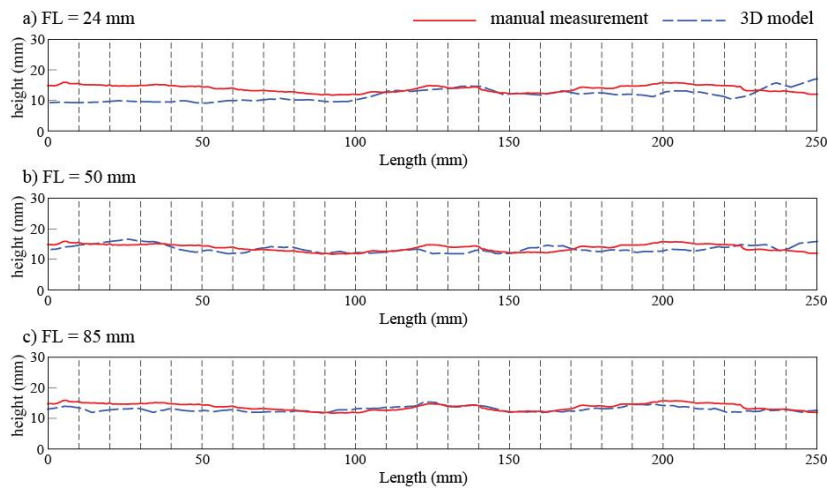
Fig. 4.13 Comparisons of photogrammetric roughness profiles with true profiles, section 1, FL = 24 mm (a), FL = 50 mm (b), FL = 85 mm (c) (Nerang-Murwillumbah road 2)

Similar trends were observed from the 3D models of the Engineering road surveys. As discussed in previous examples, some photogrammetric profiles well simulated the true profiles for large scale roughness. The results of Figures 4.14 ~ 4.16 are one of the best results of Smith road surveys with less data distortion. The location of the profiles in these figures is no.5 in Figure 4.7 which the rock surface is faced to the line of sight in nearly orthogonal direction. In Figure 4.14 ~ 4.16, in the use of 24 mm lens, it is clearly observed that the accuracy of profile correspondence is increased as the camera-to-object distance reduced. However, this trend is not clear when 50 mm and 85 mm of focal lengths are employed. The accuracy of roughness profiles appears to be similar through all range of camera-to-object distance.

Interestingly, both 50 mm lens and 85 mm lens produced similar point intervals in the 3D models. It is a difference of the general acceptance that the point intervals have linear relationships between the employed focal lengths and camera-to-object distances. This irregular trend may be due to the influences of the shapes of individual rock blocks. Actually, it was found in the procedure of 3D model creation that there were corruptions on the periphery of the models. The trend of the point intervals of the created 3D images is a considerably different with the trend obtained from the ideal laboratory conditions which will be discussed in depth in Chapter 5 and Chapter 6.
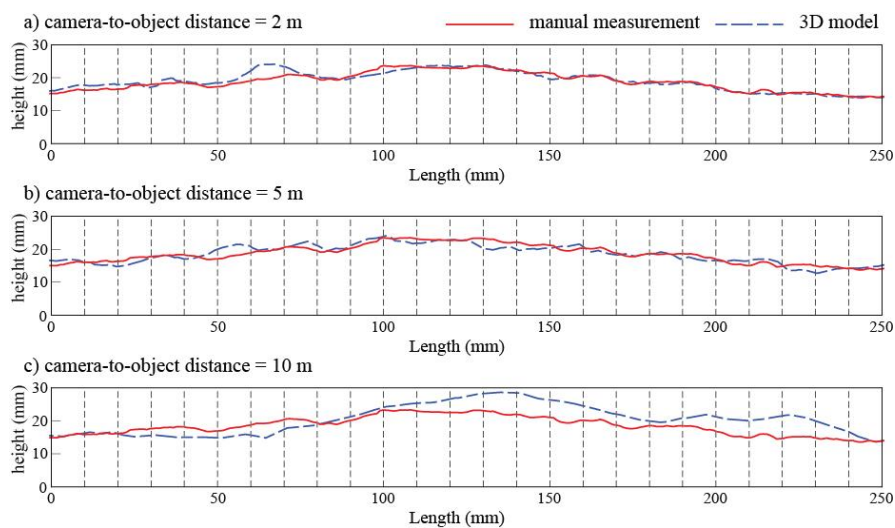
Fig. 4.14 Comparisons of photogrammetric roughness profiles with true profiles, c-to-o object = 2 m (a), 5 m (b), 10 m (c) (profile 5, FL = 24 mm, Engineering road in Gold Coast campus, Griffith University)
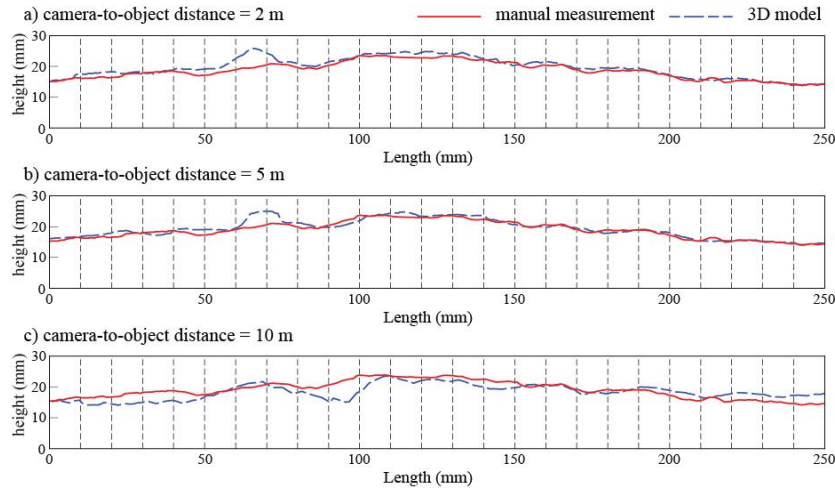
Fig. 4.15 Comparisons of photogrammetric roughness profiles with true profiles, c-to-o object = 2 m (a), 5 m (b), 10 m (c) (profile 5, FL = 50 mm, Engineering road in Gold Coast campus, Griffith University)
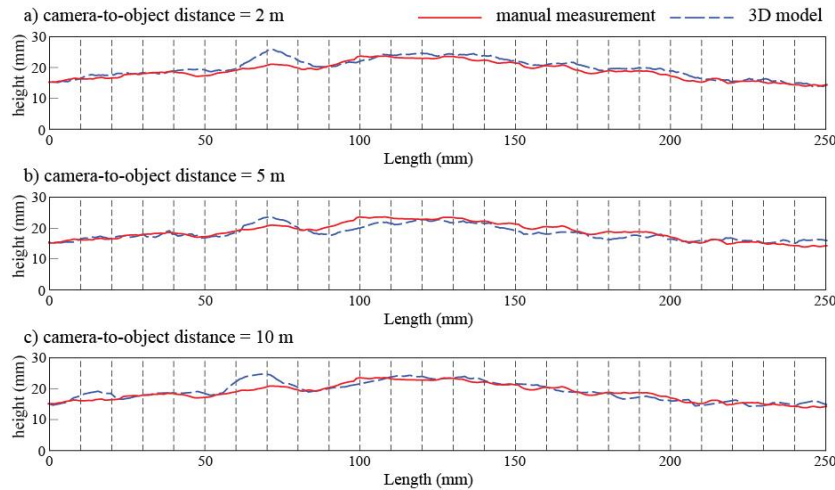
Fig. 4.16 Comparisons of photogrammetric roughness profiles with true profiles, c-to-o object = 2 m (a), 5 m (b), 10 m (c) (profile 5, FL = 85 mm, Engineering road in Gold Coast campus, Griffith University)

In the Engineering road surveys, it was observed that a fair number of photogrammetric profiles were mismatched with the manually measured profiles. The results of discrepancy are caused by various positions of the measurement profiles such as the orientation of surface and the profile direction. The inaccuracy of the photogrammetric profiles was appeared to be the forms of profile distortion in large scale and the form of data noise in small scale. The inaccurate profiles were significantly found when low resolution images are used for the comparisons. For example, a photogrammetric profile #2 has large distortion in 10 metres c-to-o distance, which leads to the overestimation of JRC values as shown in Figure 4.17 (c).

In close distances, it is observed that the photogrammetric profiles are corrupted with noise in small scale (Figs. 4.18 and 4.19). The corresponding measurement error was reported by Poropat (2008). In his study, the noise influence led the overestimation of JRC values. Also, the noise corrupted data could be fixed by an appropriate noise reduction filter. The filtering process smooth the sharp shapes of noised profiles which can reduce the overestimated JRC values. He also showed that the measurement noise is considerably in relation to the data spacing.
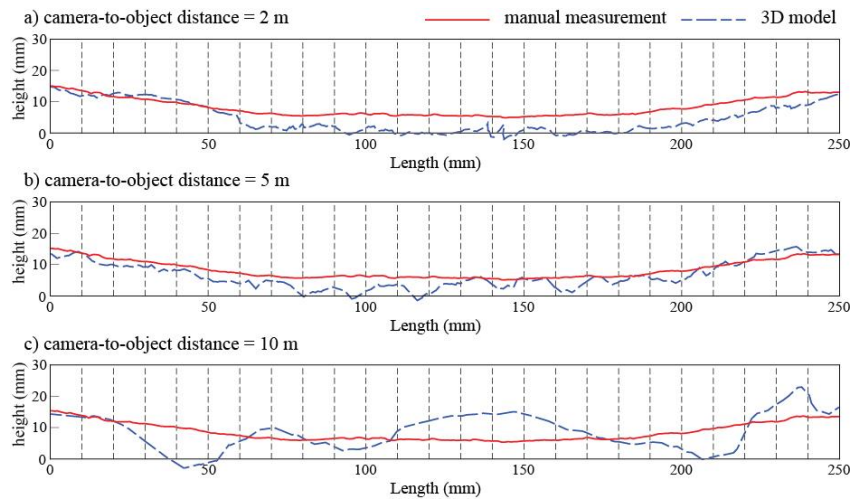
Fig. 4.17 Comparisons of photogrammetric roughness profiles with true profiles, c-to-o object = 2 m (a), 5 m (b), 10 m (c) (profile 2, FL = 24 mm, Engineering road in Gold Coast campus, Griffith University)
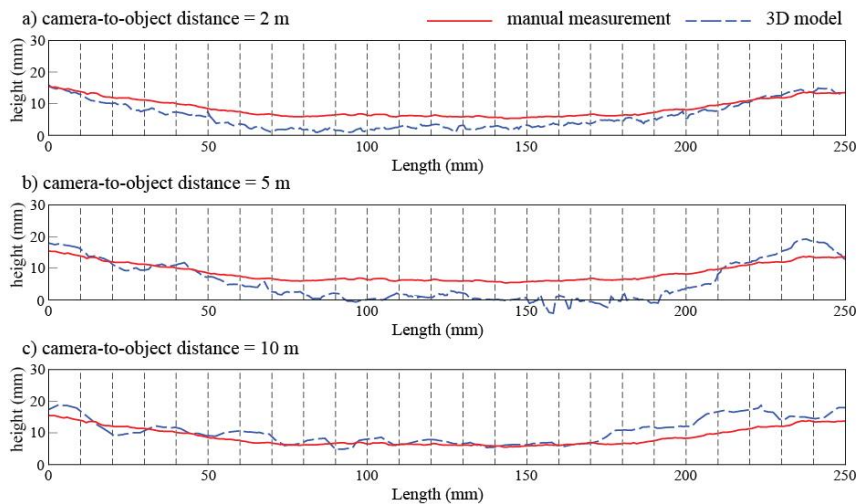
Fig. 4.18 Comparisons of photogrammetric roughness profiles with true profiles, c-to-o object = 2 m (a), 5 m (b), 10 m (c) (profile 2, FL = 50 mm, Engineering road in Gold Coast campus, Griffith University)
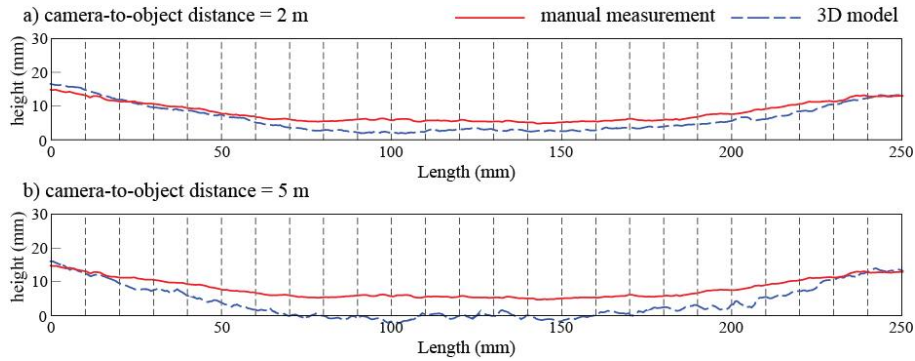
Fig. 4.19 Comparisons of photogrammetric roughness profiles with true profiles, c-to-o object = 2 m (a), 5 m (b), 10 m (c) (profile 2, FL = 85 mm, Engineering road in Gold Coast campus, Griffith University)

4.4.4 JRC estimation

Using the obtained photogrammetric profiles, JRC values were obtained based on the empirical equations suggested by Tse and Cruden (1979) (Eq. (2-8) ~ Eq. (2-10)) and Maerz et al. (1990) (Eq. (2-17) ~ Eq. (2-20)). 125 JRC values were compared by using the coordinates of the photogrammetric profiles and their manually measured profiles. To use the coordinates for the functions, the point intervals of the photogrammetric profiles were changed using the linear relationships between the adjacent points. For the various survey conditions, the obtained JRC values are demonstrated in Table 4-3 and 4-4.

In many photogrammetry conditions, considerable discrepancies of JRCs are found in the table. As the discrepancies can be caused by different factors, the comparisons of JRC values should be combined with the interpretation of the accuracy of the shapes of profiles. Generally, photogrammetric JRCs were underestimated by insufficient point intervals due to large camera-to-object distances and short focal length of lenses. For example, the JRC range was clearly underestimated by the insufficient resolution of the images in the section 1 of the Beaudesert-Nerang road survey. In fact, the photographs were taken at large distance (c-to-o distance: 17 m) with short focal length (FL: 24 mm).

In the cases of overestimation, the reasons can be explained by the following two issues. One is data noise. As previously discussed by Poropat (2008), data noise is frequently found in the photogrammetric profiles in high resolution images. For example, it is found from Table 4-4 that the overestimation of the profiles in the Engineering road survey can be explained by the data noise of the obtained profiles. The relevant roughness profiles were visually compared in Figure 4.18 and 4.19. The influence of noise can be reduced by

appropriate filtering methods (Poropat, 2008). The other is due to the distortion of 3D model, which create incorrect surface models. As shown in Figure 4.17 (c), some profiles were distorted by incorrectly formed 3D meshes. In this case, the photogrammetric JRC values are much higher than the JRC values obtained from manual measurement over the general range of JRC (e.g. JRC > 20).

Using the obtained data in this section, the reasons and the data improvement for the obtained JRC values will be discussed in Chapter 6 in detail.

4.4.5 Conclusion

In this section, photogrammetry surveys were investigated focussing on the accuracy of roughness profiles and JRC values. Based on the obtained results, following conclusions can be drawn.

- Low resolution images at far distances with short focal lengths generally created smooth undulation profiles combined with the underestimation of JRC values.

- However, the insufficient data point also causes the overestimation of JRCs. The insufficient data points may generate incorrect 3D images and the inaccurate profiles tend to produce highly overestimated JRC values. This kind of errors can be also caused by periphery conditions such as plants and heterogeneous nature. It can be concluded that the most influential factor to the accuracy of photogrammetric roughness is the distortion of 3D images due to insufficient data point.

- In high density images, data noise was found from the extracted profiles and the results overestimated the JRC values. In this case, the overall shapes of undulations were well simulated by photogrammetry method whereas the JRC values were considerably reflected by the corrupted profiles in small scale. An appropriate data filtering method is required to reduce the bias in the data.

- The JRC data obtained from this section will be reanalysed to investigate the method to improve photogrammetric JRC data in Section 6.

Table 4-3 Comparisons of JRCs between manual measurement and photogrammetry: Beaudesert-Nerang road 1 and 2, Bethania, Nerang-Murwillumbah road 1 and 2

No.	Sites	sec-tions	pro-files	FL (mm)	c-to-o distance (m)	manual		3D	
						Tse & Cruden	Maerz et al.	Tse & Cruden	Maerz et al.
1	Beaudesert-Nerang road 1	1	1	24	17.0	11.6	9.7	-1.5	3.4
2			2	24	17.0	10.6	10.6	1.2	4.2
3			3	24	17.0	11.6	11.4	6.6	7.0
4			4	24	17.0	7.7	7.7	-2.0	3.3
5		2	1	24	17.0	7.5	7.6	8.2	8.2
6			2	24	17.0	8.7	8.3	8.2	8.3
7			3	24	17.0	11.3	11.4	5.3	6.1
8			4	24	17.0	8.7	8.8	8.7	8.7
9		3	1	24	17.0	5.4	6.0	10.8	10.4
10			2	24	17.0	12.0	12.6	6.9	7.2
11			3	24	17.0	14.8	16.6	3.4	5.1
12			4	24	17.0	14.1	15.7	14.1	16.9
13	Beaudesert-Nerang road 2	1	1	24	2.0	6.4	8.9	11.3	12.0
14			1	24	5.0	6.4	8.9	11.2	12.0
15			1	24	10.0	6.4	8.9	17.7	26.3
16	Beaudesert-Nerang road 2	1	1	50	12.8	11.0	11.3	10.0	10.1
17			1	85	12.8	11.0	11.3	8.1	8.1
18			1	24	2.0	11.0	11.3	19.7	31.4
19	Bethania	1	1	24	5.0	15.0	14.6	12.9	14.3
20			2	24	5.0	10.1	10.4	18.3	27.0
21			3	24	5.0	13.7	15.8	9.7	9.9
22		1	1	24	33.0	15.0	14.6	11.8	12.6
23			2	24	33.0	10.1	10.4	10.2	10.5
24			3	24	33.0	13.7	15.8	12.4	13.6
25	Nerang-Murwillumbah road 1	1	1	24	14.0	5.6	7.5	11.1	11.5
26				50	14.0	5.6	7.5	4.6	5.6
27				85	14.0	5.6	7.5	6.5	6.8
28		2	1	24	14.8	5.7	8.0	10.7	11.0
29			2	24	14.8	3.7	6.7	9.9	9.8
30			1	50	14.8	5.7	8.0	6.7	7.0
31			2	50	14.8	3.7	6.7	5.3	6.0
32			1	85	14.8	5.7	8.0	6.3	6.7
33			2	85	14.8	3.7	6.7	2.1	4.4
34	Nerang-Murwillumbah road 2	1	1	24	11.8	7.0	8.4	9.7	9.7
35				50	11.8	7.0	8.4	8.3	8.2
36				85	11.8	7.0	8.4	5.8	6.3
37		2	1	24	12.0	7.6	9.1	17.6	24.8
38			2	24	12.0	8.7	9.9	17.6	25.4
39			1	85	12.0	7.6	9.1	11.1	11.1
40			2	85	12.0	8.7	9.9	9.2	8.5

Table 4-4 Comparisons of JRCs between manual measurement and photogrammetry; Engineering road

FL (mm)	Pro-files	Manual		3D								
				c-to-o: 2.0 m			c-to-o: 5.0 m			c-to-o: 10.0 m		
		Tse & Cruden	Maerz et al.	No.	Tse & Cruden	Maerz et al.	No.	Tse & Cruden	Maerz et al.	No.	Tse & Cruden	Maerz et al.
24	1	8.3	8.2	41	23.6	40.7	77	18.8	28.4	113	16.9	23.1
24	2	7.7	7.7	42	21.7	37.0	78	23.5	53.4	114	24.0	52.2
24	3	9.8	9.6	43	-	-	79	-	-	115	13.2	14.7
24	4	7.6	7.6	44	4.9	5.7	80	11.1	11.5	116	-3.0	3.0
24	5	10.5	10.6	45	12.0	12.5	81	13.7	15.7	117	9.5	9.6
24	6	13.7	15.0	46	13.9	15.8	82	16.3	20.4	118	7.7	7.8
24	7	10.4	10.5	47	-	-	83	-	-	119	4.0	5.3
24	8	14.0	15.9	48	19.9	33.4	84	21.7	41.5	120	15.8	20.6
24	9	8.6	8.4	49	13.8	15.7	85	19.5	30.8	121	14.2	16.6
24	10	5.1	5.8	50	12.1	12.7	86	19.5	30.7	122	23.0	41.1
24	11	7.7	7.7	51	-	-	87	-	-	123	13.6	15.6
24	12	6.7	6.8	52	10.7	11.0	88	13.4	15.2	124	13.0	14.5
50	1	8.3	8.2	53	12.6	13.5	89	15.0	18.4	125	18.2	26.4
50	2	7.7	7.7	54	19.8	32.2	90	27.5	72.4	126	20.6	32.9
50	3	9.8	9.6	55	11.7	12.4	91	-	-	127	-	-
50	4	7.6	7.6	56	12.1	12.9	92	17.5	23.3	128	11.5	11.9
50	5	10.5	10.6	57	14.7	16.8	93	13.3	13.8	129	15.2	18.6
50	6	13.7	15.0	58	14.7	17.6	94	16.8	19.3	130	17.7	23.6
50	7	10.4	10.5	59	15.0	18.1	95	-	-	131	-	-
50	8	14.0	15.9	60	23.5	50.1	96	22.3	42.8	132	24.4	57.5
50	9	8.6	8.4	61	17.7	25.4	97	14.7	19.0	133	19.6	32.1
50	10	5.1	5.8	62	11.9	12.5	98	14.7	17.5	134	12.7	13.7
50	11	7.7	7.7	63	19.5	25.5	99	-	-	135	10.5	10.6
50	12	6.7	6.8	64	8.9	8.9	100	7.2	7.3	136	8.3	8.3
85	1	8.3	8.2	65	10.3	10.4	101	-	-	137	18.3	27.0
85	2	7.7	7.7	66	10.8	11.1	102	18.7	29.5	138	-	-
85	3	9.8	9.6	67	10.7	11.0	103	-	-	139	-	-
85	4	7.6	7.6	68	11.7	12.3	104	9.6	9.5	140	-	-
85	5	10.5	10.6	69	13.5	15.1	105	13.5	15.1	141	14.2	16.4
85	6	13.7	15.0	70	15.6	19.8	106	15.4	18.4	142	13.7	15.7
85	7	10.4	10.5	71	-	-	107	-	-	143	10.9	10.8
85	8	14.0	15.9	72	-	-	108	21.0	36.8	144	17.2	24.4
85	9	8.6	8.4	73	9.5	9.5	109	-	-	145	11.9	12.3
85	10	5.1	5.8	74	9.8	9.7	110	-	-	146	10.0	9.9
85	11	7.7	7.7	75	13.4	15.2	111	7.4	7.5	147	9.8	9.8
85	12	6.7	6.8	76	11.4	11.9	112	7.4	7.5	148	13.9	15.8

5 PHOTOGRAMMETRY LABORATORY TESTS AND DEVELOPMENT OF PARABOLA ERROR MODELS

A part of this chapter was published in International Journal of Rock Mechanics & Mining Sciences journal as follows:

Dong Hyun Kim, George Poropat, Ivan Gratchev, Arumugam Balasubramaniam (2015) Improvement of photogrammetric JRC data distributions based on parabolic error models. International Journal of Rock Mechanics and Mining Sciences, 80: 19-30.

5.1 Introduction

The limit of resolutions in photogrammetry methods is an important factor in investigating rock surface roughness. The range measurement resolutions, obtained from photogrammetry surveys, are strongly dependent on the employed focal lengths and the distances between cameras and objects. The relationships between the range of resolutions and the factors (focal length and distance) can be simply a linear effect (Poropat, 2008). However, the accuracy and precision of the resolutions of the photogrammetric 3D images, which are required for estimation of rock joint roughness, have not been sufficiently investigated.

The resolutions of 3D images can be quantified by the point intervals of the 3D models. The accuracy of the roughness profiles, which are extracted from the 3D models, is thus determined by comparing the profiles with those of manually measured profiles. The roughness characteristics of the profiles are then quantified with their JRC values. Regarding the standard profile gauges for manual measurements, a 1 mm interval step size can be used as a standard to measure roughness profiles in practical purposes.

Several factors related to data intervals, which lead to inaccurate JRC values in photogrammetric methods, have been reported. If the data interval is more than 1 mm, this may lead to underestimating JRC values, due to the reduced asperity angles for the step sizes (Rangers, 1970). On the contrary, Poropat (2008) emphasized the importance of the measurement errors corrupted by noise when using small pixels less than 1 mm. It can be also generally accepted that large camera distances with short focal lengths contribute to producing large measurement errors and standard deviations for JRC estimations. This can

be supported by recent research that cameras with longer focal length lenses tend to decrease measurement errors in stereo photogrammetry systems (Fooladgar et al., 2013). However, this correlation between the photograph distance ranges and the accuracy of JRC has still been ambiguous in both laboratory and site conditions.

The primary object of this chapter is to understand the influences of camera distances to objects and focal lengths on the precision and accuracy of JRC estimation. A series of photogrammetry laboratory tests with three different focal length lenses was performed over differing distances to the object and multi-baseline conditions. The tests were carried out in ideal laboratory conditions to reduce the influences caused by other factors (e.g. shade effect, inaccuracy of distance measurement, inclination of plane).

This experimental study firstly presents the allowable distances of photogrammetry for the employed focal length of lenses to estimate JRC values based on the accuracy of manual measurements using 1 mm intervals. Secondly, the accuracies of JRC values are demonstrated according to the employed focal lengths and distances. Thirdly, quadratic error equations are suggested from the results of the laboratory tests. These functions are based on the relationship between the RMSE of JRC and the normalized JRC values with variations of distances to objects. Based on the precisions of the focal length of the various lenses, these parabolic functions are formed with different sizes and are used for predicting total measurement errors according to distances to objects, thereby improving JRC data distributions.

5.2 Photogrammetry laboratory tests

5.2.1 Test set up and conditions for laboratory tests

A single lens reflex digital camera (Nikon D7000), which has a high resolution CCD sensor ($4,928 \times 3,264 = 16$ mega pixels), was employed to capture images of a weathered sandstone sample. In order to obtain images with different resolutions, photographs of the rock sample were taken in the distance range of 1.0 m to 7.0 m, spaced 0.5 m apart, using three different focal length lenses (FS = 24mm, 50mm, 85 mm). A total of 33 different sets of photographs were created. A sliding device, which is composed of two steel pipes (D = 19 mm) and a moving wooden plate with PVC pipe brackets to guide the pipes, was developed to control the horizontal camera positions for all test conditions (Fig 5.1). This device effectively

increases the accuracy of distance measurement between the camera locations and the object for the various test conditions: As the height of the camera position is located on the same horizontal plane as the sample, the vertical locations of viewpoints are kept constant to minimize any erroneous factors, which may lead to the minimization of any insignificant occlusions of asperities due to different vertical positions.

The sample used in this experiment is weathered sandstone which was collected from an excavation site in Bethania, Brisbane. The size of the rock block is around 4,950 cm^3 (W: 150 mm, D: 150 mm, H: 220 mm). The joint plane of the rock block was prepared as a model surface which was embedded in cement plaster to keep it standing during the experiment, as shown in Figure 5.2. The sample is positioned in front of a black panel (the panel size is 1,500 mm × 500 mm). It has been found in the post-processing of the laboratory photogrammetric tests that this panel is a great help to create accurate 3D models minimizing model noise. Three types of targets are attached on the sample area and the back board. These are used for geo-referencing, and as a guideline for profile measurement, as presented in Table 5-1.
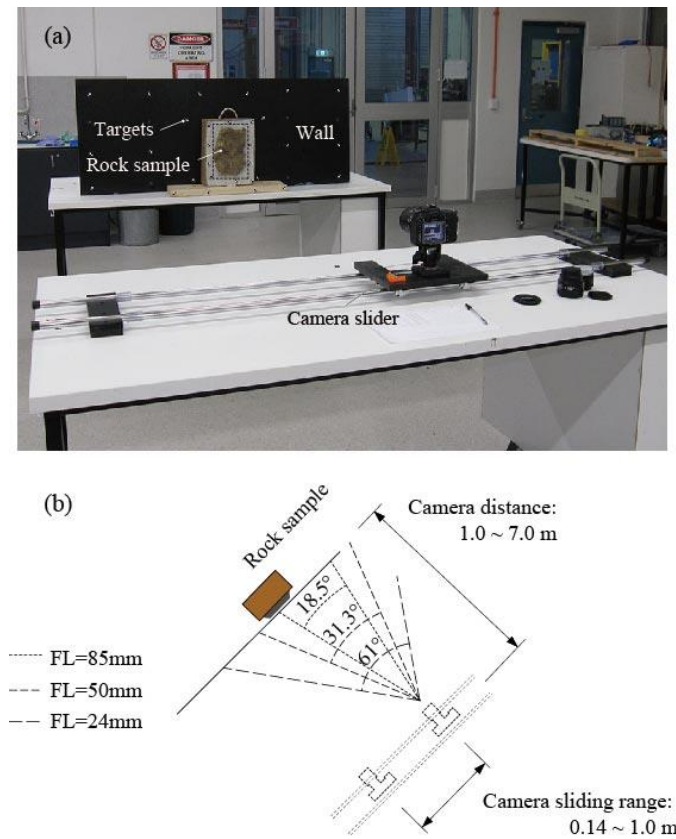
Fig. 5.1 Laboratory test setting, overview (a) and view angles with focal lengths of lenses (b)

The targets, which were drawn in AutoCAD and printed, were created by putting them on a flat plastic sticky tape. The distances between the circular targets were measured after the targets were located for using the values as standards for geo-referencing of 3D images. The target sizes of the 3D photogrammetry models in pixels varied with the resolutions of the images. The minimum preferred diameter of target in this research is at least 3 pixels (Dold, 1996). However, for the purposes of the tests, the sizes of targets were sufficient to identify the location of each target in the ranges of laboratory tests. Using the photogrammetry setup, a set of were performed in the conditions as shown in Table. 5-2.
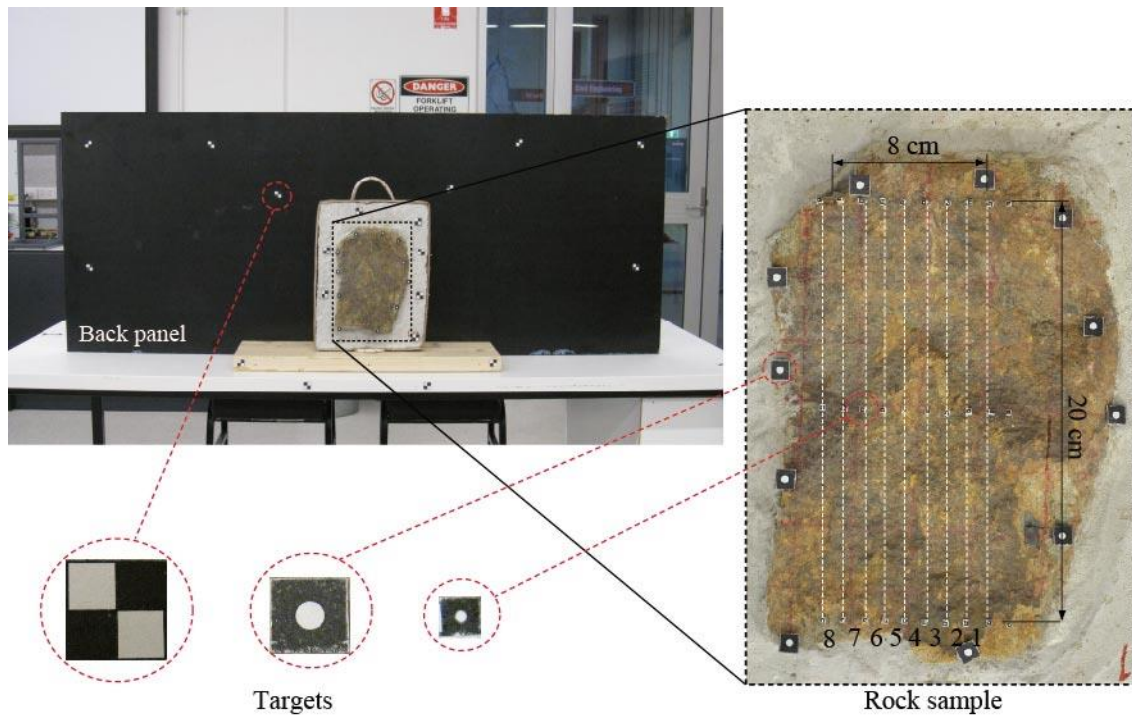
Fig. 5.2 Details of the rock sample and targets

Table 5-1. Targets used in experiments

Types	Sizes	Uses
Rectangular	D=15 mm	Matching points for 3D image generation
Medium circular	ϕ=3.5 mm	Checking the locations for geo-referencing
Small circular	ϕ=0.8 mm	Guidelines of profiles for JRC estimation

5.2.2 Equipment

This section presents the equipment used in the laboratory tests. The details and specifications of the employed camera and lenses and the developed camera slider, are related to image resolutions and measurement accuracy.

1) Camera

A normal SLR digital camera, Nikon D7000, was used for obtaining images in the laboratory tests. The specifications of this camera are described in Table 5-3. In order to obtain the highest density images in the tests given in the conditions, the image files were taken in the maximum size. As the employed file format, the camera-native format (NEF for Nikon) was originally used to allow for maximum flexibility of the image, adjusting for such factors as exposure, contrast, sharpness and/or white balance of the images (Haneberg, 2008). Then, the file format was converted to TIFF format.

Table 5-2. Laboratory test conditions

AF Nikkor 24~85 mm f3.5-4.5G		AF Nikkor 50 mm f/1.8D		AF Nikkor 85 mm f/1.8D	
Distance from sample (D, m)	Base line distance (B, m)	Distance from sample (D, m)	Base line distance(B, m)	Distance from sample (D, m)	Base line distance (B, m)
1.0	0.14	1.0	0.14	-	-
1.5	0.21	1.5	0.21	1.5	0.21
2.0	0.29	2.0	0.29	2.0	0.29
2.5	0.36	2.5	0.36	2.5	0.36
3.0	0.43	3.0	0.43	3.0	0.43
3.5	0.50	3.5	0.50	3.5	0.50
4.0	0.57	4.0	0.57	4.0	0.57
4.5	0.64	4.5	0.64	4.5	0.64
5.0	0.71	5.0	0.71	5.0	0.71
5.5	0.79	-	-	5.5	0.79
-	-	6.0	0.86	6.0	0.86
-	-	-	-	6.5	0.93
-	-	7.0	1.00	7.0	1.00

Table 5-3. Specifications of camera

Items	Specifications
Type	Single-lens reflex digital camera
Effective / Total pixels	16.2 million / 16.9 million
Image sensor	23.6×15.6 mm CMOS sensor
Maximum image size (pixels)	$4,928 \times 3,264$
File format (employed)	NEF (RAW)

2) Lenses

Three different focal lengths of lenses were employed to produce different density images in the same test distances. The specifications of the lenses are presented in Table 5-4. A zoom function is not recommended to use in photogrammetry. In this study, calibration of the lenses was achieved using the custom calibration files provided by the "Sirovision" code (CSIRO, 2012).

Table 5-4. Specifications of lenses

Items	AF Nikkor 24~85 mm	AF Nikkor 50 mm	AF Nikkor 85 mm
Camera focus mode	AF	AF	AF
Focal length	24~85, 24 mm fixed*	50 mm	85 mm
Maximum aperture	f/3.5~4.5	f/1.8	f/1.8
Angle of view	61°	31.3°	18.5°

3) Camera slider

The baselines between camera positions were adjusted by the ratio of 1:7 for the test distances to the rock sample. This ratio was kept constant for all test conditions to minimize effects derived from the variation of the ratio. The calculated camera separations for the test distances are presented in Table 5-2. In order to establish the test layout for each camera distance efficiently, a camera slider was fabricated as shown in Figure 5.3. The slide plate is composed of a built-in spirit level and a tripod head. The wooden plate could slide horizontal directions smoothly on the two steel pipes using fixed plastic brackets on the bottom of the plate.
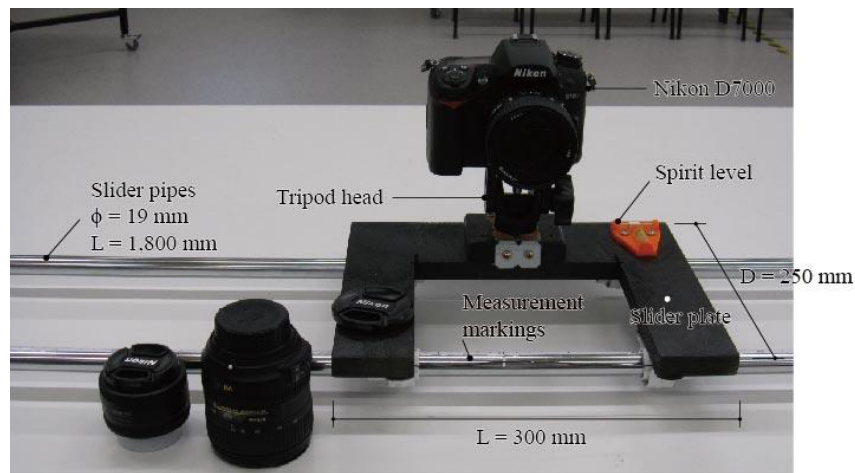
Fig. 5.3 Fabricated sliding device

5.2.3 Roughness characteristics obtained from 3D images

1) Manual measurements of roughness profiles

Roughness profiles in the targeted area are divided into eight sections (Fig. 5.2). The length and the width of the targeted area are 200 mm and 80 mm respectively. Roughness profiles for the eight sections as shown in Figure 5.4 were measured by a profile gauge (L = 300 mm). The step size of the gauge was 1 mm and the coordinates of the measured profiles were digitized by the obtained profile drawings using an AutoCAD program. The measured roughness profiles are shown in Figure 5.5.
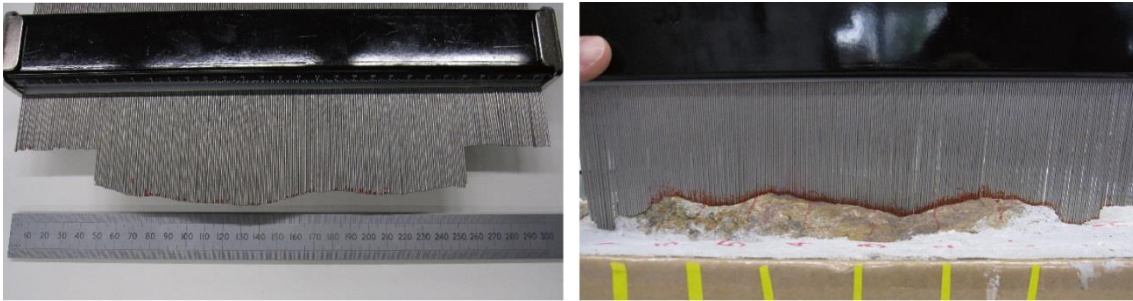
Fig. 5.4 Manual measurement of a roughness profile
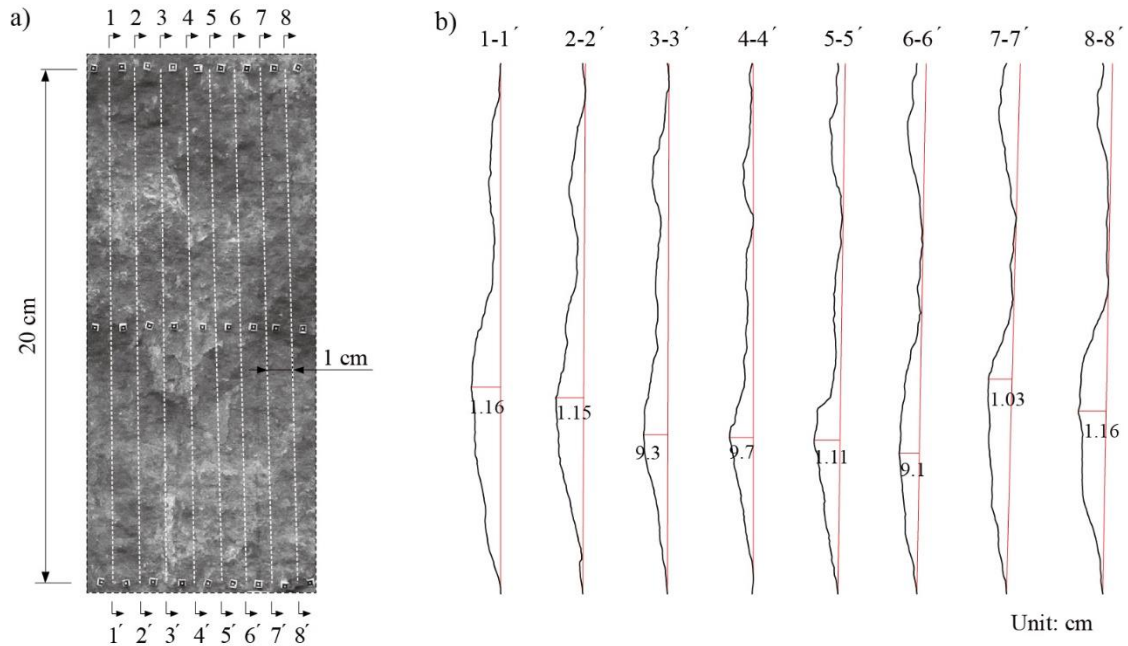
Fig. 5.5 Measured roughness profiles (1 mm intervals)

94

2) 3D model creation

The 33 sets of stereo photographs were used for creating 3D models. The images, which were taken at 2 metres and 5 metres are shown in Figures 5.6 and 5.8. The target areas of the images, which are marked by dash lines, are selected for creating 3D models in the photogrammetry code, Sirovision. It is observed from the series of the figures that the rock sample area of the total image area is decreased with the camera distances from the rock sample and increased with the employed focal lengths. This relationship is almost a linear function as shown in Figure 2.16 in Chapter 2. The size of the target area in an image, which is inversely proportional to the camera distance from an object, has a strong influence on the procedure of 3D image construction. In fact, Sirovision could not properly generate 3D models in a long distance farther than 5 metres when 50 mm and 85 mm focal lengths were used.

Figure 5.7 and 5.9 visually compare the generated 3D images of the sample area at 1.5 metres and 5.0 metres. In the case of 1.5 metre distance, the pixel sizes of the 3D images are the high resolutions producing more detailed images compared to the images generated from 5.0 metres. These differences are also shown by using different focal lengths at the same distances. Table 5-5 summarises the pixel sizes of the 2D images according to the test setup.

Table 5-5. Pixel sizes according to the test conditions

Pixel sizes (mm)				
Focal lengths (mm)		24	50	85
Distance (m)	1.0	0.14	1.0	-
	1.5	0.21	1.5	1.5
	2.0	0.29	2.0	2.0
	2.5	0.36	2.5	2.5
	3.0	0.43	3.0	3.0
	3.5	0.50	3.5	3.5
	4.0	0.57	4.0	4.0
	4.5	0.64	4.5	4.5
	5.0	0.71	5.0	5.0
	5.5	0.79	-	5.5
	6.0	-	6.0	6.0
	6.5	-	-	6.5
	7.0	-	7.0	7.0
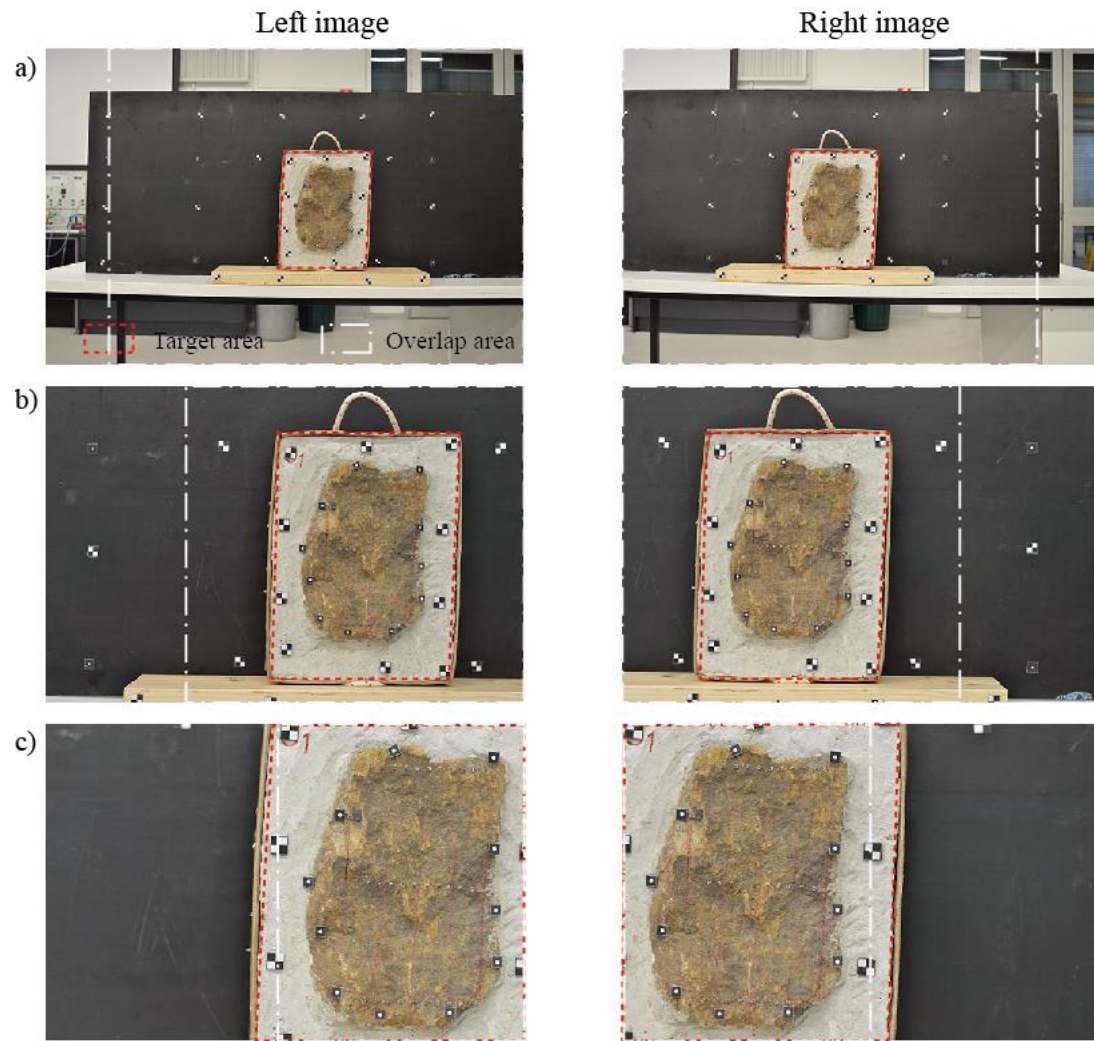
Fig. 5.6 Left and right images of stereo photographs; D = 1.5 m, FL = 24 mm (a); D = 1.5 m, FL = 50 mm (b); D = 1.5 m, FL = 85 mm (c)
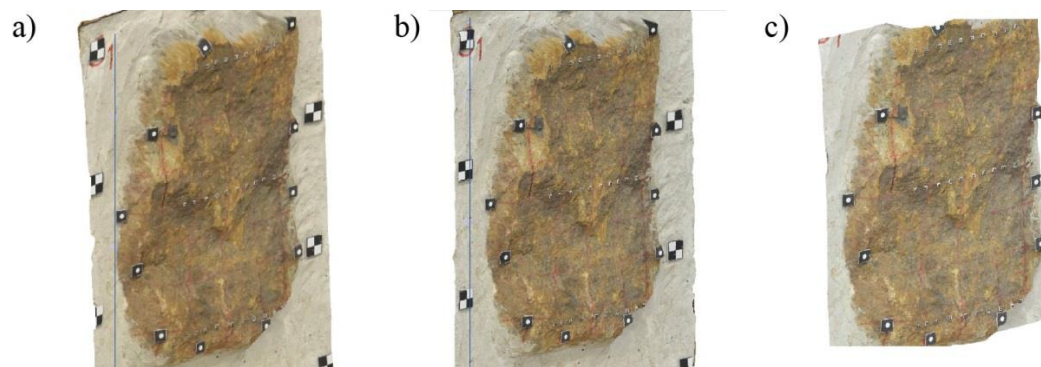
Fig. 5.7 Created 3D images; D = 1.5 m, FL = 24 mm (a); D = 1.5 m, FL = 50 mm (b); D = 1.5 m, FL = 85 mm (a)
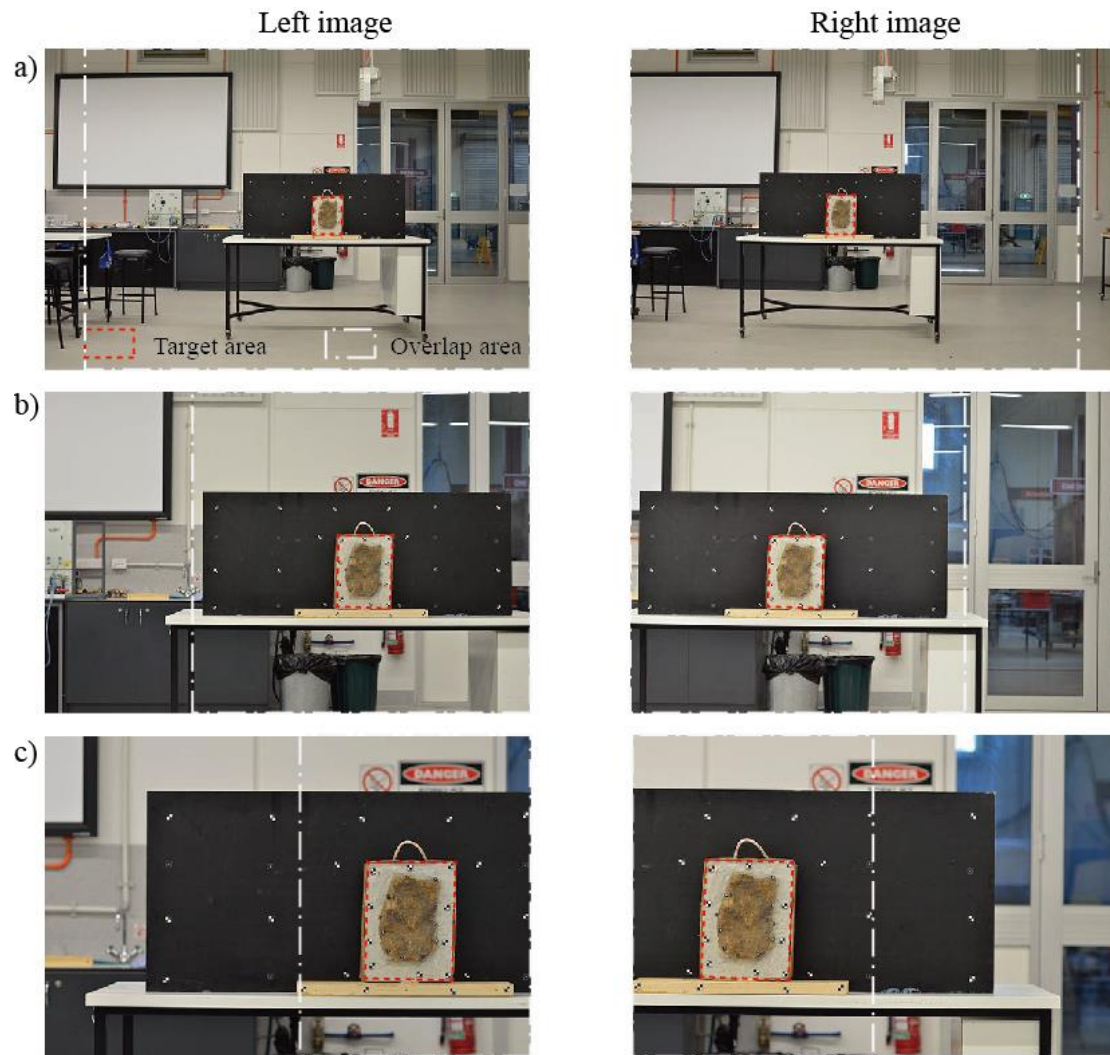
Fig. 5.8 Left and right images of stereo photographs; D = 5.0 m, FL = 24 mm (a); D = 5.0 m, FL = 50 mm (b); D = 5.0 m, FL = 85 mm (c)
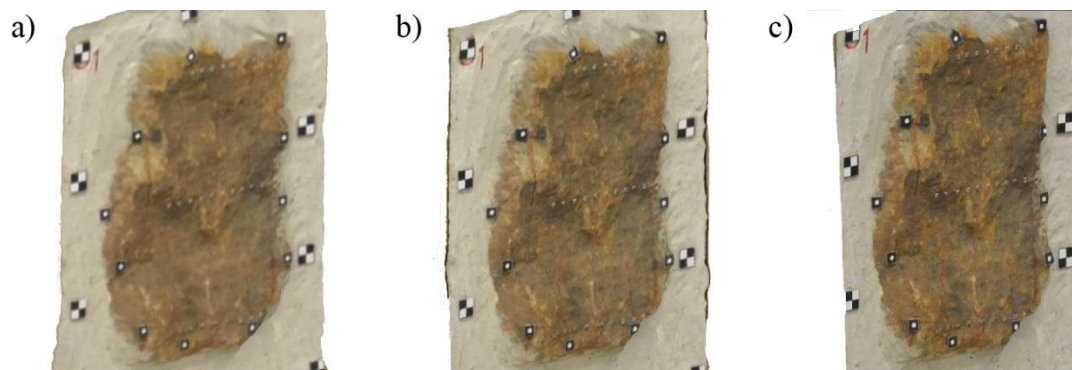
Fig. 5.9 Created 3D images; D = 5.0 m, FL = 24 mm (a); D = 5.0 m, FL = 50 mm (b); D = 5.0 m, FL = 85 mm (a)

3) Estimation of the maximum asperity heights

The 3D models were created using the photogrammetric code, "Sirovision". The scales of the initial 3D images were revised by geo-referencing procedures using the measured lengths between targets and the lengths of baselines. The program, Sirovision provides an option to extract roughness profiles by selecting four corners of an area of 3D models. However, the option is not appropriate to control the position of the profile of interest for comparison. Thus, the spatial data of the 3D images were then imported to the AutoCAD program. Two dimensional coordinates along the eight measurement directions could be selected to extract the coordinates of the roughness profiles. The extracted profiles were then visually compared with the true profiles measured by the profile gauge (L = 300 mm, 1 mm intervals). The maximum asperity heights of the obtained digitized profiles tended to be underestimated in all measurement ranges. Figure 5.10 compares the simulated profiles according to the sampling intervals and the focal length of the lenses for two representative sections.

The vertical scale was exaggerated three times as much as the real sizes for clarity. It is noticed that the undulation geometries of the simulated profiles are similar to the manually measured profiles; however, to some extent, there are discrepancies in the second order asperities. This disagreement tends to become more frequent in lower scale images. This may lead to a reduction in the accuracy as well as the precision of 3D models. The maximum asperity heights (H_a) of the profiles were estimated subtracting the lowest values of y-coordinates from the highest values. Comparison of the H_a values between the values obtained from the photogrammetric profiles and the values calculated from the true profiles can estimate the accuracy of the 3D roughness models for the large scale roughness. Figure 5.11 demonstrates the variations of the maximum asperity heights according to the employed focal length of lenses.

The graphs are plotted using the data of the same pixel sizes and the employed pixel sizes are 0.5 mm and 1.0 mm. It is interesting that even when the resolutions of the 3D images are kept constant, the H_a values are reduced with the increases of focal lengths. This directly indicates that the distance from the object is a crucial factor in controlling the accuracy of 3D photogrammetric models.
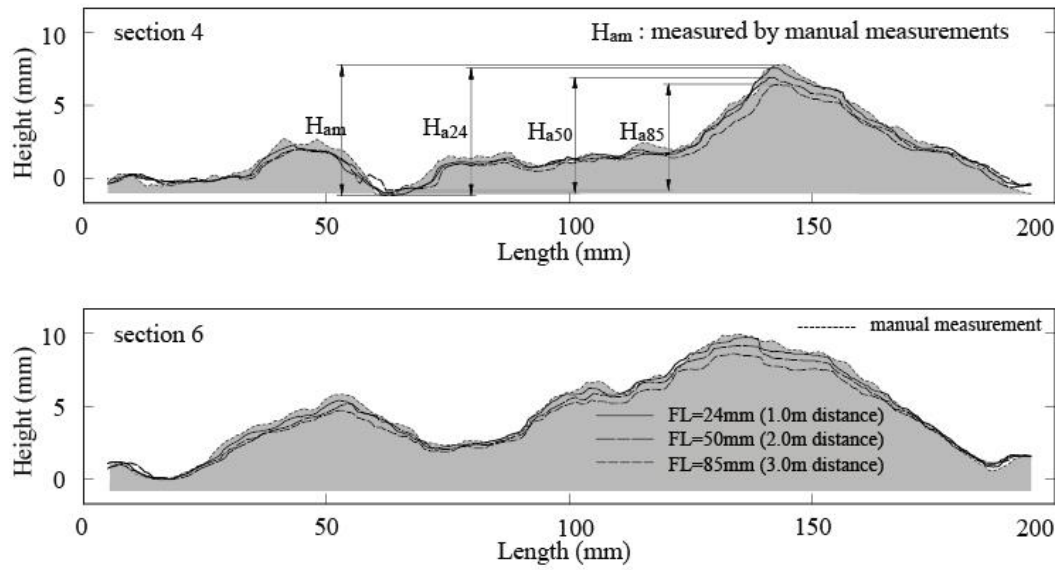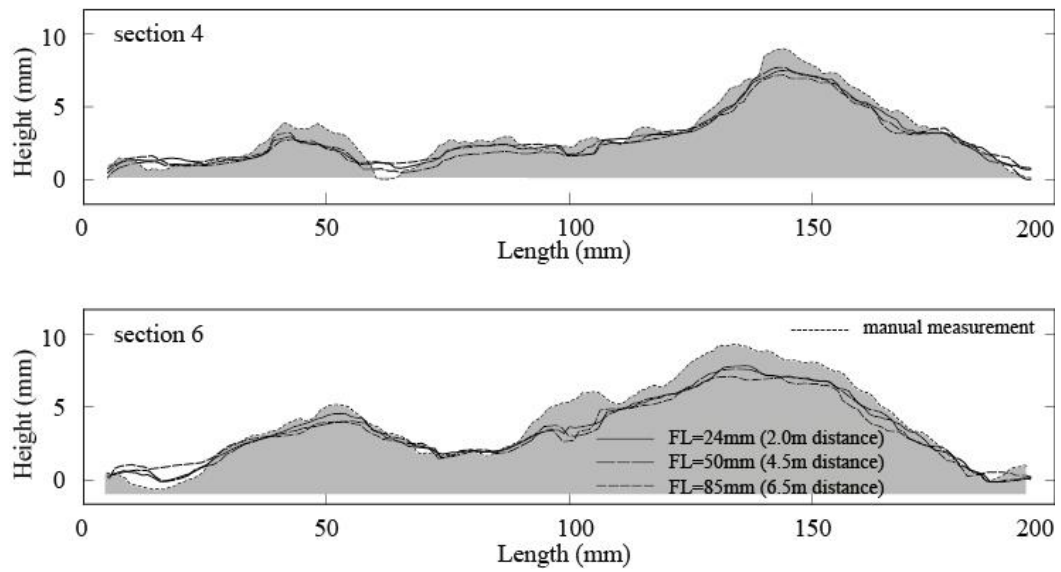
Fig. 5.10 Comparisons of roughness profiles obtained from 3D images, 0.5 mm pixel size (a), 1.0 mm pixel size (b)

99
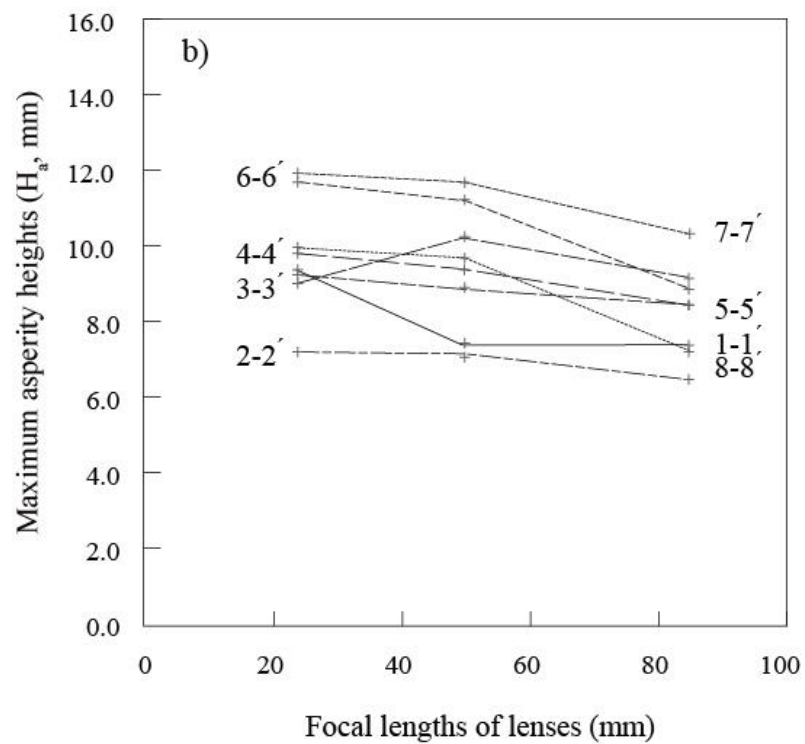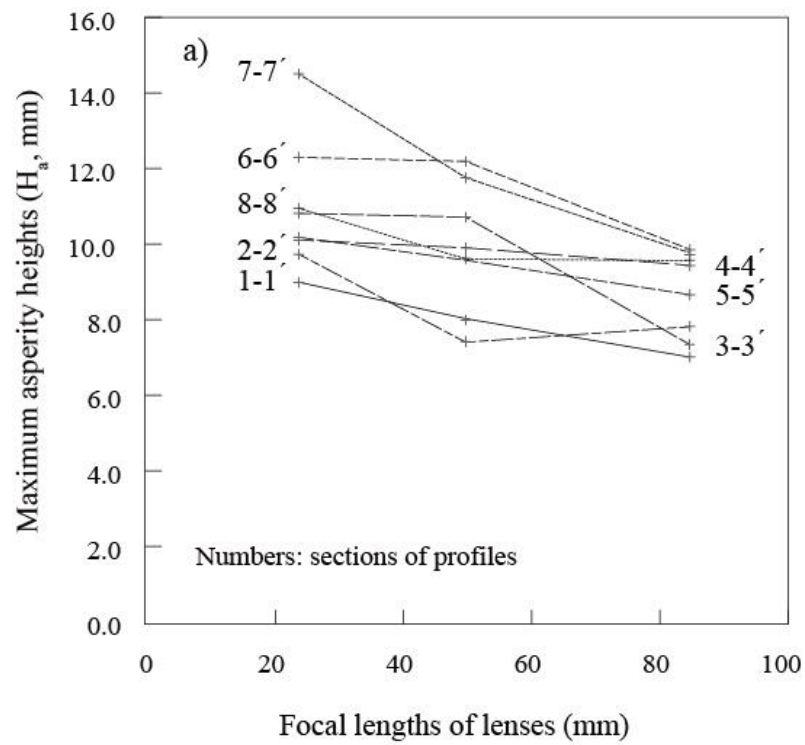
Fig. 5.11 Variation of the maximum asperity heights, H_a with photographing distance, pixel size = 0.5 mm (a), pixel size = 1.0 mm (b)

5.2.4 JRC estimation and allowable distances

Using the coordinates of the extracted profiles from the 3D models, JRC values were estimated by Eq. (2-8) and Eq. (2-9) in Chapter 2. The JRC values of the manually measured profiles were also calculated using the digitized coordinates with a step size of 1.0 mm. To compare the JRC values between photogrammetry and manual measurement, normalized JRC values, N_{JRC} presented in Eq. (5-1), are used. The normalized values are also used to identify the degrees of over- or under-estimation of JRC. The comparison, which use normalized asperity heights of the extracted profiles, are also performed using the similar equation (Eq. 5-2). The obtained JRC values and the maximum asperity heights from the eight sections are presented in Figure 5.12 and 5.13.

$$N_{JRC} = \frac{JRC_{3D\ images}}{JRC_{manual\ measurement}} \qquad (5\text{-}1)$$

$$N_{Ha} = \frac{Ha_{3D\ images}}{Ha_{manual\ measurement}} \qquad (5\text{-}2)$$

The normalized JRC values for the entire data according to the employed focal lengths are plotted in Figure 5.12. The data distributions are scattered. However, the normalised JRC values obtained from the photogrammetric 3D models obviously indicate downward trends as the camera moves further from the object. For the dispersed data, exponential curves are adopted as the best regressions which decrease at the rate with distances to objects. Based on the coefficient of determination, R^2 of the graphs of Figure 5.12, it can be said that the data ranges from 32% to 48% of N_{JRC} values can only be explained by the camera distances.

Using the regression curves in Figure 5.13, the intersections between the regression curves and the line of $N_{JRC} = 1$, indicate the allowable distances, da, which are the divisions between over and under estimation of JRC values for each lens. For the macro lens (FL = 24 mm), the normalized JRC values rapidly decrease with increasing photograph distances. Under-estimation is obvious in the entire measurement ranges where the distance is over 1.0 m. In the cases of 50 mm and 85 mm lenses, the allowable distances can be assumed as 2.0 m and 4.0 m respectively. Table 5-3 presents the allowable distances.

Table 5-3. Comparison of the allowable distances (d_a) for JRC estimation

Focal length (FL, mm)	Camera distances to object at GPS = 1.0 mm (m)	Experiment data	
		d_a (m)	Scale (d_a / FL)
24	1.8	1.0	41.7
50	3.5	2.0	40.0
85	5.5	4.0	47.1
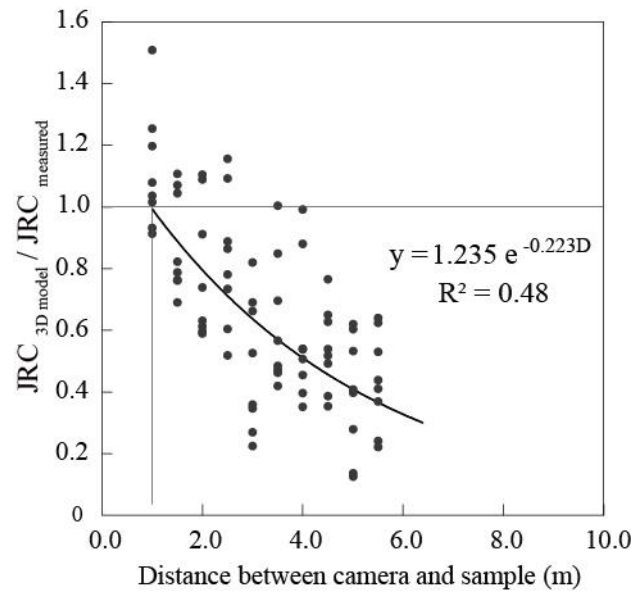
Fig. 5.12 Relationship between normalized JRC values and photographing distances with different focal length lenses, FL = 24 mm
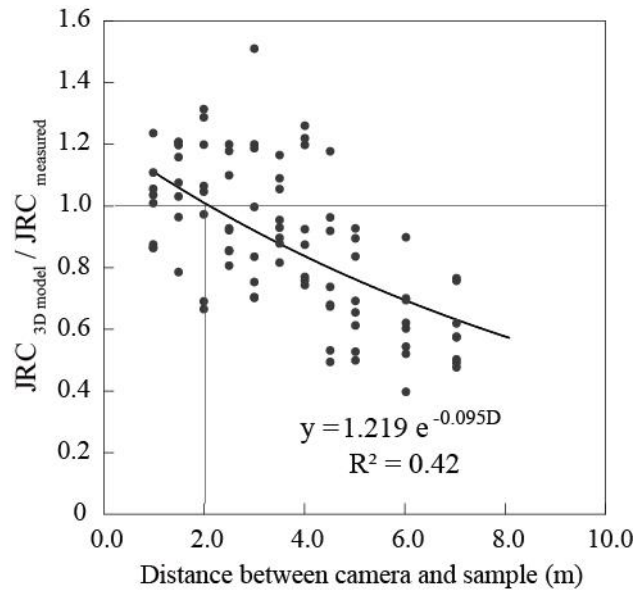
Fig. 5.13 Relationship between normalized JRC values and photographing distances with different focal length lenses, 50 mm

102
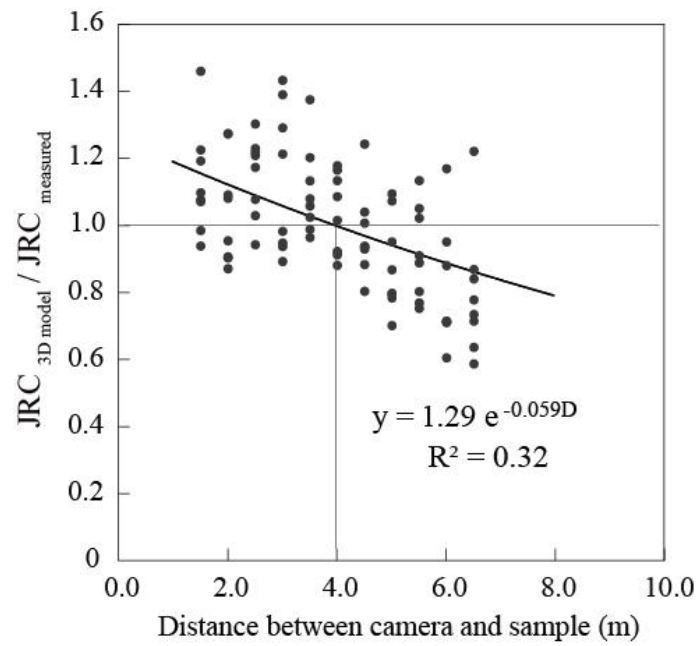
Fig. 5.14 Relationship between normalized JRC values and photographing distances with different focal length lenses, 85 mm
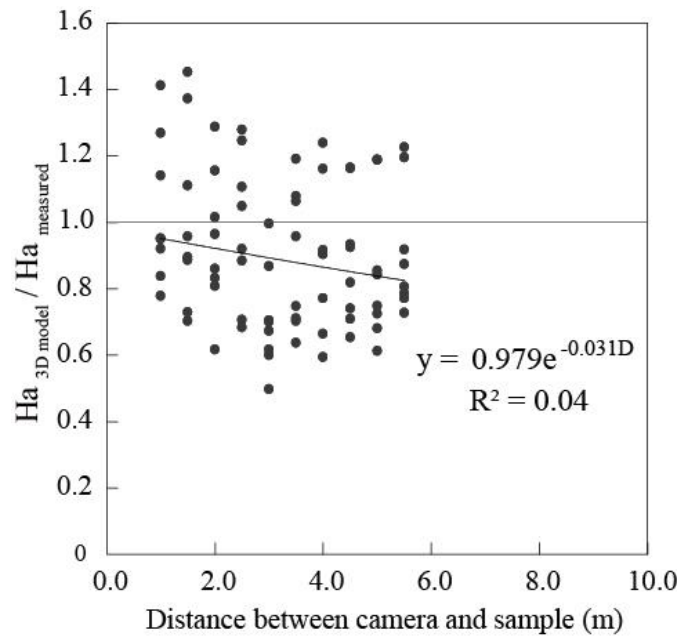
Fig. 5.15 Relationship between normalized maximum asperity heights and photographing distances with different focal length lenses, FL = 24 mm
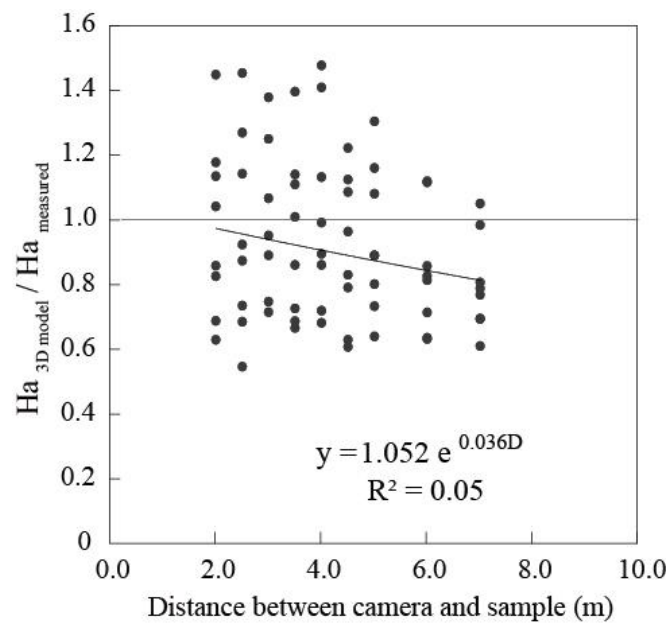
Fig. 5.16 Relationship between normalized maximum asperity heights and photographing
distances with different focal length lenses, FL = 50 mm
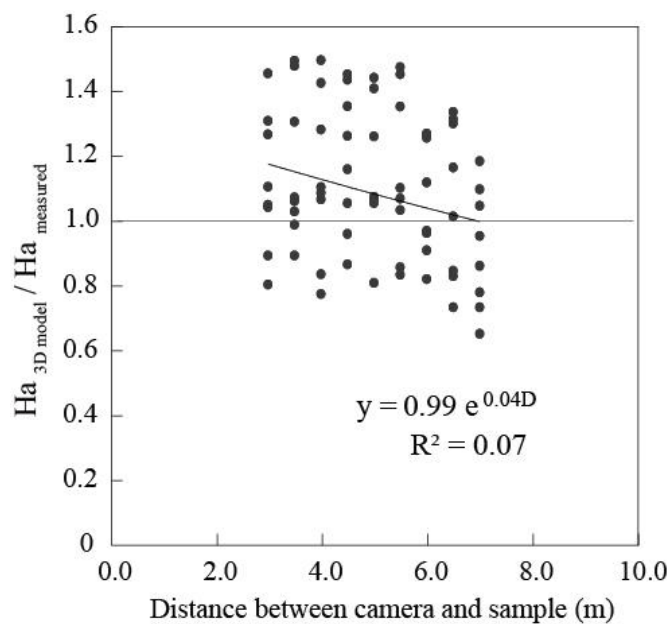
Fig. 5.17 Relationship between normalized maximum asperity heights and photographing
distances with different focal length lenses, FL = 85 mm

104

5.3 Development of parabola error models

5.3.1 Accuracy and precision in photogrammetry

The accuracy and precision of 3D images have been key issues in photogrammetry methods (Krosley & Shaffner, 2003; Poropat, 2006; Haneberg, 2008). The accuracy of obtained 3D photogrammetric models can be assessed by comparing the locations of points, the dimensions of objects and the orientations of planes between the values of the 3D models and the measured values. 'Accuracy' is a measure of the proximity of a measured value to the true value. This term is different from 'precision' which refers to the degree of repeatability of the measurement. The accuracy and precision of photogrammetric 3D models can be affected by various factors such as image resolutions, lens distortion, image occlusion or geo-referencing. Atmospheric conditions such as fog or haze may also affect the accuracy of 3D models by the reduction of the image sharpness (Haneberg, 2008).

Simply, the accuracy of an image can be calculated using the GPS values. Based on the accuracy of the image sensor, the expected accuracy of the obtained images is expressed by Eq. (5-3).

$$\sigma_{plan} = \sigma_{pixel} \times GPS \qquad (5\text{-}3)$$

where, σ_{pixel} is the accuracy in terms of pixels in the image sensor and σ_{plan} is the accuracy of the ground pixels. If the obtained accuracy is 0.1 pixels, the model is accurate to within 1/10th of the size of a ground pixel. However, assessment of the accuracy in close range photogrammetry may be difficult due to the fact that assessment should be performed using their intrinsic inaccuracy (Haneberg, 2008).

Poropot (2006) reported several components which affect the accuracy and precision of 3D photogrammetry models as follows; the accuracy of camera distance, the accuracy of measurement of the azimuth and the accuracy of the elevation of the line of sight from the camera. The accuracy of joint orientation, which indicates the simple measurement using the positions of three points on a plane, is important in discontinuity survey. Poropat (2006) suggested a relationship between a chord length, and a range of precision for the estimation of the average error of orientation as shown in Eq. (5-4).

$$\text{average error of orientation} = \arctan\left(\frac{2 \cdot \text{range\_precision}}{\text{chord\_length}}\right) \qquad (5\text{-}4)$$

Poropat (2006) obtained the range of ±0.5° for orientation accuracy using 25 points of data using Sirojoint (CSIRO). Similarly, Krosley & Shaffner (2003) reported that the value of 0.04% for spatial accuracy and the range of ±0.5° for orientation accuracy were obtained from experimental conditions using Sirovision. The accuracy and precision of joint roughness based on photogrammetry methods have been rarely mentioned due to the various factors influencing the accuracy and precision of photogrammetric 3D models. As mentioned previously, even though several leading studies sought to extract roughness profiles from 3D models in different resolution images (Tanon and Kottenstette, 2006; Haneberg, 2007; Baker et al., 2008; Poropat, 2006; Poropat, 2008; Poropat, 2009), further studies are required to quantify roughness reliability from photogrammetric data. In this study, the accuracy and precision of photogrammetry are discussed by using experimental data focusing on the camera-to-object distances and the focal length of lens.

In close range digital photogrammetry, an increase of camera distances to objects normally results in the reduction of data accuracy with corresponding measurement errors. In this case, the accuracy and precision of 3D photogrammetric coordinates can be analysed by statistical approaches. In statistics, accuracy is the proximity of measurement results to the true value and precision is the repeatability of the measurement. In photogrammetry, it is known that higher measurement precision can be achieved by longer focal lengths with a reduction in the range of measurement errors (Fraser, 1984; Fooladgar et al., 2013). This concept can be demonstrated using JRC data histograms as shown in Figure 5.18.

Longer focal length lenses show narrower widths of the data distributions than those obtained from shorter focal length lenses. To quantify the precision of the data distribution, standard deviation can represent the precision of the data group. Therefore, an increase of focal length may be required at certain photogrammetry site survey conditions to raise measurement precision. However, the increase of focal length may not be exactly proportional to the measurement precision or accuracy. This is because the modification of the scale derived from the change of focal length can modify the geometry of the images to a great or small extent due to various accompanying factors that can affect the accuracy of the results. These factors include principal distances, camera lens distortion, base line lengths and the percentage of photograph overlaps (Dai et al., 2014).

106

Therefore, based on the results from the laboratory tests, this study analyses the data using a simple statistical approach. In association with the standard of manual measurement, this study assumes that the distance limit, at which the mean values of normalized JRCs indicate 1, is defined as an allowable distance for the employed focal length. This distance is based on the manually measured JRC values using a 1 mm step size profile gauge. Secondly, parabolic shape error equations, which are related to the data distributions, are presented in this chapter. The equations are the correlations between the RMSE (Root mean square deviation) of JRC values and the normalized JRC values with variations of distances to objects. Based on the precisions of the focal lengths, these quadratic error equations are formed with different sizes and used for predicting measurement errors according to the distances between cameras to objects.
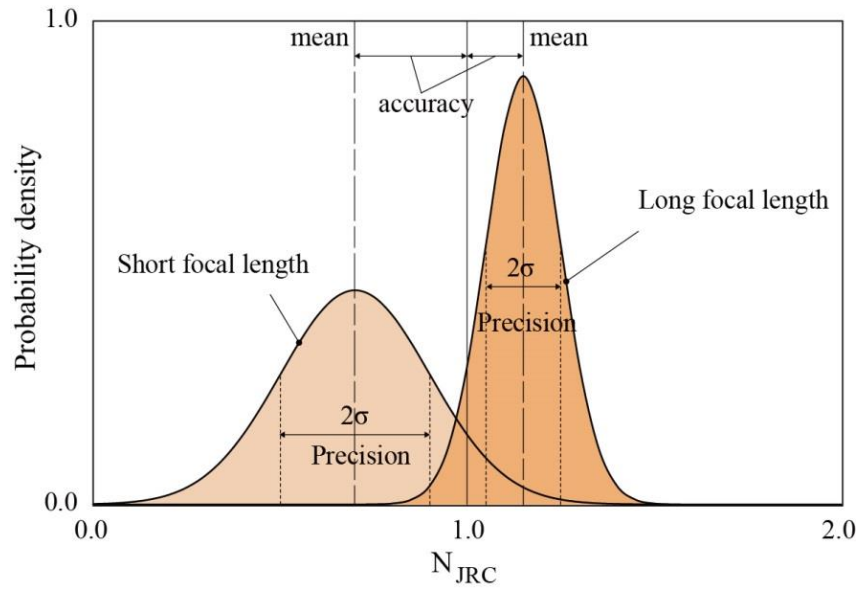
Fig. 5.18 Concept of measurement precision according to focal length of lenses

5.3.2 Estimation of measurement errors

In this study, it is assumed that the accuracy and precision of JRC values are dependent on the whole photogrammetric procedure from data acquisition to analysis. Further, the obtained JRC values contain random errors which can be caused by the main changes (e.g. camera lenses and photograph distances) under identical photogrammetric investigation conditions. In relation to two dimensional roughness parameters, two simple parameters, which are maximum asperity height (H_a) and estimated JRC values (JRC_p), are used to

analyse the errors. The root mean square deviation (RMSE) for the maximum asperity heights and JRC values are estimated by Eq. (5-5) and Eq. (5-6).

$$RMSE_{H_a} = \sqrt{\frac{\sum_{i=1}^{n}(H_{o,i} - H_{p,i})^2}{N}} \qquad (5\text{-}5)$$

$$RMSE_{JRC} = \sqrt{\frac{\sum_{i=1}^{n}(JRC_{o,i} - JRC_{p,i})^2}{N}} \qquad (5\text{-}6)$$

where H_o is the manually measured asperity height; JRC_o is the values obtained from the manually measured profiles; H_p and JRC_p are the values obtained from the profiles of photogrammetry 3D models. The parameters, $RMSE_{ha}$ and $RMSE_{JRC}$ represent the standard deviations of the data distributions for the maximum asperity heights and the JRC values.

In this study, the manually measured roughness profiles and their JRC values, which are obtained from 1 mm interval profile gauges, are regarded as the standard values for the required accuracy of the rock joint roughness investigations. Therefore, the normalized values, N_{JRC} and N_{Ha} in Eq. (5-1) and Eq. (5-2) indicate the accuracy of the photogrammetry 3D models for the rock joint roughness estimations based on the manually measured values. The normalized values also classify the photogrammetric JRC values into over- or under-estimation of JRC based on the JRC values obtained from manual measurements.

5.3.3 Parabolic error models

In photogrammetry, the modification of the 3D image scale, which is caused by the variations of focal length of lenses as well as the distances to rock cuts, can affect the $RMSE_{JRC}$ and $RMSE_{Ha}$. The influence of the camera distances to objects on the normalized roughness parameters can be expressed by means of the RMSE values. Based on the laboratory data, it is observed that the distributions of the RMSE are well regressed by symmetric curves which are centred by the normalized true value ($N_{JRC}=1.0$) associated with the camera distances to the object (Fig. 5.19). As a base form of the error functions, a parabolic equation is proposed as presented in Eq. (5-7).

$$RMSE_{JRC} \cdot d = aN_{JRC}^2 + bN_{JRC} + c \qquad (5\text{-}7)$$

where d is the camera distances to objects; a is a coefficient to determine the direction and the size of the parabola which represents the precision of the data; b and c are the coefficients to determine the locations of vertex of the parabola. In this equation, the coefficients, a, b, c are easily interpretable and varied with the employed focal length of lenses in this study. It can be assumed that larger focal length lenses create larger values of the coefficient 'a' so that the errors are distributed in the narrower ranges. The coefficient, b can be approximately correlated with the coefficient, a as shown in Eq. (5-8) because the x-coordinate of the vertex of the parabola is located near the point (1, 0). The coefficient, c, is the average value of $RMSE_{JRC} \cdot d$ when the estimated JRC value is '0'.

$$ b \cong -2a \qquad (5\text{-}8) $$

The obtained RMSE values are presented in Table 4-4. In case of the maximum asperity angles obtained from the roughness profiles of the 3D images, it is difficult to find any interesting trends from the RMSE of the maximum asperity heights according to the differences of focal lengths. The $RMSE_{Ha}$ values are similar for the three different focal lengths. However, the $RMSE_{JRC}$ values using the macro lens, FL = 24 mm, are larger than other lenses, which could be attributed to the measurement errors obtained from their low precision within the test distances. It can be also noticed that the $RMSE_{JRC}$, which were estimated from the data obtained at the allowable distances, were reduced to 1.73.

Table 5-4. Error estimation for maximum asperity heights and JRC

Focal lengths (mm)	Data numbers	$RMSE_{Ha}$ (mm)	$RMSE_{JRC}$
24	79	2.57	3.68
50	68	2.62	2.23
85	68	2.59	2.24
24, 50, 85	24 (allowable distances)	2.32	1.73

The normalized JRC values are plotted in the histograms and probability density plots of Figure 5.19. As the most common probability distribution function, with the assumption that the data fit the Gaussian distribution, the probability of NJRC can be estimated. Figure 5.19 (a) shows that there is a 60 % chance of obtaining the accuracy of JRC values within ± 20 % of differences for all data set with the mean value: μ = 0.87. In contrast with the complete data sets, the probability density function (PDF), which is formed by the data at

the allowable distances, shows higher probability (PDF = 0.85) and reasonable mean values ($\mu = 0.97$) than does the entire data sets.
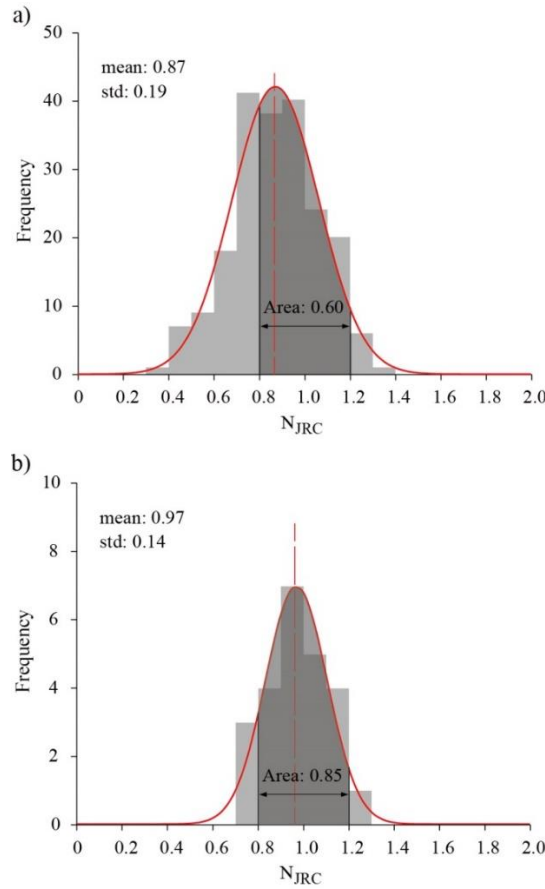
Fig. 5.19 Histograms and probability density functions of normalized JRC values in the entire ranges (a), at the allowable distances (b)

The data distributions, which are correlated between $RMSE_{JRC} \cdot d$ and N_{JRC} for the employed focal lengths, are presented with a good agreement to quadratic equations ($R^2 = 0.88 \sim 0.90$). The concavity of the parabola curve represents the precision of data. This steepness of the side of the parabola is controlled by the parameter, a, the coefficient of the x^2 term of the quadratic equation. The coefficient, a, increases as longer focal length lenses are used whereas the widths of the parabolas are decreased. This trend can be observed from Figure 5.20.

Table 5-5 presents the coefficients of the quadratic equations of the regression curves according to the used focal lengths. It is also noted from Figure 5.19 that the RMSE_JRC values increased with the camera distances and the rates of the increases are dependent on the focal length of the lenses. In order to identify the variations of RMSE_JRC with camera

distances, the average values of RMSE$_{JRC}$ are plotted in accordance with the camera distances in Figure 5.21.

Table 5-5. Coefficients of RMSE$_{JRC}$ quadratic equations according to the focal lengths

Focal lengths (mm)	a	b	c
24	655	-1,320	651
50	877	-1,774	888
85	1,041	-2,063	1,014

These data produced an exponential regression for each focal length of lenses. It can be observed from the graphs that the RMSE$_{JRC}$ values are proportional to the camera distances from the objects. However, less agreement in the data for the 85 mm lens ($R^2 = 0.43$) is also observed. This can be attributed to the fluctuated data between 6.0 to 7.0 meters.

Using the mean values of RMSE$_{JRC}$·D in close distance ranges obtained from Figure 5.21, the ranges of normalized JRC values can be approximately predicted by means of the correlations between the parabola equations and the exponential regression curves as shown in Figure 5.22 (b). The distance ranges between cameras and objects, which are used for the approximations, are also within the simulated distance range of up to 7.0 metres.
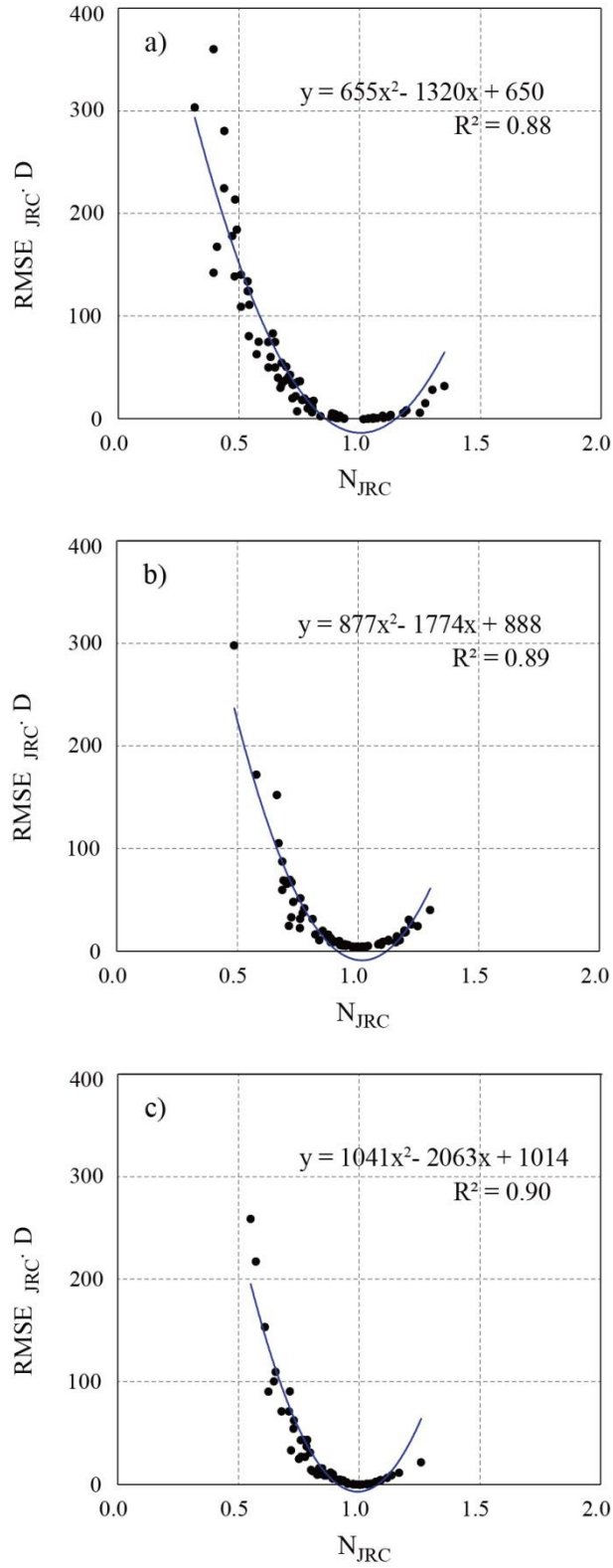
Fig. 5.20 RMSE distributions according to the camera distances based on normalized JRC, FL 24 mm (a), 50 mm (b), 85 mm (c)
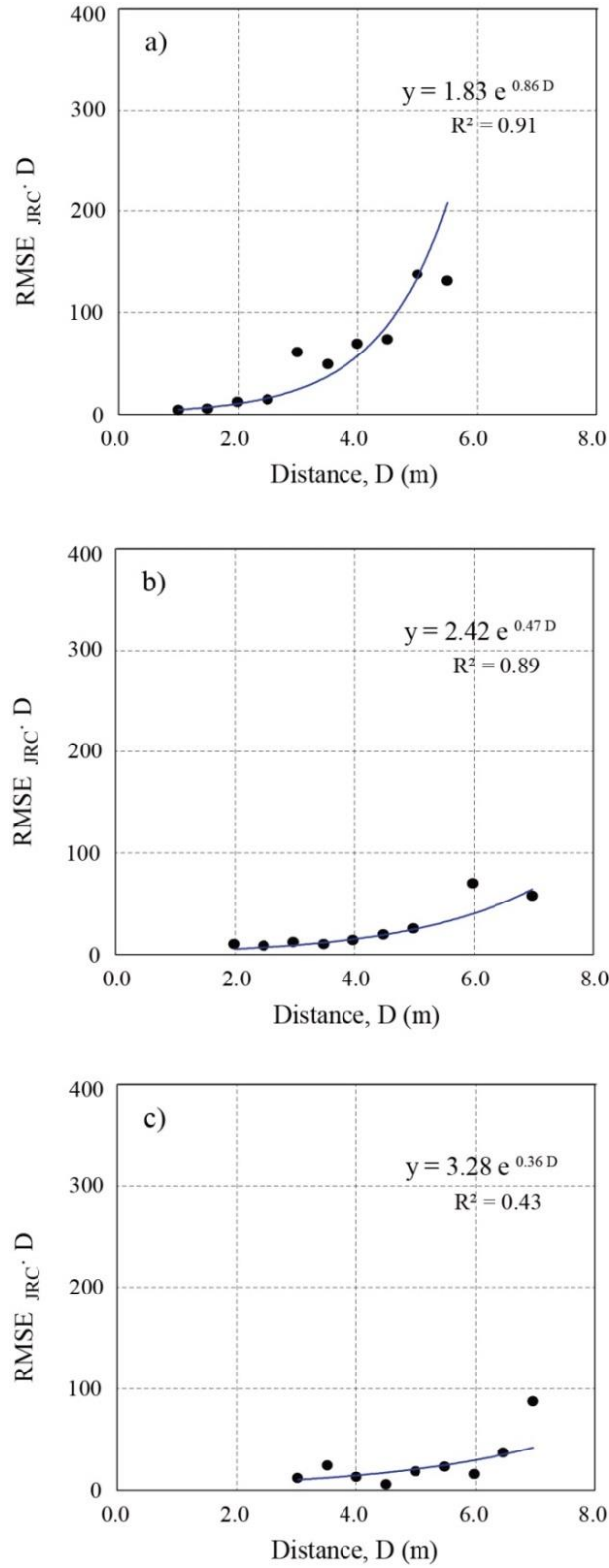
Fig. 5.21 Regression curves using mean values of RMSE$_{JRC}$ obtained from each distance to the object, FL = 24 mm (a), 50 mm (b), 85 mm (c)

In terms of the feasibility of the parabola equations, the interpolation should be limited to the verified ranges, where N_{JRC} values are less than 1.3. The data ranges over 1.3, which are drawn with dot lines in Figure 5.22, are not verified. It is observed from the data distribution that the upward trend of the parabola equations, which turn up in the N_{JRC} ranges between 1 and 1.3, is evident. However, these upward parts of the overestimated data are mainly due to the data in close distances for each focal length of lenses. Thus, the interpretation of the parabola equations in this study is focussing on the underestimated ranges less than $N_{JRC} = 1.0$.
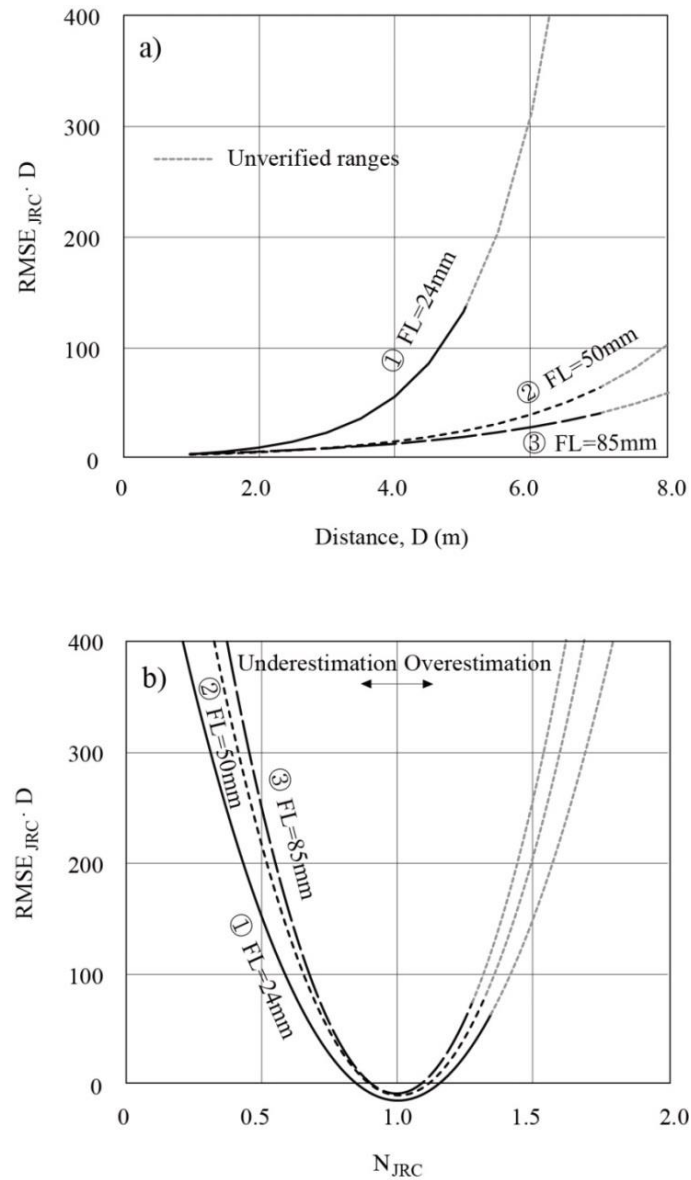
Fig. 5.22 RMSE error models based on focal length of lens, exponential regressions (a), parabola models (b)

5.3.4 Data reconciliation using the parabolic models

The histograms of N_{JRC} values obtained from the original data for each focal length lens provide reasonably distributed values with normal distribution shapes centred by $N_{JRC}=1.0$, as shown in Figure 5.20. From the probability data functions, it is assumed that the precision of data can be indicated by the values within $\pm\ \sigma$ intervals. Based on the influence of the camera distance to the object, the mean values of N_{JRC} distributions for each focal length of lens were underestimated ranging from 0.78 to 0.93. The data are spread out from the mean values indicating the standard deviation from 0.15 to 0.23 as shown in Table 5-6.

Data reconciliation, using the quadratic equations (Fig. 5.20), was able to improve the accuracy and precision of JRC data distributions by adjusting the initially biased JRC data. The redistribution of JRC values was performed by adding or subtracting the errors, which were estimated from the parabola equations, to the original JRC data. Figure 5.23 compares the probability of JRC distributions between the original data and the reconciliatory data. The results indicate that the data reconciliation using the parabola error models for each focal length lens is effective in shifting the mean values to the true values as well as to improve data precision.

The difference of mean and standard deviation before and after the data reconciliation verify the effect of the parabola error functions. Applying the parabola equations, the standard deviations were considerably reduced by half the original values and the mean values are distinctly close to '1' as shown in Table 5-6. The equations are determined for the employed lenses to ensure that the predicted error distributions, which are factored by camera distances to objects, improve on the probability of JRC estimation using photogrammetry methods.

Table 5-6. Comparison of standard deviation and mean values of the normalized JRCs before and after the data reconciliation

Focal lengths (mm)	Before reconciliation		After reconciliation	
	Standard deviation	Mean	Standard deviation	Mean
24	0.23	0.78	0.13	0.89
50	0.17	0.93	0.09	0.97
85	0.15	0.89	0.08	0.94
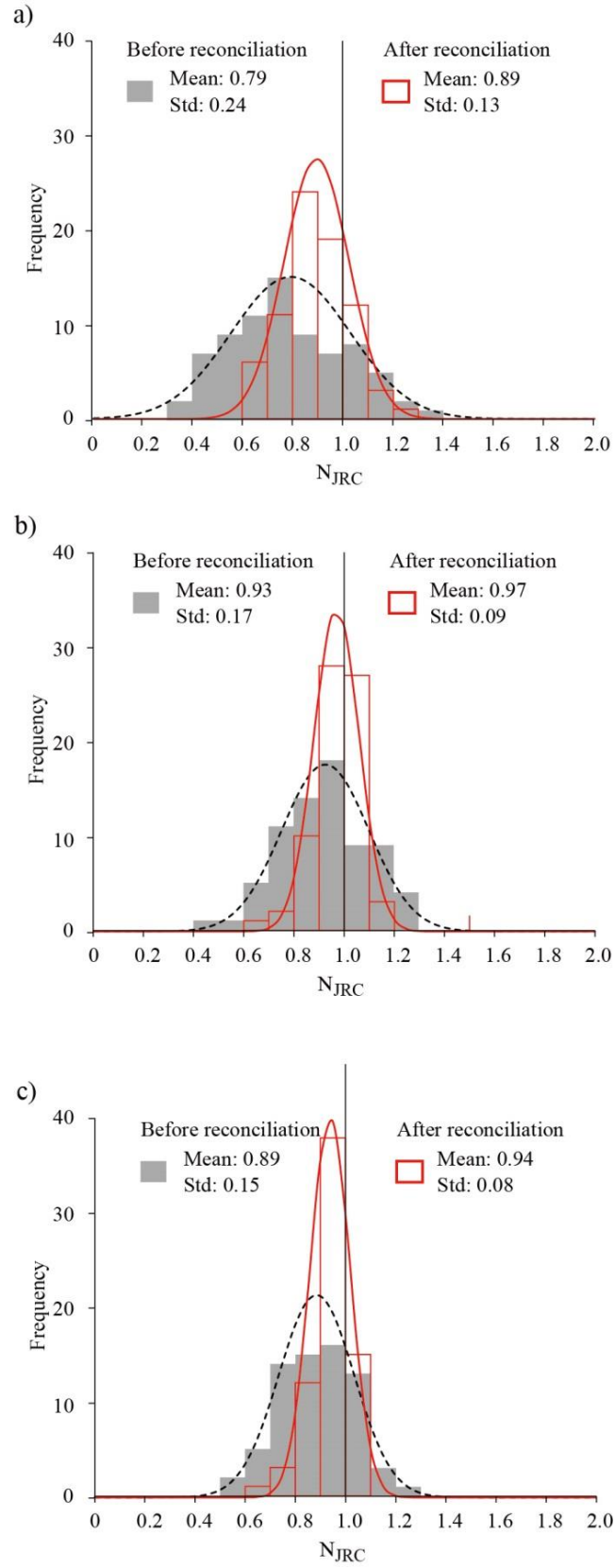
Fig. 5.23 Comparison of histograms and PDF between initial N_{JRC} data and updated N_{JRC} data; FL=24 mm (a), FL=50 mm (b), FL=85 mm (c)

5.4 Conclusion

Close range photogrammetry was employed to investigate the influence of the focal length of employed lenses and the camera-to-object distances for JRC estimation through a set of laboratory tests. Three different focal length lenses (FL=24, 50, 85 mm) were used to extract roughness profiles, as well as JRC values, for up to 7 m of photograph distances. The results recommend allowable photograph distances for the employed focal lengths to produce data with manual measurement precision (at 1 mm intervals). At the allowable distances, the accuracy and precision of JRC data distributions were increased compared to that obtained from the range of distances used in the experiments.

Normalized JRC values and normalized asperity heights are decreased with camera-to-object distances. N_{JRC} data obviously indicated downward trends with the c-to-o distances. Based on the results, allowable photograph distances are determined as 1, 2, 4 metres for the combination of Nikon D7000 with 24, 50, 85 mm focal length lenses respectively. This result is limited for the employed camera and lenses in the idealized laboratory conditions (same lighting and orthogonal photographing). Thus, the combinations of photograph equipment should be considered in the use of the results from this study. Using the data statistics, this study developed a quadratic equation which is governed by normalized JRC values and $RMSE_{JRC}$ with camera-to-object distance. The coefficient, a, which is the size of the parabola models, was directly dependent upon the focal lengths of the employed lenses. As a result, the obtained original data from each focal length lens was improved by using each parabola curve. The quadratic equations effectively shifted the biased mean values to the true values and reduced the standard deviations of the data distributions. This study also suggests that the parabola models can be verified and improved by using site photogrammetry data.

As mentioned above, the developed error models however limited in the combination of the employed camera sensor size and with the employed focal length lenses. The laboratory conditions kept constant lighting and orthogonal optical axis to the object. The use of the error models thus should consider the camera factors and the limitation of the laboratory condition. In this study scope, the parabola models are verified by using the field data collected from natural rock slopes. The analysed results will be presented in Chapter 6.

6 ANALYSIS OF THE ACCURACY OF PHOTOGRAMMETRIC ROUGHNESS DATA

A part of this chapter has been accepted for publication in Rock Mechanics and Rock Engineering journal as follows:

Dong Hyun Kim, George Poropat, Ivan Gratchev, Arumugam Balasubramaniam (2016) Assessment of the accuracy of close distance photogrammetric JRC data. Rock Mechanics and Rock Engineering. doi: 10.1007/s00603-016-1042-9

6.1 Introduction

In this chapter, the influences of camera-to-object distance, focal lengths and profile orientations on the accuracy of JRC values are investigated by using several photogrammetry field surveys. Directional photogrammetric JRC data are compared with data derived from the measured profiles so as to determine their accuracy. The extent of the accuracy of JRC values was examined based on the error models which were developed from laboratory tests and revised for better estimation in this study.

The roughness data which have been collected from surveys at six different sites are used for analysis. In each survey site, 2 ~ 8 profiles were measured in accordance with the suitability and accessibility of the target surfaces for the measurements. This allows the measured profile shapes and their JRC values to be compared with the photogrammetric roughness data. The results of each field survey are discussed associated with different site conditions. This study also investigates the influence of the oblique angles of the line of sight to the exposed rock surfaces in the photogrammetry setup, which is one of the most distinct differences with the previous laboratory condition.

As discussed in Chapter 5, based on the methodology of stereo photogrammetry, a JRC error model was developed. This model demonstrates the relationships between the RMSE of photogrammetric JRC values and the proportion of over or underestimation of the JRC values considering camera-to-object distances. As this model was created under an ideal laboratory condition and the data show dominantly underestimation, the model can be revised by the field data especially for the overestimation range. This error model is reconstructed using both the RMSE and the mean absolute error (MAE) of JRCs to seek

better correlations in this chapter. The error model can be used as a guideline for field photogrammetric JRC data which may involve additional errors induced by various field conditions. Also, this model can be verified by analysing field photogrammetric JRC values.

6.2 Evaluation of the accuracy of photogrammetric JRC values

To measure the accuracy of continuous variables, the root-mean-squared-error (RMSE) and the mean absolute error (MAE) are commonly employed. RMSE has been widely used to identify the accuracy of data due to its high correlation between the predicted values and the observed values. In a photogrammetry standard, the accuracy of geospatial data obtained from photogrammetry has been classified using the RMSE of data coordinates (American Society for Photogrammetry & Remote Sensing, 2014). As a natural measure of average error magnitude, advantages of MAE have also been reported (Willmott & Matsuura, 2005; Chai & Draxler, 2014).

In Chapter 5, the proposed quadratic functions show upward parabolic curves with different widths according to the focal length of lenses. However, since the laboratory data are predominantly plotted in the range of underestimation, the quadratic regression curves are partly lack of correlations in the range of overestimation. Considering the balance of data, it is reasonable that the data can be interpreted by dividing the data range into underestimation and overestimation categories. In this study, the JRC data obtained from the laboratory tests reconstructed error functions using MAE of the JRC values as shown in Figure 6.1 (b). With the use of absolute values, the basic form of the MAE of JRC is simpler than the RMSE form as given in Eq. (6-1).

$$MAE_{JRC} = \frac{\sum_{i=1}^{n}|JRC_{o,i} - JRC_{p,i}|}{N} \qquad (6-1)$$

In the total data range, the overall patterns of the relationship between RMSE or MAE and N_{JRC} are similar showing quadratic regression lines. The results show that the uniformly distributed errors of MAE in the range of overestimation more suitably describe the trends of the JRC errors than the previous parabola models. In this range, linear regressions between MAE_{JRC} and N_{JRC} are formed with a high range in the values of the coefficient of determination ($R^2 = 0.79 \sim 0.96$). The large focal lengths create steeper inclinations of the regression line than short focal lengths. Similarly, in the underestimation category data range, the quadratic regressions of $RMSE_{JRC}$ showed better correlations with N_{JRC} than

MAE_{JRC} and the previous parabolas. The improved relationships are shown by R^2 values as given in Figure 6.1 (a) and (b).
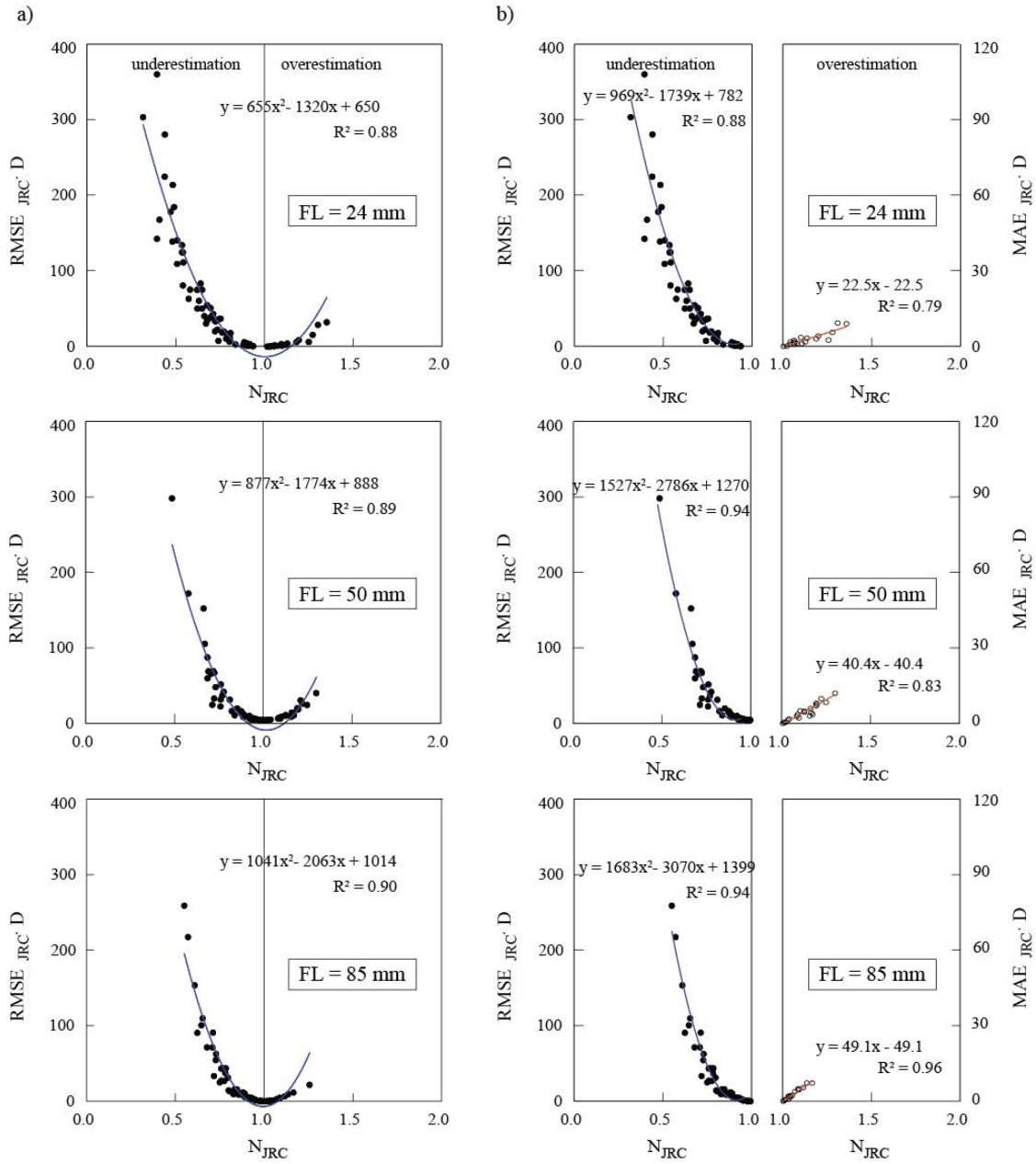
Fig. 6.1 JRC error models based on lens focal length in a laboratory condition: RMSE parabola models (Kim et al., 2015c) (a), revised RMSE and MAE error models (b)

6.3 Field conditions and data collection

The target areas at site #1 comprise clearly exposed bedding planes of shale and sandstone joints. The orientations of the surfaces were mostly slanted against the camera axis. The

target areas at site #2 included parts of exposed joint surface of shale and the road cuts were partly covered by plants. The location of the target area was lower than the camera height. The target area at site #3 was clearly exposed by excavation and the target area was a weathered joint surface. The target areas at sites #4 and #5 were parts of road cuts and the exposed joint planes are almost orthogonally oriented to the optical axis. The target areas at site #6 were parts of sandstone rock blocks for landscaping. The target surfaces of the blocks were individually oriented with different angles to the optical axes.

Table 6-1. Summary of photogrammetry site investigations

sites	number of profiles	camera-to-object distances (m)	baseline distances (m, B:D=1:7)	focal lengths (mm)	point intervals (mm)	ground sampling distance (mm)
#1*	9	14.0, 17.0	2.5	24	12.8 ~ 22.4	3.0 ~ 3.4
#2	4	2.0, 5.0, 10.0	0.3, 0.8, 1.5	24, 50, 85	0.4 ~ 10.5	0.5 ~ 2.9
#3	3	3.0, 33.0	1.5, 5.0	24	5.2 ~ 23.9	1.0 ~ 6.0
#4	3	14.0, 14.8	2.0	24, 50, 85	2.2 ~ 8.7	0.8 ~ 2.2
#5	3	11.8, 12.0	1.7	24, 50, 85	1.6 ~ 7.7	0.8 ~ 2.4
#6	8	2.0, 5.0, 10.0	0.3, 0.8, 1.5	24, 50, 85	0.2 ~ 19.8	0.1 ~ 1.7

* site #1: Beaudesert-Nerang road 1, site #2: Beaudesert-Nerang road 2, site #3: Bethania, site #4: Nerang-Murwillumbah road 1, site #5: Nerang-Murwillumbah road 2, site #6: Smith road

Through the site surveys, the range of employed camera-to-object distances varied from 2 to 33 metres. In the photogrammetry surveys, the specific sections of the rock slopes were marked using circular and rectangular targets which were 30 to 50 cm apart as shown in Figure 6.2. The targets were arranged into square, triangle or line shapes according to the measurement availability. Roughness profiles were manually measured using a profile gauge (1 mm interval) for the lines between targets. For all six site surveys, photographs were taken on bright sunny days and the sections of the slopes were unaffected by shadows.

3D images were created using Sirovision. In order to reduce a possible error due to camera factors, the calibrations of the employed lenses and camera body combinations were performed using the calibration data files provided by the manufacturer. The point cloud intervals of the 3D models generally increased with the camera-to-object distances and the intervals were inversely proportional to the lens focal length employed. However, the points in space created by a 3D image were inconsistent due to the irregularity of the natural slope

surfaces. This appearance was heightened by the fact that the surface being imaged is not flat so the points appear to be scattered in an irregular pattern.
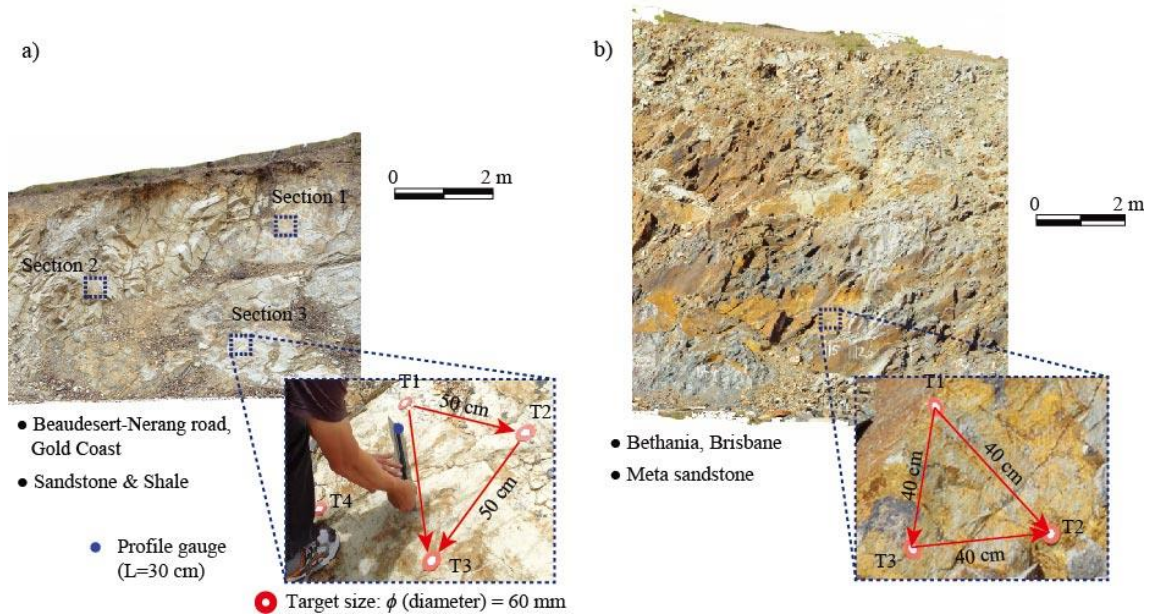
Fig. 6.2 Examples of target arrangements for roughness measurement; at site #1 (Beaudesert-Nerang road) (a), site #3 (Bethania) (b)

6.4 Accuracy of photogrammetric roughness data

6.4.1 Profile agreement

A total of 30 measured profiles were compared with the photogrammetric profiles. The photogrammetric roughness profiles were generated from the 3D data based on the point-to-line distance method as described in Section 3.3.3. Overall, a photogrammetry setup at close distance with longer focal length lenses created well matched profiles. Figure 6.3 presents an example of the profile deviations of site #4 in accordance with the employed focal length of the lenses. The vertical scale is exaggerated two times for clarity. Due to insufficient data points in the 3D models (8.7 mm point cloud distance), the profile which has been created from the 24 mm lens, showed considerable mismatch as shown in Figure 6.3 (a) where the agreement of the profile shape is governed by the point interval of 3D images. With smaller point intervals (2.2 to 4.0 mm), the large scale undulation in the profiles obtained from both the 50 mm and 85 mm lenses is comparatively consistent with the measured profiles (see Fig. 6.3 (b) and (c)).

122

The accuracy of the profiles in a 3D model can also vary with the locations of the sections of interest due to the irregular pattern of the originally formed mesh. As demonstrated in Figure 6.4, the angles between the line of sight and the normal vector of a rock surface vary with the sections of interest in an image. Consequently, the point cloud intervals of the 3 sections varied from 12.8 mm to 22.4 mm in the same 3D model.
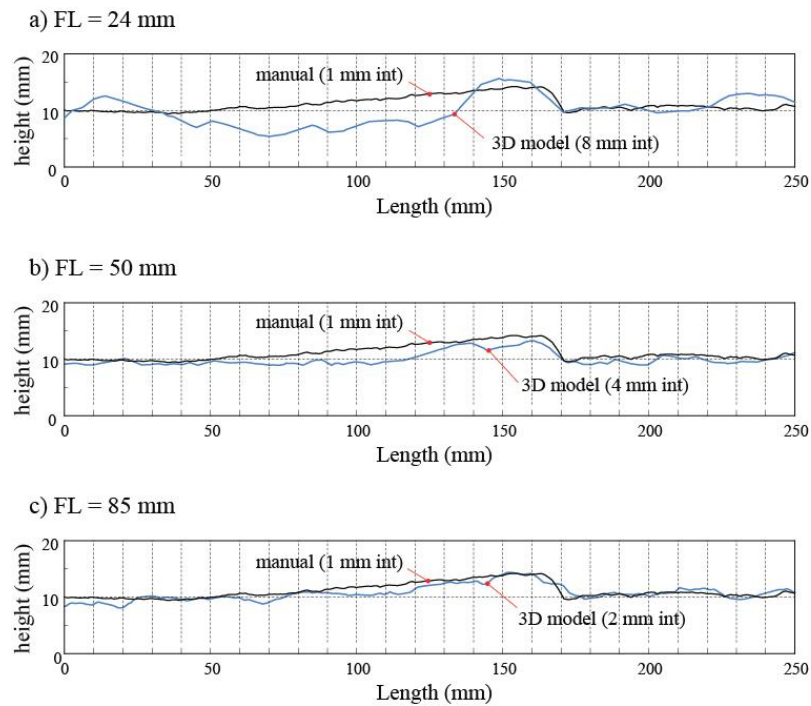
Fig. 6.3 Comparison of a roughness profile at site #4 between manual measurement and 3D models according to the employed focal length (FL): 24 mm (a), 50 mm (b), 85 mm (c)
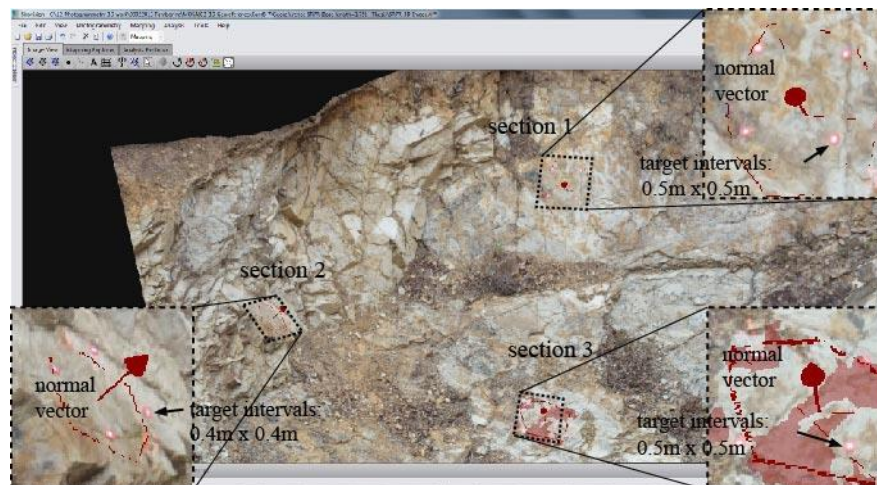
Fig. 6.4 A window shot of Sirovision and the sections of interest (Site #1, C-to-O distance: 17 m, FL=24 mm)

In Figure 6.5 (a), the obtained data on point cloud intervals from the field surveys generally shows a gradual increase with the camera-to-object distances. The point intervals show rather scattered patterns (R^2 = 0.66 to 0.84) compared to those obtained under laboratory conditions obtained in a previous study by the authors (Kim et al., 2015c). The dispersion of data is clearly shown from the results obtained using the short focal length (24 mm). Under laboratory conditions, based on orthogonal images, a linear increase of point intervals in the 3D images was obtained with increasing camera-to-object distances with R^2 = 0.95 to 0.99 as shown in Figure 6.5 (b). This reflects the irregularity of the rock surface orientations for the line of sight of the camera setup and may also explain the reason why the irregular point intervals can be attributed to the influence of the variation of the rock surface orientations.
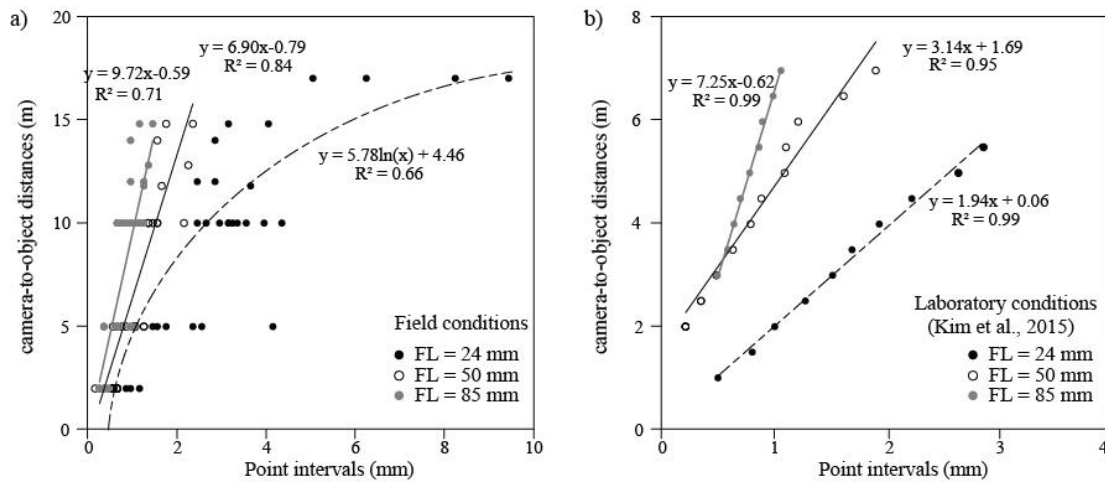
Fig. 6.5 Variation of point cloud intervals of 3D images: site investigation (a), laboratory condition (Kim et al., 2015c) (b)

The oblique angle of camera setup facing a rock slope can influence the accuracy of photogrammetric profiles. This issue was examined by Hong et al. (2008) that inclined sample surfaces can produce underestimated roughness data. In a general orthogonal photograph setup, the oblique angle of the line of sight to a plane can be identified by the angle between the line of sight and the line of interest on a plane. As shown in Figure 6.6 (a), the angles are illustrated by both the angle between the line of interest on a plane and the optical axis (θ_1°) and the angle between the optical axis and the normal vector of the plane (θ_2°). These angles can be represented on a stereographic projection which is a convenient tool to identify geological structures on rock faces in any orientations. The method of the hemispherical projection is well described by Priest (1985) and Goodman (1989).

With the strike of a plane, the angle of pitch is measured from the perimeter of the net along the great circle. In Figure 6.6 (b), line 1 in the plane `A′ has a pitch of $\alpha°$ measured from the strike line. The acute angle between the optical axis and the given line 1 is counted from the pitch $\theta_1°$. In a similar way, $\theta_2°$ is counted from the perimeter between the optical axis and the pole of plane `A′ along the great circle of plane `B′ containing the line 1. Accordingly, the discrepancies in photogrammetric profiles could occur as $\theta_1°$ decreases and as $\theta_2°$ increases. The identified angles of the all data are summarized in Appendix C.
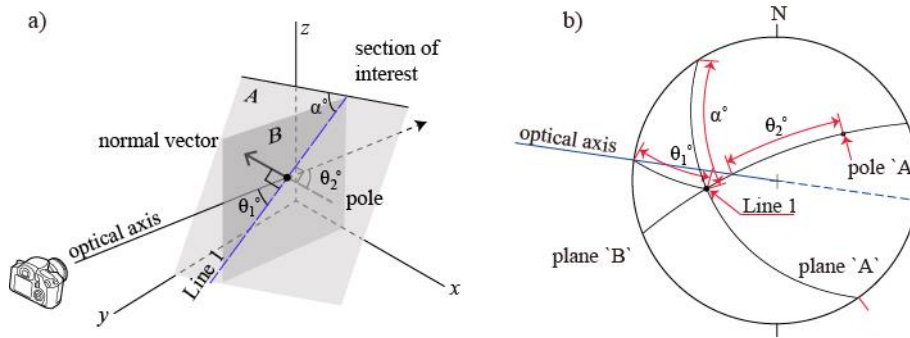
Fig. 6.6 Camera oblique angle and normal vector of a section of interest: in 3D space (a) , stereographic projection (b)

In this study, the deviation of the profile waviness between manual measurement and photogrammetry was simply quantified by using the differences in the maximum asperity heights between 3D models (h_p) and manual measurement (h_m). For all measured roughness profiles, h_p and h_m values were obtained using the same profile length (L = 30 cm) based on the straight edge method. This method has been used for roughness estimation in large scale profiles (Piteau, 1970; Milne et al., 1992; Palmström, 2001). Comparing the manually measured profiles with the photogrammetric profiles, the accuracy of profile waviness was investigated using the deviation ratio of the maximum asperity height (h_p - h_m / h_m) and the results are plotted according to the point intervals in Figure 6.7. When the values are close to `0′, better agreement between the manual profiles and the photogrammetric profiles can be achieved. The field data show scattered distribution, however, the data in the range less than 1 mm intervals tend to be close to the mean values with lower standard deviation (SD = 0.33, Fig. 6.7 (a)) than the data in the range more than 1 mm point interval (SD = 0.76, Fig. 8 (b)).

It was also found that high oblique angles for the camera axis could reduce the amount of dispersion of photogrammetric profiles. The data plotted in Figure 6.7 (a) and (b) are sorted

by the high-angle oblique range of $\theta_1 > 60°$ and $\theta_2 < 30°$. These ranges indicate that the angles between the camera axes and the profiles form acute angles close to the orthogonal photographs within the range of $60° \sim 90°$. As shown in Figure 6.7 (c) and (d), within these data ranges, the variations of the data are obviously reduced from 0.16 to 0.13 (point interval ≤ 1.0 mm) and from 0.76 to 0.34 (point interval > 1.0 mm). The result indicates that the accuracy of photogrammetric profiles is affected by the oblique angles θ_1 and θ_2 and orthogonal photographs are appropriate for the measurement of roughness.
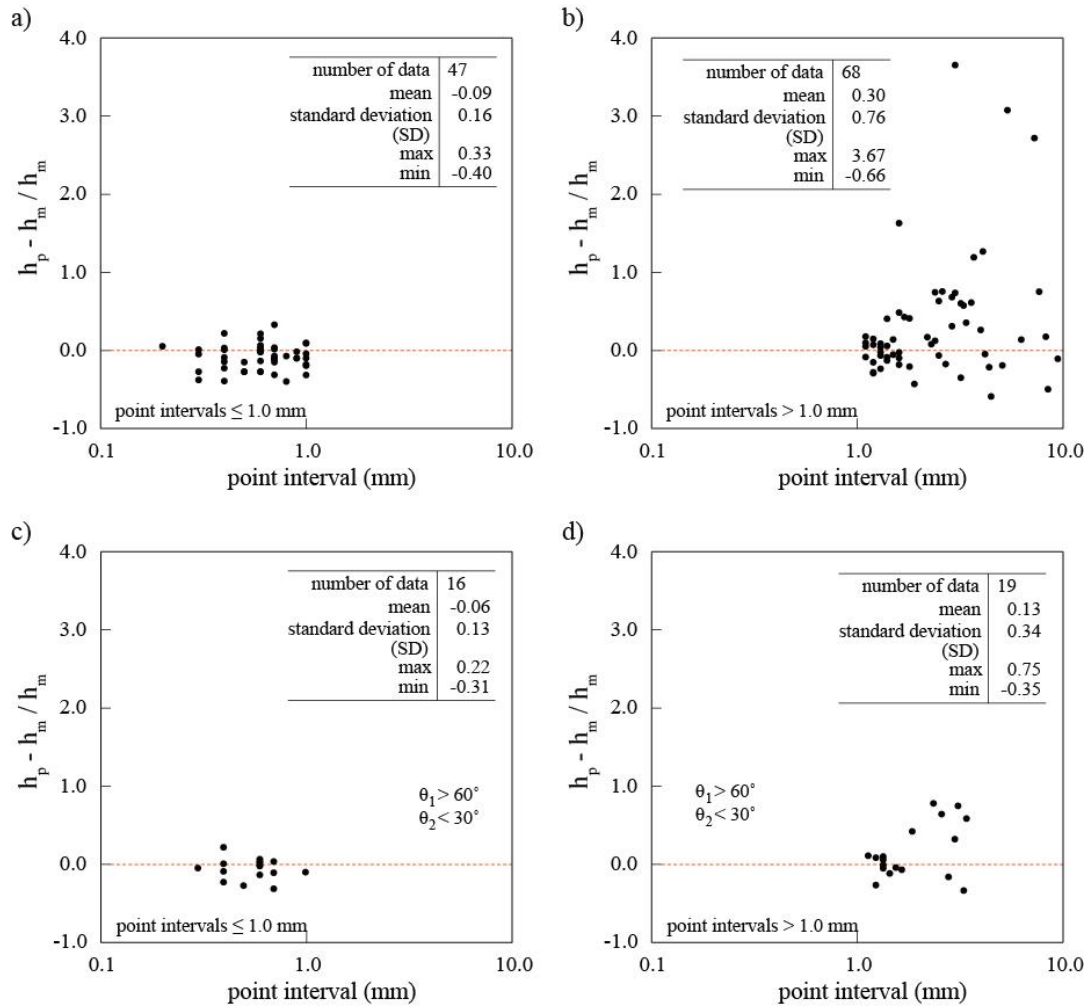
Fig. 6.7 Distribution of maximum asperity height ratio according to point cloud intervals: total data, point interval ≤ 1.0 mm (a), total data, point interval > 1.0 mm (b), data within the high-angle oblique ($\theta_1 > 60°$ and $\theta_2 < 30°$), point interval ≤ 1.0 mm (c) and data within the high-angle oblique ($\theta_1 > 60°$ and $\theta_2 < 30°$), point interval > 1.0 mm (d)

6.4.2 Accuracy and precision of photogrammetric JRC values

JRC values were estimated by using the small scale asperity heights of the photogrammetric profiles as demonstrated in Eqs. (2-4) and (2-6). A total of 111 JRC values were used to analyse the results. The obtained photogrammetric JRC values are summarized in Table 6-2 and the results of each site are demonstrated in Figures 6.8 and 6.9. According to the site conditions, the obtained JRC values showed different trends. The JRC values of site #1 and #3, which were obtained by using short focal length (FL=24 mm) and from large c-to-o distances (17 m, 33 m), were mostly underestimated due to the insufficient data points (Fig. 6.8 (a) and (c)). It was observed that some of 3D images at site #2 were influenced by plants near the target areas. Consequently, the low resolution images which were taken by 24 mm lens created distorted 3D models and resulted in overestimations of JRC values (Fig. 6.8 (b)). This tendency was similarly found from the site #4 and #5. The target areas in these sites were clearly exposed and orthogonally oriented to the camera axes, the differences of JRCs between manual and photogrammetry were relatively less than at other sites. However, large differences between the JRCs are found for low resolution images (FL=24 mm) as shown in Figures 6.8 (d) and (e).

Figure 6.9 demonstrated the variation of JRC values for site #6 for different focal lengths. It is distinct from the other sites that the photogrammetric 3D images mainly overestimated the JRC values. Also, in some profiles, large variations in JRC values are found in the all camera-to-object distance ranges when 24 mm and 50 mm lenses were used. These overestimated values were predominantly due to distorted waviness in the extracted profiles. The use of longer focal length lens (FL = 85 mm) could reduce the data deviation (Fig. 6.9 (c)).

The JRC data are plotted and compared with the error models for both the ranges of underestimation and overestimation in Figure 6.10. In contrast to the authors' previous laboratory study (Kim et al., 2015c), it appears that the plotted data are quite dispersed according to each field survey condition and dominantly distributed in the overestimated region as demonstrated in Figure 6.10. Overestimation can be found in both the high resolution and low resolution images. The reasons are due to the influences of data noise as discussed by Poropat (2008), the distortion of waviness leading to an overestimation of JRCs at low resolutions.

Table 6-2. Summary of JRC values employed to the analysis

sites	Profiles (L= 250 ~ 300 mm)	θ1 (˚)	θ2 (˚)	JRC values	
				manual	3D models
#1. Beaudesert-Nerang road 1	1	39	38.5	11.6	6.6
	2	34	48	7.5	8.2
	3	43	76.8	8.7	8.2
	4	70	42.5	11.3	5.3
	5	82	40.7	8.7	8.7
	6	83	5.8	5.4	10.8
	7	50	7.8	12.0	6.9
	8	44	40.5	14.8	3.4
	9	60	6.2	14.1	14.2
#2. Beaudesert-Nerang road 2	1	51	93.1	6.4	11.2 ~ 17.7
	2	63	25.3	11.0	8.1 ~ 19.7
	3	85	85	7.2	5.6
	4	78	78	9.0	7.3
#3. Bethania	1	63	102.7	15.0	11.8 ~ 12.9
	2	76	31.6	10.1	10.2 ~ 18.3
	3	61	64	13.7	9.7 ~ 12.4
#4. Nerang-Murwillumbah road 1	1	90	81	5.6	4.6 ~ 11.1
	2	87	20.7	5.7	6.3 ~ 10.7
	3	86	140.9	3.7	2.1 ~ 9.9
#5. Nerang-Murwillumbah road 2	1	80	57.2	7.0	5.8 ~ 9.7
	2	87	37.6	7.6	11.1 ~ 17.6
	3	79	15.7	8.7	9.2 ~ 17.6
#6. Smith road	1	51	3	7.6	4.9 ~ 12.1
	2	74	78.5	10.5	9.5 ~ 15.2
	3	74	78.5	13.7	7.7 ~ 16.3
	4	69	55	10.4	4.0 ~ 15.0
	5	55	19.9	14.0	15.8 ~ 24.4
	6	79	0	8.6	9.5 ~ 21.7
	7	51	88	5.1	9.8 ~ 23.0
	8	57	66.9	6.7	7.2 ~ 13.9

As shown in Figures 6.10 a) ~ c), the data also deviate from the error models with the deviations more obvious when shorter focal length lenses are employed. This deviation may be attributed to various sources of errors derived from different site conditions. However, I suggest that the differences are mainly due to the lack of image resolution. In the range of high resolution point intervals (less than 1 mm), the deviations are considerably reduced as demonstrated in Figures 6.10 d) ~ f). The sorted data are plotted along the error models with

stronger relationships according to the focal lengths even though there are still deviations with the error models.
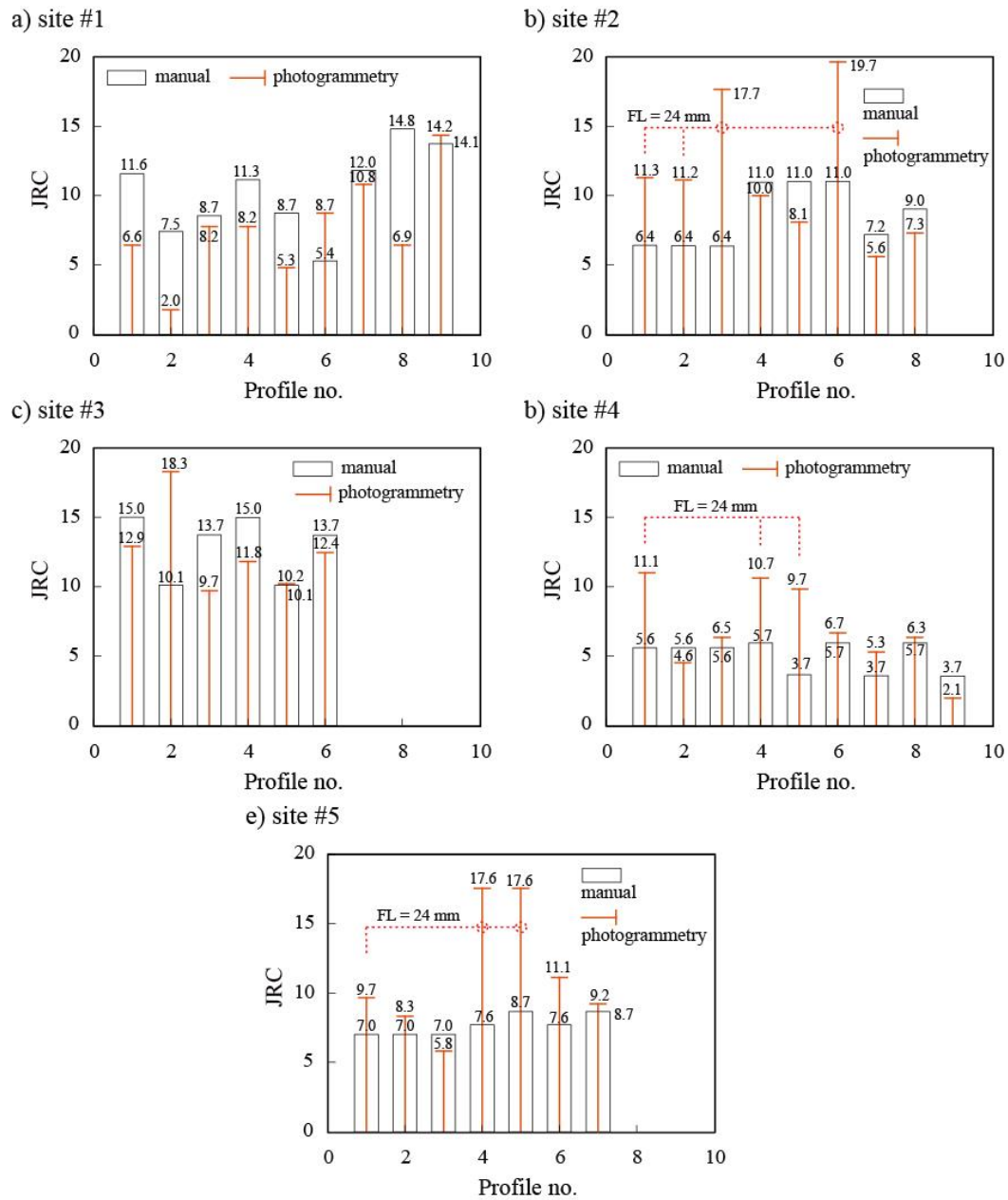
Fig. 6.8 Comparison of JRC values between manual and photogrammetry in site #1 (a), site #2 (b), site #3 (c), site #4 (d), site #5 (e)
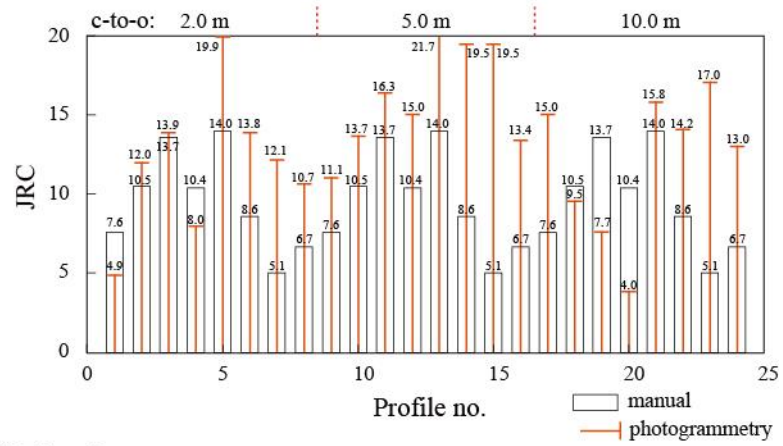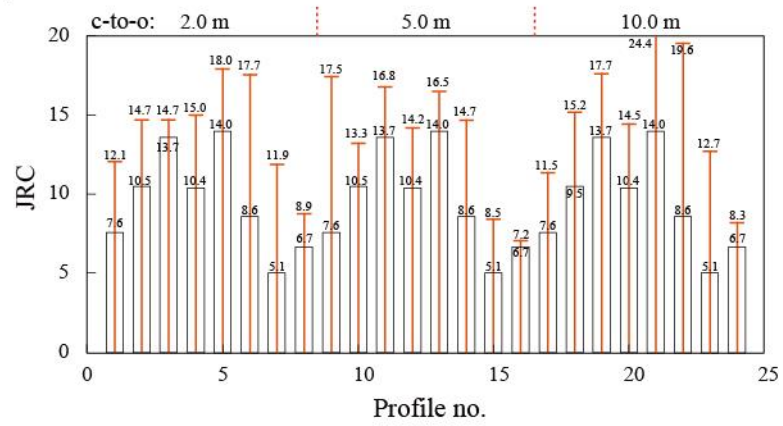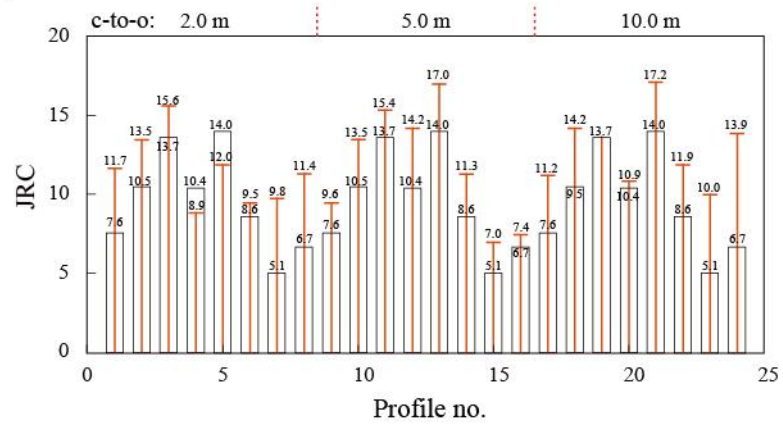
Fig. 6.9 Comparison of JRC values between manual and photogrammetry in site #6: FL= 24 mm (a), FL = 50 mm (b), FL = 85 mm

130
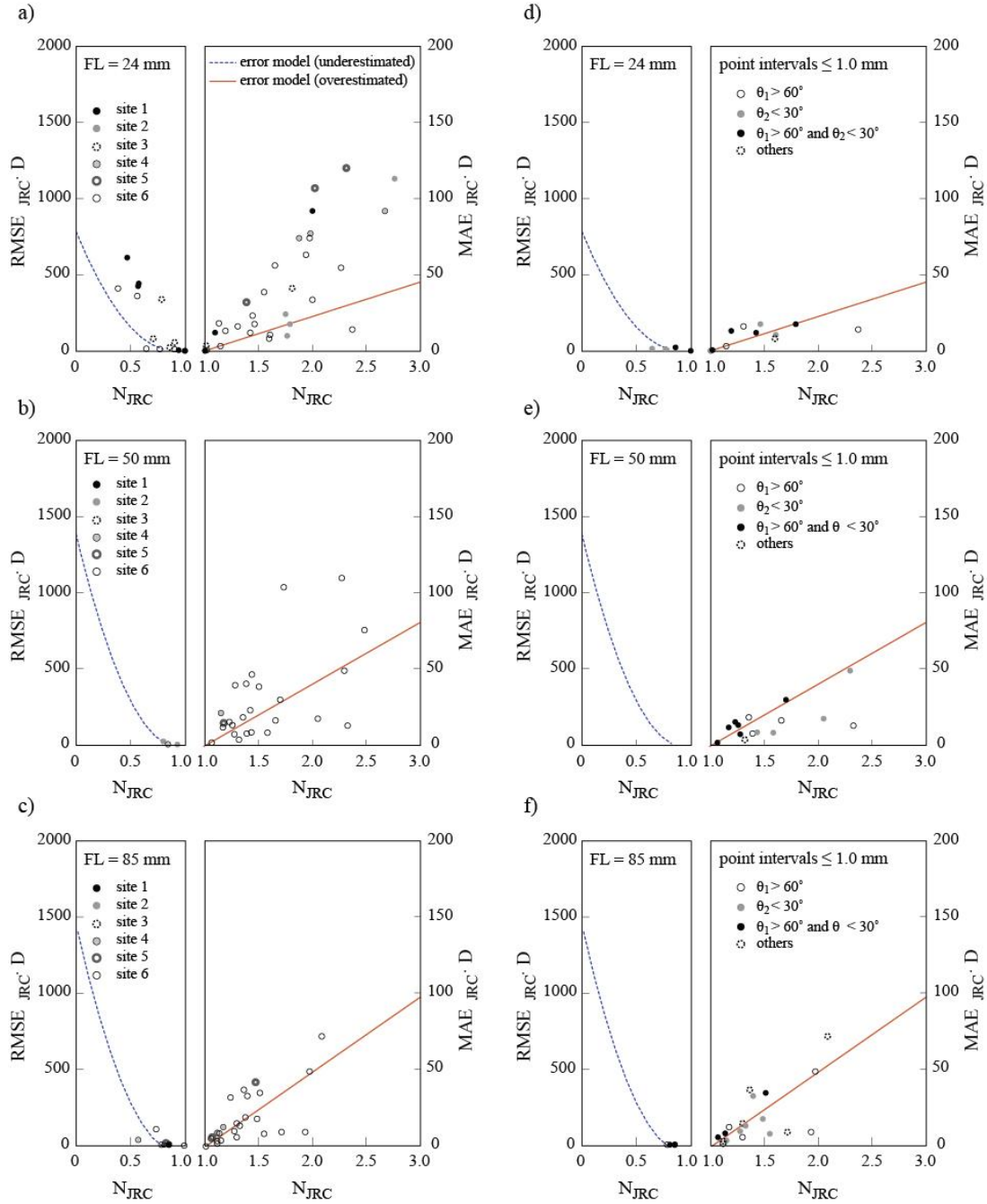
Fig. 6.10 Distribution of JRC error data and comparison to the error models: total data of FL = 24 mm (a), FL = 50 mm (b), FL = 85 mm (c) and the data of point intervals ≤ 1 mm of FL = 24 mm (d), FL = 50 mm (e), FL = 85 mm (f)

It is observed that the deviation is reduced within the range of high oblique angles (e.g. $\theta_1 > 60°$ and $\theta_2 < 30°$). The black dots in Figures 6.10 d) ~ e) show that the sorted data are closely distributed around the error curves. This distribution shows that the orthogonal photographs improve the accuracy of photogrammetric JRCs as evident from the trends of the data for each focal length. As a consequence, the data distributions obtained from the

131

site photogrammetry survey indicate that the oblique camera angles can influence on the accuracy of both the waviness of profiles in large scale and the deviations of JRC values in small scale roughness. It should be also noted that the results of data analysis could be influenced by the inconsistency in the amount of data recorded at each field survey. Further studies using more data from varied field conditions will allow improved understanding of the proposed error models.

6.5 Discussion

A combination of large sensor sizes and longer focal lengths can achieve high resolution images of joint surfaces. This combination can show linear relationships between the camera combinations and camera-to-object distances under laboratory conditions. However, under field conditions, the point intervals of the obtained 3D images vary with the complexity of the object in the field conditions. This study demonstrates that the point interval is an important factor and determines the level of accuracy of photogrammetric JRC data. For the same measurement interval with manual measurements (≈1.0 mm), this study showed the feasibility of stereo photogrammetry for JRC estimation. Within the range of point interval (≤ 1.0 mm), the errors could be interpreted using the developed error models with close correlations.

Unlike laboratory conditions, the field photogrammetry surveys which were performed under different photograph conditions, resulted in scattered data and plotted mainly overestimated JRC values. The obtained JRC values sometimes showed large discrepancies due to the distortion of 3D models and data noise. A comparison of the results from previous lab tests and field surveys is summarized in Table 6-3. The most important factor influencing on the accuracy of 3D models is an image error due to any discontinuous obstacles in target areas such as surrounding plants, large void and rock fragments. The existence of these factors causes large distortion of the 3D images and thus results in the overestimation of JRC values. In the laboratory conditions, the range of JRC values was predominantly underestimated. In the cases, distortion of 3D models was rarely found while the undulations of profiles were insufficiently represented due to a lack of points.

Table 6-3. Comparisons of the quality of JRC accuracy between the laboratory and the field conditions

conditions / frequency	laboratory conditions (Kim et al., 2015c) (c-to-o distance: ≤ 7 m)	field conditions (c-to-o distance: 2 m ~ 33 m)
often	underestimation - with small discrepancy of profiles due to insufficient accuracy of 3D models - due to lack of data intervals	overestimation - with noticeable discrepancy of profiles due to distortion of 3D models - due to data noise
seldom	overestimation - due to data noise - high level of accuracy less than $N_{JRC}=1.3$	underestimation - due to lack of data intervals

The results of the field tests also showed the influence of the orientation of profiles. To obtain better accuracy for the profiles of interest, orthogonal photographs are recommended. This study showed the effect of the photograph angles on the accuracy of roughness data within the range of high oblique angles (e.g. $\theta_1 > 60°$ and $\theta_2 < 30°$). In practice, this methodology can be an issue for the tripod based stereo photogrammetry. Actually, the limitation of the camera angles can be supplement by using SfM which is more flexible in the photogrammetry setup, the feasibility of which can be investigated in future research.

6.6 Conclusion

Photogrammetric roughness data were investigated under field condition. Linear profiles and photogrammetric JRC values were obtained from the 3D models, and the accuracy of the results was investigated by using the proposed error models focussing on the influence of data intervals and orientation of the profiles. A total of 30 profiles were manually measured and compared with the 3D models created in accordance with varying camera-to-object distances and the focal length of lenses. Based on the field data, following conclusions can be drawn:

- This study improved the previous JRC error models by using better correlations, in the overestimation range, between $MAE_{JRC} \cdot d$ and N_{JRC}.

- In comparison with the error models, the JRC values of the field data were generally overestimated and showed considerable scatters. The most influential of all the factors on the accuracy of roughness data was the point interval of 3D models and the data range in 1 mm point interval can reduce the differences from the error models.

- The field data also show that the oblique angles of the optical axis to the pole (θ_1) and to the measured profile (θ_2) can significantly affect the accuracy of both the maximum asperity height and JRC values of the profiles. The oblique angles could be usefully interpreted by the stereographic projection methods. In the range of the oblique angles ($\theta_1 > 60°$ and $\theta_2 < 30°$) close to orthogonal, photogrammetry setups could improve the accuracy of the maximum asperity heights (h_p) and JRC values. This shows that stereo photogrammetry can be used to produce linear roughness profiles and JRC estimation in a specific photographic setup.

7 APPLICATIONS OF PHOTOGRAMMETRIC JRC DATA ON ROCK ENGINEERING ISSUES

7.1 Introduction

This chapter is composed of five photogrammetry surveys and relevant analyses that describe systematic approaches in the application of photogrammetric techniques in investigating the stability of rock mass. In the surveys, photogrammetric JRC values are employed as a design value associated with different fundamentals of rock mechanical behaviours. In each case, the influences of the photogrammetric roughness values are investigated by comparisons the results of site investigation with numerical analyses. These comparative simulations can give engineers to anticipate possible implications of the biased roughness data for each safety issue. The overall schemes of the site surveys are presented as follows.

The first survey is to investigate the feasibility of photogrammetric JRC values on slope stability analysis. The estimated JRC values from the 3D model are applied for back-analysis of a failed natural rock slope. In this case study, the back analysis is performed by using a 2D Mohr-Coulomb numerical model. In the second survey, the slope models are extended to the use of the density of joint sets. This case study analyses the slope stability based on the Hoek-Brown model combined with combined with photogrammetric JRC values. The third survey is to analyse a block failure of a natural rock slope. The back-analysis is performed using photogrammetric JRC data obtained from the slid joint planes. The results are also compared with the results of the block theory analysis as an analytical method. In the fourth survey, the photogrammetric JRC data are used for the calibration of a dynamic parameter for rock fall simulation through the trials of site experiments. JRC values are obtained from an excavated slope in which rock fall experiments are performed. Comparing the rock fall behaviours to the results of parametric rock fall simulations, this site investigation tries to connect between photogrammetric JRC values and friction angles. The fifth survey describes the feasibility of photogrammetric roughness data for the investigation of rock weathering. Each case study was published in prestigious international journals during this doctoral program

7.2 Case study 1 (Mohr-Coulomb model)

A part of this section was published in Landslides journal as follows:

Kim DH, Gratchev I, Balasubramaniam AS (2013) Determination of joint roughness coefficient (JRC) for slope stability analysis: a case study from the Gold Coast area, Australia. Landslides, 10:657-664.

7.2.1 Introduction

This part of the thesis seeks to clarify whether photogrammetry can produce accurate measurements of JRC that can be used to assess the stability of slopes. In this case study, a photogrammetry survey for a natural rock slope was performed. The slope has been experienced a partial failure due to heavy rainfall in the past few years. The rock surface roughness data was obtained from the exposed slope surface by using photogrammetric 3D models and the values were compared with manually measured values. Computer analysis using the Universal Distinct Element Code (UDEC) was also performed to study the effect of JRC variation on the slope stability.

With the application of numerical analysis, the feasibility of photogrammetric JRC values is discussed in this section. The obtained results showed some discrepancy in the values of JRC obtained from the three different measurements: photogrammetry, manual measurement and tilt tests. In particular, the JRC obtained using the Barton's comb had slightly higher values compared to those determined through the photogrammetry method while the tilt test results tended to yield overestimated values of JRC. The JRC variation on slope stability analysis is sensitive under the Barton-Bandis shear strength model. It was generally found that an increase in the JRC led to an increase in the safety factor of the slope. The obtained photogrammetric JRC values have a wide range in the surveyed area.

7.2.2 Geological background of study area

The study slope is a road cut along the Beaudesert-Nerang road that connects the Gold Coast with the Tambourine Mountain area (Fig. 7.1). The lengths of this slope range from 50 m to 200 m and the heights of the rock cuts are normally less than 10 m. In the geology of the site, argillite and sandstone of the Neranleigh-Fernvale beds alternate with each other (Willmott, 2010) (Fig. 7.2).

Fig. 7.1 Overview of the rock cuts studied

The rocks are heavily weathered, fractured and steeply inclined. As a main rock type, argillite with dark grey colour, which is hardened and slightly recrystallized shale, is fine grained rock. Bedding and fractures due to metamorphism are observed in many exposures. Sandstone, which is mostly coarse grained sediment of bright brown colour, is also much fractured.
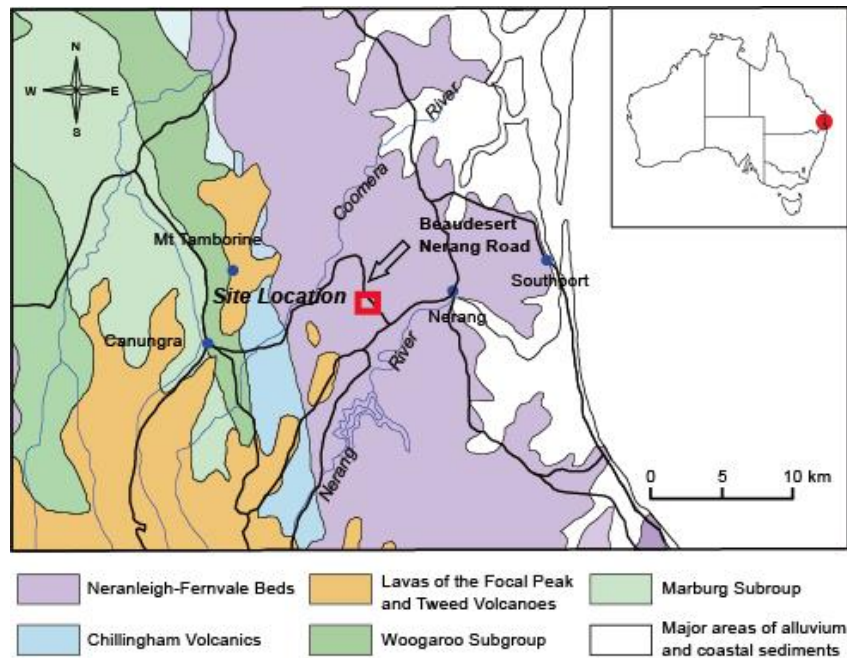
Fig. 7.2 Geological map of the study area

7.2.3 Strength characteristics of rocks

In order to identify the strength of the weathered rock, Schmidt hammer tests were performed at the site and point load tests were carried out using the collected rock fragments in the laboratory. A total of 70 Schmidt hammer test was performed for the two different rock types using a N-type Schmidt hammer as shown in Figure 7.3 (a).

A series of point load tests was also carried out on 12 argillite and sandstone samples collected from the site (Fig. 7.3 (b)) following the Australian Standard (AS 4133.4.1, 2007). The obtained results were plotted in Figure 7.4 against the corresponding values of UCS indicate that the strength of sandstone was about 6.2 MPa while the mean value of UCS for the argillite was 17.7 MPa. The values of Schmidt rebounds can be correlated to the unconfined compressive strength (UCS) using some empirical functions. The empirical equations, which were proposed by Katz et al. (2000) and Yasar & Erdogan (2004), were used to calculate the strength as follows:

$$\sigma_{UCS} = 2.21 \times e^{(0.07 \times R_N)} \qquad (7\text{-}1)$$

$$\sigma_{UCS} = 0.000004 \times R_L^{4.29} \qquad (7\text{-}2)$$

where, σ_{UCS} is unconfined compressive strength in MPa; R_L, R_N are rebound values for L and N type Schmidt hammer. The estimated strengths are presented in Table 7-1 and the detailed test results of point load tests are presented in Appendix 4.

Fig. 7.3 Strength investigations, Schmidt hammer tests (a), Point load tests (b)
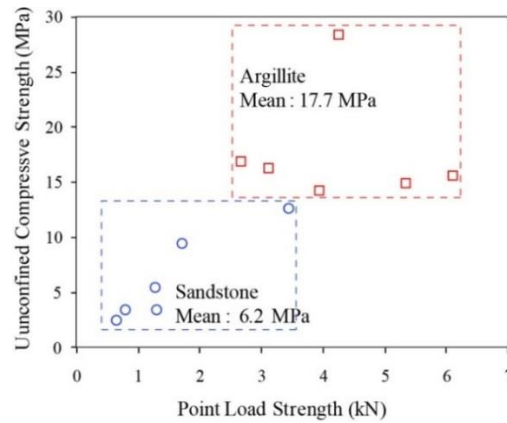
Fig. 7.4 Relationship between unconfined compressive strength (UCS) and point load strength for sandstone and argillite

Table 7-1 Unconfined compressive strengths (UCS) of sandstone and argillite

Rock types	UCS, from PLT (MPa)	UCS (MPa)from Schmidt hammer tests		Unit weight (kN/m^3)
		Yasar and Erdogan (2004)	Katz et al. (2000)	
Sandstone	6.2	13.1	20.0	25.7
Argillite	17.7	16.4	23.7	27.3

7.2.4 Photogrammetry survey and 3D models

Data on the rock surface characteristics were obtained using photogrammetry. The photogrammetry survey was only able to perform from the opposite space of the slope along the road. The distance between camera positions and the rock cut was about 17 m. The employed focal length was 24 mm. Photographs were taken at two positions with the distances between the camera positions was 2.5 m. For the geo-referencing of 3D images, the coordinates of the cameras were measured by the GPS device and their bearings (azimuth) to the centre of the slope were determined using a geological compass.

A 3D model was built using the computer code "Sirovision". The scale and orientation of the 3D model was corrected through the geo-referencing procedure. The values of dip and dip direction of the discontinuities at three different points were obtained from the 3D model and compared with the manually measured values. In terms of the image scale, the control points in the three sections on the slope were used to check the accuracy of the 3D image scale. The control points were marked with circular targets and the distances between the targets were measured by a measuring tape and compared with the values measured on the 3D models.

139

Figure 7.5 is a view of the 3D model obtained from Sirovision. The orientations (dip and dip direction) of the three joint sections were measured to verify the accuracy of the 3D model. Table 7-2 presents the results of such tests in which the distance between the control points was measured manually (by a ruler and a geological compass) and using the 3D models (by means of Sirovision).
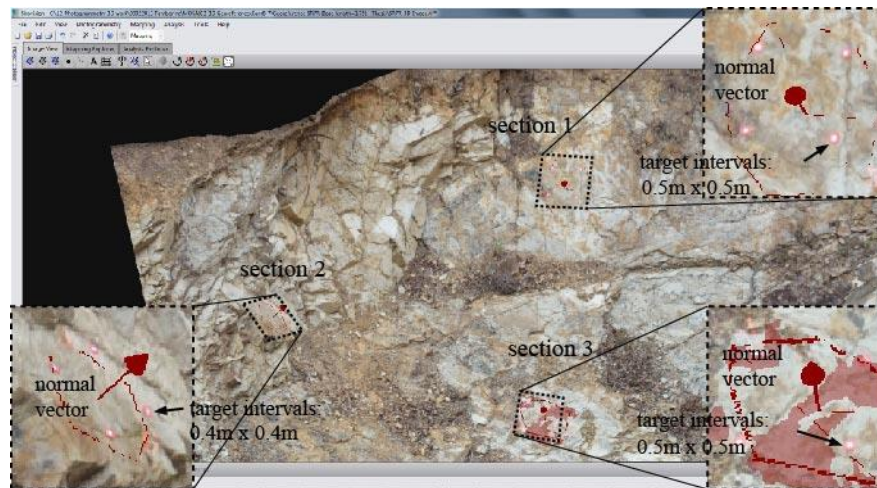
Fig. 7.5 A window shot of 3D model (Sirovision) and the sections of interests

It is evident from the results that only a marginal error exists between these two types of measurements, suggesting that the photogrammetry method can produce reliable results. The obtained 3D model showed that the intervals of the point clouds were ranged from 8 mm to 14 mm. The pixel size of the 3D image was 3.5 mm / pixel as demonstrated in Figure 7.6.

Table 7-2 Accuracy of 3D model

Dip / Dip direction	Sections	Manual measurement		3D model		Deviation	
		Dip (°)	Dip direction (°)	Dip (°)	Dip direction (°)	Dip (%)	Dip direction (%)
	1	55	3.0	49.6	8.9	1.5	1.6
	2	42	279.0	48.3	290.6	1.7	3.2
	3	32	5.0	37.6	357	1.6	2.2
Size of section area	Sections	H_m (m)	W_m (m)	H_{3D} (m)	W_{3D} (m)	$H_m - H_{3D}$ (%)	$W_m - W_{3D}$ (%)
	1	0.5	0.5	0.503	0.497	0.6 %	0.6 %
	2	0.4	0.4	0.397	0.404	0.7 %	1.0 %
	3	0.5	0.5	0.502	0.504	0.4 %	0.8 %

* H: height of section, W: width of section

a) Image density

3.5 mm per pixel

≒ 17 pixels
60 mm

b) Point clouds density

section 1

point clouds intervals: 10 ~ 12 mm

section 2

point clouds intervals: 9 ~ 14 mm

section 3

point clouds intervals: 8 ~ 10 mm
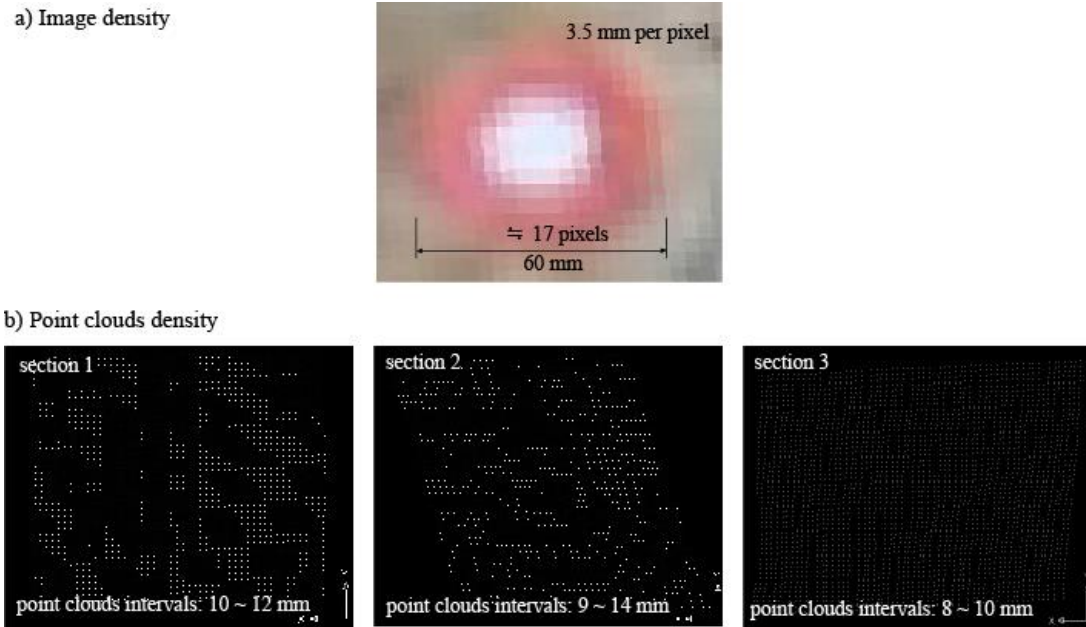
Fig. 7.6 Comparison of image density between the pixel size of 3D image a) and density of the point clouds of the 3D model b)

7.2.5 JRC estimation

In order to investigate the accuracy of the 3D models for JRC estimation, roughness profiles were manually measured in three different positions using a profile gauge. The measurements were carried out along the horizontal, vertical and diagonal directions of each position as shown in Figure 7.7. The measured profiles were digitized by drawing coordinates 1 mm intervals using AutoCAD (ver. 2008) program. The measured roughness profiles were then compared with the extracted profiles from the 3D models at the same locations.

JRC values were calculated by the empirical equations suggested by Tse and Cruden (1979) and Maerz et al. (1990) (Eqs. 2-8 to 2-10 and Eqs. 2-17 to 2-20) based on the coordinates of the roughness profiles. JRC values can be obtained using a function provided by Sirovision. However, it was observed that from the previous trials that the values, which were directly obtained from Sirovision, were changed sensitively according to the selected boundary points. Table 7-3 summarizes the JRC values obtained from the photogrammetry method and the manually measured profiles. It is evident from this table that the JRC values obtained from the manual measurement are considerably higher than those determined

141

through photogrammetry method. However, it was also found that there was a considerable overestimation of JRC values due to a distortion of 3D models.

The comparison between the measured profiles and the extracted profiles from the 3D model are presented in Figure 7.8. The comparison indicates that the overall shapes of the roughness profiles extracted from the 3D image are consistent with the manual measurements. It could be noticed that quite similar undulations were created using photogrammetry method in this site condition. However, it was found that the agreement of profiles was sensitive according to the orientations of the profiles. The profiles of steepest direction (dip direction) were comparatively well agreed with the measured profiles. The profile comparisons in steepest directions in each section are presented in Figure 7.8.

The asperity angles are lower than those of manual measurement due to the larger values of measurement intervals than those of manual measurements. As shown in Figure 7.8, even though the step sizes of the extracted profiles are between 0.4 mm and 2.0 mm, the average pixel size of the 3D image is 3.5 mm. It is noted that the distributed profile data are generated by the algorithm of "Sirovision" based on the original data with the pixel size of 3.5 mm. This result directly indicates that the measurement interval is 3.5 times larger than that of the standard interval of the profile gauge. Thus, the underestimation of JRC using photogrammetry can be attributed to the differences of the measurement intervals. The results are agreed with the results studied by Haneberg (2007) and Guo et al. (2011) that the resolution of digital images needs to be increased to ensure the reliability of JRC values using photogrammetry.
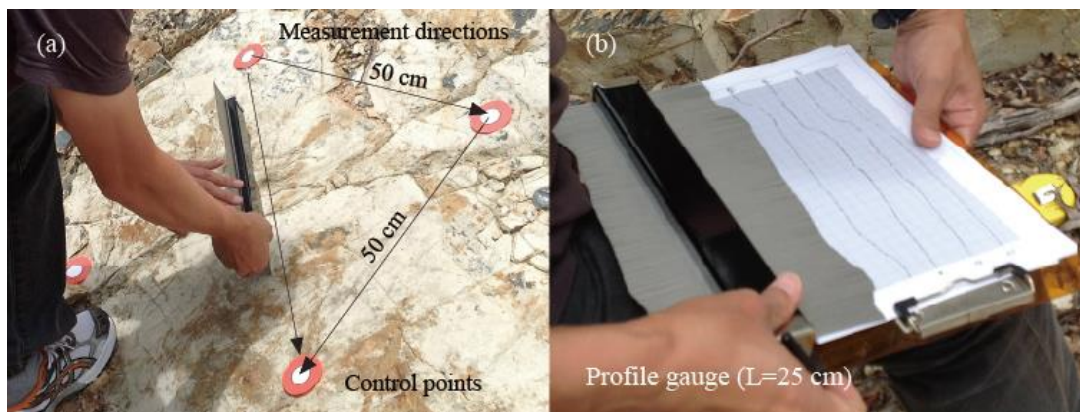
Fig. 7.7 Roughness measurement, the positions (a), measurement (b)
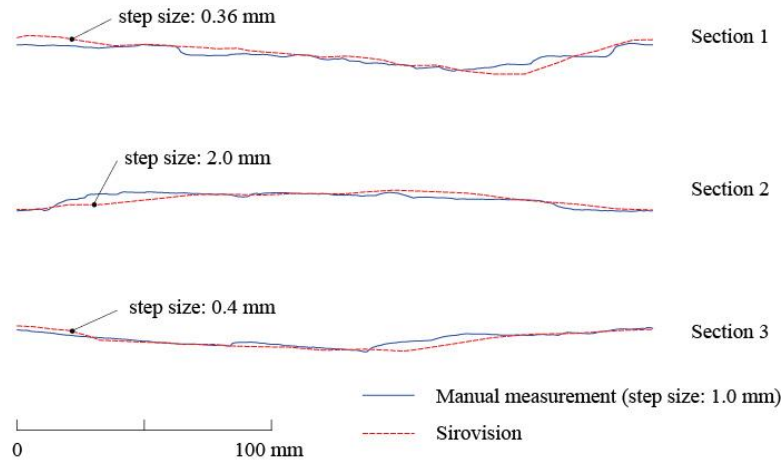
Fig. 7.8 Comparison of roughness profiles between 3D models and manual measurement (steepest direction)

Table 7-3 Comparison of JRC values

Sections		Calculated JRCs and Roughness parameters	Measurement directions			
			Vertical (steepest)	Diagonal (45° to steepest)	Horizontal (90° to steepest)	Diagonal (135° to steepest)
1	3D	Maerz JRC	3.56	0.91	4.03	2.28
		Tse and Cruden JRC	6.63	-5.67	12.22	1.83
		Roughness profile index	1.0087	1.0022	1.0098	1.0056
		RMS of local slopes	0.16315	0.068179	0.24251	0.11602
	Manual	Tse and Cruden	11.6	10.6	11.6	7.7
		Maerz	11.3	10.6	11.4	7.7
		Z_2	0.232	0.217	0.233	0.176
		R_p	1.028	1.026	1.028	1.019
2	3D	Maerz JRC	4.75	3.79	2.58	2.90
		Tse and Cruden JRC	6.64	4.35	1.84	2.53
		Roughness profile index	1.0116	1.0092	1.0063	1.0071
		RMS of local slopes	0.1634	0.13878	0.11611	0.12204
	Manual	Tse and Cruden	7.5	7.5	11.2	8.8
		Maerz	7.6	7.4	11.4	8.8
		Z_2	0.173	0.174	0.226	0.190
		R_p	1.018	1.018	1.028	1.022
3	3D	Maerz JRC	5.48	15.45	35.03	18.30
		Tse and Cruden JRC	6.92	19.27	27.68	21.21
		Roughness profile index	1.0134	1.0377	1.0856	1.0447
		RMS of local slopes	0.16661	0.3999	0.72608	0.45872
	Manual	Tse and Cruden	5.4	12.0	14.8	14.1
		Maerz	6.1	12.6	16.6	15.6
		Z_2	0.150	0.238	0.291	0.277
		R_p	1.015	1.031	1.040	1.038

7.2.6 Application of photogrammetric JRCs on stability analysis

Thirty JRC values were obtained from 30 blocks of 30 ~ 50 cm at different locations using the photogrammetry 3D model as shown in Figure 7.9 to study the overall distribution of JRC in the study slope. Figure 7.10 summarizes the data distributions indicating that the mean value of JRC was 5.4 (using the Maerz equation) and 6.5 (using the Tse and Cruden equation). The mean values of JRCs were employed to analyse the stability of this slope. Compared to the manual measurements, the photogrammetric JRC values were underestimated due to the large pixel sizes of the 3D image. However, this comparison is limited in the specific area so that the comparison does not represent all the area of the locations of the obtained data.

Locations of Joint roughness coefficient extraction
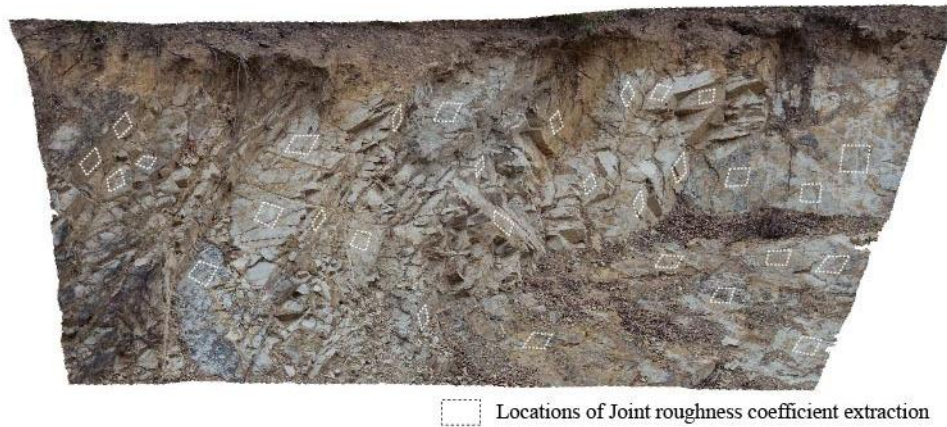
Fig. 7.9 Locations for JRC estimation on 3D model
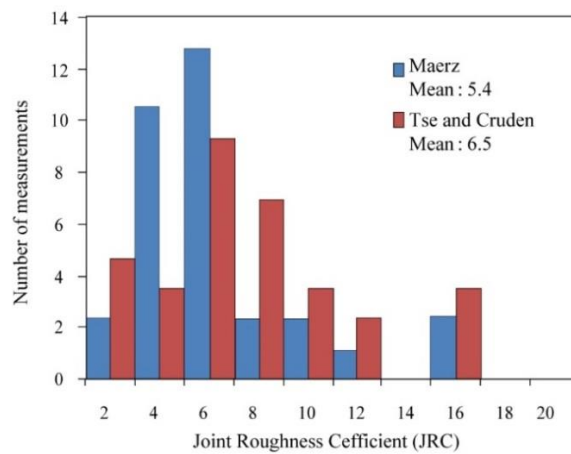
Fig. 7.10 JRC data distribution

The failure mechanism of the slope was analysed by means of a computer code called UDEC ver. 5.0 (Universal Distinct Element Code). This code is a two dimensional numerical software that simulates the quasi-static response of discontinuous media containing multiple, intersecting joint structures (Itasca Consulting Group Inc., 2011). The use of two dimensional codes is associated with long structures with constant cross-section acted on by loads in the plane of the cross sections. The condition of the cross section of the study area is assumed as a representative jointed slope feature oriented normal to the slope of analysis.

The joint spacing, dip and dip directions of major discontinuities were obtained from the 3D model. Three representative joint sets were analysed by using stereo projection methods in Sirovision. The orientation information of the joint sets is presented in Figure 7.11. The cross-section of the slope was determined based on the near slope geometry and the joint sets were modelled in the failed area of the model as shown in Figure 7.12. The Mohr-Coulomb slip joint model was employed for the joints of the numerical model. The groundwater condition was not considered in the numerical model. More details of the constitutive models in UDEC analysis are well discussed in the User's manual (Itasca Consulting Group Inc., 2011).

This analysis was performed under an assumption that the JRC data obtained from exposed rock surface can represent the joint roughness of the failed rock mass. The rock strength properties (Table 7-4) were used to determine the joint strength properties. Joint shear stiffness (K_s) was calculated using Eq. (7-3) (Barton and Choubey, 1977), and the joint normal stiffness was estimated by assuming the K_n/K_s ratio to 3.
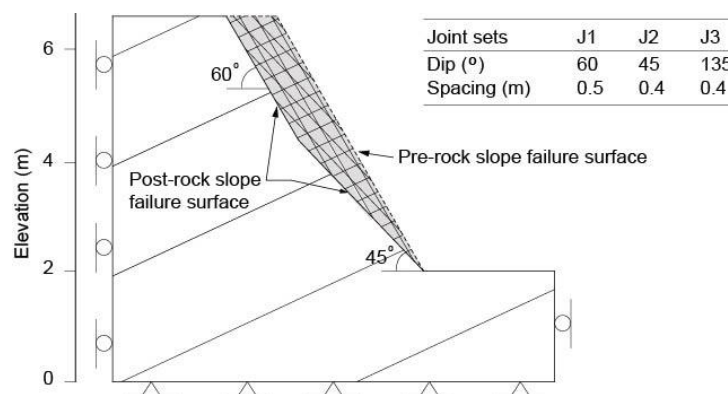
Fig. 7.11 Schematic profiles of numerical model

Fig. 7.12 Assumed pre-rock slope failure surface

Table 7-4 Input parameters used for the UDEC simulation and safety factor

Properties	Analysis cases		
	1	2	3
Density (kN/m^3)	25.7	25.7	25.7
Peak joint friction angle (˚)	35.0	38.3	41.9
Joint roughness coefficient (JRC)	5.4 (Maerz)	6.5 (Tse & Cruden)	8.0 (Manual)
Joint shear stiffness, K_s (MPa/m)	3.35E+02	4.25E+02	5.68E+02
Safety factor	0.48	0.50	0.62
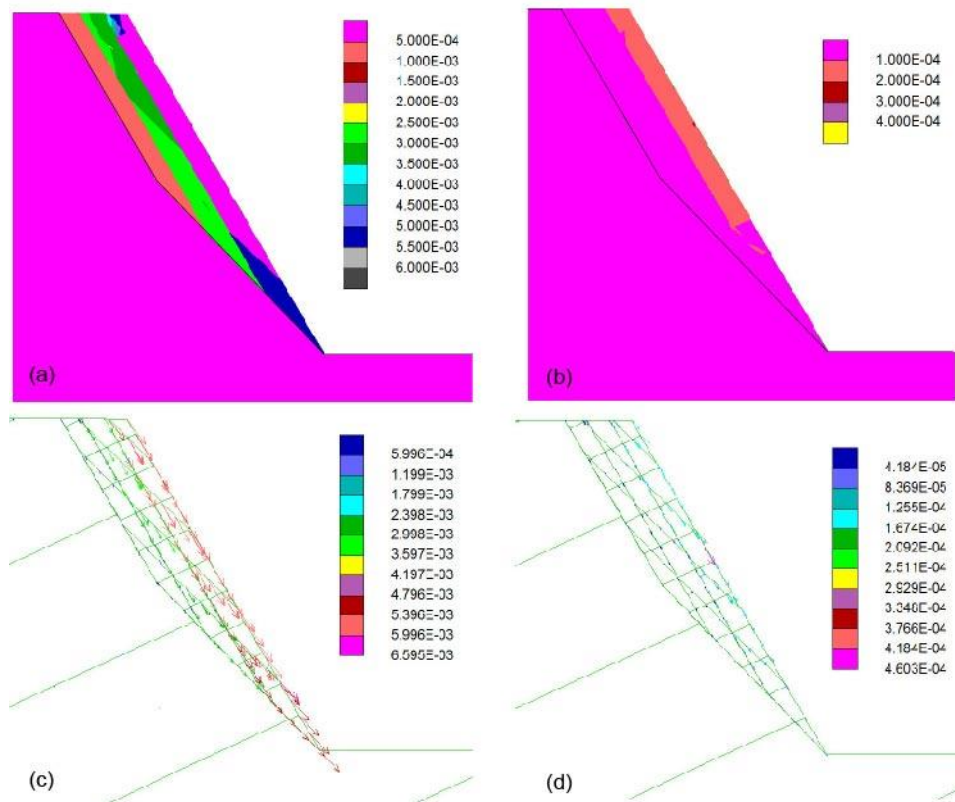
Fig. 7.13 Results of computer analysis using UDEC: displacement magnitude a JRC = 5.4 and b JRC = 8.0; displacement vector: c JRC = 5.4 and d JRC = 8.0

146

$$K_s = \frac{100}{L_x} \sigma_n tan \left[JRC \cdot log_{10} \left(\frac{JCS}{\sigma_n} \right) + \phi_r \right] \qquad (7\text{-}3)$$

where K_s is the joint shear stiffness (MN/m^2/m) and L_x is the joint length in metres.

The analysis results indicated that the slope was unstable (the SF was less than 1) for all three values of JRC. However, it was evident that an increase in the JRC resulted in an increase in the safety factor. As the slope has been failed, the safety factors were ranged from 0.48 to 0.62. The numerical analysis also demonstrated that the thickness of the sliding mass increased as the JRC dropped from 8.0 to 5.4 (Fig. 7.13).

7.2.7 Conclusion

The results of numerical analysis obtained from different JRC values were compared and their effect on the stability of a rock slope was assessed. Based on the obtained results, the following conclusions can be drawn:

- Roughness profiles can be extracted from the sections of photogrammetry 3D models to investigate rock surface roughness and the profiles can be used to estimate JRC values.
- The overall shapes of profiles can be produced similar to those obtained from field measurements using a Barton's comb in accordance with the extent of accuracy of the 3D models.
- The photogrammetric JRC values were underestimated compared to manual measurements under the photography setup setting (FL=24 mm and camera-to-object distance = 17 m). This discrepancy may be due to the lower density of 3D models (point interval = 3.5 mm) compared to the step size of profile gauge (measurement interval = 1.0 mm) in manual measurement.
- In the obtained JRC ranges, there was also considerable overestimation of JRCs. This could be explained by the influence of model distortion.
- The numerical analysis showed that the differences of JRC values were not very sensitively influence on the safety factors in the range between JRC = 5.4 and 8.0 showing the SF range from 0.48 to 0.62. This result shows that the obtained JRC ranges from photogrammetry reasonably explain the slope failure under the assumption that the slope stability is governed by the behaviour of joints.

7.3 Case study 2 (Hoek-Brown model)

A part of this section was published in Geotechnical and Geological Engineering journal as follows:

Dong Hyun Kim, Ivan Gratchev, Arumugam Balasubramaniam (2015) A photogrammetry approach for stability analysis of weathered rock slopes. Geotechnical and Geological Engineering, 33: 443-454.

7.3.1 Introduction

The Geological Strength Index (GSI) system is dependent on the rock block volumes and the joint surface conditions. The weathering degree of rock slopes and their strength properties also depend on these characteristics. This section of the thesis thus focuses on the use of photogrammetric roughness data in the GSI system and the Hoek-Brown strength criterion to estimate the engineering parameters for weathered rock masses. Photogrammetric methods based on 3D surface models are used to obtain reliable data on the joint sets in rock slopes, instead of general site investigation using labor-intensive techniques. Photogrammetric surveys were conducted on a weathered rock slope to obtain the joint spacing, orientation and roughness. The 3D models are then used to estimate the block sizes the joint roughness coefficients (JRC). The block volumes and JRC values were then used to estimate GSI values. Then parametric studies using the finite element method is conducted to investigate the stability of the slope using the GSI values.

7.3.2 Application of photogrammetry to GSI system

This study seeks to estimate GSI values using photogrammetry to assess the stability of a weathered rock slope. This study also focused on the attempts for the estimation of GSI values using photogrammetric JRC values. The GSI system is mainly used in the studies that follow a combination of the approaches of Hoek and Brown (1997), Ehlen (1999), Palmström (2001), Cai and Kaiser (2006) and Admassu et al. (2012). This system, which was introduced by Hoek and Brown (1997), has been a powerful tool for rock mass characterization which concentrates on the extent of blockiness and the surface condition of discontinuities. As the GSI values are estimated from visual observation of exposed outcrops, the use of GSI is subjective and requires much experience. Thus, as an effort to quantify GSI values for engineering purposes, Cai and Kaiser (2006) proposed a

148

quantitative method to estimate GSI using relationship between joint roughness number (J_R), joint alteration number (J_A) and block volume (V_b) in three dimensional space.

Photogrammetry methods have enabled the estimation of the scale of rock block and orientation of the main joint sets. The technique also has provided the 2D profiles and joint JRC values from 3D surface models using high resolution 3D digital images, for inaccessible rock slopes (Haneberg, 2007; Poropat, 2009; Guo et al., 2011; Kim et al., 2013a, b). The feasibility of photogrammetry can thus be extended to the investigation of weathered rocks. In weathering process, the rock mass becomes decomposed and the number of joint sets may be increased. In this case, photogrammetry can be alternative methods to identify the properties of joint roughness.

The degree of weathering in blocky rock mass can be investigated by measuring the degree of jointing, which is related to the number of joint sets and joint spacing. However, this approach should be carefully considered due to the fact that the frequency of joints can also be caused by different geological processes such as tectonic disturbances (Marinos et al., 2005). Block size and joint spacing are the main parameters to assess the degree of jointing in rock masses. Palmström (2001) presented correlations between block sizes and joint frequency (J_v) and also RQD and J_v using numerous measurement data. In terms of weathering, Ehlen (1999) showed the correlation between mean joint spacing and weathering grades. Similarly, Admassu et al. (2012) suggested that joint spacing is an important factor contributing to slope failure.

The slake durability and Schmidt rebound values can be used to estimate the strength of the weathered rock joints. Dick et al. (1994) noted that the durability of most rock is one of the most important parameters to the stability of the slopes. The slake durability test is to evaluate the influence of weathering on rocks by measuring the resistance to degradation and decomposition as simulated by being exposed to wetting and drying cycles. The study of Franklin and Chandra (1972) reported that slaking of rocks is an important consideration to evaluate the engineering behavior of rock mass and rock materials in geotechnical practices. Also, Schmidt hammer rebound values showed reliable results to classify weathering in the less weathered material (Arikan et al., 2007). Due to the reduction of strength of the weathered rock surface, rebound energy of Schmidt hammer can be absorbed. Sharma et al. (2011) showed a linear relation between the Schmidt rebound number and the impact strength index (ISI) and the slake durability index (SDI).

149

In this study, the relationships between the strength properties and the slake durability are investigated by performing point load tests, Schmidt hammer tests and slake durability tests. In order to investigate the influence of rock joint roughness on different weathering conditions, finite element analyses were also performed using the Hoek-Brown criterion based on the calculated GSI values.

7.3.3 Quantification of GSI values using JRC values

The GSI is the geological index based on rock mass structures and joint surface conditions. This index was introduced by Hoek (1994) and Hoek and Brown (1997) provided a system for estimating rock mass strength in accordance with the geological conditions using field observations. The rock mass rating chart is demonstrated in Figure 7.14. Marinos et al. (2005) suggested that the GSI values in weathering condition can be estimated by shifting the values of the unweathered rock mass in the chart. However, this procedure tends to be subjective and requires long term experience. As the GSI values are estimated from visual observation of exposed outcrops, the GSI values for weathered rock masses can be assessed using the degree of jointing on the slope surfaces. Cai and Kaiser (2006) proposed a quantitative method to estimate GSI using the joint condition factor (J_c) and rock block volume (V_b) in three dimensional space. The GSI is defined from the following function,

$$GSI = \frac{26.5 + 8.79 \ln J_c + 0.9 \ln V_b}{1 + 0.0151 \ln J_c - 0.0253 \ln V_b} \qquad (7\text{-}4)$$

where V_b is the block volume and J_c is a quantitative characterization factor to show joint condition. This condition factor, J_c can be said as the term of joint roughness. The joint condition factor, J_c is defined as follows;

$$J_c = \frac{J_W \, J_S}{J_A} \qquad (7\text{-}5)$$

where J_W is a factor to describe large scale waviness of joints which is in meters from 1 to 10m and J_S is a term to describe small scale smoothness. J_S is a parameter to describe joint surface roughness which is closely related to the joint roughness coefficient (JRC) defined by Barton et al. (as cited in Palmström, 2001). J_A is the joint alteration factor which defines the filling of the joints. In terms of the importance of GSI values, as a main parameter, GSI values are applied in the Hoek-Brown failure criterion. The normal form of the Hoek-Brown failure criterion is Eq. (7-6),

Geological Strength Index

From the description of structure and surface conditions of the rock mass, pick an appropriate box in this chart. Estimate the average value to the Geological Strength Index (GSI) from the contours. Do not attempt to be too precise. Quoting a range of GSI from 36 to 42 is more realistic than stating that GSI=38. It is also important to recognize that the Hoek-Brown criterion should only be applied to rock masses where the size of individual blocks is small compared with the size of the excavation under consideration.

Surface conditions

Very good
Very rough and fresh unweathered surfaces

Good
Rough, maybe slightly weathered or iron stained surfaces

Fair
Smooth and/or moderately weathered and altered surfaces

Poor
Slickensided or highly weathered surfaces or compact coatings with fillings of angular fragments

Very poor
Slickensided or highly weathered surfaces with soft clay coating or fillings

Structure

Deacreasing surface quality →

Decreasing interlocking of rock pieces

Blocky - very well interlocked undisturbed rock mass consisting of cubical blocks formed by three orthogonal discontinuity sets

80

70

Very Blocky - interlocked, partially disturbed rock mass with multifaceted angular blocks formed by four or more discontinuity sets

60

50

Blocky/disturbed - folded and/or faulted with angular blocks formed by many intersecting discontinuity sets

40

30

Disintegrated - poorly interlocked, heavily broken rock mass with a mixture of angular and rounded rock pieces

20

10

Fig. 7.14 Characterisation of rock masses on the basis of interlocking and joint alteration (Hoek and Brown 1998 adjusted from Hoek 1994) (Hoek et al., 1998)

$$\sigma_1' = \sigma_3' + \sigma_{ci}(m_b \frac{\sigma_3'}{\sigma_{ci}} + s)^\alpha \qquad (7\text{-}6)$$

where σ'_1 and σ'_3 are the major and minor effective principal stresses and σ_{ci} is the uniaxial compressive strength of the rock. m_b, s and α are material constants for rock mass as follows;

$$m_b = m_i exp(\frac{GSI-100}{28-14D}) \qquad (7\text{-}7)$$

$$s = exp(\frac{GSI-100}{9-3D}) \qquad (7\text{-}8)$$

$$\alpha = \frac{1}{2} + \frac{1}{6}(e^{-\frac{GSI}{15}} - e^{-\frac{20}{3}}) \qquad (7\text{-}9)$$

The deformation modulus in the GSI system can be estimated as follows;

$$E = (1 - \frac{D}{2})\sqrt{\frac{\sigma_c}{100}}10^{(\frac{GSI-10}{40})} \text{ GPa} \qquad (\text{for } \sigma_c < 100 \text{ MPa}) \qquad (7\text{-}10)$$

where D is the disturbance factor that depends on the degree of disturbance by blasting and stress relaxation (Hoek et al., 2002). For weathered rock masses, the constants m_i and the unconfined strength of intact rock σ_{ci} in the Hoek-Brown criterion should be reduced in comparison with the unweathered rock masses (Marinos et al., 2005).

7.3.4 Strength properties of weathered rocks

The study area is located in the same slope with the previous site in Section 7.2. The site is mainly composed of layered argillite and sandstone in Neranleigh-Fernvale beds (Willmott, 2010; Gratchev et al., 2013). A series of point load tests, using the both collected samples and core samples, were added on the results obtained from the previous tests and slake durability tests were also performed (Fig. 7.15). The core samples from near sites were used as unweathered rocks which were not exposed to surface weathering. Figure 7.16 shows the range of point load index (PLI) and the slake durability indices (SDI) of the rock samples. The samples were classified by the point load strength (Broch & Franklin, 1972). A large number of weathered argillite samples exist in the 'high' strength category of PLI while the weathered sandstone samples are categorized as the 'medium' PLI. The unconfined compressive strengths (UCS) were estimated from the results of the point load tests. The

approximate conversion of UCS was performed using the conversion factor 24 as shown in Eq. (7-11) (Broch & Franklin, 1972),

$$UCS = 24 \times I_{s(50)} \qquad (7\text{-}11)$$

where, $I_{s(50)}$ is the point load strength index at a reference diameter of 50 mm for core samples. The laboratory tests also show that the samples with low values of unconfined compressive strength tend to have low values of slake durability index (see Table 7-5). The slake durability indices from the argillite samples range from 92.5 % to 97 % and the point load strength indices range from 1.53 to 3.31 MPa. The durability of argillite is classified as 'high' to 'extremely high' durability according to the slake durability index classification (Franklin & Chandra, 1972). In contrast, a considerable difference in slake durability index (Id_2) of the sandstone was indicated between 'low to medium' ($Id_2 = 50$ %) and 'very high' durability ($Id_2 = 90.7$ %). As a result, the argillite has higher unconfined compressive strength and more durability than the sandstone.

During the site investigations, a total of 40 Schmidt hammer tests were performed on the discontinuities of the argillite and sandstone areas. Table 7-6 shows that the range of rebound values are between 11 and 49, which are classified as weathering grade III or IV for the both argillite and the sandstone areas (Arikan et al., 2007). The different weathering grades also indicate that the sandstone of the study area is less durable than the argillite.
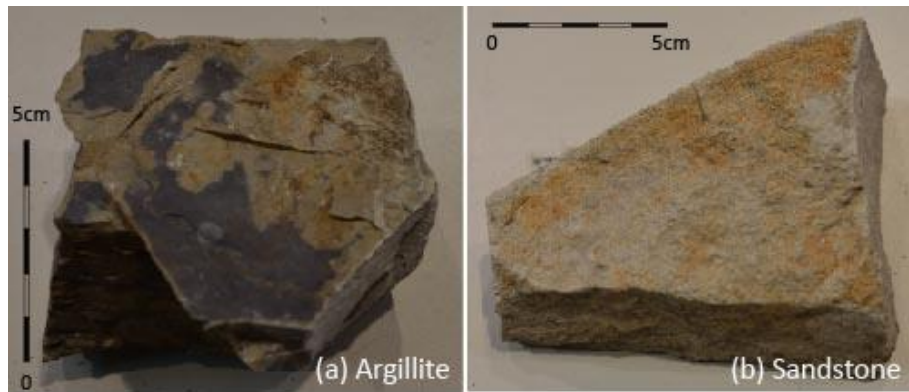
Fig. 7.15 Collected rock samples

Table 7-5 Unconfined compressive strength based on point load tests

Rock types	Fresh				Weathered			
	Test Number	UCS (MPa)			Test Number	UCS (MPa)		
		Min	Max	Mean		Min	Max	Mean
Argillite	5	85.3	100.1	92.7	23	9.4	70.6	41.0
Sandstone	15	22.9	77.6	46.4	12	6.0	16.2	12.7

Table 7-6 Results of Schmidt hammer tests

Rock types	Schmidt hammer rebounds			Weathering grade
	Range of data	Mean	SD	
Argillite	17 – 49	31.3	8.3	III (20 – 30)
Sandstone	11 – 46	27.7	10.9	IV (30 – 40)
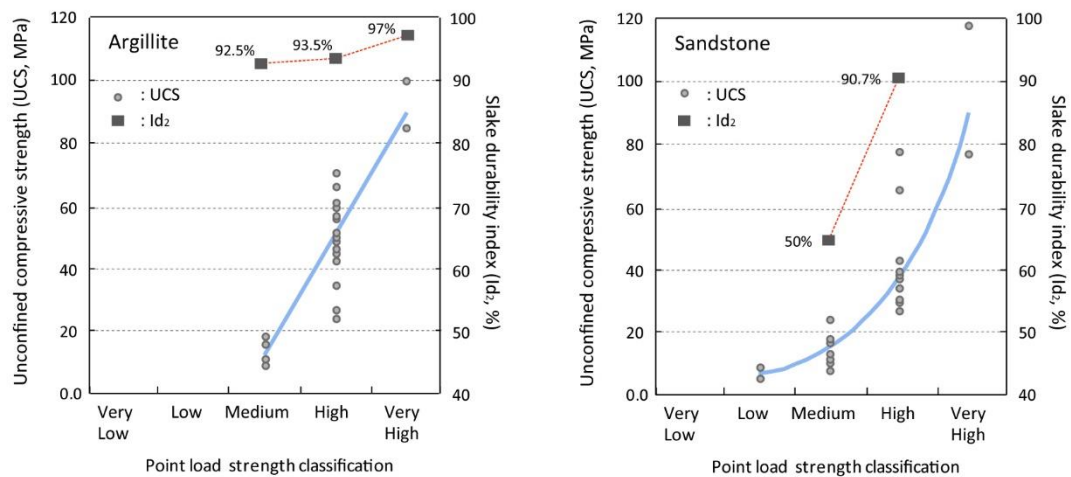
Fig. 7.16 Unconfined compressive strength (UCS) and slake durability index (Id_2) according to point strength classification

7.3.5 Assessment of jointing degree using 3D models

Photogrammetry survey was performed to produce 3D models of the slope surface model and determine the density of joints as well as the range of JRC values. The spacing and the orientations of joints were obtained from the 3D models. Mapping and tracing for the joint information was conducted manually on screen and provided the spacing and the length of the joint sets. The discontinuities data obtained from the 3D model were plotted on stereonets to determine the main joint sets. For the both argillite and sandstone,

representative sampling areas, which are 3m × 3m in dimension, were considered in this study (Fig. 7.17).
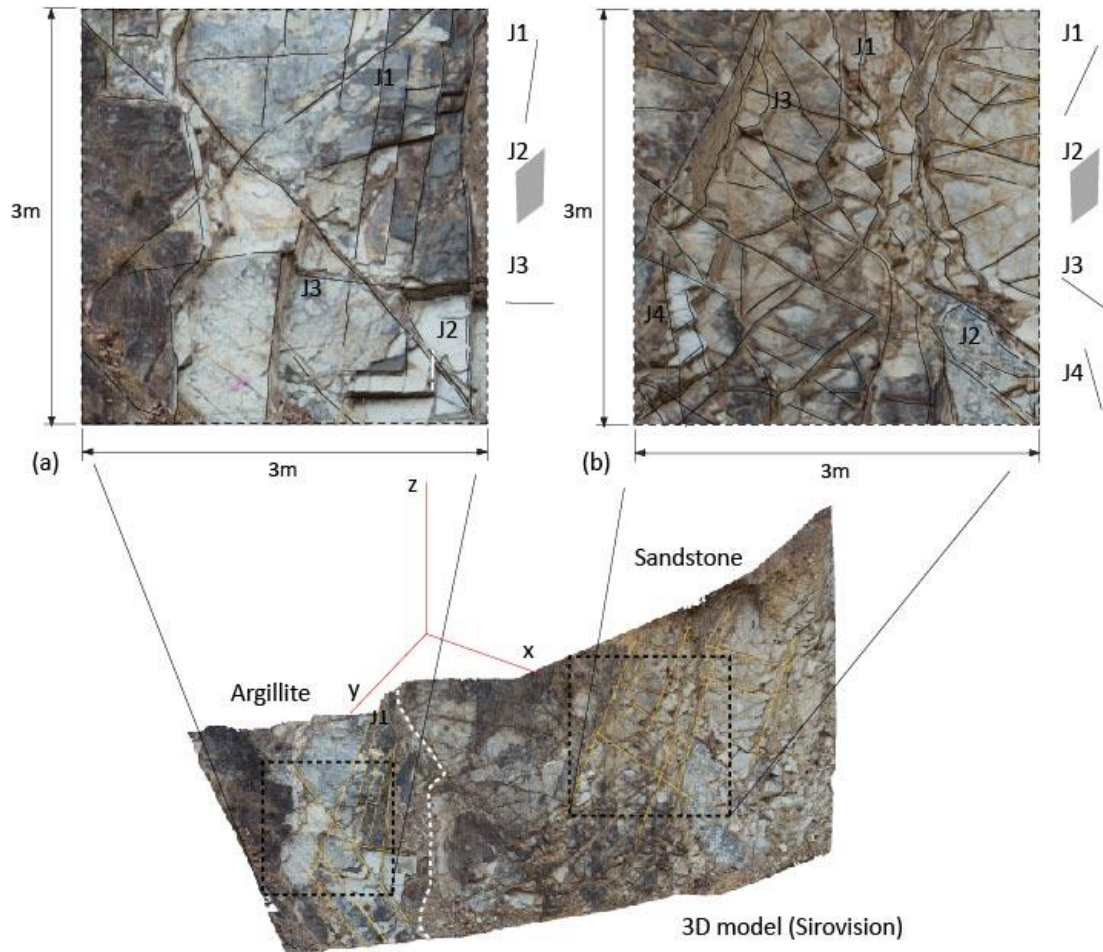
Fig. 7.17 Main joint sets of the selected areas based on the 3D model

The block shapes in the sandstone area are more irregular than those of argillite. Figure 7.18 shows the joint spacing of the main joint sets for the argillite and the sandstone. The overall joint spacing of the sandstone area is smaller than that of the argillite area. The measured distances and orientations of the discontinuity sets were used to assess the degree of jointing; block volumes, volumetric joint count and RQD. As a result, the block volumes and RQD values of argillite indicates higher values than those of sandstone as presented in Table 7-7. Even though the block sizes of both rock types can be formed based on different geologic processes such as tectonic movement, it is interesting that the sandstone area shows lower block volumes with lower weathering degrees (IV) than that of argillite (III).

In this study, the waviness of joint wall (J_w) was estimated using undulations obtained by the roughness profiles extracted from the 3D models. This measurement was performed on the roughness profiles, which were extracted from 3D models. The procedure was applied in the AutoCAD program placing a 0.9 m line on the digitized roughness profiles. The asperity heights were then measured from the distances between the lines as shown in Figure 7.19. This concept is the same as the procedure described by Piteau (1970).
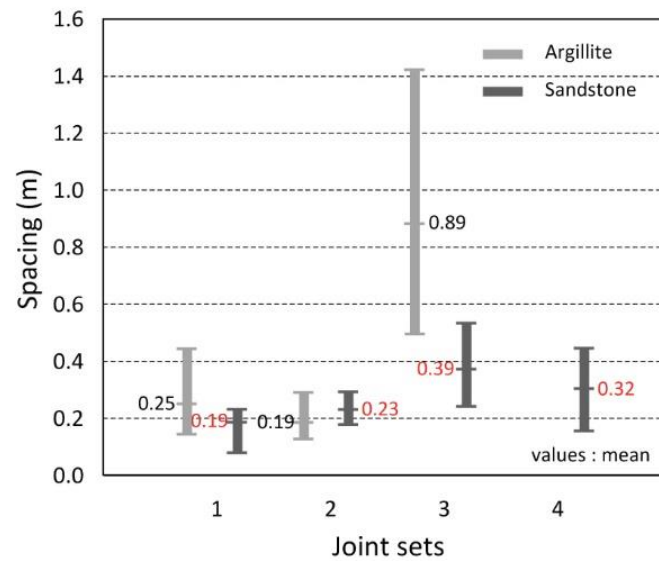
Fig. 7.18 Variation in the spacing of joints

Table 7-7 Estimated degree of jointing in the study areas based on 3D models

Degree of jointing	Argillite	Sandstone
Volumetric joint count (J_v)	6.4 – 16.4 (Mean: 10.5)	11.6 – 22.1 (Mean: 15.3)
Block volume (V_b, $\times 10^3$ cm^3)	7.0 – 113.0 (Mean: 26.0)	3.0 – 19.0 (Mean: 8.0)
RQD (%)	61.0 – 93.8 (Mean: 80.4)	42.1 – 76.8 (Mean: 64.7)

In a small scale roughness, the joint smoothness factor (J_s) can be associated with JRC values. In this study, J_s values were estimated using the linear interpolation relationship between JRC values and J_s (Eq. 7-12). This relationship is developed by the assumption that the range of J_s (0.6 ~ 3.0) is directly proportional to the range of JRC (0 ~ 20). The JRC values were obtained using the Maerz et al. (1990) and Tse and Cruden (1979) approaches based on the surface profiles in 10cm lengths which were extracted from the 3D models for the dip directions of the joints. 20 JRC values were calculated at different locations in each

section. Figure 7.20 presents an example of roughness profiles extracted from the 3D model. JRC values were calculated using the code "Sirovision" with functions as follows,

$$J_s = 0.1125 \times JRC + 0.75 \qquad (7\text{-}12)$$

$$JRC = 32.2 + 32.47 log Z_2 \quad \text{(Tse \& Cruden, 1979)} \qquad (7\text{-}13)$$

$$JRC = 411(R_p - 1) \quad \text{(Maerz et al., 1990)} \qquad (7\text{-}14)$$
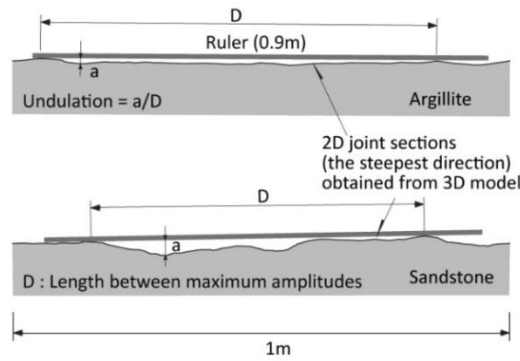
Fig. 7.19 Estimation of undulation using 3D models
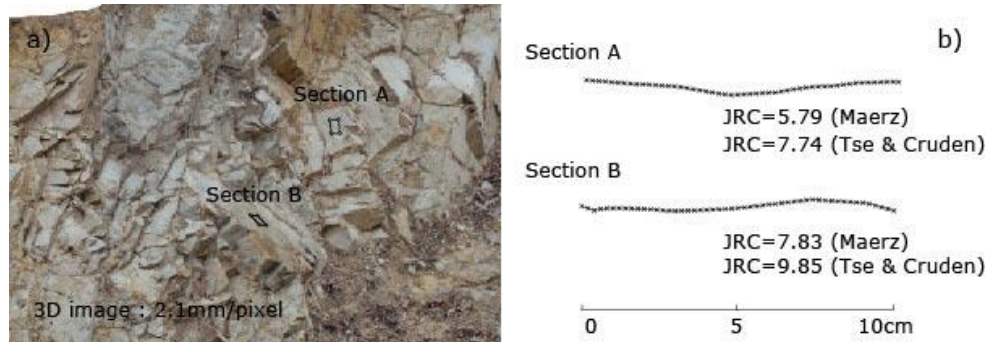
Fig. 7.20 JRC values estimated from 3D models, 3D image (a) JRC values and roughness profiles (b)

where, Z_2 is a roughness parameter using variances within asperity heights, and where R_p is a roughness parameter which is related to the inclination angle (*i*) of the sawtooth surface of the roughness profile. The accuracy of the obtained photogrammetric roughness data has not been identified. Therefore, the accuracy of Js values are linearly proportional to the level of accuracy of the photogrammetric JRC values according to Eq. (7-12). In this study, parametric analyses on the influence of the variation of the joint factors are thus included. Figure 7.21 summarizes the obtained data, indicating a similar range of JRC values between both the argillite and sandstone areas from 7.4 to

157

10.3. Consequently, there is no significant difference between the mean values of J_s; however, in the large scale joint condition, the more undulating surfaces of the sandstone produced larger J_c values than the argillite section, as presented in Table 7-8.

The GSI values were then obtained from Eq. (7-4). The values were quantified by the estimated block volumes and joint condition factors (J_c). The variation of GSI as a function of block volume (V_b) and joint condition factor (J_c) are plotted in Figure 7.21. The block volume is a less sensitive parameter to estimate GSI values than the joint condition factor. Figure 7.21 (a) shows that even much larger blocks (100 times) with the same joint condition factors produce an increase only 10 GSI values. Therefore, joint condition factors can be more influential and thus should be carefully examined to quantify GSI values. For the study areas, the estimated GSI and the Hoek-Brown strength parameters were given in Table 7-9. The numerical code 'RocData' (Rocscience) was used to estimate the Hoek-Brown strength parameters and the elastic modulus.

Table 7-8 Estimated joint surface properties based on 3D models

Joint surface conditions	Argillite	Sandstone
Waviness of joints (J_w)	1.5	2.0
Smoothness factor (J_s)	1.7 – 1.9 (Mean: 1.8)	1.6 – 1.8 (Mean: 1.7)
Joint condition factor (J_c)	0.64 – 0.72 (Mean: 0.68)	0.79 – 0.88 (Mean: 0.83)

Table 7-9 Estimated GSI values and Hoek-Brown properties using RocData (Rocscience, 2011b)

Strength properties	Argillite	Sandstone
UCS (MPa)	41.0	12.7
GSI	44	43
mb	0.83	0.742
s	0.0003	0.0003
α	0.509	0.509
Young's modulus (MPa)	1.11	0.6
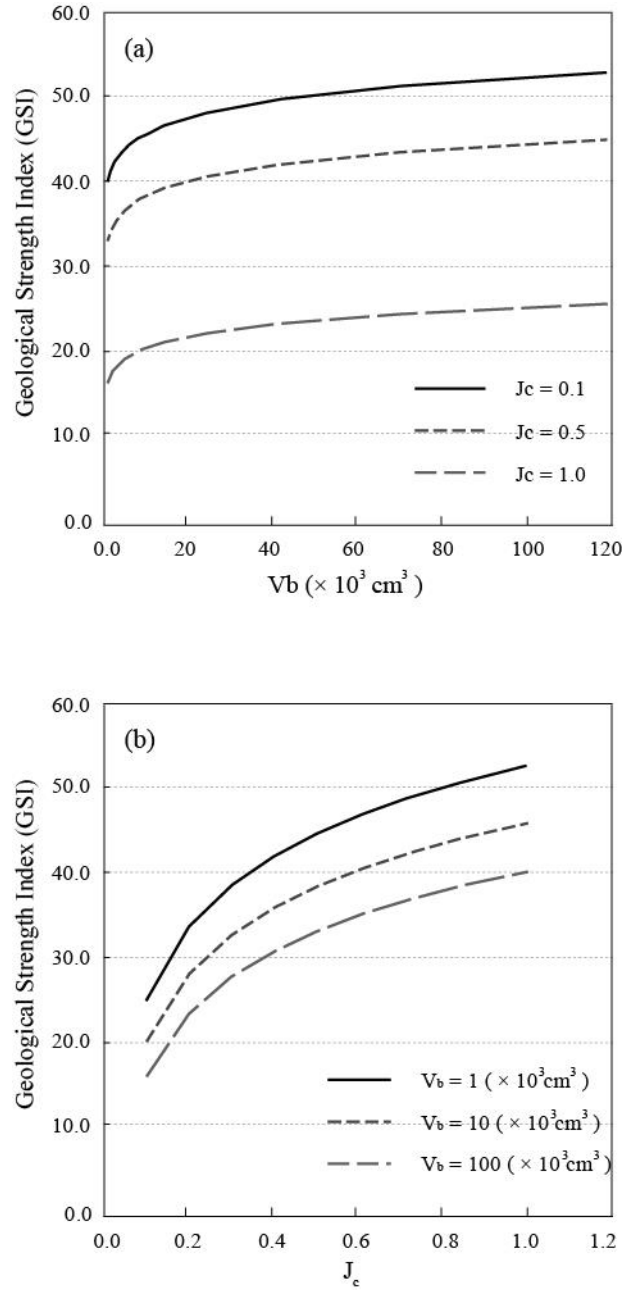
Fig. 7.21 GSI variations with V_b (a) and J_c (b)

7.3.6 Parametric study on the weathered rock slope

Based on the estimated GSI values and the block sizes obtained from the 3D models, the parametric analyses were performed using a numerical code, Phase2 (Rocscience Inc., 2011a). This code is an elasto-plastic finite element program for calculating stresses and displacements of geotechnical structures for both soil and rock. This software also provides

a variety of modelling options for the modelling of jointed rock. Rock joints can be explicitly modelled as joint boundaries. The failure mechanisms of the study area were simulated by two different criteria in numerical analyses. One was to investigate the influence of the block sizes on the behaviour of weathered slopes using the Mohr-Coulomb model, and the other was to examine the influence of GSI values on the failure behaviour for the same analysis section. In order to model the blocks in the failed area, joint networks were simulated with joint patterns in accordance with the orientations of the joint sets and the block sizes. Figure 7.22 demonstrates the numerical models for both cases.

Firstly, the numerical models using the Mohr-Coulomb criterion have one main joint set dipping 43˚ along the slope and another cross-joint set generated perpendicular to the slope. In the parametric study, three different joint spaces – 10 cm, 20 cm and 40 cm for the main joint set and 20 cm, 40 cm and 80 cm for the cross-joint set – were considered in order to simulate different block sizes (Fig. 7.22 (a)). For the joint parameters, the Barton-Bandis rock joint strength criterion was adopted and the peak friction angle which represents joint roughness condition, was estimated using the JRC values of Eq. (7-15) suggested by Barton et al. (1977),

$$\phi = \phi_r + JRC_n \log_{10}\left(\frac{JCS_n}{\sigma_n}\right) \qquad (7\text{-}15)$$

where, ϕ_r= residual friction angle of joint; JCS = joint wall compressive strength; σ_n = normal stress acting on the joint plane. The residual friction angles which represent a critical state in shearing were simply predicted from the results of Schmidt hammer tests. This methodology is well presented by Bandis et al. (1981).
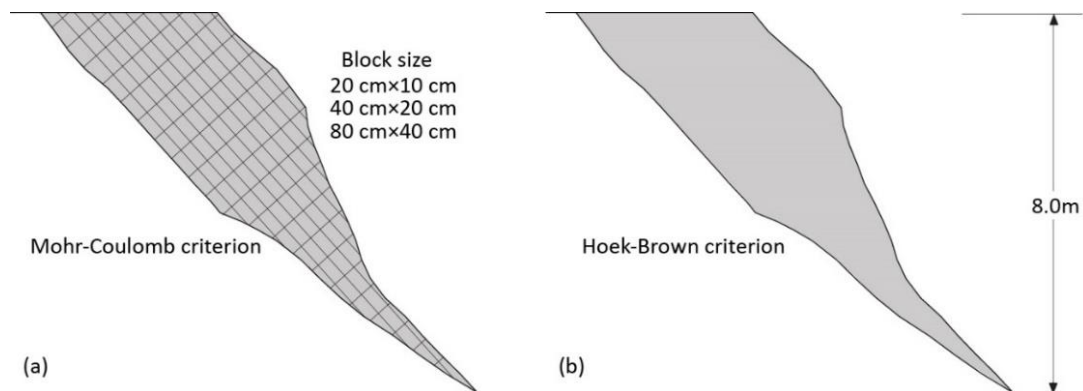
Fig. 7.22 Numerical models for the parametric study using Phase 2, Mohr-Coulomb model (a), Hoek-Brown model (b)

Secondly, the numerical models of the Hoek-Brown failure criterion were simulated for the same failure area. Based on three different GSI values, corresponding material constants described in Eqs. (7-7, 7-8, 7-9) were estimated by RocData (Rocscience Inc., 2011). The software RocData provides functions for testing based on hypotheses on four widely used strength models of soils and rock. The program provides simple and intuitive implementations of the generalized Hoek-Brown, Barton-Bandis, Power Curve and Mohr-Coulomb failure criterion. Users can easily check the effects on the relevant parameters by the changes in input parameters. The conditions for both numerical analyses are summarized in Table 7-10.

Using the results of FEM analysis, slope failure mechanisms can be inferred from the assessment of total displacement. Figure 7.23 shows the total displacements from the parametric analyses of the slope models. Figure 7.23 (a) indicates that the variation in block size can affect the deformation of the slopes. As the block sizes increase, the deformation values diminish. However, increasing the block size does not significantly reduce the displacement of the slope. This is mainly because there are no other changes in the strength parameters except for block sizes. Based on the JRC values obtained from the 3D image, block size itself is not an influential factor for the study slope.

Table 7-10 Conditions of numerical analysis (strength criteria and estimated parameters)

Model	Criteria and parameters	Argillite	Sandstone
1	Mohr-Coulomb criterion (rock mass)	Cohesion: 0.13 MPa Friction angle: 55.0˚ JRC: 9.4 JCS: 41 MPa Block size: 0.002, 0.008, 0.032 (m^3)	Cohesion: 0.07 MPa Friction angle: 47.0˚ JRC: 8.2 JCS: 12.7 MPa Block size: 0.002, 0.008, 0.032 (m^3)
2	Hoek-Brown criterion	GSI: 20, 40, 60 Material constants, m_b: 0.22 ~ 1.99 Material constants, s: 9.2e-6 ~ 0.003 Material constants, a: 0.54 0.503	GSI: 20, 40, 60 Material constants, m_b: 0.21 ~ 1.88 Material constants, s: 9.2e-6 ~ 0.003 Material constants, a: 0.54 0.503

On the other hand, the results analysed from the Hoek-Brown criterion shows more sensitive variations of slope displacement. Figure 7.23 (b) shows total displacement of the slope according to the variations of GSI values and material constants. The results of the analyses demonstrated that when the GSI value increased from 20 to 60, the maximum value of total displacement of the slope was considerably reduced. This means that the GSI values which are controlled by the block sizes and by joint conditions can affect strength characteristics in the Hoek-Brown criterion. Consequently, it can be said that joint condition factor J_c, which are sensitive to the variation of joint roughness, should be cautiously determined. More accurate photogrammetry models can also provide reliable roughness parameters in rock mechanical analyses. Figure 7.24 shows the deformed mesh and the total displacement contours for each analysis.
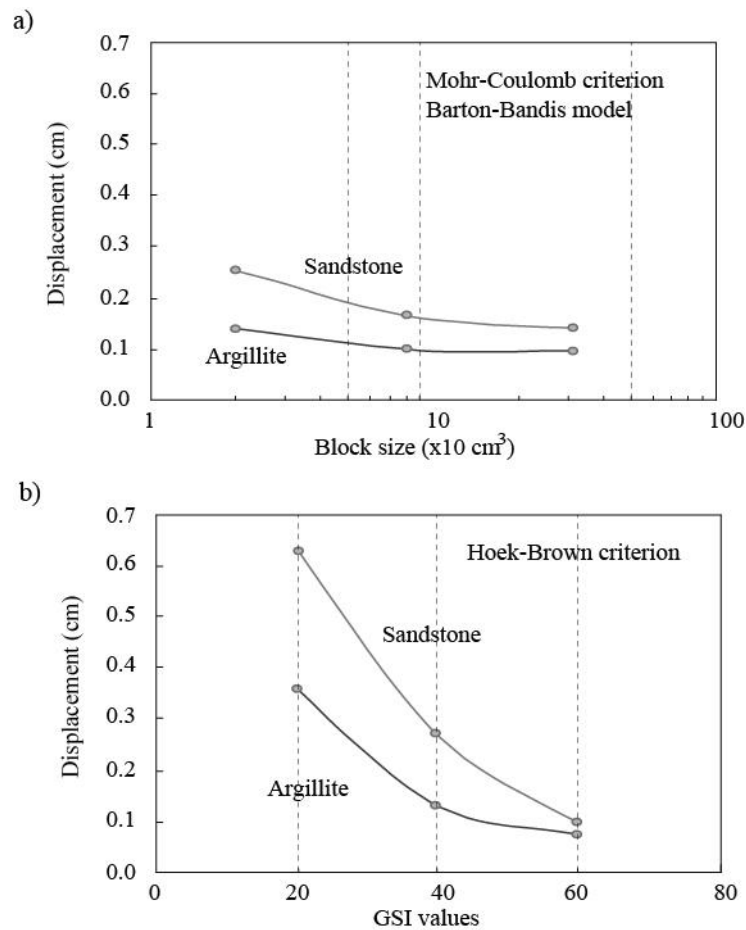
Fig. 7.23 Variation of maximum displacement with block volumes (a) and with GSI values (b)
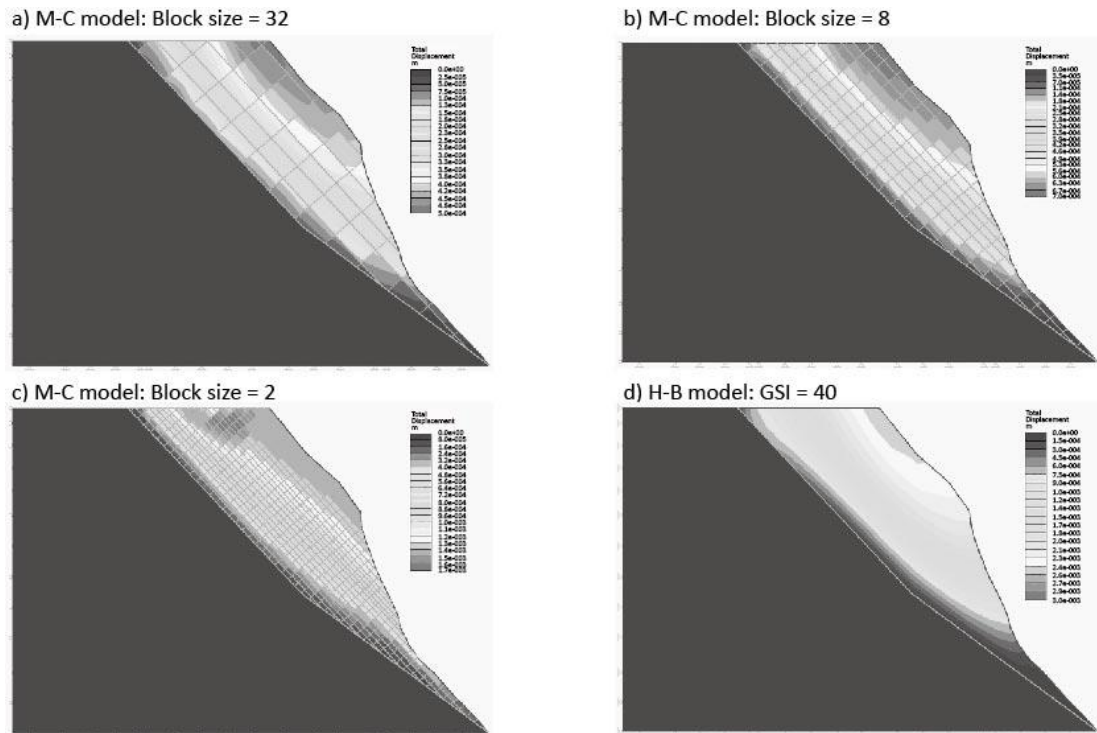
Fig. 7.24 Contours of total displacement (sandstone), Mohr-Coulomb model (a-c), Hoek-Brown model (d)

7.3.7 Conclusion

In this section, geological strength index (GSI) values were estimated using a photogrammetry 3D model to assess the stability of a weathered rock slope. The GSI values were estimated in relation to the information of joint geometry such as joint intervals, block sizes and roughness data obtained from the 3D model. Two dimensional numerical analyses were performed and the results were discussed considering the accuracy of the photogrammetric roughness data. Based on the obtained results, the following conclusions can be drawn:

- Joint smoothness factor (J_s) attempted to be calculated by using photogrammetric JRC data. The suggested correlation between JRC and J_s in this case study is acceptable under the assumption that the parameter, J_s in the GSI system can indicate the same ranges of JRCs as a small scale roughness parameter.

- Because of the level of accuracy of the photogrammetric JRC data was not clearly identified, the results of the simulations could not reflect the real slope situations. However, it can be said that within the reliable range of photogrammetric JRC values,

photogrammetry is an appropriate method for the Hoek-Brown criterion to provide joint information of rock mass in terms of the availability of the method for creating roughness parameters as well as providing reliable data on joint spacing and the block sizes of rock slopes based on the discontinuity sets in 3D models.

- In the Hoek-Brown criterion, the joint condition factor (J_c) is sensitively influenced by joint roughness. The numerical analysis also shows that joint condition factor (J_c) is more influential than the block sizes to the displacement of the slope model. Consequently, the extent of accuracy of photogrammetric 3D models for roughness data is more importantly affect to estimate GSI values than the accuracy of the data of block volumes.

7.4 Case study 3 (Block theory)

A part of this section was published in Landslides journal as follows:

Dong Hyun Kim, Ivan Gratchev, Arumugam Balasubramaniam (2015) Back analysis of a natural jointed rock slope based on the photogrammetry method. Landslides, 12: 147-154.

7.4.1 Introduction

The stability of jointed rock masses is strongly affected by the orientations of joints sets. Based on the discontinuity data, feasible failure mechanisms can be initially assessed by kinematic analyses. Further, in hard rock slopes, if the rock blocks are assumed to be rigid and the joint sets are assumed to be fully persistent through the volume of interest, block theory can investigate the finiteness and removability of individual blocks surrounded by multiple joint systems.

Block theory is an analytical method developed by Goodman and Shi (1985) to assess the stability of rock mass with discontinuities. The method provides a three-dimensional graphical presentation of the problem and assists in identifying removable blocks and also finding the applicable failure modes. This simple approach has provided research with a comprehensive stability evaluation of jointed rock slopes with a clearly defined geometry of blocks (Goodman and Shi, 1985; Mauldon and Goodman, 1996; Hatzor and Goodman., 1997; Tonon, 1998; Huang et al., 2003; Hatzor and Feintuch, 2005; Kulatilake et al., 2011).

The application of block theory should be based on accurate measurements of the discontinuity characteristics, however it has limited application as it is difficult to obtain during field investigations of large slopes. Thus, the geo-referenced three-dimensional models obtained from remote sensing techniques such as laser scanning and terrestrial digital photogrammetry started to be employed to provide the geo-structural data for the key block analyses (Pötsch & Schubert, 2006; Ferrero et al., 2011a, b).

This study seeks to apply the block theory in combination with photogrammetry to back-calculate the rock block failure in a potentially unstable slope in the Tamborine Mountain area, Gold Coast, Australia. Especially, JRC values are estimated from a 3D surface model and employed to estimate the range of friction angles of joints for the back analysis. This slope has long experienced stability issues affecting the serviceability of the adjacent road.

Thus, the slope has been visited and observed occasionally. After the failure, photogrammetry was employed to provide discontinuity characteristics to key block analysis, so as to identify key blocks at failure conditions. The behaviour of rock failures was then produced by the 3D distinct element code "3DEC" simulations. The friction angles based on photogrammetric JRC values along joint surfaces were back-calculated using parametric simulations, comparing them with the safety factor for removable blocks. The feasibility of photogrammetric roughness data is discussed in this section using the obtained safety factors from the key block analysis and the numerical analysis.

7.4.2 Site overview

The studied slope (Fig. 7.25) is located along Henri Robert Drive in the Tamborine Mountain area, Gold Coast, Australia. The height of the slope is up to 25 meters and the geological composition is mainly greywacke of the Neranleigh-Fernvale Beds (Willmott, 2010, Gratchev et al., 2013). This slope has experienced stability issues in the past few years especially during heavy rainfalls, and for this reason, its condition has been regularly monitored due to the importance of the adjacent traffic route. A block failure occurred at the study area in January 2013 during heavy rainfall. The rock mass in the failed area posed a threat to the serviceability of the road, and its stability became a concern for the local community. Figure 7.25 compares the failed rock mass with the picture taken during the 2012 pre-failure site investigation.
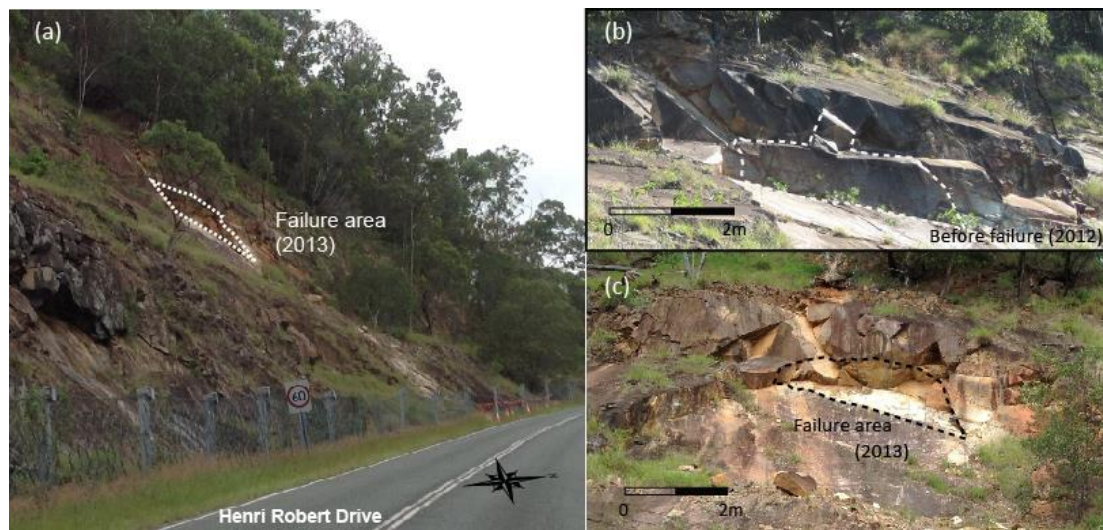
Fig. 7.25 Overview of the study area (a), before failure (b) and enlarged image of the failed area (c)

Field observations indicated that the rock in each section was relatively hard and slightly weathered; with most of the joints found to be either planar or undulating without cohesive infill. The rock mass generally consisted of polygonal blocks with the average block volume being in the range of 0.4~1.8 m^3. Several samples were collected for point load tests to estimate the strength of the rocks. From the obtained data, the average unconfined compressive strength (UCS) of 59 MPa was calculated using the empirical correlations between UCS and the point load index proposed by Look and Griffiths (2001) for the rocks in the Gold Coast area.

7.4.3 Photogrammetry survey

Photogrammetry was employed to produce 3D models of the slope and determine the characteristics of blocks and discontinuities. Two images were captured at two camera positions using a Nikon D7000 camera with a 24 mm lens. The computer code "Sirovision" (CSIRO, 2012) was then used to analyze the images and create 3D models of the slope. Sirovision requires the approximate target distance (i.e., the distance between the camera locations and the rock slope) or the baseline length (i.e., the distance between the two camera positions). The camera height above the ground was also determined by a measuring tape. Because the slope was inaccessible due to the safety barrier along the road, the measurements for photogrammetry were performed by measuring the distances and heights of specific target points on the slope using a laser range finder. The accuracy of range finders, as stated by the manufacturers, is reported as measurement errors ranging from 0.1 to 3% (Wing et al., 2004).

In this study, the accuracy of the measurement was evaluated by comparing the measurement values of the range finder to the measured distance (from a column of the barrier to the range finder) by a measuring tape. The result shows that the measurement using the laser range finder produced around 1.6% of measurement error as presented in Table 7-11. The slope height was calculated as schematically shown in Figure 7.26.

Geo-referencing was performed by measuring the bearing (azimuth) of each camera position to the center of the slope (using a geological compass) and determining the coordinates of the camera position (using a GPS device), following the procedure described by CSIRO (2005). Figure 7.27 (a) shows an image of the geo-referenced 3D model which is taken in the direction of the photograph (N82˚W). 35 joint data were obtained from the 3D

model and plotted in a stereonet. The computer code "Dips ver. 5.0 (Rocscience, 2010)" was then used for the identification of the main joint sets based on the data distribution. Dip and dip directions of the main joint sets are summarized in Table 7-12. Potential failure modes were identified based on the direction of the slope cut as presented in Figure 7.27 (b). According to the results from kinematic analysis, wedge slides on the intersection line of J1 and J2, and planar sliding modes along the joints J3 and J4 were feasible.
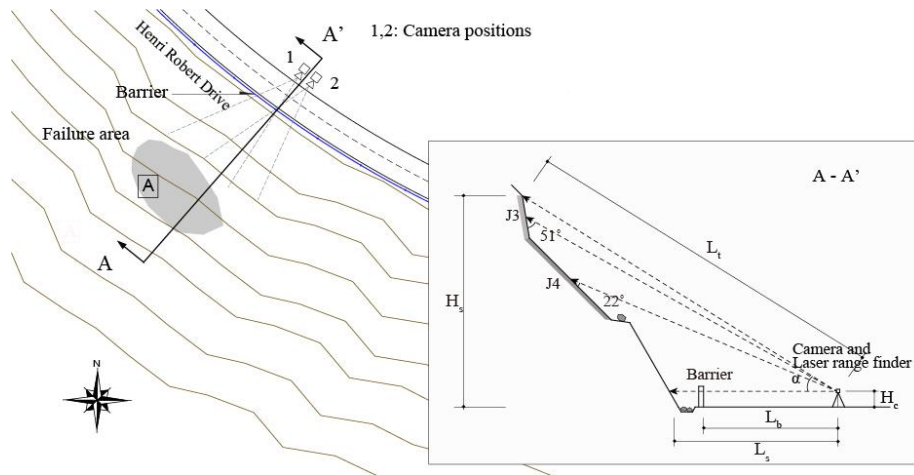
Fig. 7.26 Photogrammetry and survey setup

Table 7-11 Summary of measured values for photogrammetric survey

Measurement	Measurement tape (m)	Laser range finder (m)	Errors (%)
Distance (camera/barrier), L_b	12.2	12.0	-1.6
Distance (camera/slope face), L_f	-	15.9	-
Distance (camera/top of failure area), L_t	-	33.4	-
Baseline length (between cameras)	4.0	-	-
Height of camera, H_c	1.5	-	-
Height of slope, H_s	-	21.0 (calculated)	-

Table 7-12 Summary of discontinuity sets in failure area

Joints	Number of data	Dip, ° (mean)	Dip direction, ° (mean)	Joint spacing, m (mean)
J1	10	42 – 51 (47)	0.7 – 11 (3)	0.4 – 0.8 (0.6)
J2	10	43 – 74 (60)	107 – 130 (123)	0.4 – 0.7 (0.6)
J3	10	58 – 75 (66)	34 – 50 (42)	0.3 – 0.5 (0.4)
J4	10	30 – 33 (31)	17 – 37 (27)	0.3 – 0.8 (0.4)
Failed slope	-	70	82	-
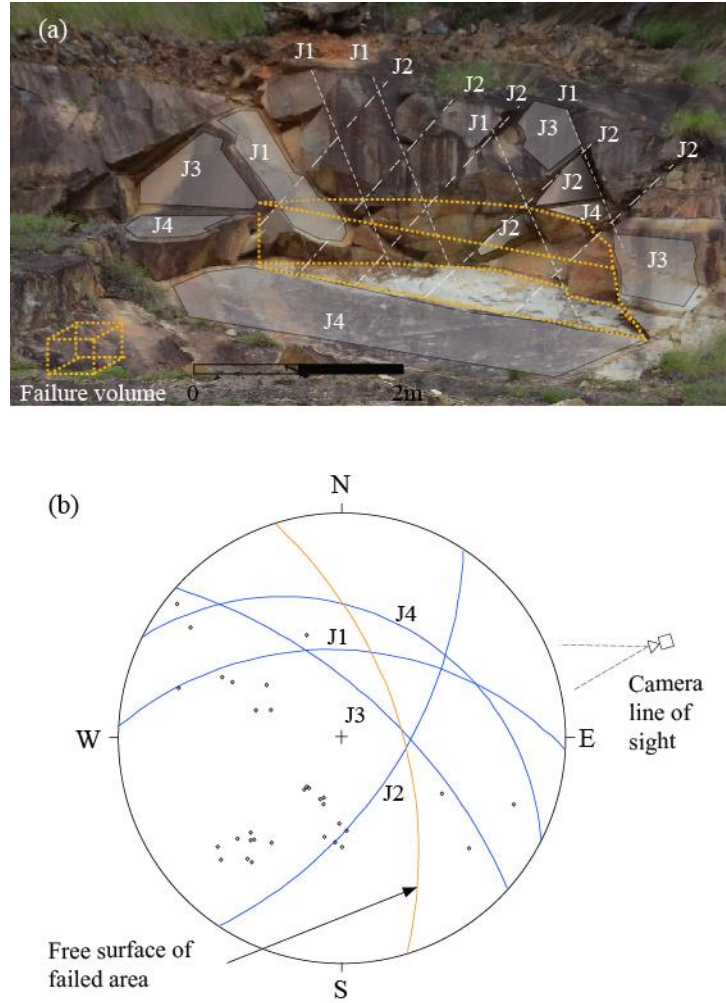
Fig. 7.27 3D surface model and main joint sets identified by using "Sirovision" (a) and stereonet projection (b) of the main joint sets

7.4.4 Friction angles of joints obtained from photogrammetric JRCs

JRC is an important parameter that contributes to the overall friction of joints. JRCs of the major joint sets were obtained from the 3D photogrammetry model. Sirovision computes the JRC values using the functions suggested by Maerz et al. (1990) and Tse and Cruden (1979). The functions are presented in Eq. (2-17) ~ Eq. (2-20) in Chapter 2. Using the equations, JRC values at ten different locations on each joint set in the failure area were obtained from the roughness profiles which were extracted from the 3D image. It was found that the range of JRC obtained from J4 showed considerably lower values than other joints as shown in Table 7-13. The lower values may be attributed to limitations of photogrammetry survey according to surveying conditions.

Firstly, the resolution of image was relatively low due to the far distance from the slope (Fig. 7.27 and Table 7-11) which created an image with a large pixel size (2.9mm / pixel). Considering the typical size of a profile gauge (1mm interval), smaller pixel size of images (less than 1.0mm/pixel) is preferable to produce accurate value of roughness parameters, such as Z_2 and SF. Haneberg (2007) stressed the importance of image density to estimate JRC values from 3D models.

Secondly, the values can be affected by a potential orientation bias which means an occlusion when the vertical line-of-sight of the camera is close to parallel to an upward discontinuity (Sturzenegger and Stead, 2009). The inclined roughness profiles may calculate underestimated values of JRC in photogrammetry methods as studied by Hong et al., (2006). Indeed, the vertical line-of-sight of the camera made an acute angle (around 22˚) with the dip angle of J4 as shown in Figure 7.26. However, as planar sliding along the joint J4 was considered as the primary failure mechanism, the range of JRC for J4 (0.3 ~ 7.3) was selected to investigate the friction angles of the joint sets (Table 7-13).

Using the range of JRC values, friction angle of the joints was calculated using the Barton's empirical equation (Eq. 7-16, Barton et al., 1985) for parametric analyses which will be mentioned later on. The range of residual friction angle (ϕ_r) was assumed from the test results performed by Barton (1973).

$$\phi = \phi_r + JRC_n \log_{10}(\frac{JCS_n}{\sigma_n}) \qquad (7\text{-}16)$$

where, ϕ_r= residual friction angle of joint; JCS = joint wall compressive strength; σ_n = normal stress acting on the joint plane was calculated using the average height of the blocks. Results from point load tests were utilized to estimate the joint wall compressive strength (JCS). Using the Barton's equation, the friction angle of joints considering JRC values was estimated to be from 25˚ to 55˚ as shown Table 7-14.

Table 7-13 JRC values obtained from Sirovision

JRC	J1	J2	J3	J4
Maerz (1990)	11.2 – 18.9	10.8 – 19.2	15.7 – 19.8	1.6 – 5.5
Tse and Cruden (1979)	12.3 – 18.9	12.9 – 19.6	15.2 – 15.1	0.3 – 7.3

Table 7-14 Range of friction angle of joint considering JRC values

Parameters	Values
Residual friction angle of joints (ϕ_r°)	25 – 35
JCS (MPa)	23 – 40
JRC	0.3 – 7.3
Calculated values of joint friction angles (ϕ°)	25 - 55

7.4.5 Basic principle of block theory

Block theory utilizes a kinematic approach to identify the removability of a block bounded by an arbitrary number of surfaces, in addition, to finding the applicable failure mode and the state of static equilibrium (Goodman and Shi, 1985; Hatzor and Goodman, 1997). The objective of block theory is to find potentially unstable blocks that can slide/move during excavation. There are five block types considered in block theory, as illustrated in Figure 7.28.
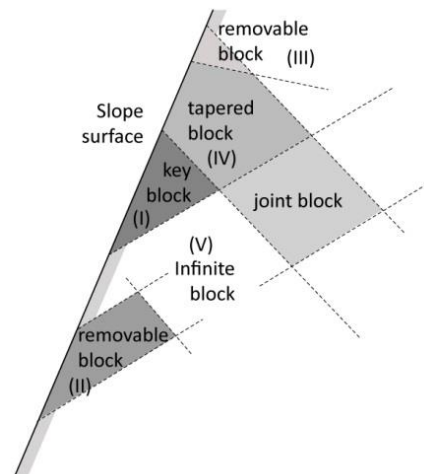
Fig. 7.28 Types of blocks considered in block theory (Goodman and Shi, 1985)

An infinite block (V) poses no hazard during excavation, while finite blocks are divided into removable (I-III) and non-removable (IV) blocks. The removable blocks can exist in the forms of tapered blocks (III), potential key blocks (II), and key blocks (I). When the rock mass is excavated, it is the key block/s that will first slide along discontinuities, a process that may cause failure of other blocks.

Using block theory one can identify the key block (type I), and its mode of failure. To achieve this task, the following assumptions are made (Goodman and Shi, 1985): (1) all

171

joint surfaces are perfectly planar, (2) joints are continuous within the blocks, (3) blocks are rigid, and (4) all failures occur along the initially designated discontinuities. Using a stereonet projection method, the removability of blocks then can be determined.

Figure 7.29 presents an example of a joint pyramid bounded by three joint sets and one free surface/plane that will be used to briefly explain the principles of block theory. The joints (J1, J2, and J3) are first plotted on stereographic projections using their dip and dip direction. According to block theory, each region is termed a "joint pyramid" (JP) and it is identified by a three-number code (Fig. 7.29) relating to which side of the joint plane the block resides in space. The portion of the circle surrounded by joint planes represents a JP. The number '0' indicates the block is above the joint plane while a number '1' means the JP is below the joint plane. In Figure 7.29, the JP code 001 indicates that the joint pyramid is above joint 1 (J1) and joint 2 (J2) but below joint 3 (J3). According to Goodman and Shi (1985), if a joint pyramid (JP) is included entirely in a free plane (dotted line in Fig.7.29) of excavation, the block is removable. Thus, in the example presented in Figure 7.29, the block coded JP001 is removable.
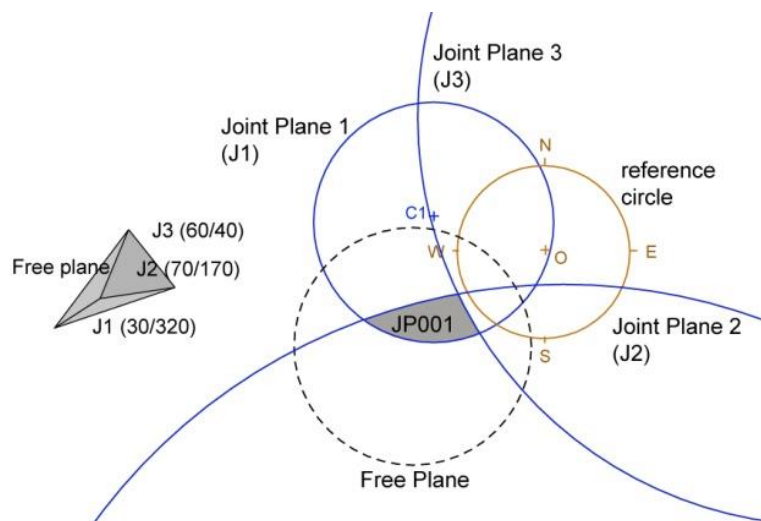
Fig. 7.29 Identification of removable blocks using 3D stereographic projection

Once a block has been identified as removable, it is necessary to determine what kinematic mode of failure such as planar or wedge are possible based on the block geometry and orientation of the forces being applied to the block. Then limit equilibrium analysis can be performed to assess the stability of this block and obtain the safety factor of the whole rock mass.

7.4.6 Theoretical analysis (key block analysis)

Using the analysed joint structure, the removable blocks were analysed with the friction angles in the range of JRC values based on key block theory. Sixteen blocks were analyzed for the failure area the results of which are summarized in Table 7-15. Four major joint sets (J1-J4) together with the slope surface (the dashed line in Figure 7.30 (a)) produced three joint pyramids (JP) coded 0001, 1000 and 1001 which were entirely located inside the slope circle. These blocks were considered to be removable following the block theory concept.

To back-calculate the safety of the removable blocks, a safety factor analysis, which defines the relationship between the resultant force and the effective strength in the direction of sliding, was carried out. This analysis was performed for the dominant plane sliding along the joint J4. Figure 7.30 (b) graphically represents the shape of removable blocks obtained from the results of block theory analysis. The shapes of vulnerable blocks were also identified based on the 3D models of the failed slope area. Single face sliding (planar mode) along the intersection of J4 and J3 was identified for the failure area and the plane sliding along J4 could be the dominant failure mode for the failure area.

Using the equilibrium equation (Eq. 7-18) (Goodman and Shi, 1985), the net of sliding force (F) was computed. The calculation was performed with a different range of friction angles from 25˚ to 55˚ according to the results of the JRC measurements (Table 7-14). A positive F corresponds to a key block (type I) while a negative F defines the removable block (type II). Table 7-16 summarizes the results of this analysis using different friction angles. The net of sliding forces indicates negative values when the friction angle is more than 35˚. Thus, when the friction angle becomes 35˚, JP 0001 changes its block type from key block (type I) to potential key block (type II) as shown in Table 7-16.

$$F = W\sin\alpha_i - W\cos\alpha_i\tan\phi_i \quad : \text{For single face sliding} \qquad (7\text{-}17)$$

where, W = the weight of a block; α_i = dip angles of plane i; ϕ_i= friction angles of plane. The stability of key blocks was assessed using the ratio of the resisting and driving forces. In case of a single plane sliding, the safety factor of key blocks was calculated as follows (Qingyan and Helin, 2011):

$$F_s = \frac{W\cos\psi_p\tan\phi + cA}{W\sin\psi_p} \qquad (7\text{-}18)$$

where, Ψ_p = the dip of the sliding plane; c = cohesive strength of joint; A = the area of the joint; W = the weight of the sliding block; ϕ = the friction angle of joint.
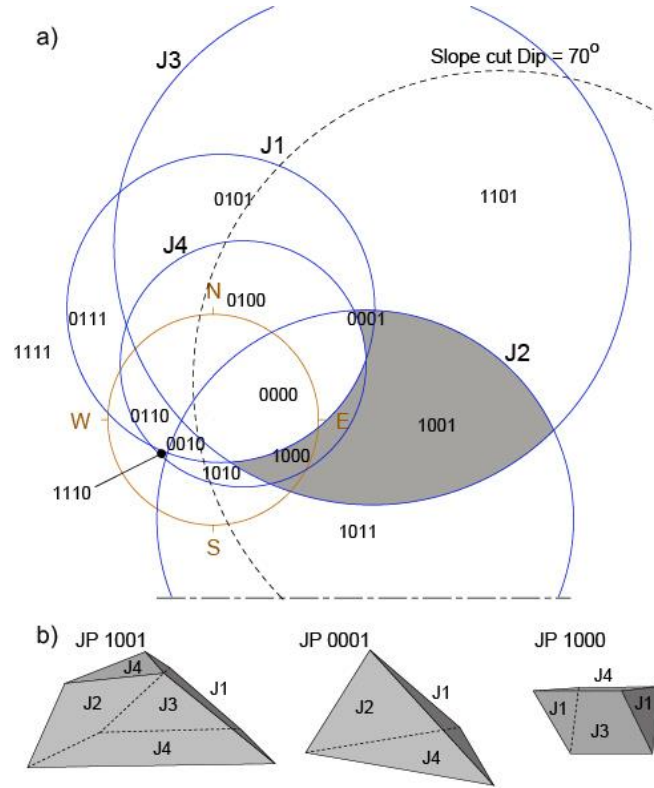
Fig. 7.30 Identification of removable blocks using stereographic projection (a) and the removable blocks (b)

Assuming the sliding plane has no cohesive component, Eq. (7-19) can be modified to include the surface roughness of joints using the Barton's joint shear strength equation (1976).

$$F_s = \frac{\sigma \tan\left(\phi + JRClog_{10}\left(\frac{JCS}{\sigma}\right)\right)A}{W sin\psi_p} \qquad (7\text{-}19)$$

where, JCS = the compressive strength of joints; σ = normal stress acting on the sliding surface. The effect of water pressure on the safety of the key blocks was considered by investigating the water force acting in the tension crack and also in the bedding plane. The safety factors were calculated using the ratio of the resisting and driving forces (Wyllie and Mah, 2004).

Table 7-17 summarizes the obtained data in the form of safety factors representing likelihood of the key block sliding along the joint J4 for different values of joint friction.

When the slope is saturated, the block is unstable even the friction angle is increased up to 40˚. The calculation shows that the key blocks are stable when the friction angle of joint is 35˚ in dry condition. However, in saturated conditions, the effective friction angle to keep stability is around 45˚. This indicates that this result is consistent with the field observations (the blocks indeed failed during heavy rainfall).

Table 7-15 Identification of block types with two repeated joint sets

Infinite	Finite	
	Tapered	Removable
0111, 0110, 0010, 1110, 1010, 0000, 1011, 1101, 1111, 0101, 0100	0011, 1100	0001, 1000, 1001

Table 7-16 Results of block analysis with different friction angles

Friction angle (ϕ,°)	Sliding plane	Net sliding force (F)	Key block (type I)	Potential key block (type II)
25	J4	0.12 W	1001, 0001, 1000	-
30	J4	0.02 W	1001, 0001, 1000	-
35	J4	-0.10 W	1000	1001, 0001
40	J4	-0.20 W	1000	1001, 0001
45	J4	-0.34 W	1000	1001, 0001
50	J4	-0.51 W	1000	1001, 0001
55	J4	-0.71 W	1000	1001, 0001

Table 7-17 Safety factors of key blocks

Friction angle (ϕ,°)	Sliding plane	Safety factors (key blocks)		Safety factors (3DEC)
		Dry	Saturated	
25	J4	0.78	0.52	0.71
30	J4	0.96	0.64	0.88
35	J4	1.17	0.78	1.08
40	J4	1.40	0.93	1.26
45	J4	1.66	1.11	1.53
50	J4	1.98	1.33	1.83
55	J4	2.38	1.59	2.19

7.4.7 Numerical analysis (3D distinct element method)

In order to investigate the failure mechanism of the rock mass, a 3D numerical analysis was carried out using a three dimensional distinct element code, 3DEC ver.5.0 (Itasca Consulting Group Inc., 2013) which can simulate large displacement and rotation of individual blocks surrounded by discontinuities. This code supports simulations of blocky structures in three dimensions and this code is suitable for the simulation of joint movement induced by the changes of the friction angles of joints. The geometry of the numerical model was created using coordinates obtained from the photogrammetry 3D model and the scale of the failure area was constrained by the pre-failure photographs in 2012 and the debris at the base of the slope. 3D models in the upper part of the failure range could not sufficiently have been created because of the image noise caused by surrounding leaves and trees. Due to the limited geometry information from the pre-failure photographs and the insufficient data of the photogrammetric 3D model, the numerical model was created with simplified block shapes and restricted to the failure range.

The dominant 4 discontinuity sets were generated in the rock mass with an assumption that the joints obtained from the 3D photogrammetry model are fully persistent through the investigated rock mass. The discontinuity spacing for the failed area was also modeled according to the data measured from the 3D model. The origin of the joint sets in the numerical model was determined by trial and error comparing the locations and directions of the joint sets with the 3D model. Figure 7.31 presents the numerical model of the failed slope.

The analyses were performed on the assumption that there is no movement derived from the surrounding blocks. Thus, the model has fixed blocks which represent the existing rock structure on the slope, as well as kinematically free blocks which could develop sliding failure. A series of simulations investigated the safety of the jointed rock mass when the friction angles along the joints were reduced from $55°$ to $25°$. In the numerical models, joint stiffness properties were estimated using the equations suggested by Barton and Choubey (1977). The shear stiffness, K_s values are calculated by Eq. (7-3) in Section 7.2.6. In the calculations, the normal stress (σ_n) acting on the joint plane was calculated using the average height of the blocks. Table 7-18 summarizes the properties of rock joints adopted for the numerical analyses.
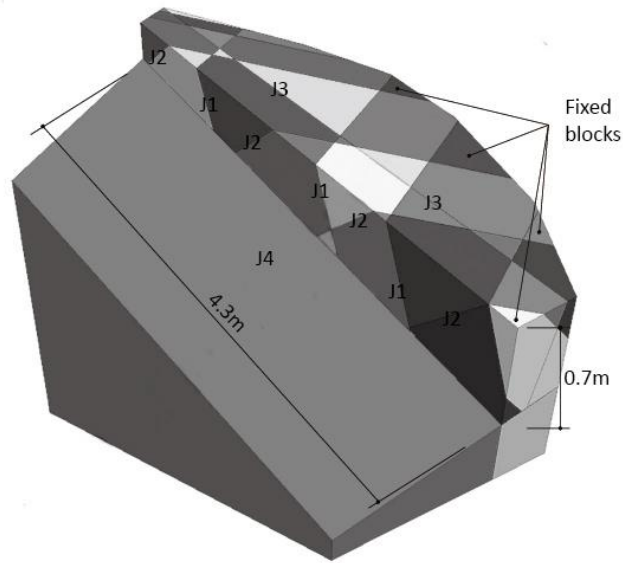
Fig. 7.31 Dimensions and geometry of the 3DEC model

The results indicated that the overall stability of the jointed rock mass was controlled by the friction angle of joints (Table 7-17). The safety factor (SF) calculated by 3DEC decreased with a reduction in joint friction angles. Also, the values of SF are in agreement with the data obtained through the key block analysis, which indicate the range of values between dry conditions and saturated conditions. In the simulation, the critical friction angle (35˚) is close to the dip angle of the joint J4 (32˚). At the condition of failure, the mechanism appeared to be planar sliding. Along the joint J4, sliding of blocks with rotation started from the upper portion of the slope. This result can be due to the fixed block located in the lowest portion (block no.9 in Figure 7.32 (a)) which remained on the slope after the failure. In addition, this was attributed to the dip direction of the flat joint plane oriented northeasterly 32˚.

The results are consistent with the calculation obtained by block theory. Note that the maximum displacement vectors are associated with the key blocks as shown in Figure 7.32 (a) ~ (d). It was observed that the displacement started from the blocks shaped JP 1001 and JP 0001 (block no. 1, 3, 4, 6 in Figure 7.32). Then, the sliding of 2, 5 and 7 blocks (tapered) occurred due to the space created by the first sliding blocks.

Table 7-18 Rock and joint properties for numerical model

Rock density (kg/m³)	Friction angle (ϕ, °)	Shear stiffness of joints, K_s (MPa/m)	Normal stiffness of joints, K_n (MPa/m)
2,700	25 - 55	40	120
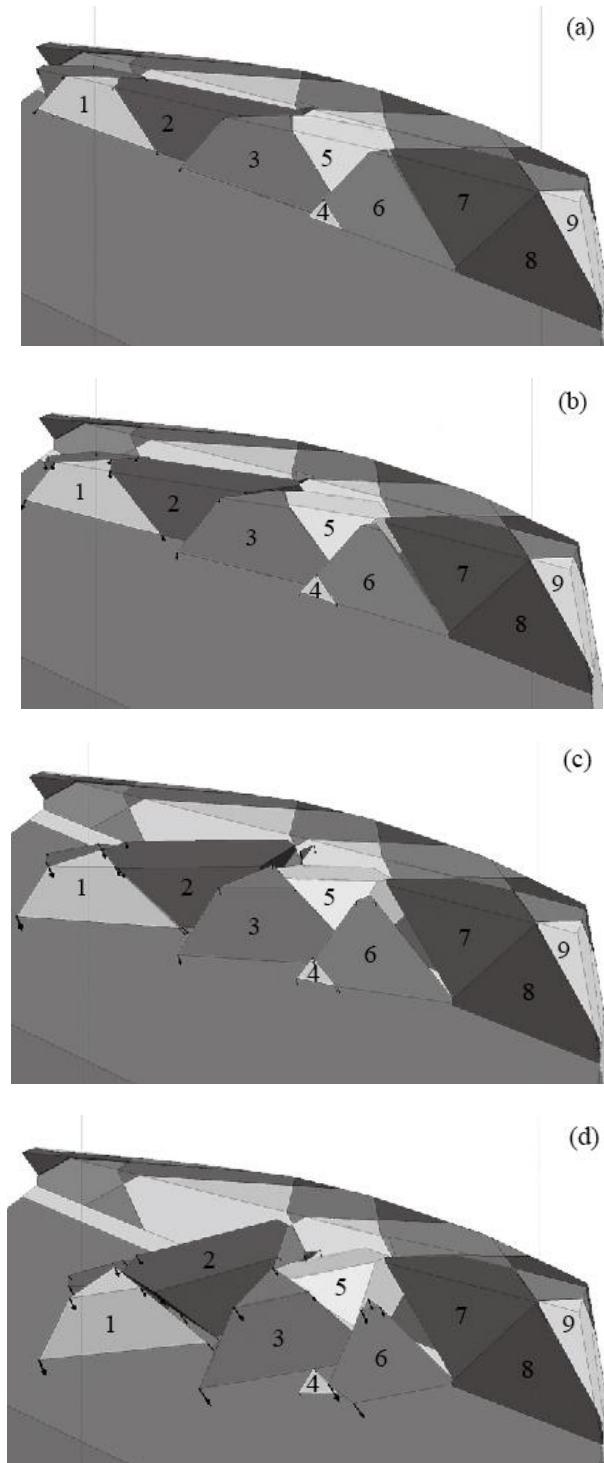
Fig. 7.32 3DEC simulation results at 10,000 (a), 15,000 (b), 20,000 (c) and 25,000 cycles

7.4.8 Conclusion

In this study, photogrammetric JRC values are employed to estimate the range of friction angles and the strength of joint sets of a natural rock slope. Safety factors of the rock blocks were computed by both analytical and numerical approaches. The key block theory was applied to back calculate the critical friction angle of the joints on the locally failed blocks. Parametric numerical analyses were also performed using a DEM model to assess the critical friction angle of the joint sets. Based on the obtained results, the following conclusions can be drawn:

- Photogrammetry method was effectively used to obtain roughness data on the remained joint plane from the failed rock mass. To identify the orientation of the joint sets in the already failed rock mass, the 3D model of the remained rock mass was utilized. The obtained joint orientation was visually verified by using the photographs taken from a pre-failure investigation.

- The failure modes were successfully simulated by both the block theory and the 3D DEM model. The safety factor of key blocks was greatly reduced when pore water pressure was considered and the critical friction angle to satisfy the stability in the saturated condition increased from 35° to 45°. The analyses showed that the failure was occurred in the range of friction angles between 30° and 45°. The photogrammetric JRC ranges reasonably estimated the range of friction angle (25° ~ 55°).

- The reliability of the collected and analysed data was totally dependent on the accuracy of the 3D surface model. The camera-to-object distance is relatively large (33 m) and the section of interest is highly positioned to be taken in orthogonal direction. These factors can cause planning errors of the 3D photogrammetry models. It is thus noticeable that the accuracy of the JRC values can be affected by the angles between the vertical line-of-sight of the camera and the joint dip angles as well as the resolution of the image.

7.5 Case study 4 (3D, 2D rock fall analysis)

A part of the study in this section was published in Natural Hazards journal as follows:

Dong Hyun Kim, Ivan Gratchev, Jeroen Berends, Arumugam Balasubramaniam (2015) Calibration of restitution coefficient using rockfall simulations based on 3D photogrammetry model: a case study. Natural Hazards, 78: 1931-1946.

7.5.1 Introduction

Rockfall hazards have been generally quantified using two (2D) and three (3D) dimensional rockfall simulations based on in situ rockfall experiments. Traditionally, 2D analyses were used successfully for rock slopes by many researchers (Pfeiffer, 1989; Azzoni et al., 1995; Stevens, 1998). However, this approach works well only in cases where the computed sections are a representative of the rockfall trajectories. This is due to the actual path of rockfall being varied depending on the shape of the falling body and topography of slopes.

Thus, the use of 3D rockfall simulations, such as CRSP (Pfeiffer, 1989; Andrew et al., 2012), STONE (Guzzetti et al., 2002), RAMMS: Rockfall (Christen et al., 2010) and Trajec3D (Basson, 2012) can overcome the limitations of 2D simulations by allowing the rock blocks to move on three dimensional surfaces. The 3D analysis requires accurate topography of slope surfaces. Recent field survey data, remote sensing techniques such as LIDAR (Light Detection and Ranging), photogrammetry and TLS (Terrestrial Laser Scanning) are used to provide 3D slope models for the rockfall simulations (Dorren et al., 2006; Giacomini et al., 2012; Harami et al., 2013; Giovanni et al., 2014).

Throughout the rockfall simulations, the most important parameter for reliable prediction of rockfalls is the coefficient of restitution, which controls the trajectories of the rock blocks. In general, there are two approaches to assess the parameter: by back analysis of field tests (Azzoni et al., 1995; Agliardi & Crosta, 2003) or by calculation through laboratory tests (Chau et al., 2002; Buzzi et al., 2012; Asteriou et al., 2012). In fact, laboratory tests have limitations such as varying in scale effects and different material types (Chau et al., 2002; Buzzi et al., 2012). Furthermore, even though back analysis is based on field rockfall tests which can lead to better predictions to obtain practical values of the coefficients for the slope materials, an investigation using many high speed cameras and heavy rock samples can make it difficult to conduct tests in the field due to the high costs of equipment.

This section presents a case study to obtain the coefficients of restitutions through a combined method with field rockfall tests and a photogrammetric 3D surface model. The performed simple field tests could be used as reliable guidelines for predicting rockfall trajectories as well as obtaining practical coefficients of restitutions. Then, the rockfall behavior and the coefficients for the slope material are back-calculated by means of simulations based on accurate 3D rock slope models. The friction angles of the rock surfaces, which were calculated based on the JRC values obtained from the photogrammetric 3D models. The JRC values were verified by the measured values. This combined method is feasible when establishing methods for mitigation of rockfall hazards.

Field rockfall tests using ten collected rocks from the site were performed at an excavated rock slope. Trajectory and elapsed time of each rockfall event were obtained by analyzing the results from video recordings using a normal HD video camera. To assess the coefficient of normal restitution and friction angle, Schmidt hammer tests and roughness profile measurements were carried out on the slope. A photogrammetry survey was carried out to create 3D surface models and 3D, 2D rockfall simulations were performed based on the 3D slope surface models. Rockfall trajectories were produced to reflect the shape of the slope surface. The coefficients of restitution of the rock material were then back-calibrated by parametric rockfall simulations, comparing them with the field data.

7.5.2 Site overview

The study area is an excavated slope located in Brisbane, Australia. The study slope is up to approximately 20 meters in height and 120m in length and the slope is prepared for the installation of a drapery system for rockfall protection (Fig. 7.33). The slope comprises weathered metasiltstone and metasandstone from the Neranleigh-Fernvale beds (Gratchev et al., 2013; Willmott, 2010). The weathered rock can range from a moderately to slightly weathered grade, based on Schmidt hammer rebounds according to the weathering classification system suggested by Arikan et al. (2007).

181
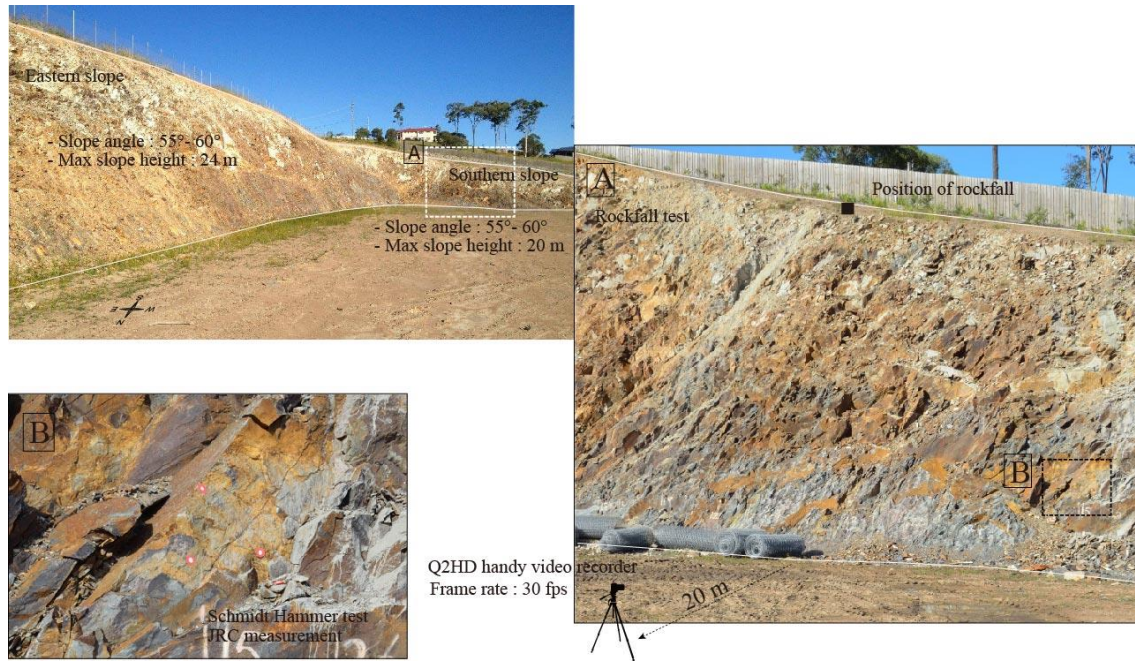
Fig. 7.33 Overview of the study area

To identify dynamic and strength properties of the slope materials, Schmidt hammer tests were performed to the discontinuity surface of the slope and collected rock samples. The results of 40 Schmidt hammer blows for both the field tests and the laboratory tests are shown in Table 7-19. It has been reported that the Schmidt number of the slope materials showed a good relation with the coefficient of normal restitution (R_n) (Peng, 2000). In general, the R_n is an important dynamic parameter of slope material for rockfall simulation and is defined as the ratio of normal component of the rebound velocity to the approach normal velocity. The relation between R_n and Schmidt rebounds was suggested by Peng (2000) through a series of laboratory rockfall tests, and expressed as:

$$R_n = -0.110 + 0.00919N_1 + 0.00392N_2 + 0.00358A \qquad (7\text{-}20)$$

where, N_1/N_2 are Schmidt numbers of rock slab and rock blocks and A is the slope angle.

This regression was obtained from the data using various 23 different rock types of igneous, metamorphic and sedimentary rocks ranging from hard rocks to soft rocks. Based on the assumption that the material of the study area is categorized in the sedimentary rocks, the R_n value was obtained by the empirical equation (Eq. 7-20) as shown in Table 7-19. Unconfined compressive strengths (UCS) were also calculated using relations of the Schmidt hammer rebound values with uniaxial compressive strength suggested by Katz et al.

(2000) (Eq. 7-21), where x is Schmidt rebounds. The unconfined strengths of the rocks are presented in Table 7-19.

$$UCS \ (MPa) = 2.208 \ e^{0.067x} \qquad\qquad (7\text{-}21)$$

Table 7-19 Results of Schmidt hammer tests

Location	Schmidt rebounds	Unconfined compressive strength (UCS, MPa)	Coefficient of normal restitution (Rn)
Slope surface	36 – 46 (mean: 40.2)	37.7	0.58
Rock blocks	30 – 38 (mean: 32.0)	27.2	

7.5.3 Roughness profiles and JRC values

To estimate the friction angle of rock surface, a standard method of joint roughness coefficient (JRC) determination was performed using a profile gauge (L=25cm). JRC values, which vary from 0 to 20, are obtained through the comparison of the measured joint surface geometry with the one presented in the Barton's standard profile chart (Barton and Choubey, 1977). The measurements were carried out between targets on a joint surface where the manual measurement was possible (Fig. 7.34).

Measured profiles are demonstrated in Figure 7.35. The coordinates of the measured profiles were digitized using AutoCAD program and the JRC values were estimated using a roughness parameter Z_2, and the regression equation suggested by Tse and Cruden (1979) (Eq. (2-4) and Eq. (2-5) in Chapter 2). The estimated JRC values are ranged from 11.1 to 14.3.
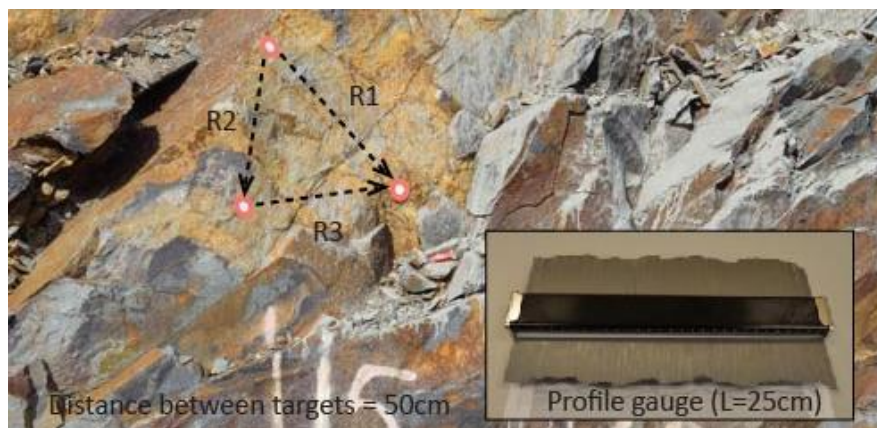
Fig. 7.34 Location and results of JRC measurement
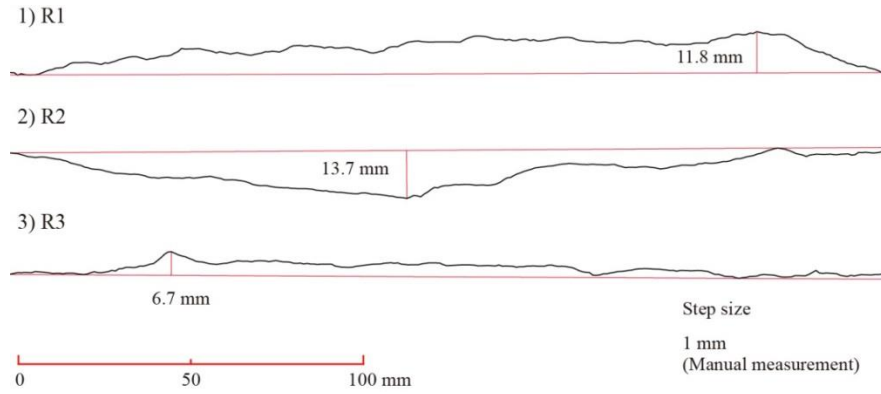
Fig. 7.35 Measured roughness profiles with 1 mm step sizes

7.5.4 Rock fall experiments

Rockfall experiments were carried out on a cut slope of the site (Fig 7.33). A total of 10 rocks, which were collected from the site, were manually thrown from the top position the slope. Horizontal and vertical falling distances from the toe of the slope were measured and the motion of falling rocks was recorded by a HD handy video recorder with an operating speed of 30 fps, which was positioned in front of the slope (Fig 7.33). The analysis of video recordings allowed for determination of the numbers of clear collisions and calculation of the arrival time of falling bodies. The analyses were focused on the recognition of trajectory directions, number of bounces and arrival times based on the observation.

The shape of rock directly affects the rockfall trajectory. Leine et al., (2013) presented the influence of rock shapes on the rolling behavior of bodies introducing the 3D rockfall module 'RAMMS'. In the simulation, an arbitrary polyhedron block model was used as a falling body based on a high resolution digital elevation model. To describe the rock shapes of the collected rocks of this research project, a three dimensional shape index (γ) developed by Wang et al., (2003) was used. The index which was the ratio of block volumes to the sphere volumes with a diameter equal to the maximum block size, could be estimated by Eq. (7-22).

$$\gamma = \frac{6 \cdot V}{\pi \cdot l_{max}^3} \qquad (7\text{-}22)$$

where, γ = 3D rock shape index, V = volume of a block, l_{max} = the maximum distance between two vertex points on the block. Figure 7.36 shows the rock blocks used for the rockfall tests. The blocks were collected near the slope of the site with consideration for the

184

range of the size of fallen rock fragment and the movability of specimens. The size and weight of the specimens are summarized in Table 7-20. The rock block shapes were then classified into five categories according to the shape index using Eq. (7-22). The collected rock blocks were labeled as 'Block' or 'Cube' shapes as shown in Table 7-20 and the examples of the measurement dimensions are shown in Figure 7.37.

Fig. 7.36 Collected rock blocks

Fig. 7.37 Examples of rock shapes and collected rocks

Table 7-20 Details of the rock blocks

Rock No.	Weight (kN)	Volume (V,cm^3)	Shape index (γ^*)	Shape descript -tion	Rock No.	Weight (kN)	Volume (V,cm^3)	Shape index (γ^*)	Shape descript -tion
1	62.5	2,360	0.37	Cube	6	10.0	377	0.21	Block
2	57.0	2,150	0.23	Cube	7	23.0	868	0.21	Block
3	12.5	472	0.18	Block	8	22.5	849	0.20	Block
4	22.5	849	0.26	Cube	9	19.5	736	0.15	Block
5	25.5	962	0.10	Block	10	36.0	1358	0.32	Cube

* $\gamma \leq 0.001$: Bar, $0.001 < \gamma \leq 0.077$: Plate, $0.077 < \gamma \leq 0.22$: Block, $0.22 < \gamma \leq 0.37$: Cube, $0.37 < \gamma \leq 1.0$: Sphere (Wang et al., 2003)

7.5.5 Behaviour of rock fall

General modes of motion of rocks during their descent on slopes are composed of free falling, rolling and bouncing phases based on slope gradients. In this rockfall test, the motions created various collision times through rockfall trajectories. It was observed from each rockfall test that the orientation of the joint sets at the impact points on the slope affected the trajectories of rockfalls. The lateral dispersion ratio (D_r) is a proportion of the lateral distance (D_H) of the rockfall paths from the center line as seen looking at the face of the slope to the length of the slope (L) as shown in Eq. (7-23). This definition of D_r is similar to the concept presented by Azzoni and Freitas (1995) and is schematically shown in Figure 7.38.

$$D_r = \frac{D_H}{L} \times 100 \text{ (\%)} \qquad\qquad (7\text{-}23)$$

In the field tests, the dispersion ratios (D_r) of rockfalls were in the range of 5 to 50%, which was much larger than the general dispersion ratio ($< 20\%$) suggested by Azzoni and Freitas (1995). This large percentage of dispersion can be explained by the orientation of dominant joint sets dipping to a northeastern direction influencing the rockfall paths. Thus, the final positions of falling rocks were located at the left side from the center line including the falling point ranging from 0.6 to 6.3 meters as described in Table 7-21. It was observed from the field tests that the collision numbers through the rockfall trajectories directly correlated with the modes of rockfall. Less impact numbers such as 2 or 3 showed bigger jumping heights after collision with extruded rock surfaces. In contrast, sliding and rolling movement were predominant when the rock path showed more than 5 impacts.
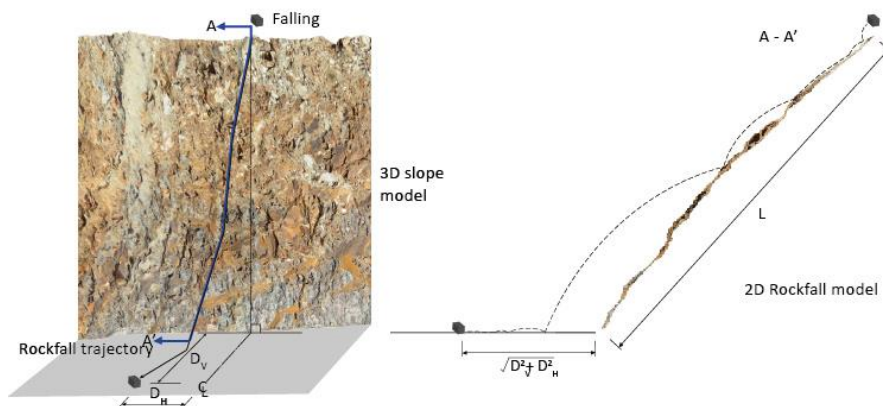
Fig. 7.38 Description of lateral dispersion (D_H) and extraction of 2D simulation section from 3D slope surface model

Rock shape was also a major factor influencing the direction of trajectory of falling rocks. Figure 7.39 indicates the relationships between the rock shapes and the rockfall behaviour. Even though the coefficients of determination, R_2, are relatively low, it can be said that the obtained linear regressions obviously indicate downward or upward trends according to the rock shape indices. Figure 7.39 (a) shows distances of falling rocks from the toe according to their shape indices. As rock shape index increased, the distances of rockfall rose. Similarly, The rocks categorized as cube shape ($\gamma = 0.23 \sim 0.37$) created higher lateral dispersion ratio of trajectories ranging from 31 to 51%, than the block shaped rocks ($\gamma = 0.10 \sim 0.21$) (Fig. 7.39 (c)). The rockfall mode was also associated with rock shape index. It was also observed that sliding and rolling modes are predominant when the rock shape indices were relatively less (Fig. 7.39 (b)).

Table 7-21 Results of rockfall tests

Event no.	1	2	3	4	5	6	7	8	9	10
Measured distance (m)										
- Vertical (Dv)	2.1	4.2	1.5	3.3	1.0	2.6	5.1	2.8	1.2	2.5
- Horizontal (DH)	5.8	6.3	1.2	5.1	2.1	0.6	2.8	2.5	2.8	3.9
- $\sqrt{D_V^2 + D_H^2}$	6.1	7.5	1.9	6.1	2.3	2.7	5.8	3.8	3.0	4.6
Lateral dispersion ratio (DH/L, %)	46.5	50.5	9.6	40.9	16.8	4.8	22.5	20.0	22.5	31.3
Number of collision	3	2	2	3	6	5	2	3	8	4
Arrival time (sec)	3.5	2.5	3.5	2.5	3.5	3.0	2.5	3.5	4.5	3.5
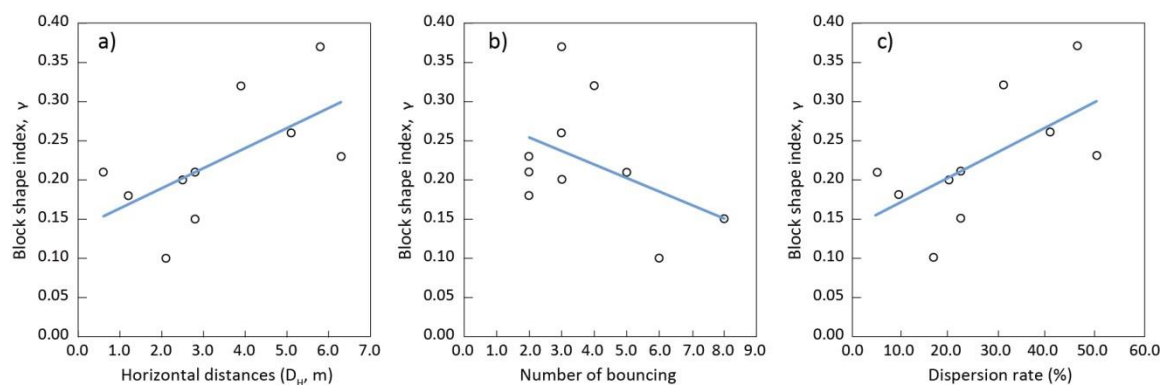
Fig. 7.39 Relation between block shape index and horizontal distance (a), collision numbers (b) and dispersion rate (c)

7.5.6 Photogrammetry survey

Geo-referenced 3D surface model were derived from the photogrammetry field survey. Target points were marked on an area as shown in Figure 7.34. The height of the section was almost same as the camera heights (Fig. 7.40). Geo-referenced 3D surface models were derived from the photogrammetry survey. The Nikon SLR D7000 with a 24 mm focal length lens was employed and two digital pictures were taken at two different distances from the rock slope as shown in Figure 7.40. The computer program, Sirovision was then used to build the 3D models. The large distance (L = 33 m) produced a 3D slope model with 1,620 pixels/m^2 for the entire slope height (Fig. 7.41). Using more than 1,000 joint orientation data generated from the 3D model, the orientations of joint sets were analysed. Computer code 'DIPS 6.0 (Rocscience)' which is designed for the stereonet plots based on geological data was used to define sets of the joint groups using mapping data obtained from the 3D model as presented in Figure 7.42.
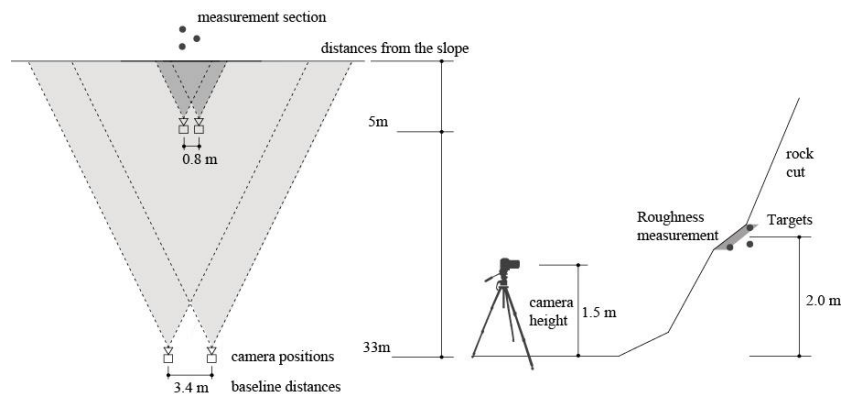
Fig. 7.40 Photogrammetry survey setup
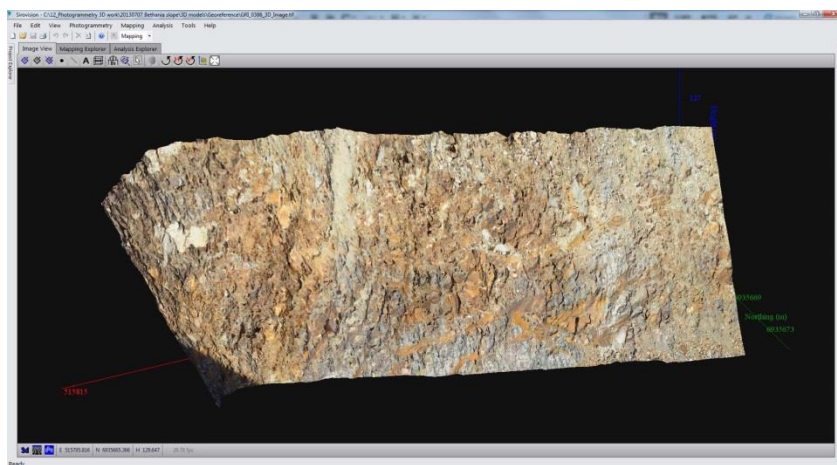
Fig. 7.41 A window shot of 3D model of Sirovision (taken from 33 metre distance)
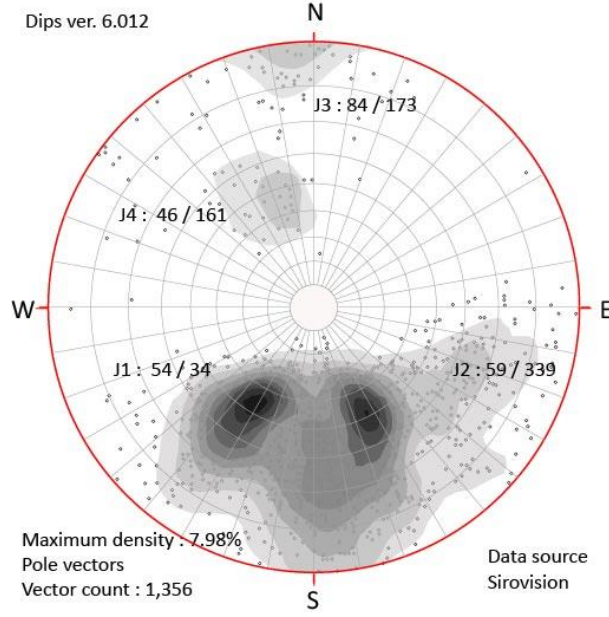
Fig. 7.42 Identified joint sets using DIPS 6.0

The slope gradient within the study slope varied between 50° and 60°. Ranges of dip and dip directions and joint spacing of the four prominent joint groups are presented in Table 7-22. Spacing of each joint set was obtained by measuring distances between joints on the 3D model to identify block shapes on the slope. As the dip direction of joint set 1 (J1) and joint set 2 (J2) face to the dip direction of the slope, it was expected that dip direction of the two prominent joints sets affect the directions of rock fall paths.

As rockfall events can be initiated by the detachment of rock fragments from their existing locations, characterizing the shape of distributed blocks on the slope surface can provide probable shapes of falling rock. Using the information of four joint sets, probable block shapes of the study slope were characterized by Eq. (7-24). To identify the rock shapes, block volumes were estimated using joint spacing and their orientations. Assuming that the main joint sets were persistent, in the cases that three or more joint sets are present, the block volume can be calculated using Eq. (7-24) proposed by Cai et al. (2004),

$$V_b = \frac{s_1 s_2 s_3}{sin\gamma_1 sin\gamma_2 sin\gamma_3} \qquad (7-24)$$

where, s_1, s_2, s_3 = spacing between discontinuity sets; $\gamma_1, \gamma_{2,}\gamma_3$ = angles between discontinuity sets. For practical purposes, this equation can be used to determine block sizes regarding the intersection angles between joint sets. In combination with four joint sets, using the average value of the joint orientation and distance data obtained from the 3D

189

surface model, block volumes were analyzed as summarized in Table 7-22. Based on this procedure, it was found that the estimated block sizes ranged from 0.04 to 6.45 m^3 and the block shapes were categorized as 'Sphere', 'Cube' or 'Block' shapes by the three dimensional shape index (γ).

Table 7-22 Results of block volume and shape estimation using 3D surface model

Plane	Dip (°)	Dip direction (°)	Joint spacing (m)	Block volume (V,m^3),	Shape index, γ	Shape description
Slope	55 ± 5	20 ± 10	-	0.04~6.45	0.08~0.82	Sphere / Cube / Block
J1	54 ± 15	34 ± 14	0.30~1.41			
J2	59 ± 17	320 ± 20	0.31~1.65			
J3	84 ± 7	173 ± 13	0.28~1.01			
J4	47 ± 5	162 ± 17	0.34~0.55			

7.5.7 Roughness investigation

The results of the details of the geo-referenced 3D models are presented in Table 7-23. The range of point intervals of the 3D models which are obtained from the images taken at 33 metres is from 7.7 to 14.3 mm whereas the step size of the roughness profiles of the 3D image is between 1.1 and 2.6 mm. As presented in Table 7-23, the 3D images taken at 5 metres produced much smaller step size of the roughness profiles. The difference of pixel size can be visually compared using the pixels of targets on the slope as shown in Figure 7.43 and 7.44. It can be found that the density of mesh in the area of a target in 5 metre distance is much higher than that of 33 metres.

Roughness profiles were extracted from the 3D models and the JRC values were calculated using the roughness parameter, Z_2 (Tse and Cruden, 1979). As presented in Table 7-24, the calculated JRC range obtained from far distance (33 m) underestimated the JRC values, while close distance (5 m) created a large bias from overestimation to underestimation. This tendency can be explained by the error factors of photogrammetry as mentioned in the Section 2.8. In the 3D model of 5 metre distance, it can be explained that data noise influenced the accuracy of the photogrammetric JRC data. Considering the orientation of the joint plane was not orthogonal to the camera direction, the influence of profile orientation can be also important to the accuracy of JRCs.
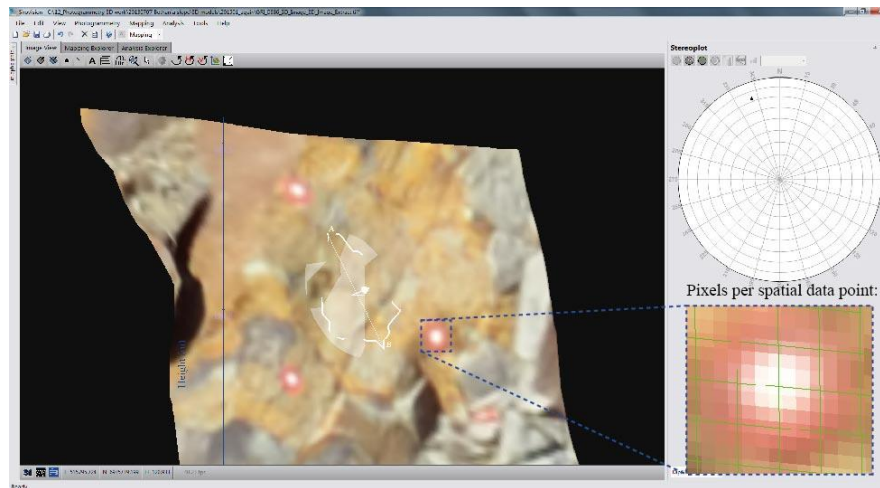
Fig. 7.43 Extracted 3D model for an area of interests and the image pixels of a target at long distance (33 m)
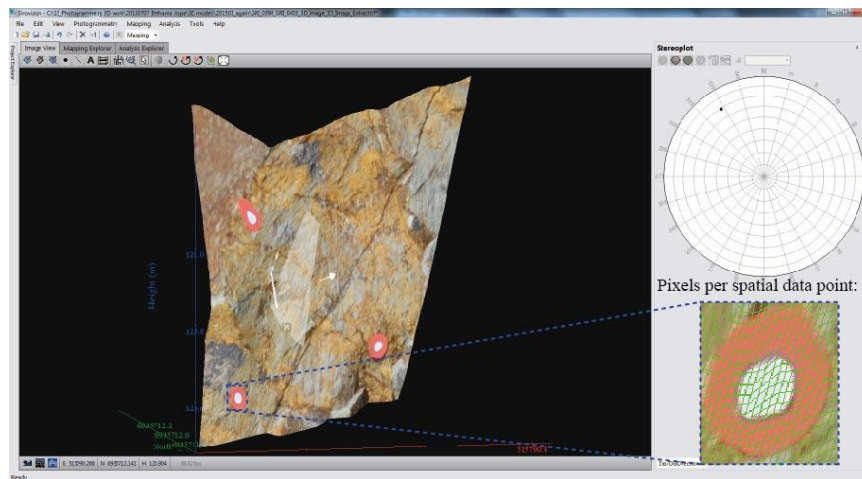
Fig. 7.44 Extracted 3D model for an area of interests and the image pixels of a target at close distance (5 m)

Table 7-23 Details of photogrammetry survey and density of 3D models

Item	3D image (L=33 m)	3D image (L=5 m)
Distances from targets (m)	33.0	5.0
Baseline distances (m)	3.4	0.8
Point intervals of 3D images (mm)	7.7 ~ 14.3	1.1 ~ 2.6

Table 7-24 JRC values according to the photogrammetric distances

Profiles	Distances (m)	JRC (Manual)	JRC (3D, 33m / 5m)	Error (%, 33m / 5m)
R1	33 / 5	15.0	11.8 / 12.9	78.7 / 86.0
R2	33 / 5	13.7	12.4 / 9.7	90.5 / 70.8
R3	33 / 5	10.1	10.2 / 18.3	100.1 / 181.2

7.5.8 3D Rockfall simulation

In this study, 3D and 2D rockfall simulations were performed and the 3D simulations were focused on evaluation of probable rockfall trajectories in accordance with the topography of the slope and back calculation of the coefficient of restitution values based on rockfall arrival times. The 2D simulation was used to analyze the energy, bounce and the location of the falling rocks using the analysis section obtained from 3D simulation and to back calculate the tangential coefficient of restitution. In the simulations two software programs were used and detailed information are shown in Table 7-25.

Table 7-25 Computer codes for rockfall simulation

Programs	Required data	Outcomes
Trajec3D (3D) (Basson, 2012)	3D surface model Rock shapes * Source area of rockfall Coefficients of restitution (COR)	Rock fall trajectories - numbers of collisions - horizontal displacement Rock arrival time Kinematic energy envelope
RocFall (2D) (Stevens, 1998)	Rock fall trajectories Initial velocity of rockfall Coefficients of tangential restitution Coefficients of normal restitution	Rock fall trajectories (Vertical) Rock travelling distances Kinematic energy envelope

* Applicable fall body shapes: Sphere, Cube, Plate and irregular blocks

The 'Trajec3D' software (Basson, 2012) was used for the 3D simulation. This program estimates rockfall paths using realistic slope topographies that can be created from remote survey techniques, such as photogrammetry and LIDAR. 3D coordinates of the georeferenced 3D surface model generated from 'Sirovision (CSIRO, 2005)' were imported to the program 'Trajec3D' to create the slope surface model. The coefficient of restitution (COR) in the program represents the ratio of velocities before and after the rockfall impact as indicated in Eq. (7-25),

$$COR = \frac{v}{V} \qquad (7\text{-}25)$$

where v : the velocity of the fall body after impact, V : the velocity of the fall body before impact. 'COR=1' shows that the impact is perfectly elastic so there is no loss of energy. 'COR=0' indicates that the impact is perfectly plastic.

In this study of the examined slope, a number of simulations were performed to back calibrate the coefficient of restitution (COR) from rockfall simulations. The COR values used in this parametric study were ranged from 0.3 to 0.9. The results of 'rock no. 2' in the field test were compared with the simulation results. In the simulations, cube shape was selected as a rockfall shape as classified using the rock shape index (Table 7-20).

The friction angle was calculated using Barton's empirical equation (Barton and Choubey, 1977). JRC values obtained from site measurement and the photogrammetric 3D model were used to estimate the friction angle as discussed in Section 7.5.7. In Eq. (7-26), the basic friction angle (ϕ_b) of 30˚ was obtained from a series of tilt tests using flat surface samples. Results from Schmidt hammer tests were used to estimate the joint compressive strength (JCS). Using Eq. (7-27), the friction angle of joints considering JRC was ranged from 30˚ to 40˚.

$$\phi_r = (\phi_b - 20°) + 20(r/R) \qquad (7\text{-}26)$$

Where, ϕ_b is basic friction angle estimated from tilt tests; R is Schmidt rebound on dry unweathered joint surface; r is Schmidt rebound on wet joint surfaces.

$$\phi = \phi_r + JRC \log_{10}(\frac{JCS}{\sigma_n}) \qquad (7\text{-}27)$$

where, ϕ_r is residual friction angle of joints; JCS is joint wall compressive strength; σ_n is normal stress acting on the joint plane. The input parameters used in the parametric study are presented in Table 7-26.

Table 7-26 Parameters in 3D rockfall simulation

Parameters	Unit	Value	Reference
Density of rock	kN/m^3	27	ASTM D5030
Block shape	-	Cube	Block shape index (γ)
Block size (cube length)	m	0.13	Equivalent length based on volume
Coefficient of restitution (COR)	-	0.3, 0.5, 0.7, 0.9	Range from intermediate to hard rock (Andrew et al., 2012)
Friction angle	°	30 ~ 40	Barton's empirical equation

As the three dimensional model simulated detailed slope geometry, the rock paths obtained from the 3D simulation were considerably varied with the positions of dropping points on the slope. However, it was also observed that the rockfall trajectory was controlled by the

orientation of the joint at the starting point. At the same starting points of rockfalls with the field tests, most rockfall paths headed towards the left side (Northeast) due to the orientation of the joint of dropping positions. Dip and dip direction of the joint indicates 44°/ 60° heading to northeast direction as shown in Figure 7.45. Therefore, the orientation of the joint at the starting point had a strong influence on the lateral dispersion rate. Even though similar trajectories were obtained from the same starting point, in the 3D parametric simulations, the trials were repeated twenty times for each COR value in order to obtain reliable data.
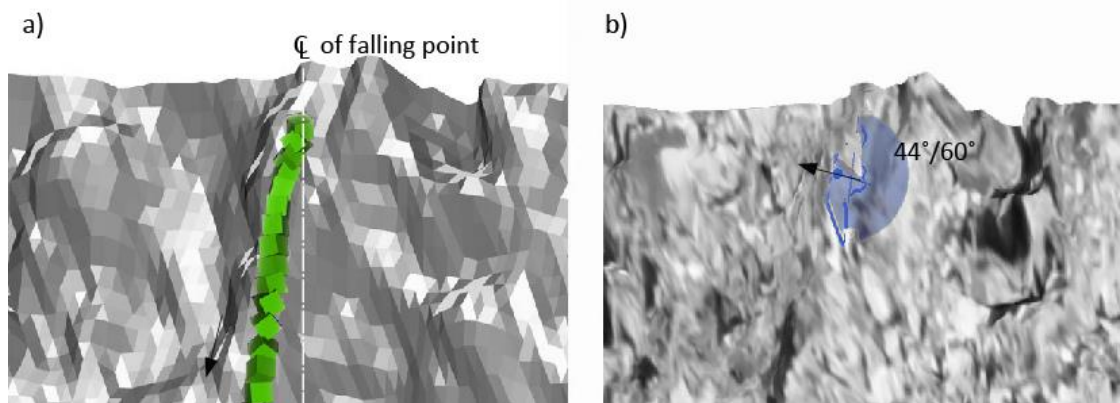
Fig. 7.45 Rockfall trajectory on Trajec3D (a) and joint orientation (Sirovision) (b) at the starting point

In terms of comparison of collision numbers with different COR values, it was natural that the rock collision numbers were decreased when the COR increased from 0.3 to 0.9. The range of COR in Trajec3D simulation was relatively higher than the results from the previous research performed by Graf et al., (2013). The range of restitution coefficients in his tests for hard rocks was from 0.003 to 0.644. In comparison, the range in this simulation was reasonably determined by considering trends of collision numbers with the results from the field tests. The number of collisions was varied from 3 to 5 with COR of 0.3 and then reduced to 2 or 3 times using the COR of 0.9. As the COR indicates the characteristic of the elasticity of slope surfaces, the rockfall pattern tended to change from bounce to rolling with decreased COR values. However, the change of collision numbers does not show tangible differences with COR values between 0.5 and 0.9 (Fig. 7.46 (a)).

It is clear that the increasing of COR resulted in faster falling. The results showed that the average arrival time obtained from the data distribution was reduced from 2.8 to 2.2 seconds as demonstrated in Fig. 7.46 (b). Due to the data noise along the edge of the 3D

model, the top and ground bench parts were not fully generated in the slope model. Therefore, the arrival times were measured at the time when the rocks arrived at the toe of the slope. Figure 7.46 (b) showed that the rockfall elapsed time in the 3D simulation can demonstrate clearer tendencies according to the change of COR than the number of collision. Figure 7.47 shows a simulated rockfall path comparing it with the observed rockfall event when the COR value was 0.5. Despite slight differences, the simulated collision numbers and the rockfall direction agreed well with those of the rockfall test.
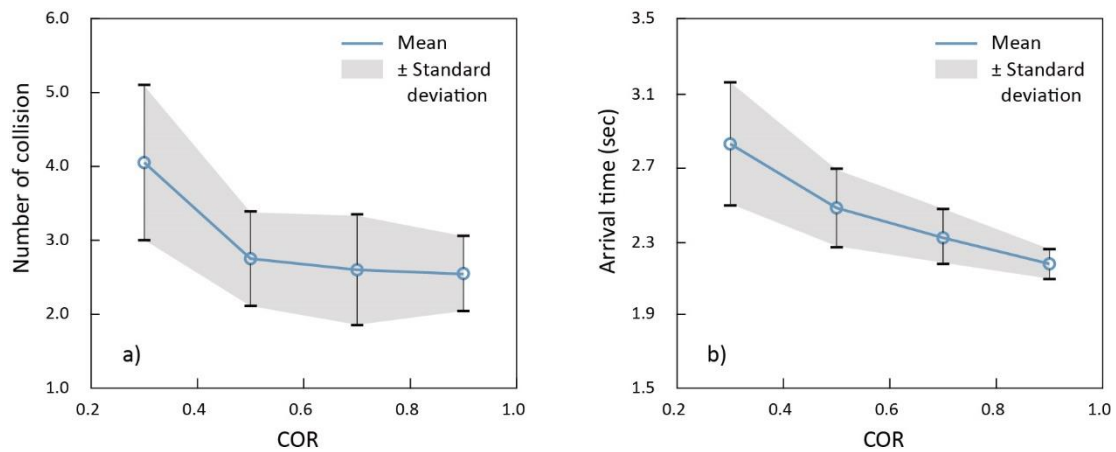
Fig. 7.46 Relation between a) numbers of collision, b) arrival time and coefficient of restitution
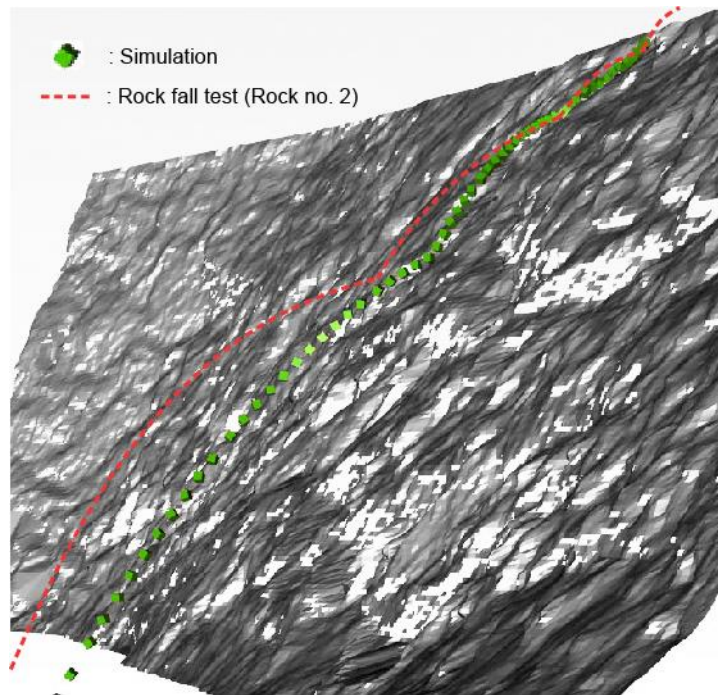
Fig. 7.47 Comparison of a simulated trajectory with field rockfall result (rock no. 2)

195

7.5.9 2D Rockfall simulation

In 2D rockfall simulations, the analysis model was assisted by 3D rockfall simulation to derive pre-defined rockfall path. The commercial software RocFall (Rocscience, 2003) was used for the simulation and the program is based on a lumped mass approach with separate coefficients of normal and tangential restitutions. The coefficients of restitution used in the simulation are presented in Table 7-27. The normal coefficient of restitution (R_n) was calculated by the relation between Schmidt rebounds and R_n as mentioned in Eq. (7-20). To determine the tangential coefficient of restitution (R_t), four different R_t values were used for parametric analyses comparing the results of rock endpoints from the field data. The 2D analysis model defined by a section along a 3D rockfall trajectory is shown in Figure 7.47. This section was obtained by irregular cutting along the 3D simulation trajectory using the computer code 'Sirovision'.

It is obvious from the result that the coefficient of tangential restitution controls the distance of rockfall endpoints from the slope. As shown in Figure 7.48, with the rise in R_t values, the mean values of the endpoints, which indicate most probable runout distances in the statistical simulations, increased from 4.4m to 8.6m. In comparison with the measured distances in the field, the data distribution also suggests that proper R_t value can be determined between 0.7 and 0.8.

Table 7-27. Parameters in RocFall (Rocscience) simulation

Parameters	Value	Reference
Coefficient of normal restitution (R_n)	0.58	Schmidt hammer test
Coefficient of tangential restitution (R_t)	0.6, 0.7, 0.8, 0.9	Rocscience Inc., (2003)
Friction angle (°)	35	Barton's empirical equation

7.5.10 Discussion

The results of the simulations show that there is a clear relation between the COR and rockfall elapsed times in the 3D simulations. In the 2D analysis, there is also a good relationship between R_t and rock endpoints. By establishing the linear relationship between the parameters shown in Figure 7.49, the coefficient of restitution (COR) and tangential restitution (R_t) can be back calibrated. In the graphs, ts/tr is the ratio of simulated elapsed time to measured elapsed time and Ds/Dr is the ratio of simulated rock endpoints to measured rockfall endpoints respectively.
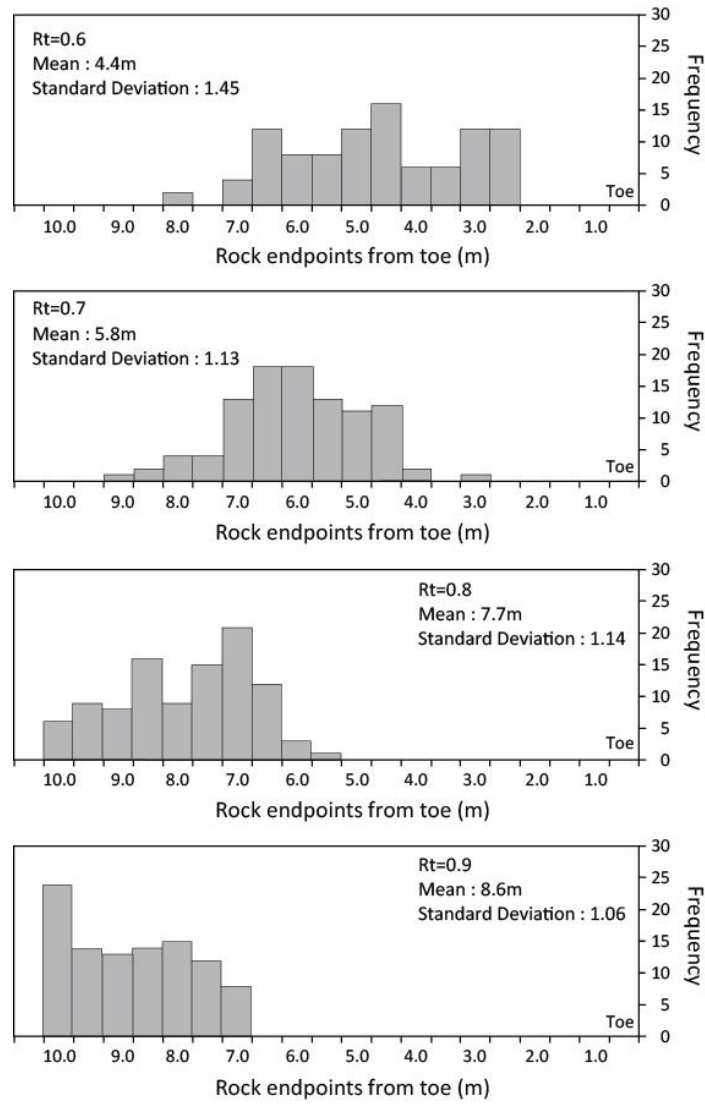
Fig. 7.48 Data distribution of rock endpoints from toe according to coefficient of tangential restitution (RocFall analysis)
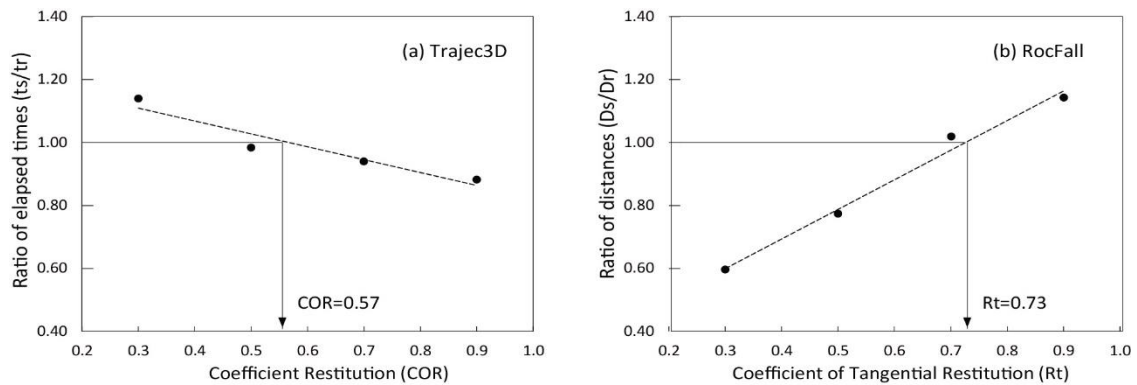
Fig. 7.49 Determination of coefficient of restitutions by back calibration

The results of the back calibrated coefficients (COR=0.57, R_t=0.73) were used to simulate 2D and 3D rockfall events again. From the comparison between 2D and 3D analyses for similar trajectories, the plot in Figure 7.50 shows the total kinetic energy curves values. In the upper part of the slope, where the block started to travel in the beginning, the simulated kinematic energies by both the simulations showed a different trend. This can be simply explained by the RocFall starting with bouncing patterns, while rocks on Trajec3D were thrown by a rolling pattern. Nevertheless, it is worth pointing out that the kinetic energy of both the simulations created similar values which were 0.42 kJ and 0.33 kJ respectively at the slope toe position.
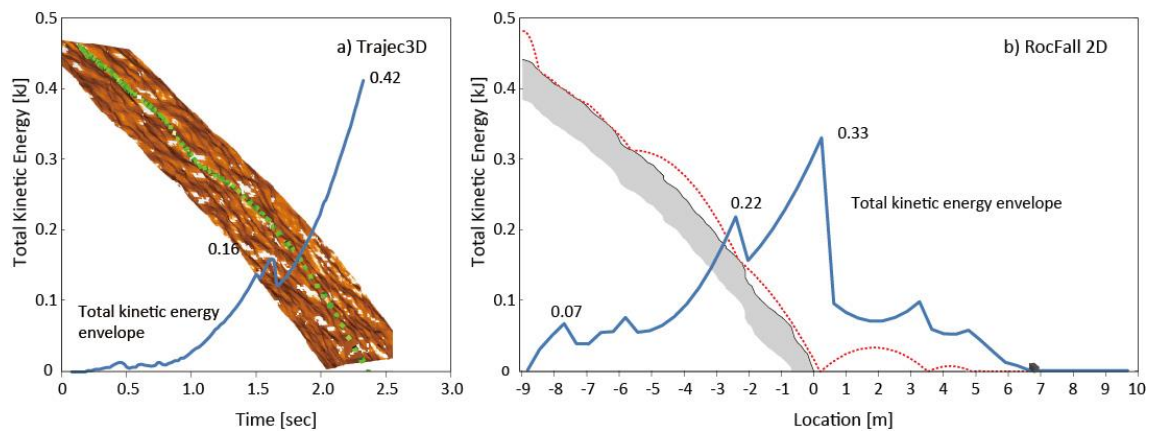
Fig. 7.50 Comparison of kinetic energy distribution of RocFall (a) and Trajec3D (b) simulation

Friction angles were estimated from the photogrammetric JRC values. However, because of a difficulty of field investigation, insufficient data were used for the estimation of friction angle. Likewise the issue of the accuracy of photogrammetric JRCs, this uncertainty of friction angle may influence the accuracy of the results of the simulations.

7.5.11 Conclusion

This section of the thesis is to verify the photogrammetric JRC values for assessing coefficients of restitution using a combined numerical analysis with the results of field rockfall tests. A set of rock fall tests and a photogrammetry survey were carried out and the results were back calculated using 3D and 2D rockfall simulations. Based on the obtained results, the following conclusions can be drawn:

- Photogrammetry model was used to create realistic slope surface for rockfall simulation. The combination of the simple field tests and the photogrammetry survey, which reflects the practical slope material and the realistic slope surface simulating exposed joint orientation, provided reliable coefficients of restitutions of the studied slope.

- The results from the field test showed that the shape of rocks had a significant influence on the falling paths. The falling rocks with high rock shape index (γ) produced higher lateral dispersed distances. Also, the surface geometry especially in the source area, directly affected the direction of rockfall paths.

- The simulation with different restitution coefficients (COR) indicated that rockfall elapsed time is a suitable factor to calibrate COR values from 3D simulations. The results of 2D simulation using a pre-defined rockfall path derived from a 3D analysis demonstrated that rockfall end points were sensitively varied with the coefficient of tangential restitution (R_t). Consequently, the results of 2D simulation using a pre-defined rockfall path with the calibrated R_t value showed a good agreement with the 3D rockfall trajectories.

- JRC values were employed to estimate the friction angle of the study slope. The friction angle of the slope influenced the number of bounces and the bouncing directions. Using the range of friction angle ($30\degree \sim 40\degree$), parametric 3D rockfall simulations were performed and the results were visually compared with the real trajectories. Through the parametric simulations, friction angle $35\degree$ was used to the 2D rockfall simulation.

- The accuracy of photogrammetric JRC values depends on the extent of data noise as well as the resolution of the images. The photogrammetric JRC ranges were generally underestimated because of the low resolution images (c-to-o distance: 33 m). However, the 3D model obtained from the close distance (c-to-o distance: 5 m) also created inaccurate JRC ranges due to a data noise.

- In this simulation, the number of data to estimate friction angle can be an issue in terms of the reliability of the simulation results. The use of photogrammetric JRC data in various locations can be thus achieved under an identification of the level of accuracy in the photogrammetric setup.

7.6 Case study 5 (Assessment of rock weathering)

A part of the study in this section was published and included in the proceedings of 19SEAGC & 2AGSSEA conference as follows:

Dong Hyun Kim, Ivan Gratchev, Erwin Oh, Arumugam Balasubramaniam (2016) Assessment of rock slope weathering based on the alteration of photogrammetric roughness data. Proceeding of the 19th Southeast Asian Geotechnical Conference & 2nd AGSSEA Conference (19SEAGC & 2AGSSEA), Kuala Lumpur, pp. 901-906.

7.6.1 Introduction

The weathering grades and the weathering rates of rock material have been of significant interest to geologists and engineers. From a geological perspective, many weathering indices have been investigated and these indices are generally derived from chemical and mineralogical analysis. As an indicator of the degree of weathering, many studies have attempted to analyze rock surface roughness combined with the weathering states (McCarroll & Nesje, 1996; White et al., 1998; Gómez-Pujol et al., 2006; Pinho et al., 2006; Medapati et al., 2013). McCarroll and Nesje (1996) suggested that roughness is a useful indicator to quantify the degree of weathering through a set of measurements of roughness profiles using profile gauges. Using the triangulate point clouds obtained from a laser scanned 3D model, Medapati et al. (2013) attempted to use the γ-values, which are the angles from the vertical axis to the normal vector, for identifying the rock surface roughness in different weathering conditions.

From an engineering point of views, weathering is studied using quantitative approaches rather than geological approaches, where rock masses are classified based on the durability and the strength of the rock mass in respect to the degree of weathering. As a significant engineering value, the rock joint roughness coefficients (JRC) can be used for describing the weathering characterization. In this study, photogrammetric JRC data has been collected over a two-year period between 2012 and 2014. With the comparisons of the annual JRC data with the durability of rocks, JRC variation rates were investigated to suggest an index to quantify the weathering degree for engineering purposes. The JRC values were calculated using digitized roughness profiles extracted from photogrammetric 3D models, which included exposed joint sets.

Photogrammetric 3D models simulate joint planes based on the clearly extended planes or the extruded parts of the joint planes from the rock slope surfaces. Due to the limitation of the camera's view and the brightness of the joint space, the inside information between joints is rarely created and the creation is dependent on the thickness of the joints. However, when a roughness profile of an exposed joint set is changed by weathering, the loss of roughness between the joint edges can be measured from the roughness profiles as presented in Figure 7.51.
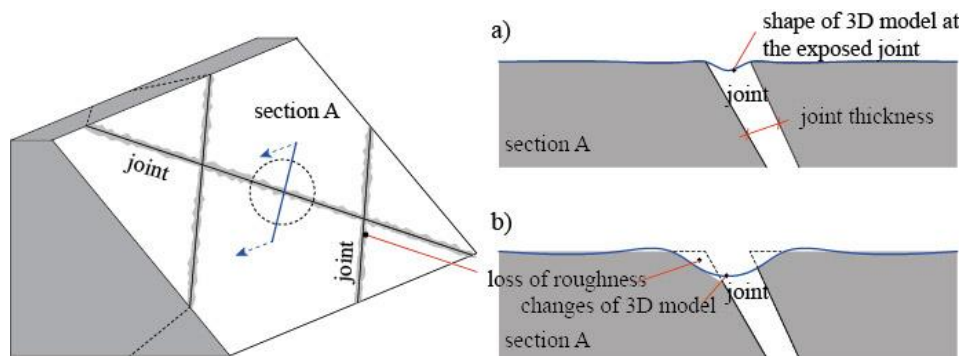
Fig. 7.51 Schematic drawing of a photogrammetric 3D model of the intersection of a joint, before weathering (a), and after loss of roughness by weathering (b)

7.6.2 Influence of weathering on JRC

If a rock type is vulnerable to weathering, the variations of roughness on the exposed rock slopes can be mostly observed at the intersections of the exposed joints within the surface areas of slopes in a short term period. Weathering typically erodes the edges of joints. Depending on the geological components of rocks, the roughness alterations will produce the different forms of weathering products. Typically, the exposed edges of joints become rounded. Therefore, it is generally accepted that loss of roughness leads to a decrease of JRC values of the areas. However, the decrease in JRC values are not necessarily proportionate to the loss of roughness. Indeed, a partial loss of roughness in a specific area along a joint may actually produce an increase of JRC values.

Similarly, in the case of laminated structure rocks such as shales and mudstones, exfoliations with a shape of flakes can be more dominant than other types of breaks. The partial exfoliations with the shapes of flakes can cause a significant increase in JRC values of rock surfaces due to the step-like profiles on the altered surfaces near joint intersections.

Therefore, it can be said that the JRC variations by the weathering process can reflect the geological structural characteristics of the rock material as well as its durability. To establish the indicator, this study suggests a JRC variation rate (JVR) as presented in Eq. 7-28. This can be obtained by the comparison of JRC values collected from annual investigations. In order to collect sufficient data and to cover the investigations in large slope surface areas, remote sensing methods such as photogrammetry methods, can be more efficiently used for the historical JRC records.

$$\text{JRC variation rate (JVR)} = ((JRC_{t2} - JRC_{t1}) / JRC_{t1}) / year \qquad (7\text{-}28)$$

where JRC_{t1} is the previously measured value in a particular year and JRC_{t2} is a measured value at present. Thus, if the JRC variations are negative, the roughness values have been decreased during the specific periods. In consideration of the measurement accuracies of 3D models, collected JRC variation rates can be evaluated by statistical methods. As presented by Medapati et al, (2013), roughness data can form specific distributions according to their weathering condition. Accordingly, JVR data can show different shapes of distribution curves depending on the structure and durability of rock material. The data distributions are distinguished by several statistical indices such as mean, median and skew (see Fig. 7.52). It is worth mentioning that the statistical indices obtained from the annually observed data can supplement weathering characteristics with reasonable correlations with the durability indices of the rocks.
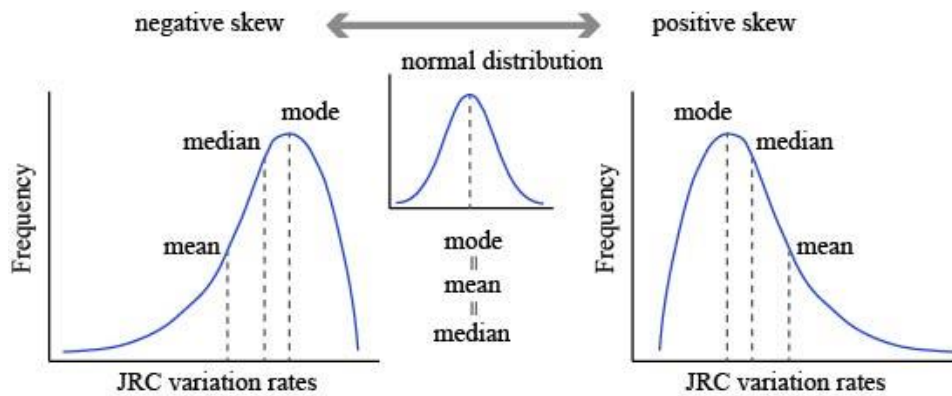
Fig. 7.52 Examples of data distribution

7.6.3 Comparison of roughness data

The photogrammetry code "Sirovision (CSIRO, 2012)" was employed to create 3D images. Geo-referencing was performed for the two different 3D models by giving the coordinates of the left camera position (using a GPS device) and measuring its bearing to the centre of the slope (using a geological compass). Figure 7.53 shows 2012 3D models of both selected shale and sandstone zones for JRC estimations.
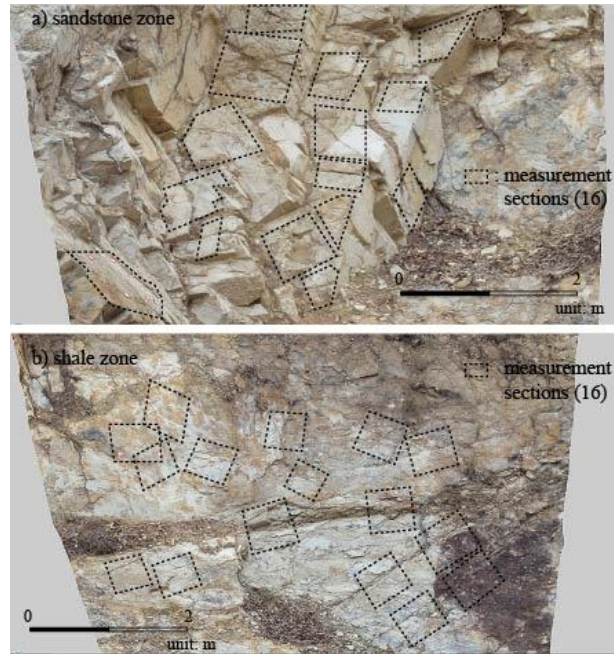
Fig. 7.53 Photogrammetric 3D models (surveyed in 2012) and selected surface area, sandstone (a), shale (b)

7.6.4 Alteration of surface roughness

With visual comparisons of the 3D models of 2012 and 2014, it was found that there had been roughness alterations, especially on the periphery of exposed joints in both rock zones. The images show a large alteration of colours on the surfaces in the shale sections. This exfoliation phenomenon was not found in the slake durability tests. An example of the changes is presented in Figure 7.54 (a, b). This alteration was accompanied by the exfoliation of thin rock flakes. In sandstone sections, however, dominant changes occurred around the edges of joints as shown in Figure 7.54 (c, d). It was also found that in both rock types, several sections lost large portions of surface roughness resulting in large variations of profile shapes.

203
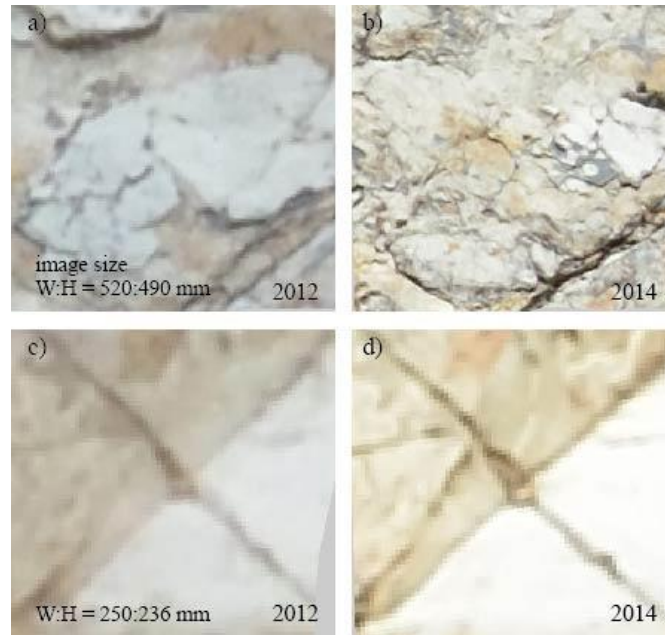
Fig. 7.54 Examples of the 3D image cuts showing the alteration of rock surfaces due to weathering process over two years; shale, section 2 (a, b), sandstone, section 4 (c, d)

JRC values were estimated in 16 measurement sections in both rock types respectively. As shown in Figure 7.55, the measured directions are radially positioned, centred by the steepest direction (dip direction) at 45 degree intervals. Since JRC values are highly dependent on the measurement scales, the measurements were performed in different window sizes ranging from 150 mm to 1000 mm in this study. The measurement window positions were determined in accordance with the locations of exposed joints, where the joints are distinctly exposed on the rock surfaces. The JRC values were estimated using roughness profiles which were extracted by the photogrammetric code, Sirovision. This program provides a function which estimates JRC values by selecting the corners of a specific area on the 3D model.
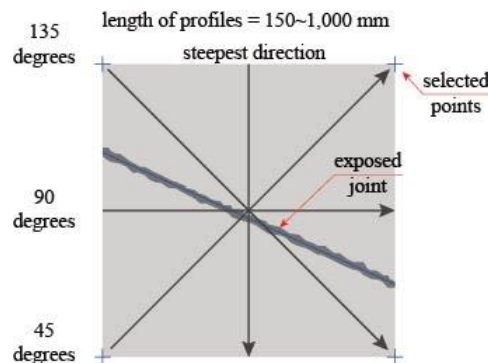
Fig. 7.55 Selected areas for JRC estimation in Sirovision and the directions for directional JRCs

7.6.5 JRC variation rate

The JRC values obtained from the 3D models at two yearly intervals using 'Sirovision' were analysed to estimate the JRC variation rates between the models. In two years, the variation rates have been changed from -0.45 (decreasing to 45% of previous JRC values) to 0.8 (increasing to 180% of previous JRC values). Figure 7.56 presents the JRV values in accordance with the measurement scales. Overall JRC data were formed with scattered patterns for both shale and sandstone zones. It is obvious that the strength of the relationships between JRV and measurement scale is "weak" or "moderate". The data distributions of the shale sections show weak correlations with the measurement scales (R_2 = 0.02). However, negative associations between the variables are also noticeable in the distributions. In the sandstone zone, the data distribution shows moderate positive correlations between JRV values and measurement scales ($R_2 = 0.12$).
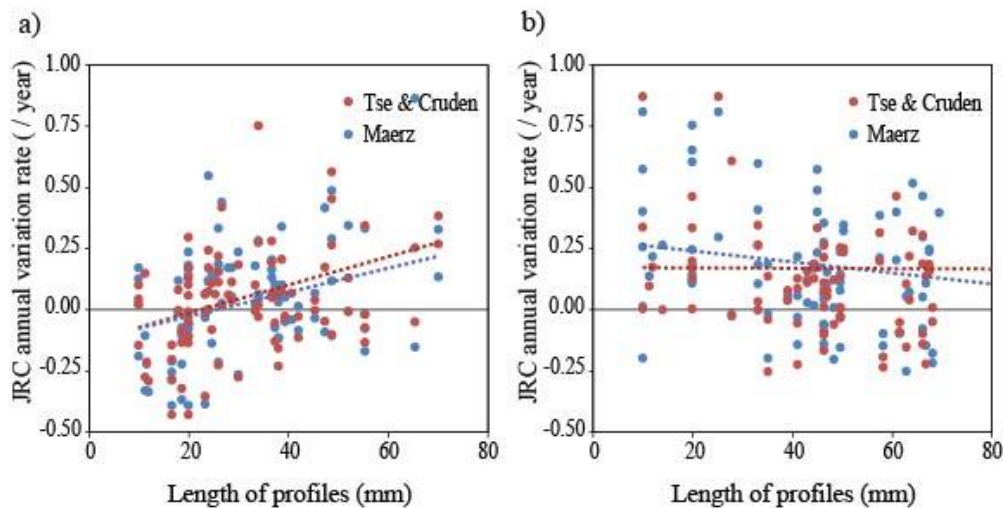
Fig. 7.56 JRC variation rate according to the scales of profiles, shale (a), sandstone (b)

It is interesting that an increase of JRC values by weathering is dominant in the shale zone rather than the sandstone sections. This is due to the different breaking patterns from the rock surfaces as mentioned in Section 7.6.4. In the small measurement scale range (L = 150 ~ 300 mm), on the other hand, a considerable amount of data from the sandstone zone shows a decrease of JRC values for two years. This can be explained by the fact that the loss of small scale roughness is more influential on the JRC values when the changes of undulations are negligible. To address the changes of JRC values, each example of the alteration of roughness profiles for both rock types is demonstrated in Figure 7.57.

The roughness profiles composed of regenerated 2 mm interval coordinates. It is worth mentioning that the accuracy of photogrammetric JRC values is beyond the scope of this study. Generally, photogrammetric JRC values tend to be underestimated in the data interval (2 mm) compared to manually measured values. The accuracy of photogrammetric JRCs can vary with a quadratic function which depends on the camera-to-object distance and the employed focal lengths of lenses (Kim et al., 2015c). However, this study compares the JRC values in the same density data condition.
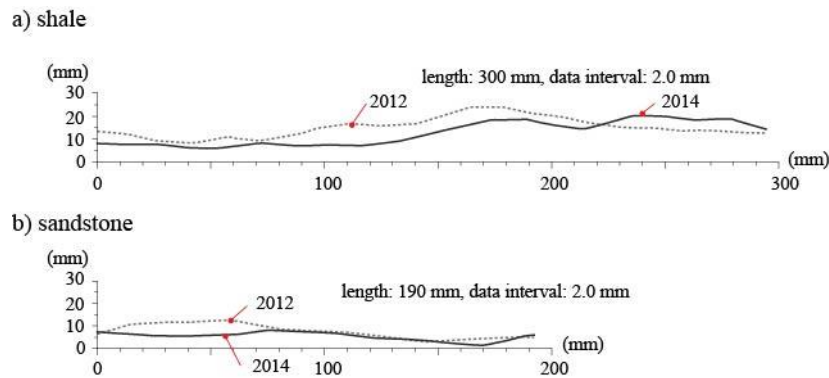
Fig. 7.57 Examples of roughness profiles, shale (a) and sandstone (b)

7.6.6 Statistical indices for weathering

Based on the JRV data, the distributions of JVR according to the estimation functions (Tse & Cruden, 1979; Maerz, 1990) were plotted and the statistical indices were calculated. Figure 7.58 demonstrates that most data distributions form skewed distribution curves. It is obvious that the statistical results show the differences of JVR values between shale and sandstone. In the shale zone, the surface of the selected area has considerably changed due to the exfoliations controlled by the textural properties of the shale bedding structures as shown in Figure 7.53 (a) and (b). This has resulted in increasing of JRC values. The JRV distributions indicate higher average values ($\mu = 0.17 \sim 0.19$) (see Fig. 7.58 (a), (b)) than those of sandstone distributions ($\mu = 0.03 \sim 0.05$) (see Fig. 7.58 (c), (d)). The distribution of sandstone data is moved toward negative portions of the JRC variation rates. These negative data probably reflect the smoothly eroded rock surface profiles.

As the indicators of weathering for describing roughness variations, "mean" and "skew" values of JRC variation rates are used in this study. The mean values indicate the increased roughness of surfaces resulting in an increase of JRC values for one year. The geological

structures of rocks have a strong influence on the values as well as the strengths of rocks. As shown in this study, the stepped roughness profiles of the shale zone produced larger JVR values than the sandstone sections, even though the shale samples have higher strength properties (UCS and Id$_2$) than those of the sandstone. As shown in section 7.6.4, the geological characteristic of shale, i.e. the exfoliations, which are composed of similarly shaped broken particles with thin and flat flakes, resulted in sharp edges on the surfaces. Therefore, the mean values of JVR can be used to describe a time dependent roughness variations in terms of the strength and geological characteristics of rocks.
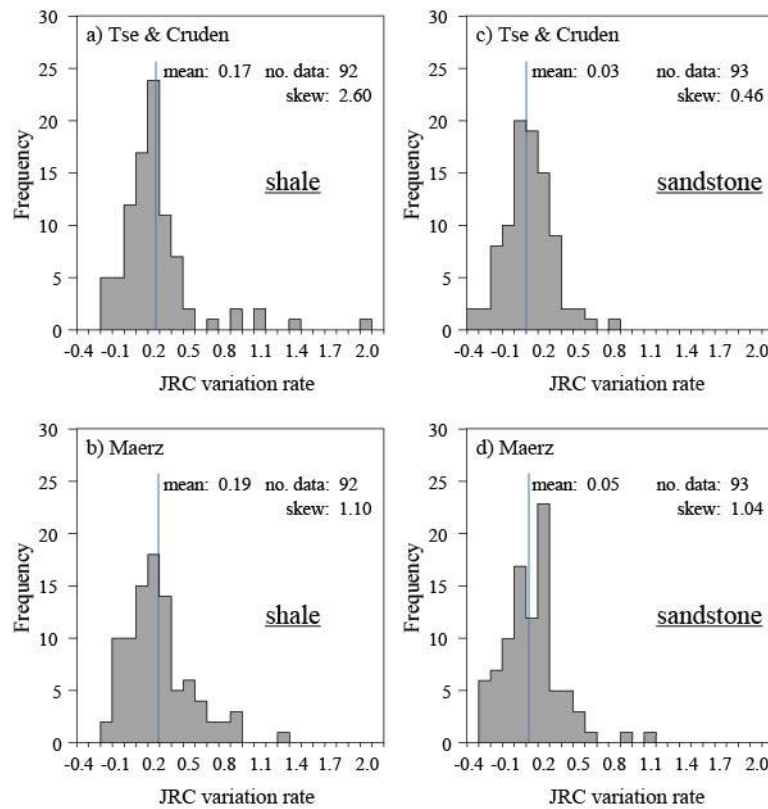
Fig. 7.58 Histograms of JRC variation rates obtained using Tse & Cruden function (Eq. 2-4), shale (a), sandstone (c); Maerz (Eq. 2-19), shale (b), sandstone (d)

However, a quantitative explanation of the skewness of JVR is complicated. The authors regard the skewness of the roughness distributions in this study as the tendency of data deviation from the mean values. In Figure 7.58, JVR data of the all these analysis cases form positive skewed histograms, which means asymmetrical distributions with long tails can be expected from the considerably increased JRC values. A large values of skewness can indicate large range of data sets which may be caused by geological differences between the data sets as well as the locality of the data sets. Further studies may be needed

207

to identify the skewness of JVR data. It is interesting that JVR values increase with the slake durability index (Id_2) values of the rocks. This trend is different from the general understanding of the durability of rock material. In the study area, the durability of the shale sample is larger than the durability of sandstone data. However, the statistics indicate that the roughness alteration on the shale samples is larger than that of the sandstone samples. The relationships between the mean values of JVR and the Id_2 values of the shale and the sandstone zones are demonstrated in Figure 7.59. To compare the statistical indices of JVR data with the durability of both rock types, relevant properties are summarized in Table 7-28.
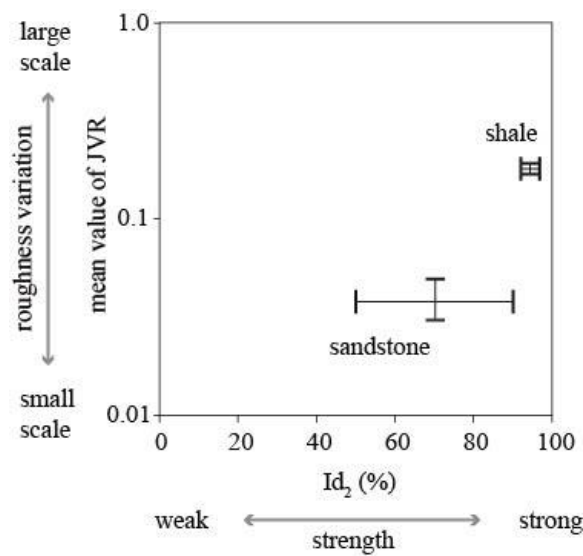
Fig. 7.59 Correlations between mean values of JRC variation rates and Id_2 values for each rock type

Table 7-28. Statistical indices of JRC variation rates for shale and sandstone

Data distribution indices	JRC variation rate			
	Shale		Sandstone	
	Tse & Cruden	Maerz	Tse & Cruden	Maerz
No. of data	92	92	93	93
Mean	0.17	0.19	0.03	0.05
Standard deviation	0.33	0.28	020	0.24
Median	0.132	0.143	0.021	0.043
Mode	0.871	0.809	-0.43	-0.391
skew	2.604	1.103	0.466	1.042

7.6.7 Conclusion

The weathering characteristics of shale and sandstone in a cut slope within the Naranleigh-Fernvale beds in Australia, was investigated by an analysis based on historical photogrammetry surveys. In both the shale and sandstone zones of the study area, JRC data were collected over two years. With the comparisons of the JRC data, the present study suggests the use of the joint roughness variation rate (JVR) to show the annual changes of JRC values for a rock surface area. Through a statistical analysis, it was found that JVR values indicate the alterations of rock surfaces caused by weathering in a short term.

As a result, the mean values of JVR were considerably different according to the rock types (shale: 0.17 ~ 0.19, sandstone: 0.03 ~ 0.05). This study shows that the "mean" of JVR values can be used as an indicator for quantifying the weathering degree of rocks while also considering the slake durability index (Id_2) in terms of both geological and mechanical characterizations.

8 DISCUSSION AND CONCLUDING REMARKS

This chapter discusses the feasibility of close range photogrammetry for any future investigation into rock joint roughness, and summarizes the contribution of this study for the purposes. The accuracy of photogrammetric roughness data is reviewed in depth for practical purposes. For the estimation of rock surface roughness, guidelines for close range photogrammetry are also suggested in this chapter. In relation to the improvement of roughness investigations using photogrammetry, future works are proposed in various aspects.

8.1 Feasibility of photogrammetry for roughness investigation

Photogrammetry is a powerful technology in many engineering applications. This technique has proven to be inexpensive and efficient in creating geospatial data of large scale rock slopes. This advantage has contributed to the widespread use of photogrammetry for discontinuity characterization. With regard to roughness investigation, the literature review presented in Chapter 2 highlights that photogrammetry is questionable due to various influencing factors caused by both camera and planning. When dealing with these two factors, uncertainties in one may be associated with uncertainties in another. That can be one of the reasons why photogrammetry for joint roughness investigations, combined with the application of rock mechanics, has been insufficiently studied and used to date.

However, many examples of successful roughness simulations using photogrammetry can be found in different areas such as geology, archaeology and medical science. In these areas, at very close range, photogrammetry creates 3D models simulating detailed surface roughness, where high accuracy is required. In this respect, it is important to mention that the feasibility of photogrammetry depends on the required accuracy of the produced models. From an engineering point of view, the influence of the accuracy of 3D models on the corresponding JRC values of profiles should be evaluated when considering the influence of the values on the mechanical behaviour.

The study presented in this thesis emphasizes the benefits of JRC data provided by close range photogrammetry, which can produce accurate surface models with dense point intervals in comparison to traditional measurement techniques. Photogrammetric JRC values obtained from various field surveys have been used as analysis parameters for the

corresponding engineering issues as shown in Chapter 7. In order to estimate the 'stiffness' parameters of Mohr-Coulomb slip joint model in Section 7.2 and the 'joint factors' of Hoek-Brown criterion in Section 7.3, the accuracy of photogrammetric JRC data alone may lead to an incomplete final conclusion. The factor of safety for slope stability depends on various strength properties as well as on the roughness properties in the study cases in Chapter 7. It can be said that the techniques used in this study are adequate when the obtained data are within reasonable ranges. Therefore, close range photogrammetry can be a useful part of providing deterministic design values in the field of rock slope engineering.

Measurement of the maximum asperity height (h) is also a good solution to avoid measurement errors of JRC values due to data noise. As presented in Section 7.6, the data noise tended to occur when the images were taken at close distances with long focal lengths and thus the point intervals were short. The corrupted profiles can be filtered by a smoothing process to estimate a reasonable range of JRC values (Poropat, 2008). However, it has been also found that the corrupted profiles created satisfactory undulations in large scale. If the straight edge method is applied to estimate rock joint roughness, photogrammetric profiles can be alternatively used for the measurement profiles.

There are unknown factors that can affect the accuracy of the roughness data, including camera factors and inappropriate planning factors. As the planning factors, camera-to-object distances, baseline distances, percentage of image overlaps, camera intersection angles and angles of incidence can affect the accuracy of the obtained photogrammetric 3D models (Dai et al., 2014). This research emphasizes that inappropriate planning factors could more influence than camera factors in very close distances. In order to minimize data bias and to obtain reasonable ranges of roughness data, the plans of photogrammetry should be established by adequate guidelines. This limitation can be a different issue when SfM methodology is employed. However, in this study, the methodology has not been considered.

As a guideline, this study developed a JRC error model based on a set of laboratory tests. The laboratory study of this thesis presents that there are allowable distance for photogrammetry survey in accordance with the employed focal length of lens. Even though the proposed allowable distances are developed under a laboratory condition, the error model is still valid as an ideal standard. Field photogrammetry tests in this thesis showed that if photographs are taken in close camera-to-object distances and the camera axis to

objects is close to orthogonal, the obtained photogrammetry roughness data are distributed in a predicted error ranges. This is extremely useful to review the obtained roughness data from photogrammetry surveys.

Current practice in field tests largely relies on manual measurement of the roughness on rock joint surfaces by profile gauges. Due to constraints of sites, such measurements only apply to a limited number of sample sections and the sample sections can be selected from the areas within the accessible sections of the rock slopes. Accordingly, an important issue when undertaking close range photogrammetry can be the portability of equipment. The specific distant range of close range photogrammetry in this study is less than 10 metres. This issue is evident when the target areas are determined by geological conditions so that the areas are specifically separated. Technical feasibility of the use of close range photogrammetry, which is for inaccessible parts of fractured rock masses, has been verified by the use of recent UAV (unmanned aerial vehicle) technology. This method is useful to control a survey system to record specific randomly located exposed discontinuities.

8.2 Standardization for photogrammetry survey

For roughness characterization, site investigators should consider the influencing factors and several important guidelines to minimize measurement errors as well as the basic knowledge of photogrammetry. With regard to this topic, the practical limitations of photogrammetry surveys have been mainly discussed on the influence of measurement scales and the data noise (Haneberg, 2007; Poropat, 2008, 2009; Oppikofer, 2009). The planning of photograph setups should be thus properly established to minimize the influences on the accuracy of roughness data. In this thesis, it has been experimentally reviewed that the constraints are usually desirable distances, focal length of lens and angle of camera axis toward objects. The results of experiments have led to develop a JRC error model as a guideline for applying close range photogrammetry.

8.2.1 Proposed method for prediction of JRC errors using error curves

For many cases, it is convenient to approximate the probabilistic distribution by a mathematical function. This study sought to systemize the families of photogrammetric JRC data through laboratory tests as presented in Chapter 5 and 6. The developed JRC error functions, using a simple parabola curve and a line to plot the relationship between

normalized JRC data and RMSE and MAE of JRC, can be used for verifying the JRC values obtained by specific photogrammetry setups. The advantage of this approach is that the error functions can provide the ranges of expected errors under the functions. In the next step, an issue of this study was how the field data can be fit to the empirical distribution.

It is worth mentioning that the use of the error models is only valid when the photograph setups are followed by the guideline mentioned in this section and when the 3D models are not affected by data noise.

8.2.2 Allowable distances

In Chapter 5, the proposed allowable camera-to-object distances in accordance with employed focal lengths attempts to ensure that measurement errors can be increased beyond the allowable distances. The standard values are obtained from the regression curves of mean values of $RMSE_{JRC} \cdot D$ values in an ideal laboratory condition. The allowable ranges are 1, 2, 4 metres for the combination of Nikon D7000 with 24 mm, 50 mm, 85 mm focal length lenses respectively. Field roughness data also verified the inclined trend of $RMSE_{JRC} \cdot D$ with distance. However, the regression curves in accordance with the focal lengths could not be distinguished from each other unlike the laboratory results. In the field conditions, this trend is preferably explained by the relationship with the point intervals of 3D models, which are consequent results from the combination of the camera-to-object distance and the employed focal length.

The allowable distances according to the employed lenses in field test conditions are not established in this thesis. The allowable camera-to-object distance can be guided by further studies using intensive data collections through field photogrammetry surveys.

8.2.3 Measurement sections

Through the field data analysis, it has been clearly observed that both camera factors and planning factors simultaneously affect the error of 3D models. However, the bias of roughness profiles is more influenced by planning factors such as adjacent environment, angles of line of sight and additional factors bringing model distortions than camera factors within the camera-to-object distance range of this study. In this study, the most influential factors on the accuracy of 3D models have been found as following aspects of field conditions:

▪ overall shapes of the rock surface of interest (flat, round and edges)

▪ complexity of overall surface structure including the adjacent environment

▪ orientation of the rock surface and the profiles of interest

▪ data density of 3D point clouds

8.2.4 Orientation of line of sight and profile directions

The orientations of measurement surfaces in relation to the line of sight for cameras have considerable influence on the accuracy of JRC data. Field photogrammetric roughness data proposed a high-angle oblique range to provide a good match between the parabola error functions and photogrammetric JRC data distributions.

The influence of the orientation of measurement surfaces and the measured profiles on the accuracy of JRC values has been analysed in Chapter 6. It is argued that the accuracy of photogrammetric JRC values is increased in the range of high-angle oblique range ($\theta_1 > 60°$ and $\theta_2 < 30°$). The ranges of the angles are close to the orthogonal angles to line of sight. This result was derived from the comparison of data with the error models.

8.2.5 Preferred baseline distances

In the conventional photogrammetry methodology employed in this study, the depth accuracy of 3D images relies on the base-to-distance ratio in photogrammetry setup. However, the base-to-distance ratio is kept constant to the mean value (1:7) of the recommended range of Sirovision in this study. It is firstly because the experimental and field surveys are based on the practical photogrammetry setup for rock slope survey. The preferable range of the base-to-distance ratio, which is recommended by several photogrammetry programs, is from 1:10 to 1:2 (3DM Analyst) and from 1:8 to 1:6 (Sirovision). It can be said that this range is due to the limitation of the matching process of the photogrammetry algorithm to create 3D models. In the unreported works of this study, there were trials to create 3D models with varying base-to-distance ratios in the same laboratory conditions. However, there was difficulty in the creation of 3D models and the outcomes in fact, were not successful.

8.2.6 Extraction of roughness profiles (post-processing)

It has been highlighted in Section 3.3 that an appropriate way to obtain profile coordinates is necessary to extract roughness profiles from 3D models. In order to obtain a roughness profile in a specific direction on a 3D surface model, a rotation procedure of 3D coordinates may be required as suggested by Haneberg (2007). The rotation process can be worked by using MATLAB® scripts presented in Section 3.3.1. This method is appropriate to the occasion when the dip and dip directions of a rock surface is clearly defined and the representative profiles for specific directions are required. This method can be applied combined with photogrammetry algorithms. For example, Sirovision (CSIRO, 2012) provides a function to extract roughness profiles for a selected area on a 3D model. The profile extraction is executed along several representative directions centred by the steepest direction of the surfaces. This method is recommended for the investigation of roughness properties relating to the behaviour along dip directions. However, in many cases, the automated approach, if not used carefully, tend to provide biased roughness data, such as distorted profiles and excessive deviation of roughness parameters.

8.3 Concluding remarks

This study provides guidelines for the successful application of close range photogrammetry in rock surface roughness investigation based on experimental results. In order to increase existing knowledge of photogrammetric errors, laboratory tests and field works were conducted to investigate the effects of several crucial factors on the accuracy of the roughness data of rock surfaces.

The findings of the photogrammetry laboratory tests provided a shape of errors for JRC values according to the main influencing factors; camera-to-object distances and focal length of lenses. This error model is particularly helpful as a guide line which can compare with the obtained photogrammetric JRC data in specific photograph setups to estimate the accuracy of the JRC values. The experimental works in this thesis may help engineers and site surveyors understand the performance of the close range photogrammetry and thus better plan the roughness measurement in field conditions.

8.4 Future works

In relation to the main issues of the feasibility of photogrammetry for roughness investigation, future works can focus on following aspects:

▪ First of all, further field surveys under appropriate plans in accordance with the proposed guide lines of this study are recommended to verify the developed parabolic error models. Abundant data obtained from various field conditions can improve the prediction of JRC errors and increase the reliability.

▪ In this study, the development of error models express indirect relationships between the camera-to-object distance and the precision of JRCs. In other words, both variables of the functions are composed of JRC errors. In order to provide convenience to users, direct relationships between distance and JRC errors are preferred for quick understanding. A clear trend of error models can be established by using other metrics considering other various factors. Better findings of optimal camera-to-object distance and allowable ranges and the clear error models are required in the future. In that case, the findings in this PhD study can be an intermediate stage to the direct error functions.

▪ Roughness investigation for rock slope surface is generally performed on specific locations where are worth investigating roughness properties as exposed rock joints. The regions of interest can be located much higher than ground levels or the regions can be spread over whole large slopes. This means that close range photogrammetry can frequently reach the limitation of camera setups due to the preferred ranges of camera-to-object distances and the preferred orientation of camera axis. Thus, the methodology of this study can be expanded to the use of more convenient and movable survey tools such as UAV (unmanned aerial vehicle) technology combined with SfM methodology.

Appendix 1. Photogrammetry survey data

A1.1 Geo-referencing data (Beaudesert-Nerang road 1)
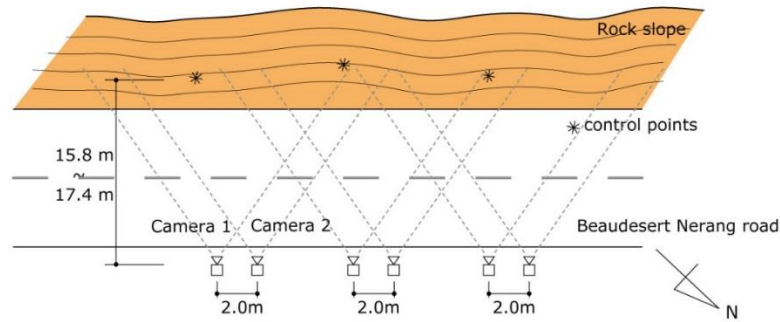
Fig. A1.1 Photogrammetry setup in Beaudesert-Nerang road 1

Table A1-1. Beaudesert-Nerang road 1 (2013)

1. Survey date	8 Feb 2013
2. Camera-to-object distance (m)	17.0
3. Bearing (°)	198
4. Camera location (Left)	
Cartesian - Easting	527802.275
- Northing	13096579.152
UTM - Latitude (°, ′, ″)	27° 59′ 38.7″S
- Longitude (°, ′, ″)	153° 16′ 57.9″E
5. Tilting angle (°)	0
6. Employed lens	FL = 24 mm

Table A1-2. Beaudesert-Nerang road 1 (2015)

1. Survey date	10 Feb 2015
2. Camera-to-object distance (m)	16.6
3. Bearing (°)	201
4. Camera location (Left)	
Cartesian - Easting	527802.275
- Northing	13096579.152
UTM - Latitude (°, ′, ″)	27° 59′ 38.7″S
- Longitude (°, ′, ″)	153° 16′ 57.9″E
5. Tilting angle (°)	0
6. Employed lens	FL = 24, 50, 85 mm

A1.2 Geo-referencing data (Beaudesert-Nerang road 2)
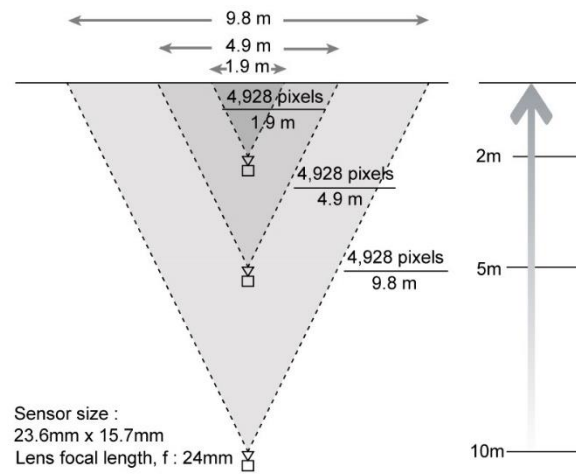
Fig. A1.2 Photogrammetry setup in Beaudesert-Nerang road 2

Table A1-3. Beaudesert-Nerang road 2 (2015)

1. Survey date	10 Feb 2015
2. Camera-to-object distance (m)	2.0 / 12.8
3. Bearing (°)	15
4. Camera location (Left)	
Cartesian - Easting	527693.226
- Northing	13096490.278
UTM - Latitude (°, ′, ″)	27° 59′ 35.82″S
- Longitude (°, ′, ″)	153° 16′ 53.9″E
5. Tilting angle (°)	0
6. Employed lens	FL = 24, 50, 85 mm

Table A1-4. Beaudesert-Nerang road 2 (2013)

1. Survey date	8 Apr 2013
2. Camera-to-object distance (m)	2.0, 5.0, 10.0
3. Bearing (°)	13
4. Camera location (Left)	
Cartesian - Easting	527693.226
- Northing	13096490.278
UTM - Latitude (°, ′, ″)	27° 59′ 35.82″S
- Longitude (°, ′, ″)	153° 16′ 53.9″E
5. Tilting angle (°)	0
6. Employed lens	FL = 24 mm

A1.3 Geo-referencing data (Bethania)
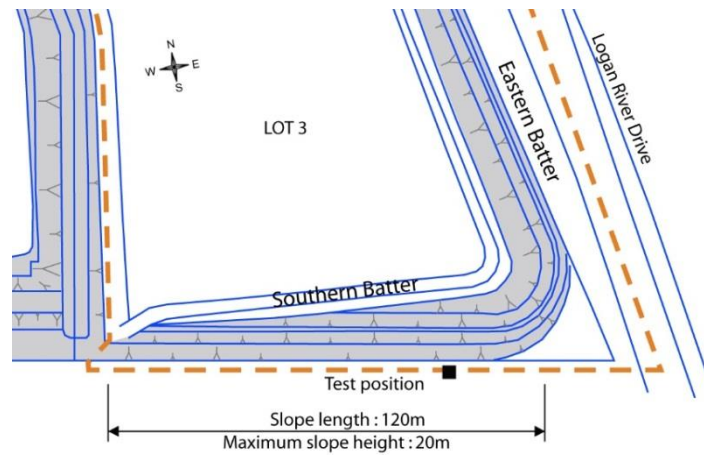
Fig. A1.3 Photogrammetry setup in Bethania

Table A1-5. Bethania, Brisbane (2013)

1. Survey date	7 Jul 2013
2. Camera-to-object distance (m)	5.0 / 33.0
3. Bearing (°)	175
4. Camera location (Left)	
Cartesian - Easting	527693.226
- Northing	13096490.278
UTM - Latitude (°, ′, ″)	27° 42′ 16.93″S
- Longitude (°, ′, ″)	153° 9′ 32.65″E
5. Tilting angle (°)	0
6. Employed lens	FL = 24 mm

A1.4 Geo-referencing data (Nerang-Murwillumbah road 1)

Fig. A1.4 Photogrammetry setup in Nerang-Murwillumbah road 1

219

Table A1-6. Nerang-Murwillumbah road 1 (2015)

1. Survey date	25 May 2015	
2. Camera-to-object distance (m)	14.0	14.8
3. Bearing (°)	220	
4. Camera location (Left)		
Cartesian - Easting	526039.546	526015.119
- Northing	13102367.031	13102349.615
UTM - Latitude (°, ′, ″)	28° 2′ 46.92″S	28° 2′ 46.36″S
- Longitude (°, ′, ″)	153° 15′ 53.6″E	153° 15′ 55.2″E
5. Tilting angle (°)	0	
6. Employed lens	FL = 24, 50, 85 mm	

A1.5 Geo-referencing data (Nerang-Murwillumbah road 2)

Fig. A1.5 Photogrammetry setup in Nerang-Murwillumbah road 2

Table A1-7. Nerang-Murwillumbah road 2 (2015)

1. Survey date	25 May 2015	
2. Camera-to-object distance (m)	11.8	12.0
3. Bearing (°)	260	
4. Camera location (Left)		
Cartesian - Easting	526288.807	526282.212
- Northing	13102769.604	13102758.196
UTM - Latitude (°, ′, ″)	28° 2′ 59.98″S	28° 2′ 59.61″S
- Longitude (°, ′, ″)	153° 16′ 3.2″E	153° 16′ 5.2″E
5. Tilting angle (°)	0	
6. Employed lens	FL = 24, 50, 85 mm	

A1.6 Geo-referencing data (Engineering road)

Fig. A1.6 Location of photogrammetry tests in Engineering road

Table A1-8. Engineering road (2015)

1. Survey date	20 Aug 2015
2. Camera-to-object distance (m)	2.0, 5.0, 10.0
3. Bearing (°)	89
4. Camera location (Left)	
Cartesian - Easting	537716.751
- Northing	13093237.660
UTM - Latitude (°, ′, ″)	27° 57′ 49.23″S
- Longitude (°, ′, ″)	153° 23′ 0.5″E
5. Tilting angle (°)	0
6. Employed lens	FL = 24, 50, 85 mm

Appendix 2. Extracted roughness profiles from 3D models in field surveys

A2.1 Beaudesert Nerang road, Gold Coast

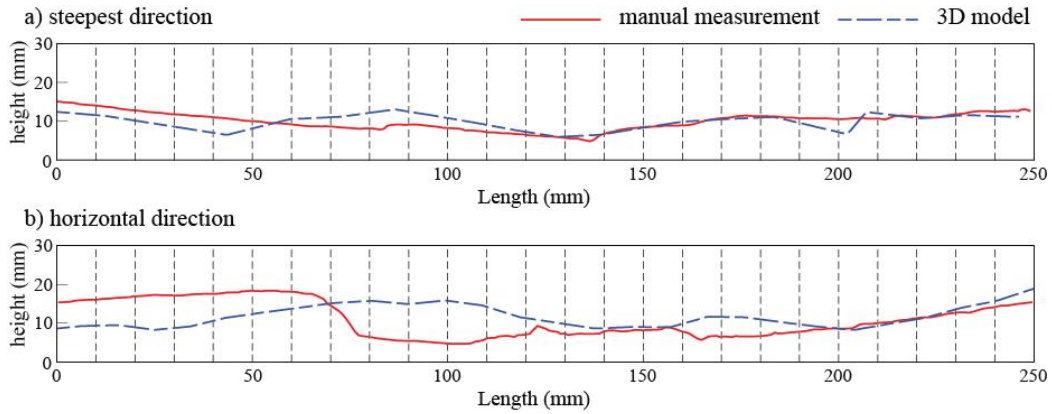Fig. A2.1 Beaudesert Nerang road 1, section 1 (bottom)
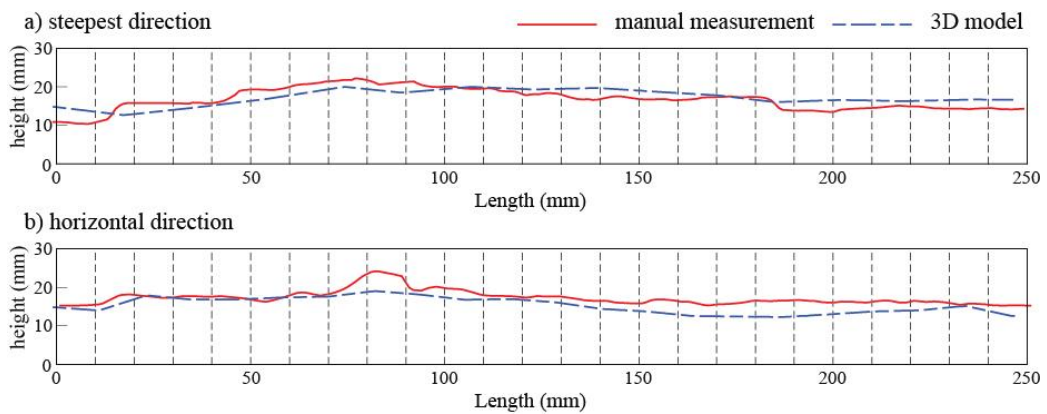
Fig. A2.2 Beaudesert Nerang road 1, section 1 (front)
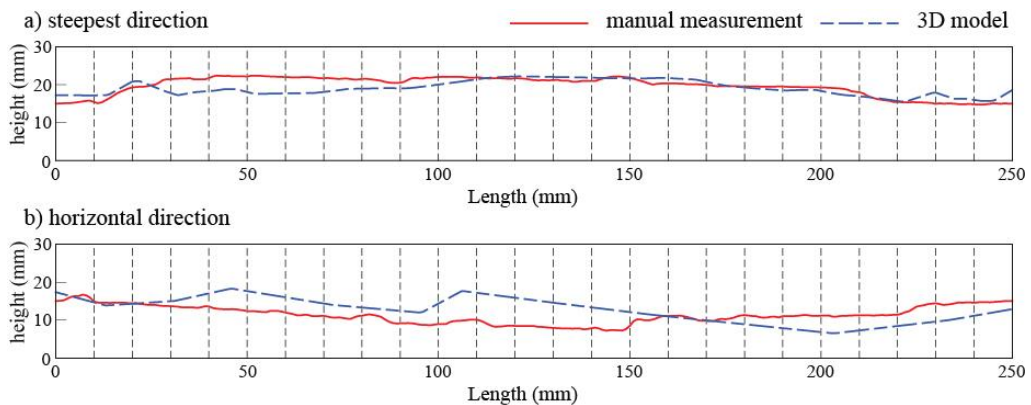
Fig. A2.3 Beaudesert Nerang road 1, section 1 (left)

a) camera-to-object distance = 2 m

b) camera-to-object distance = 5 m

c) camera-to-object distance = 10 m
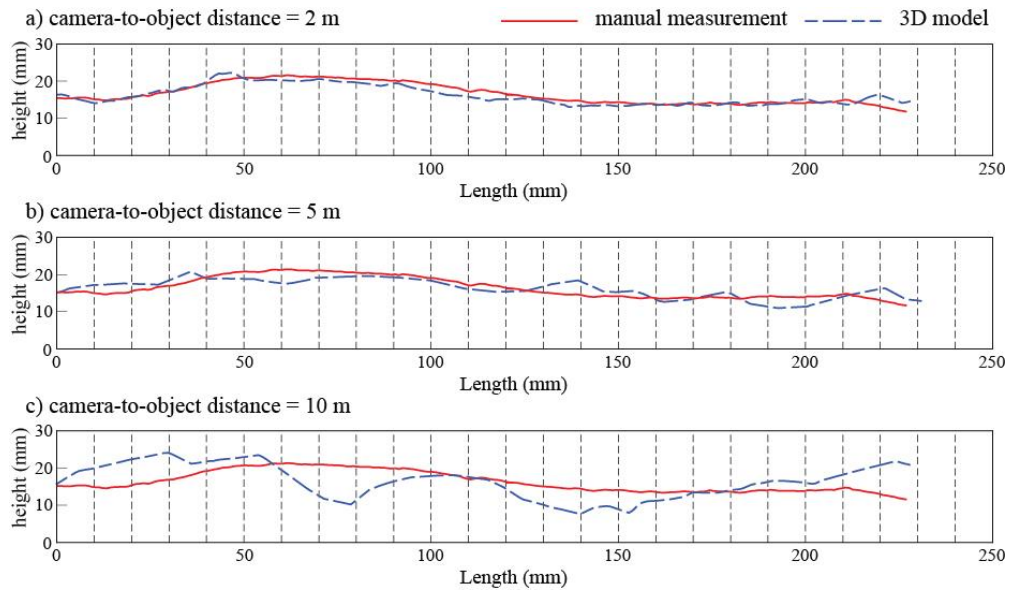
Fig. A2.4 Beaudesert Nerang road 2, section 1

a) FL = 50 mm

b) FL = 85 mm
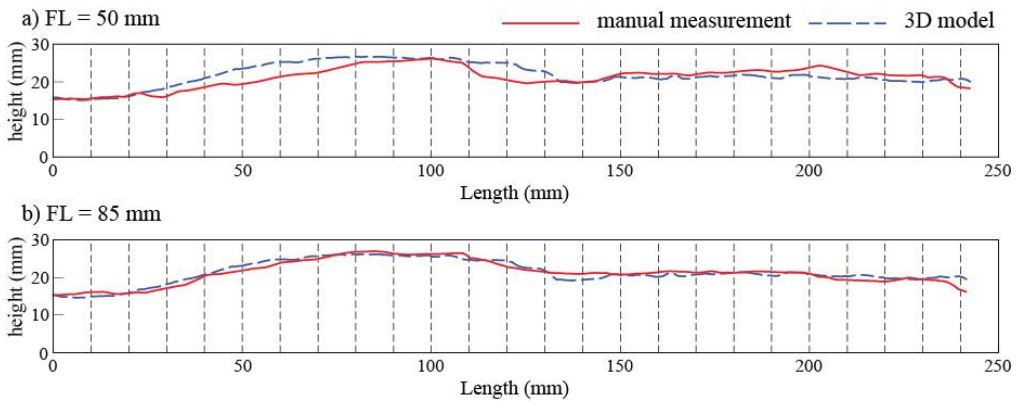
Fig. A2.5 Beaudesert Nerang road 2, section 1

A2.2 Bethania, Brisbane
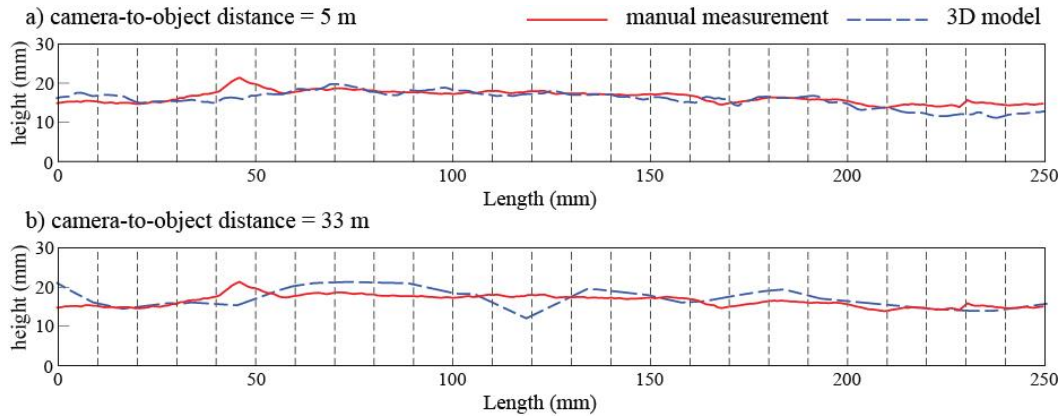
Fig. A2.6 Bethania, profile #1
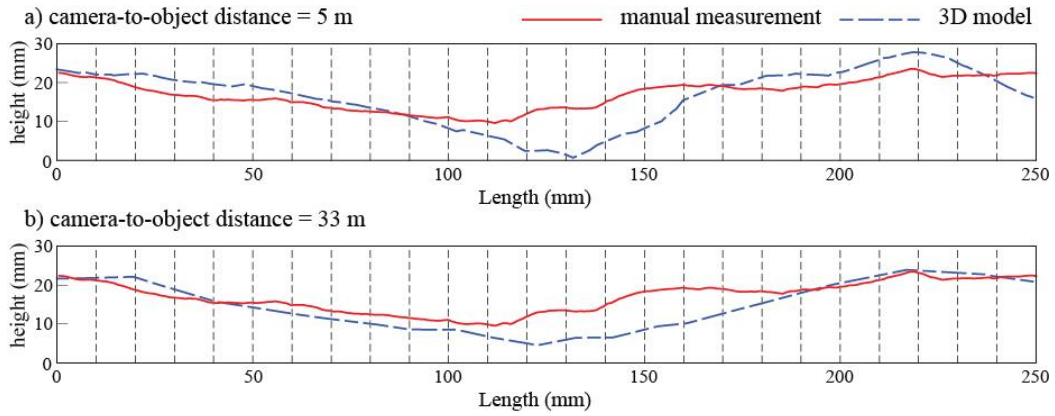
Fig. A2.7 Bethania, profile #2
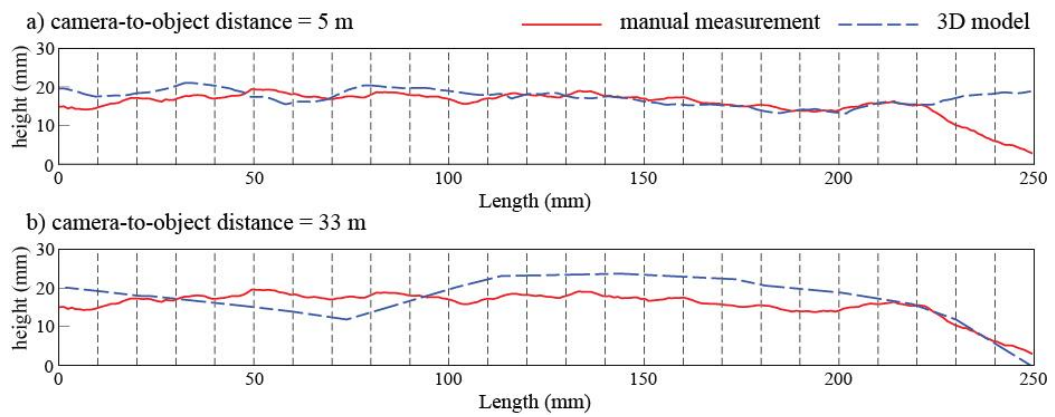
Fig. A2.8 Bethania, profile #3

A2.3 Nerang-Murwillumbah road, Gold Coast
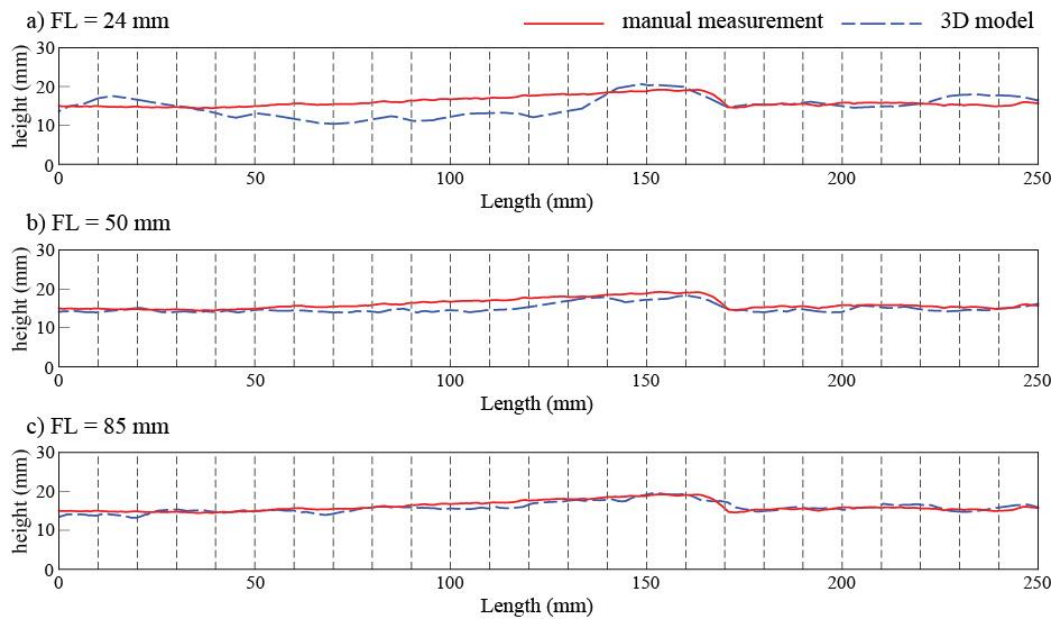
Fig. A2.9 Nerang-Murwillumbah road 1, section 1
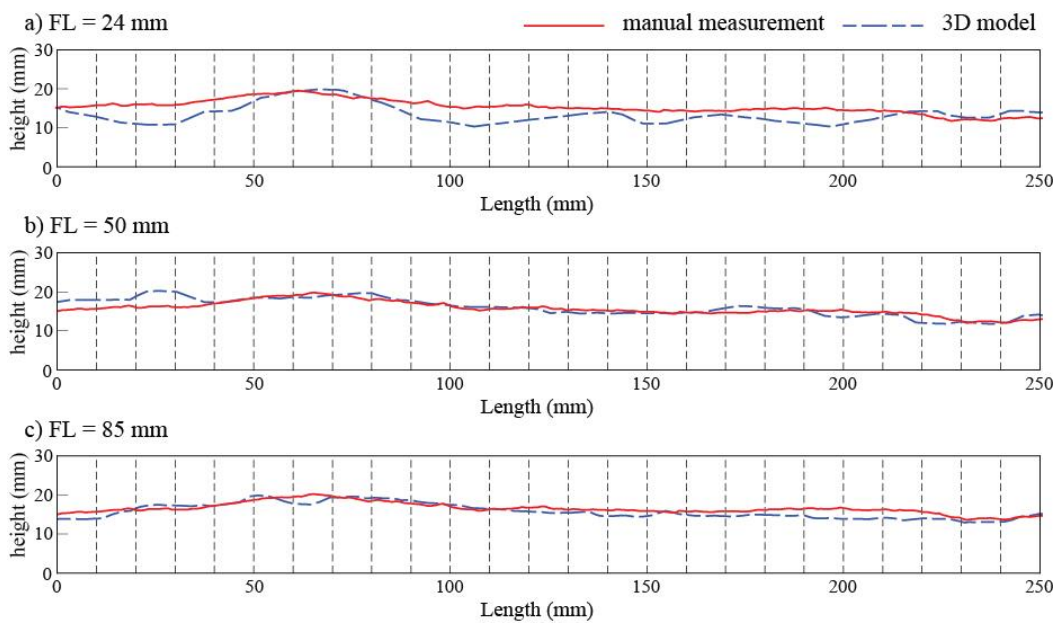
Fig. A2.10 Nerang-Murwillumbah road 1, section 2-1

225
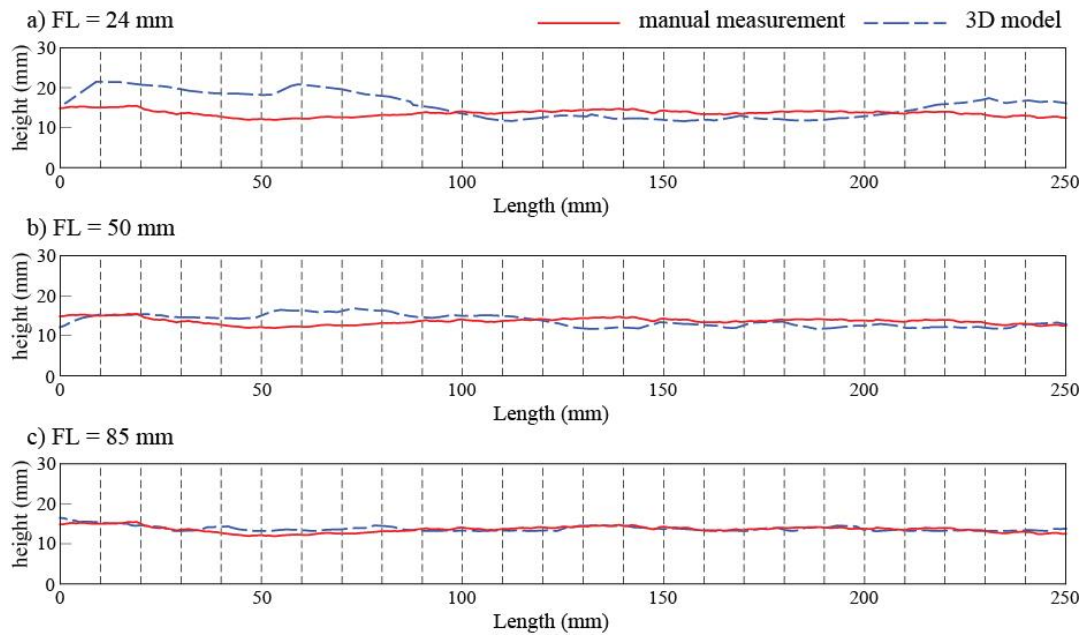
Fig. A2.11 Nerang-Murwillumbah road 1, section 2-2
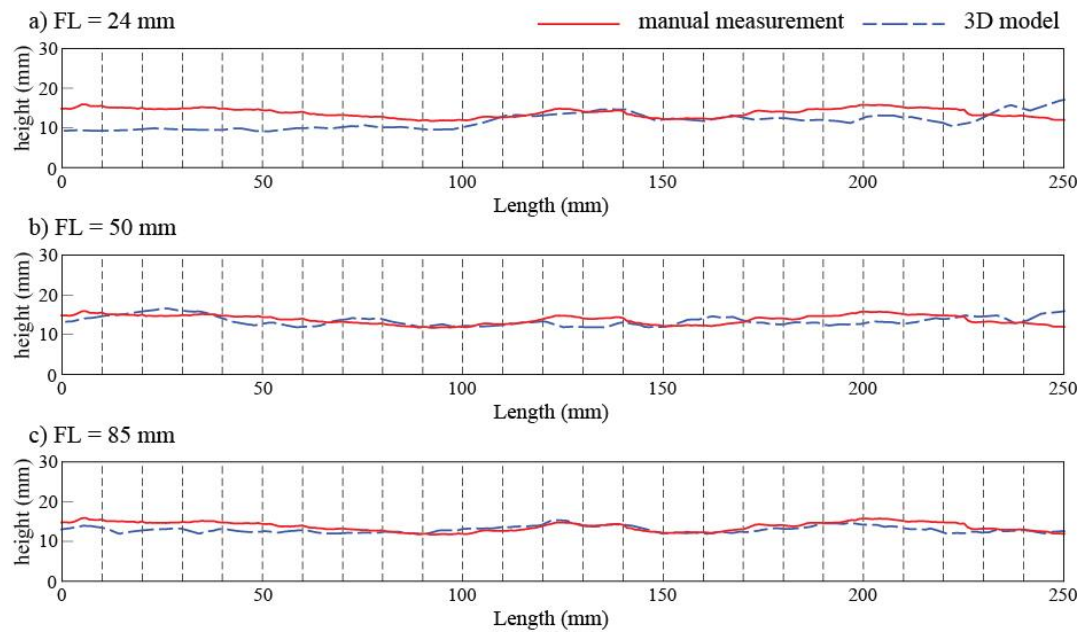
Fig. A2.12 Nerang-Murwillumbah road 2, section 1

226
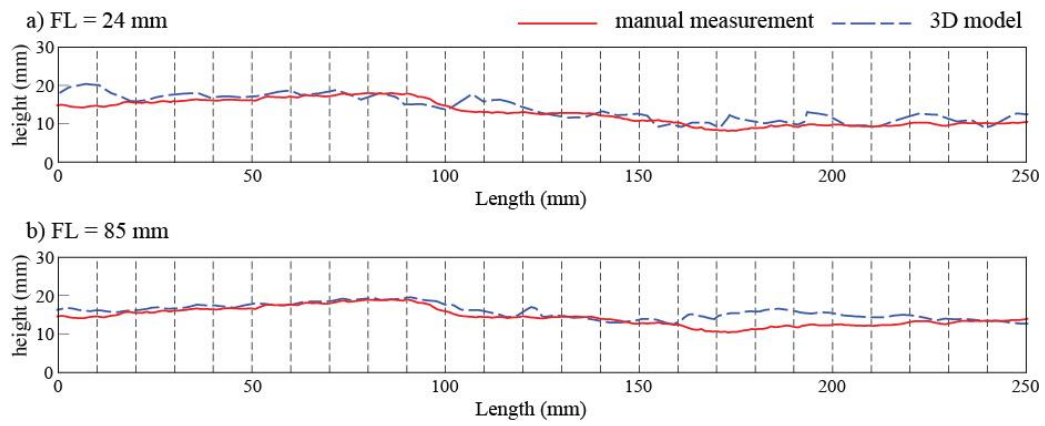
Fig. A2.13 Nerang-Murwillumbah road 2, section 2-1
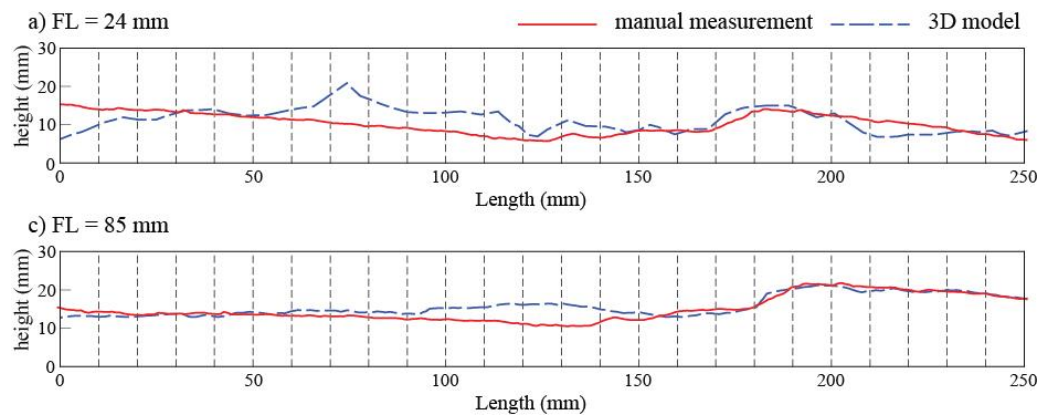
Fig. A2.14 Nerang-Murwillumbah road 2, section 2-2

A2.4 Engineering road, Gold Coast
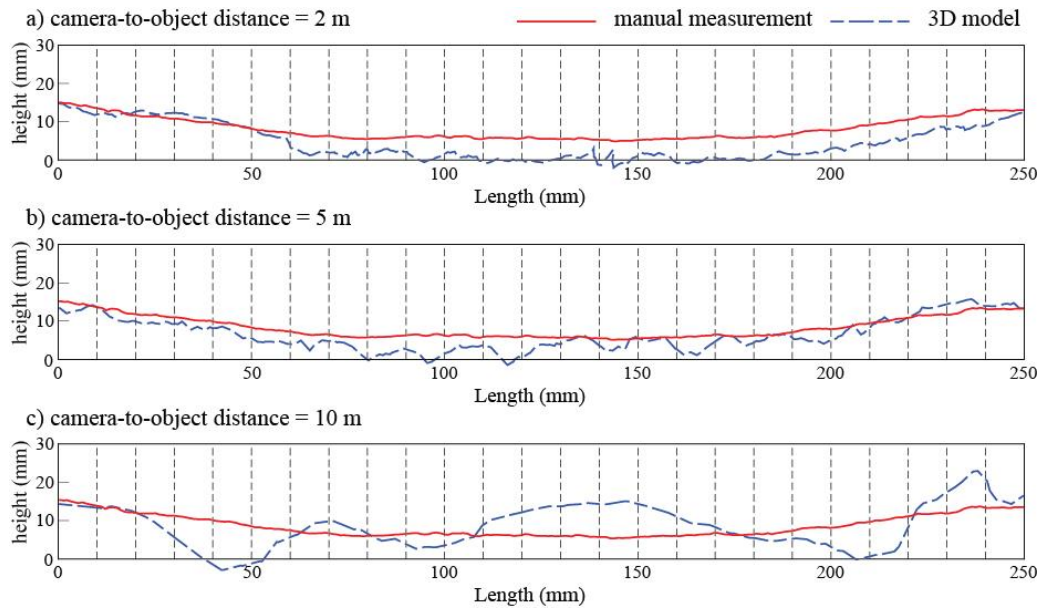
Fig. A2.15 FL = 24 mm, profile #2
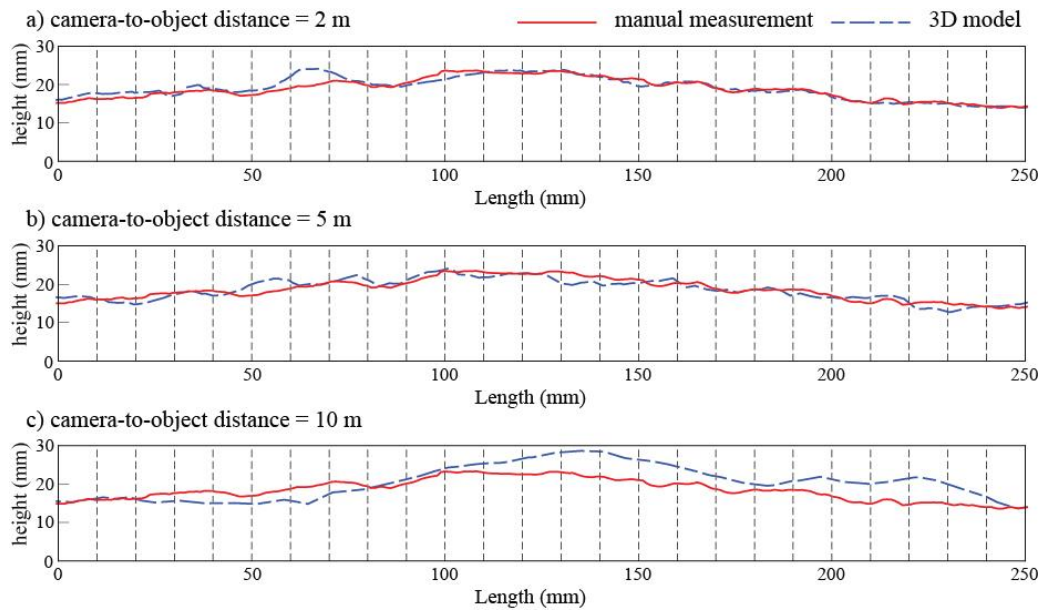
Fig. A2.16 FL = 24 mm, profile #5
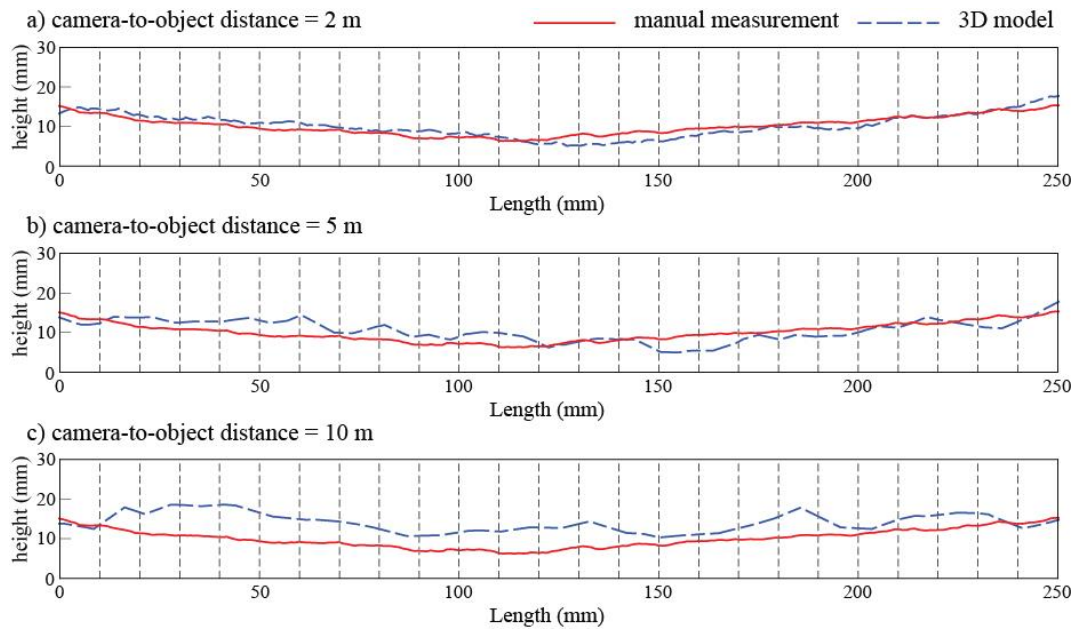
Fig. A2.17 FL = 24 mm, profile #12
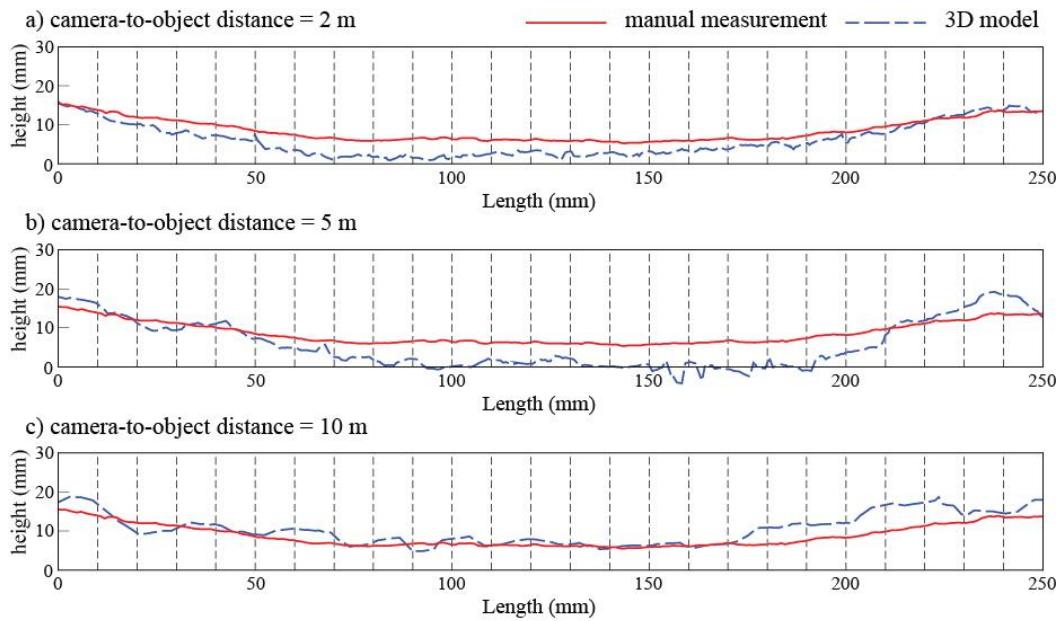
Fig. A2.18 FL = 50 mm, profile #2
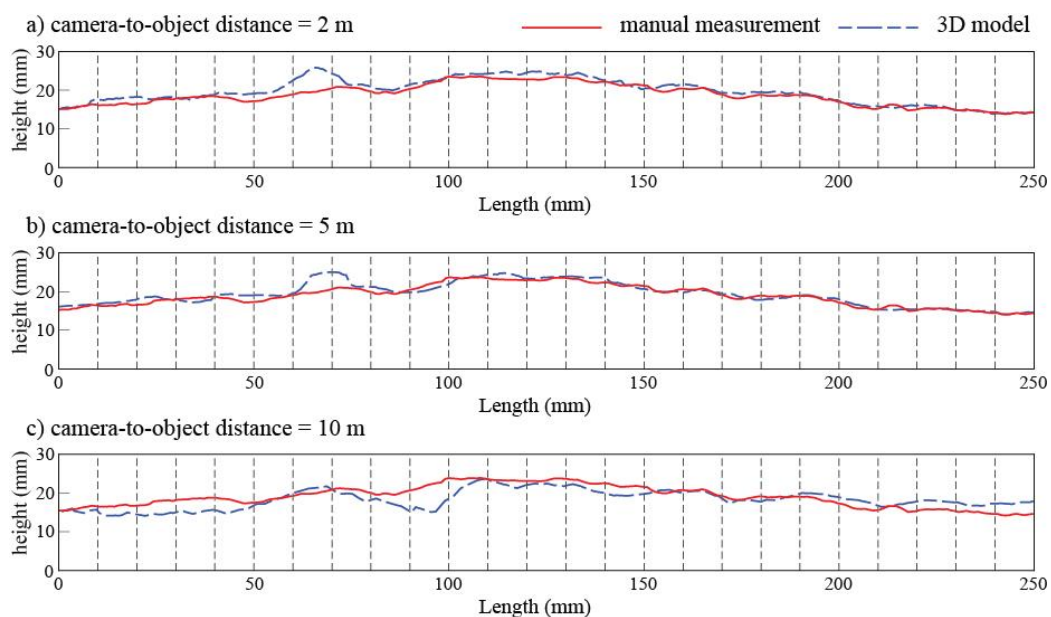
Fig. A2.19 FL = 50 mm, profile #5
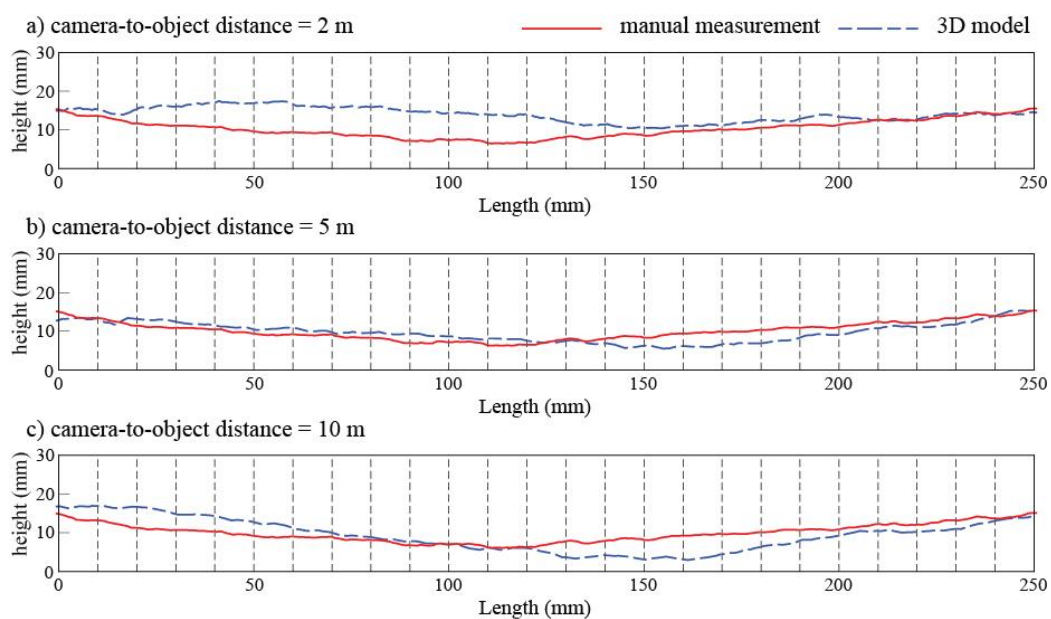
Fig. A2.20 FL = 50 mm, profile #12
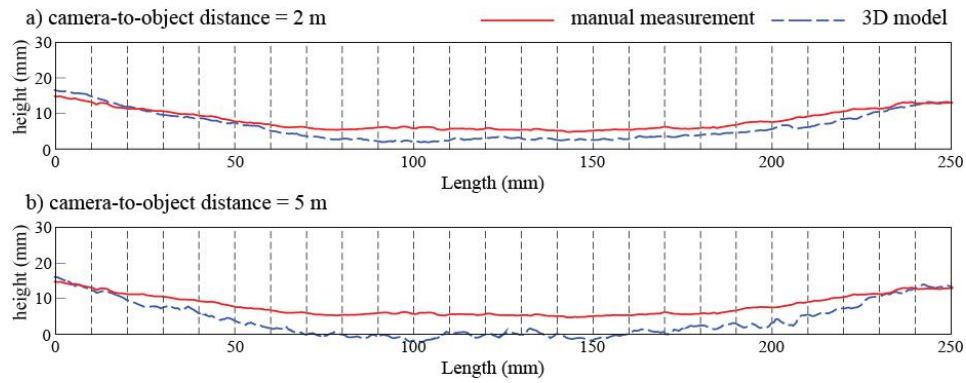
Fig. A2.21 FL = 85 mm, profile #2
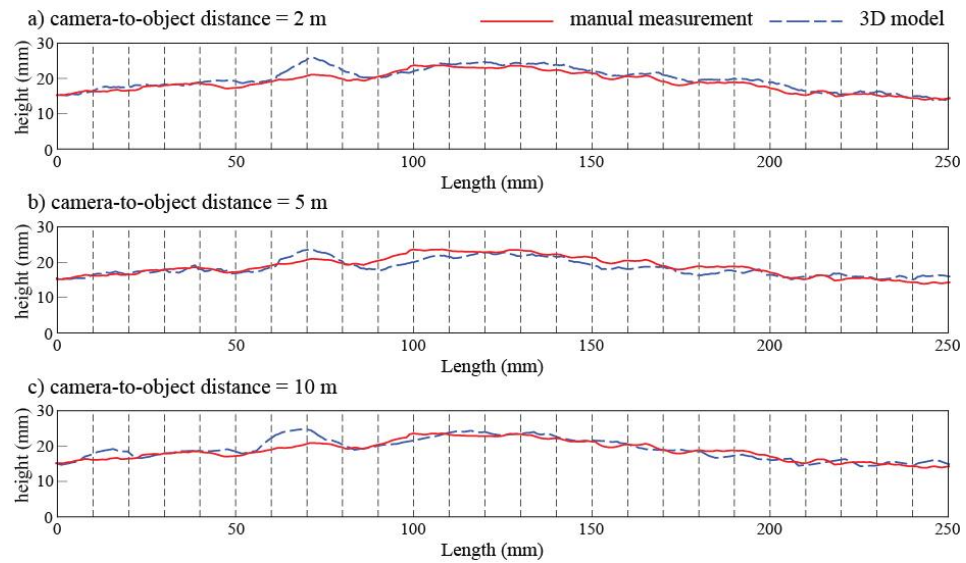
Fig. A2.22 FL = 85 mm, profile #5
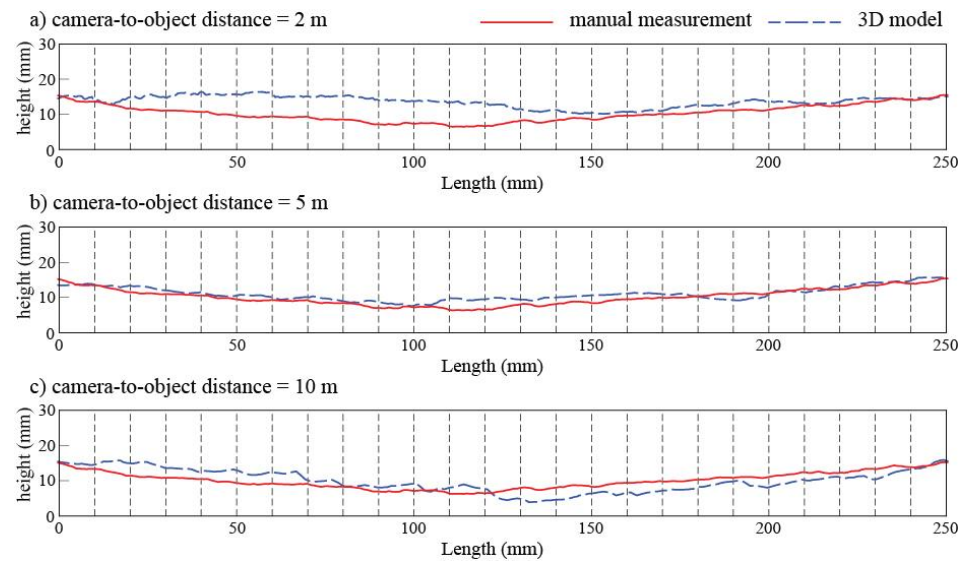
Fig. A2.23 FL = 85 mm, profile #12

231

Appendix 3. Stereographic projections of the fields

A3.1 Beaudesert Nerang road
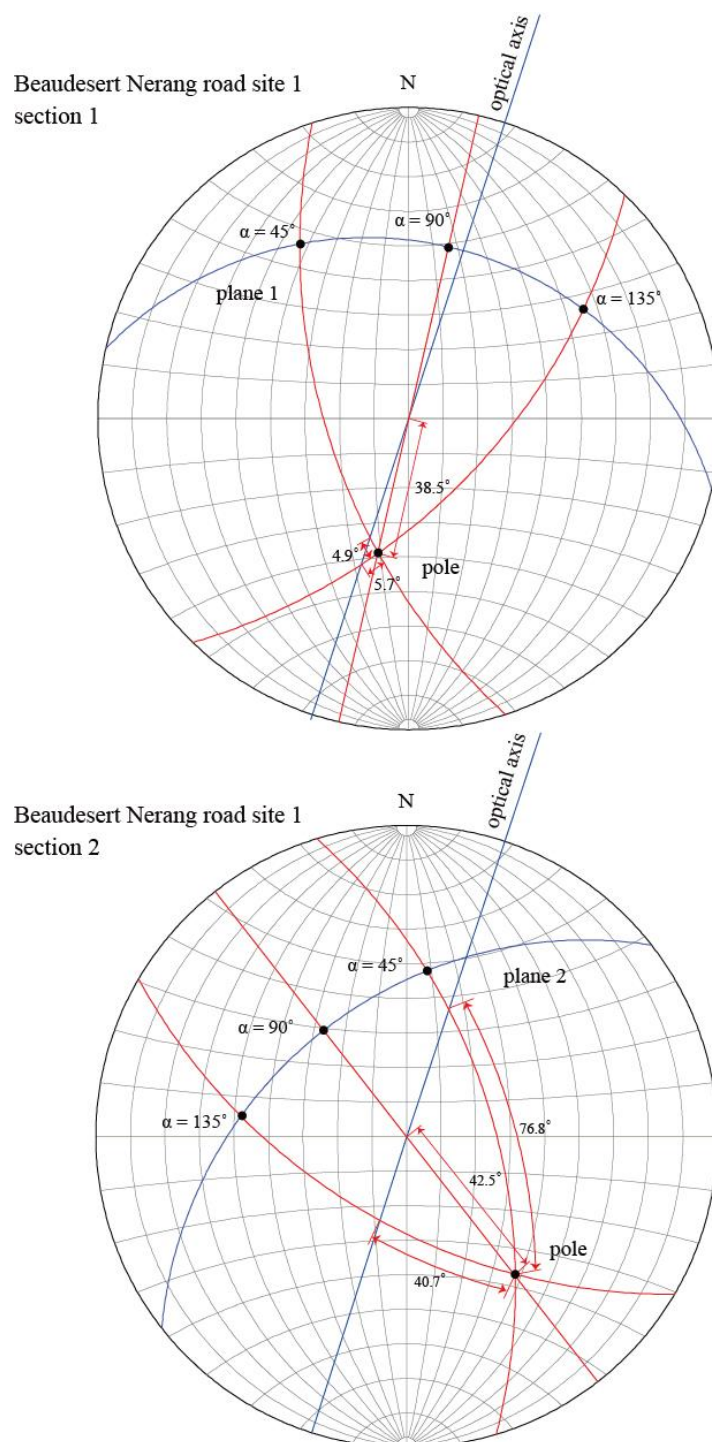
Fig. A3.1 Stereographic projections: Beaudesert Nerang road site 1 section 1 and 2
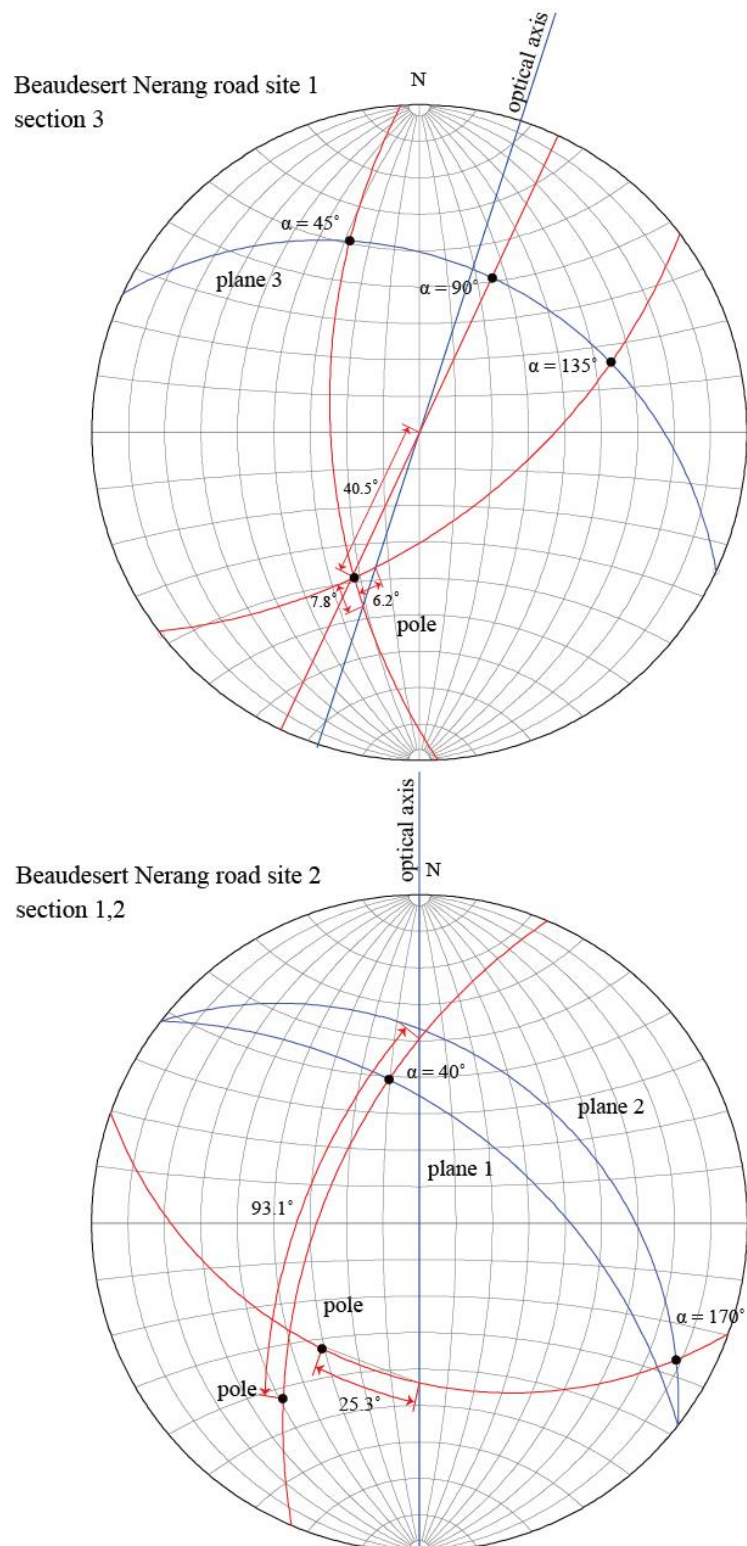
Fig. A3.2 Stereographic projections: Beaudesert Nerang road site 1 section 3, site 2 section 1 and 2

A3.2 Bethania, Brisbane, Nerang-Murwillumbah road 1
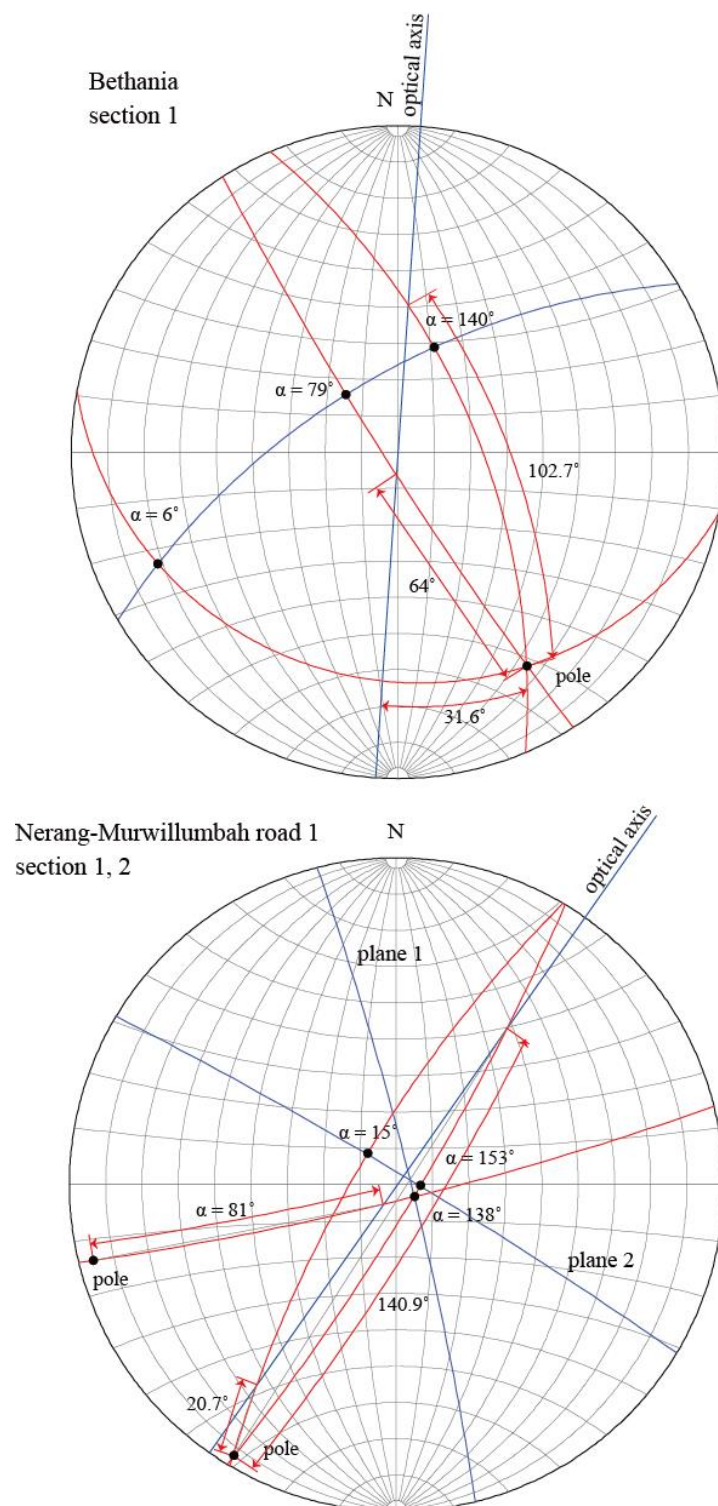
Fig. A3.4 Stereographic projections: Bethania site section 1, Nerang-Murwillumbah road 1 section 1 and 2

A3.3 Nerang-Murwillumbah road 2, Engineering road (section 1, 2)
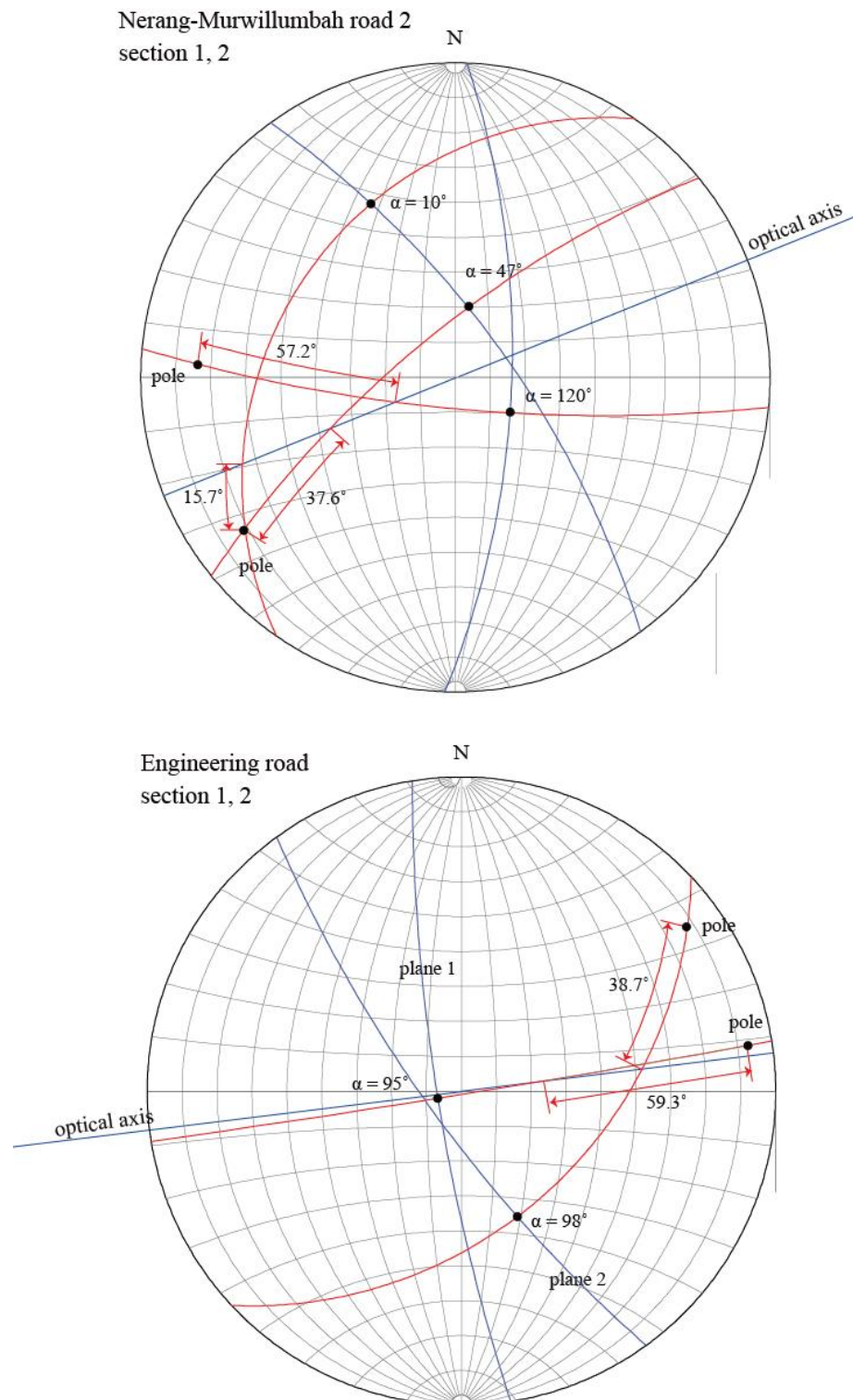
Fig. A3.5 Stereographic projections: Nerang-Murwillumbah road 2 section 1 and 2, Engineering road section 1 and 2

A3.4 Engineering road (section 3 ~ 6)
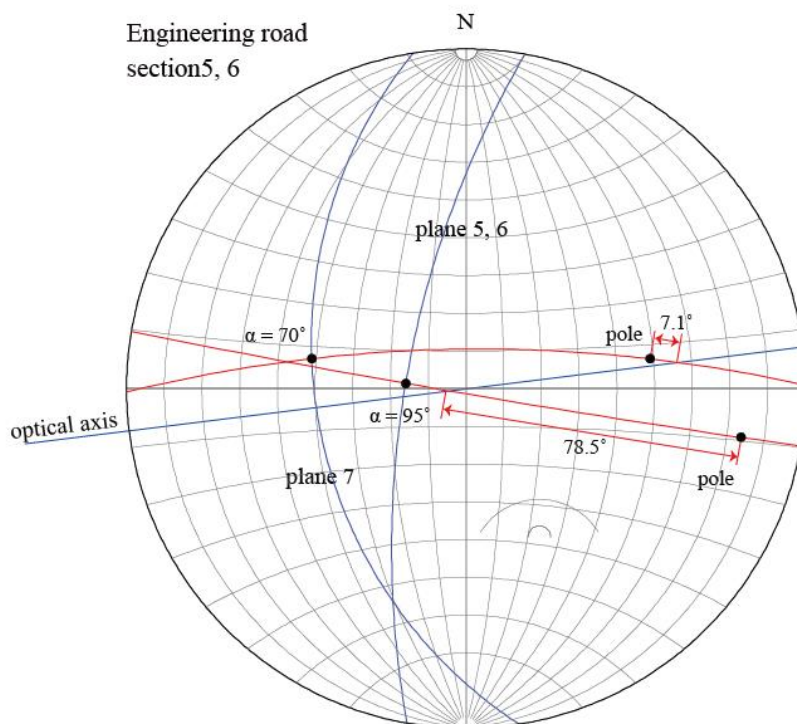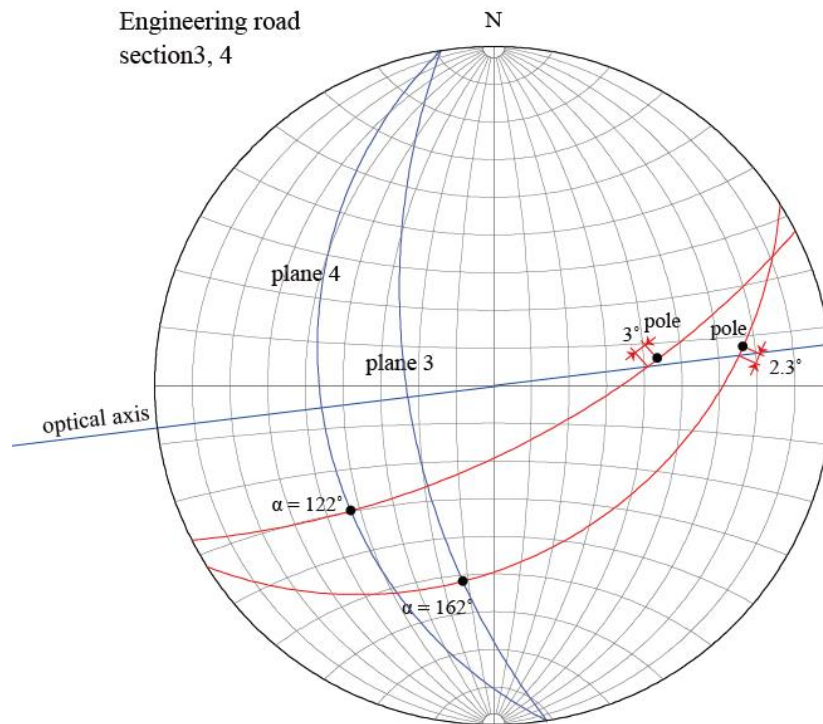
Fig. A3.6 Stereographic projections: Engineering road section 3 ~ 6

A3.5 Engineering road (section 8 ~ 12)
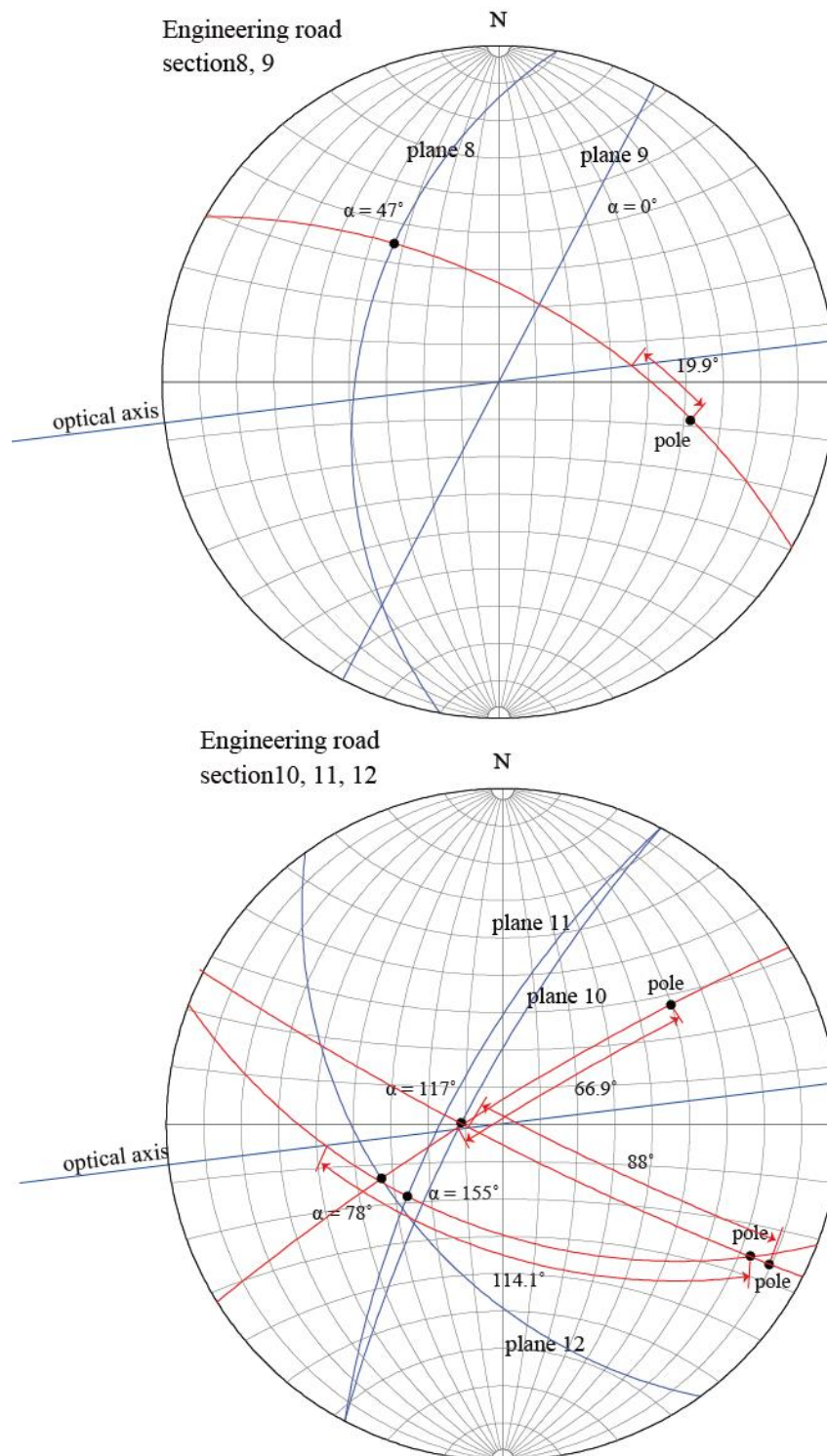
Fig. A3.7 Stereographic projections: Engineering road section 8 ~ 12

Appendix 4. Strength properties of the rock samples used in the study

A4.1 Point load test

Table A4-1. Point load test data sheet #1

Site:	Beaudesert Nerang road 1							
Date:	2 Oct 2012							
Rock type:	Sandstone							
Calculations	Unit	Samples						
		1	2	3	4	5	6	7	8
1. Width, W	mm	44.0	42.8	56.0	69.1	25.5	35.6	36.3	37.5
2. Depth, D	mm	38.0	56.8	28.5	24.9	44.5	41.5	40.0	71.5
3. Minimum cross sectional area, A	mm^2	1672.0	2431.0	1596.0	1720.6	1134.8	1477.4	1452.0	2681.3
4. Equivalent core diameter, D_e	mm	46.1	55.6	45.1	46.8	38.0	43.4	43.0	58.4
5. Point load strength, P	kN	0.667	1.318	6.339	3.460	1.711	0.815	1.292	0.861
6. Uncorrected point load strength, I_s	Mpa	0.313	0.426	3.149	1.579	1.184	0.433	0.699	0.252
7. Point load strength index, $I_{s\ (50)}$	-	0.302	0.447	3.006	1.533	1.047	0.406	0.653	0.271
8. Unconfined compressive strength, UCS*	Mpa	2.51	3.41	25.19	12.64	9.47	3.47	5.59	2.02

*, conversion factor (F) = 8

Table A4-2. Point load test data sheet #2

Site:		Beaudesert Nerang road 1							
Date:		2 Oct 2012							
Rock type:		Argillite, Shale							
Calculations	Unit	Samples							
		1	2	3	4	5	6	7	8
1. Width, W	mm	50.0	78.5	51.4	51.4	21.4	20.2	25.9	48.3
2. Depth, D	mm	24.0	22.0	43.4	47.8	46.3	34.6	36.4	45.2
3. Minimum cross sectional area, A	mm^2	1200.0	1727.0	2230.8	2456.9	990.8	698.9	942.8	2183.2
4. Equivalent core diameter, D_e	mm	39.1	46.9	53.3	55.9	35.5	29.8	34.6	52.7
5. Point load strength, P	kN	3.113	3.915	5.343	6.085	2.649	3.712	4.264	1.088
6. Uncorrected point load strength, I_s	Mpa	2.037	1.780	1.881	1.945	2.100	4.171	3.552	0.391
7. Point load strength index, $I_{s\,(50)}$	-	1.824	1.730	1.936	2.046	1.800	3.306	3.012	0.401
8. Unconfined compressive strength, UCS*	Mpa	16.30	14.24	15.05	15.56	16.80	33.37	28.42	3.13

*, conversion factor (F) = 8

A4.2 Schmidt hammer test

Table A4-3. Schmidt hammer test sheets 1

Site:		Beaudesert Nerang road 1		
Date:		25 Oct 2012		
Rock type:		Sandstone		
Test sections		Density (gm/cm^3)	Rebound no.	σ_{UCS} (MPa)	
				Yasar and Erdogan (2004) $\sigma_{UCS} = 0.000004 \times RL^{4.29}$	Katz et al. (2000) $\sigma_{UCS} = 2.21 \times e^{(0.07 \times RN)}$
A	1	2.57	19	1.22	8.36
	2	2.57	14	0.33	5.89
	3	2.57	19	1.22	8.36
	4	2.57	11	0.12	4.77
	5	2.57	17	0.76	7.26
B	6	2.57	16	0.59	6.77
	7	2.57	36	18.99	27.47
	8	2.57	35	16.83	25.61
	9	2.57	38	23.95	31.59
	10	2.57	29	7.51	16.83
C	11	2.57	37	21.36	29.46
	12	2.57	30	8.69	18.05
	13	2.57	16	0.59	6.77
	14	2.57	17	0.76	7.26
	15	2.57	45	49.47	51.57
D	16	2.57	32	11.46	20.76
	17	2.57	46	54.36	55.31
	18	2.57	28	6.46	15.69
	19	2.57	29	7.51	16.83
	20	2.57	40	29.85	36.34
Average				13.1	20.0

Table A4-4. Schmidt hammer test sheets 2

Site:		Beaudesert Nerang road 1			
Date:		25 Oct 2012			
Rock type:		Argillite, Shale			
Test sections		Density (gm/cm^3)	Rebound no.	σ_{UCS} (MPa)	
				Yasar and Erdogan (2004) $\sigma_{UCS} = 0.000004 \times RL^{4.29}$	Katz et al. (2000) $\sigma_{UCS} = 2.21 \times e^{(0.07 \times RN)}$
A	1	2.73	27	5.53	14.63
	2	2.73	31	10.00	19.36
	3	2.73	29	7.51	16.83
	4	2.73	30	8.69	18.05
	5	2.73	27	5.53	14.63
B	6	2.73	29	7.51	16.83
	7	2.73	35	16.83	25.61
	8	2.73	25	3.97	12.72
	9	2.73	41	33.18	38.98
	10	2.73	32	11.46	20.76
C	11	2.73	17	0.76	7.26
	12	2.73	24	3.34	11.86
	13	2.73	23	2.78	11.06
	14	2.73	27	5.53	14.63
	15	2.73	26	4.70	13.64
D	16	2.73	46	54.36	55.31
	17	2.73	33	13.08	22.26
	18	2.73	49	71.29	68.24
	19	2.73	29	7.51	16.83
	20	2.73	46	54.36	55.31
Average				16.4	23.7

Reference

ADAM Technology (2002) 3DM Analyst focussing on the future, www.adamtech.com.au 10 pages

ADAM Technology (2008) Laser scanning vs digital photogrammetry, technical report, 8 pages

Admassu Y, Shakoor A, Wells NA (2012) Evaluating selected factors affecting the depth of undercutting in rocks subject to differential weathering. Eng Geol 124: 1-11

Agliardi F, Crosta GB (2003) High resolution three-dimensional numerical modelling of rockfalls. Int J Roc Mech Min Sci 40:455-471

American Society for Photogrammetry & Remote Sensing (2014) ASPRS positional accuracy standards for digital geospatial data. PE & RS 81(3): A1-A26

Andrew R et al., (2012) CRSP-3D User's Manual Colorado rockfall simulation program. Technical report, FHWA-CFL/TD-12-007

Arikan F, Ulusay R, Aydin N (2007) Characterization of weathered acidic volcanic rocks and a weathering classification based on a rating system. Bull Eng Geol Env 66: 415-430

AS 4133.4.1 (2007) Method 4.1 : Rock strength tests – Determination of point load strength index

Asteriou P, Saroglou H, Tsiambaos G (2012) Geotechnical and kinematic parameters affecting the coefficients of restitution for rock fall analysis. Int J Roc Mech Min Sci 54:103-113

Aydan Ö, Shimizu Y, Kawamoto T (1996) The anisotropy of surface morphology characteristics of rock discontinuities. Rock Mech. Rock Engng 29:1:47-59

Azzoni A, La Barbera G, Zaninetti A (1995) Analysis and prediction of rockfalls using a mathematical model. Int J Rock Mech Min Sci Geomech Abstr 32: 709-724

Azzoni A, de Freitas MH (1995) Experimentally gained parameters, decisive for rock fall analysis. Rock Mech Rock Eng 28(2): 111-124

Bae D, Kim K, Koh Y, Kim J (2011) Characterization of joint roughness in granite by applying the scan circle technique to images from a borehole televiewer. Rock Mech. Rock Engng. 44:497-504

Baker BR, Gessner K, Holden EJ, Squelch A (2008) Automatic detection of anisotropic features on rock surfaces. Geosphere 2008 4(2): 418-428

Baltsavias EP (1999) A comparison between photogrammetry and laser scanning. ISPRS Journal of Photogrammetry & Remote Sensing, 54:83-94.

Bandis S, Lumsden AC, Barton NR (1981) Experimental studies of scale effects on the shear behaviour of rock joints. Int J Rock Mech Min Sci Geomech Abstr 18:1-21.

Bandis SC, Lumsden AC, Barton NR (1983) Fundamentals of rock joint deformation. Int J Rock Mech Min Sci & Geomech. Abstr 20: 6: 249-268

Barton N (1973) Review of a new shear-strength criterion for rock joints. Engineering Geology. 7:287-332

Barton N (1976) The shear strength of rock and rock joints. Int J Rock Mech Min Sci Geomech Abstr 13:255-279.

Barton N (1981) Shear strength investigations for surface mining. Chapter 7 and discussion, Vancouver :171-196.

Barton N, Bandis S (1980) Some effects of scale on the shear strength of joints. Int J Rock Mech Min Sci Geomech Abstr 17:69-73.

Barton N, Bandis S, Bakhtar K (1985) Strength, deformation and conductivity coupling of rock joints. Int J Rock Mech Min Sci & Geomech Abstr 22(3):121-140

Barton N, Choubey V (1977) The shear strength of rock joints in theory and practice. Rock Mech 10:1-54.

Basson FRP (2012) Rigid body dynamics for rock fall trajectory simulation. The 46th US Rock Mechanics / Geomechanics Symposium, ARMA 12-267

Belem T, Souley M, Homand F (2007) Modeling surface roughness degradation of rock joint wall during monotonic and cyclic sharing. Acta Geotechnica 2:227-248

Bemis SP, Micklethwaite S, Turner D, James MR, Akciz S, Thiele ST, Bangash HA (2014) Ground-based and UAV-based photogrammetry: A multi-scale, high-resolution mapping tool for structural geology and paleoseismology. J Struct Geol 69: 163-178

Birch J (2006) Using 3DM analyst mine mapping suite for rock face characterization. In: Tonon F, Kottenstette JT (eds) Laser and photogrammetric methods for rock face characterization, American Rock Mechanics Association, Alexandra, pp 13-32

Bistacchi A, Griffith WA, Smith SAF, Di Toro G, Jones R, Nielsen S (2011) Fault roughness at seismogenic depths from LIDAR and photogrammetric analysis. Pure Appl Geophys, 168: 2345-2363

Brideau M-A, Sturzenegger M, Stead D, Jaboyedoff M, Lawrence M, Roberts N, Ward B, Millard T, Clague J (2011) Stability analysis of the 2007 Chehalis lake landslide based on long-range terrestrial photogrammetry and airbone LiDAR data. Landslides 9:75-91

Broch E, Franklin JA (1972) The point load strength test. Int J Rock Mech Min Sci 9: 669-697

Buzzi O, Giacomini A, Spadari M (2012) Laboratory investigation on high values of restitution coefficients. Rock Mech Rock Eng 45(1): 35-43

Butler JB, Lane SN, Chandler JH (1998) Assessment of DEM quality for characterizing surface roughness using close range digital photogrammetry. Photogrammetric Record 16(92): 271-291

Cai M, Kaiser PK, Uno H, Tasaka Y, Minami M (2004) Estimation of rock mass deformation modulus and strength of jointed hard rock masses using the GSI system. Int J Rock Mech Min Sci 41: 3-19

Cai M, Kaiser PK (2006) Visualization of rock mass classification systems. Geotech Geol Eng 24: 1089-1102

Carr JR, Warriner JB (1989) Relationship between the fractal dimension and joint roughness coefficient. Bull. Association of engineering geologists, XXVI(2): 253-263.

Chai T, Draxler RR (2014) Root mean square error (RMSE) or mean absolute error (MAE)? - Arguments against avoiding RMSE in the literature. Geosci Model Dev, 7: 1247-1250

Chau KT, Wong RHC, Wu JJ (2002) Coefficient of restitution and rotation motions of rockfall impacts. Int J Roc Mech Min Sci 39: 69-77

Christen M, Kowalski J, Bartelt D (2010) RAMMS: Numerical simulation of dense snow avalanches in three-dimensional terrain. Cold Reg Sci Technol, 63: 1-14

Cravero M, Iabichino G, Ferrero AM (2001) Evaluation of joint roughness and dilatancy of schistosity joints. In: Proceedings of Eurock 2001, Espoo, pp 217-222

CSIRO (2005) Field procedures for photogrammetric pit mapping. CSIRO Exploration & Mining

CSIRO (2012) Field procedures for photogrammetric pit mapping. CSIRO Exploration & Mining

Dai F, Feng Y, Hough R (2014) Photogrammetric error sources and impacts on modelling and surveying in construction engineering applications. Visualization in engineering 2:2:1-14.

Dai F, Lu M (2008) Photo-based 3d modelling of construction resources for visualization of operations simulation: case of modelling a precast façade. In: Proceedings of the 2008 Winter Simulation Conference, Washington, D. C., pp 2439-2466

Dai F, Lu M (2010) Assessing the accuracy of applying photogrammetry to take geometric measurements on building products. J Constr Eng Manag 136: 242-225

Dick JC, Shakoor A, Wells N (1994) A geological approach toward developing a mudrock-durability classification system. Can Geotech J 31: 17-27

Dold J (1996) Influence of large targets on the results of photogrammetry. International Archives of Photogrammetry and Remote Sensing, Vol.31, Part B5, Vienna, p.119-123

Dorren LKA, Berger F, Putters US (2006) Real-size experiments and 3-D simulation of rockfall on forested and non-forested slopes. Nat. Hazards Earth Syst Sci, 6: 145-153

Duncan CW, Christopher WM (2004) Rock slope engineering. 4th edition, Taylor & Francis.

Ehlen J (1999) Fracture characteristics in weathered granites. Geomorphology 31: 29-45

Fardin N (2008) Influence of structural non-stationarity of surface roughness on morphological characterization and mechanical deformation of rock joints. Rock Mech Rock Eng; 41:267-97.

Fardin N, Feng Q, Stephansson O (2004) Application of a new in situ 3D laser scanner to study the scale effect on the rock joint surface roughness. Int J Rock Mech Min Sci ;41:329-335.

Fekete S, Diederichs M, Lato M (2010) Geotechnical and operational applications for 3-dimensional laser scanning. Tunn Undergr Sp Tech;25:614-28.

Feng Q, Fardin N, Jing L, Stephansson O (2003) A new method for in-situ non-contact roughness measurement of large rock fracture surfaces. Rock Mech Rock Eng;36:1:3-25.

Ferrero AM, Migliazza M, Roncella R, Rabbi E (2011a) Rock slopes risk assessment based on advanced geostructural survey techniques. Landslides 8:221-231

Ferrero AM, Migliazza M, Roncella R, Segalini A (2011b) Rock cliffs hazard analysis based on remote geostructural surveys: The Campione del Garda case study (Lake Garda, Northern Italy). Geomorphology 125:457-471

Firpo G, Salvini R, Francioni M, Ranjith PG (2011) Use of digital terrestrial photogrammetry in rocky slope stability analysis by distinct elements numerical methods. Int J Rock Mech Min Sci 48:1045-1054

Fonstad MA, Dietrich JT, Courville BC, Jensen JL, Carbonneau PE (2013) Topographic structure from motion: a new development in photogrammetric measurement. Earth Surf Process Landforms 38: 421-430

Fooladgar F, Samavi S, Soroushmehr SMR, Shirani S (2013) Geometrical analysis of localization error in stereo vision systems. IEEE sensors journal 13:11:4236-4246.

Fraser CS (1984) Network design considerations for non-topographic photogrammetry. Photogrammetric engineering and remote sensing 50:8:1115-26.

Fraser CS (1992) Photogrammetric measurement to one part in a million. Photogrammetric Engineering and Remote Sensing 58(3): 305-310.

Fraser CS (1996) Network design. Close range photogrammetry and machine vision, Whittles Publishing UK, 371p.

Franklin JA, Chandra A (1972) The slake durability test. Int J Rock Mech Min Sci 9: 325-341

Franklin JA, Maerz NH, Bennett CP (1988) Rock mass characterization using photoanalysis. Int J Min Geol Eng 6: 97-112

Gaich A, Potssch M, Schubert W (2006) Basics and application of 3D imaging systems with conventional and high-resolution cameras. In: Tonon F, Kottenstette JT (eds) Laser and photogrammetric methods for rock face characterization, American Rock Mechanics Association, Alexandra, pp 33-48

Giacomini A, Thoeni K, Lambert C (2012) Improved management of the rock fall hazard at the base of the highwalls. ACARP project report C19026

Giovanni G, Stefano M, Simone F, Nicola C (2014) Terrestrial laser scanner and geomechanical surveys for the rapid evaluation of rock fall susceptibility scenarios. Landslides, 11: 1-14, DOI 10.1007/s10346-012-0374-0

Goodman RE (1989) Introduction to rock mechanics. John Wiley & Sons, New York

Goodman RE, Shi G-H (1985) Block theory and its application to rock engineering, Prentice-Hall Inc., New Jersey

Gómez-Pujol L, Fornos JJ, Swantesson OH (2006) Rock surface millimetre-scale roughness and weathering of supratidal Mallorcan carbonate coasts (Balearic Islands). Earth Surface Processes and Landforms 31: 1791-1801

Graf CC, Peryoga T, McCartney G, Rees T (2013) Verification of Trajec3D for use in rockfall analysis at Newmont Boddington Gold. Proc. Slope Stability 2013, Brisbane: 1231-1241

Grasselli G (2001) Shear strength of rock joints based on quantified surface description. Ph.D. dissertation, Ecole Polytechnique Fédérale de Lausanne.

Grasselli G, Egger P (2000) 3D surface characterization for the prediction of the shear strength of rough joint. In: Proceedings of Eurock 2000. Wittke: Aachen, Germany;p.281-6.

Grasselli G, Wirth J, Egger P (2002) Quantitative three-dimensional description of a rough surface and parameter evolution with shearing. Int J Rock Mech Min Sci ;39:789-800.

Grasselli G, Egger P (2003) Constitutive law for the shear strength of rock joints based on three-dimensional surface parameters. Int J Rock Mech Min Sci ;40:25-40.

Gratchev I, Shokouhi A, Kim DH, Stead D, Wolter A (2013) Assessment of rock slope stability using remote sensing technique in the Gold Coast area, Australia. Proceedings of Advances in geotechnical infrastructure, Singapore, pp 729-734

Guo H, Karekal S, Poropat GV, Soole P, Lambert C (2011) Pit wall strength estimation with 3D imaging. CSIRO project paper, ACARP.

Guzzetti F, Crosta G, Detti R, Agliardi F, (2002) STONE: a computer program for the three-dimensional simulation of rock-falls. Computers and Geosciences, 28: 1079-1093

Haneberg WC (2007) Directional roughness profiles from three-dimensional photogrammetric or laser scanner point clouds. In: Proceedings of the 1st Canada-U.S. rock mechanics symposium, Vancouver; p.101-6.

Haneberg WC, Norrish NI, Findley DP (2006) Digital outcrop characterization for 3-D structural mapping and rock slope design along interstate 90 near Snoqualmie pass, Washington. In: Proceedings of the 57th annual highway geology symposium, Colorado; p.1-14.

Haneberg WC (2008) Using close range terrestrial digital photogrammetry for 3-D rock slope modelling and discontinuity mapping in the United States. Bull Eng Geo Environ, 67:457-469

Harami KY, Zhang R, Rock A (2013) CRSP-3D Application for remediating a rockfall at Yosemite national park. Proc. Geo-Congress ASCE: 592-603

Hatzor YH, Goodman RE (1997) Three-dimensional back-analysis of saturated rock slopes in discontinuous rock-a case study. Geotechnique 47(4):817-839

Hatzor YH, Feintuch A (2005) The joint intersection probability. Int Jour Rock Mech Min Sci 42:531-541

Hoek E (1994) Strength of rock and rock masses. ISRM News Journal 2(2): 4-16

Hoek E, Brown ET (1997) Practical estimates of rock mass strength. Int J Rock Mech Min Sci 34(8): 1165-1186

Hoek E, Carranza-Torres C, Corkum B (2002) Hoek-Brown failure criterion-2002 edition. In: Proceedings of NARMS-TAC conference, Toronto, pp 267-273

Hoek E, Marinos P, Benissi M (1998) Applicability of the geological strength index (GSI) classification for very weak and sheared rock masses. The case of the Athens Schist Formation. Bulletines of Engineering Geology and Environment 57: 151-160

Hong ES, Lee IM, Lee JS (2006) Measurement of rock joint roughness by 3D scanner. ASTM Geotechnical Testing Journal ;26: 6: 482-9.

Hong ES, Lee JS. Lee IM (2008) Underestimation of roughness in rough rock joints. Int. J. Numer. Anal. Meth. Geomech; 32:1385-1403

Hsiung SM, Ghosh A, Ahola MP, Chowdhury AH (1993) Assessment of conventional methodologies for joint roughness coefficient determination. Int J Rock Mech Min Sci Geomech Abstr 30(7): 329-343

Hsiung SM, Kana DD, Ahola MP, Chowdhury AH, Ghosh A (1994) Laboratory characterization of rock joints. Ctr. for nuclear waste regulatory analyses, San Antonio, Tex., Tech. Rep. Prepared for U.S. Nuclear Regulatory Commission.

Huang TK, Chen JC, Chang CC (2003) Stability analysis of rock slopes using block theory, Journal of the Chinese institute of Engineers 26(3):353-359

Hudson J, Harrison J (1997) Engineering rock mechanics: An introduction to the principles. Oxford, Elsevier Science Ltd.

Hudson JA, Priest SD (1983) Discontinuity frequency in rock masses. Int J Rock Mech Min Sci Geomech Abstr 20(2):73-89.

ISRM (1978) Suggested methods for the quantitative description of discontinuities in rock masses. Int J Rock Mech Min Sci Geomech Abstr 15: 319-368

Itasca Consulting Group Inc. (2011) Universal Distinct Element Code (UDEC) User's guide. Third edition, www.itascacg.com

Itasca Consulting Group Inc. (2013) 3 dimensional Discrete Element Modeling (3DEC) User's guide. www.itascacg.com

James MR, Robson S (2012) Straightforward reconstruction of 3D surface and topography with a camera: Accuracy and geoscience application. J Geophys Res 117: F03017

James MR, Robson S (2014) Mitigating systematic error in topographic models derived from UAV and ground-based image networks. Earth Surf Process Landforms 39: 1413-1420

Jessell MW, Cox SJD, Schwarze P, Power W (1995) The anisotropy of surface roughness measured using a digital photogrammetric technique. Fractography: fracture topography as a tool in fracture mechanics and stress analysis, Geological Society Special Publication 92: 27-37

Jian Y, Tanabashi Y, Li B, Xiao J (2006) Influence of geometrical distribution of rock joints on deformational behaviour of underground opening. Tunnelling and Underground Space Technology 21: 485-491

Jing L, Nordlund E, Stephansson O (1992) An experimental study on the anisotropy and stress-dependency of the strength and deformability of rock joints. Int J Rock Mech Min Sci & Geomech. Abstr 29: 6: 535-542

Katz O, Reches Z, Roegiers J-C (2000) Evaluation of mechanical rock properties using a Schmidt Hammer. Int J Rock Mech Min Sci 37 : 723-728

Khoshelham K, Altundag D, Ngan-Tillard D, Menenti M (2011) Influence of range measurement noise on roughness characterization of rock surface using terrestrial laser scanning. Int J Rock Mech Min Sci;48:1215-23.

Kim DH, Gratchev I, Balasubramaniam AS (2013a) Determination of joint roughness coefficient (JRC) for slope stability analysis: a case study from the Gold Coast area, Australia. Landslides 10:657-664

Kim DH, Gratchev I, Poropat GV (2013b) The determination of joint roughness coefficient using three-dimensional models for slope stability analysis. In:

Proceedings of the 2013 International symposium on slope stability in open pit mining and civil engineering, Brisbane, pp 281-289

Kim DH, Gratchev I, Balasubramaniam AS (2014) Back analysis of a natural jointed rock slope based on the photogrammetry method. Landslides; 12; 147-154

Kim DH, Gratchev I, Balasubramaniam AS (2015a) A photogrammetric approach for stability analysis of weathered rock slopes. Geotechnical and Geological Engineering, 33, 443-454

Kim DH, Gratchev I, Berends J, Balasubramaniam AS (2015b) Calibration of restitution coefficients using rockfall simulations based on 3D photogrammetry model: a case study. Nat Hazards 78: 1931-1946

Kim DH, Poropat GV, Gratchev I, Balasubramaniam AS (2015c) Improvement of photogrammetric JRC data distributions based on parabolic error models. Int J Rock Mech Min Sci 80: 19-30

Kim DH, Gratchev I, Oh E, Balasubramaniam AS (2016) Assessment of rock slope weathering based on the alteration of photogrammetric roughness data. In: Proceedings of the 19th Southeast Asian Geotechnical Conference & 2nd AGSSEA Conference (19SEAGC & 2AGSSEA), Kuala Lumpur, pp 901-906

Krosley L, Shaffner P (2003) Applications and accuracy of photogrammetry for geological and geotechnical data collecting. Association of Engineering Geologist 2003 annual meeting abstracts

Kulatilake PHSW, Balasingam P, Park J, Morgan R (2006) Natural rock joint roughness quantification through fractal techniques. Geotechnical and Geological Engineering 24: 1181-1202.

Kulatilake PHSW, Shou G, Huang TH, Morgan RM (1995) New peak shear strength criteria for anisotropic rock joints. Int J Rock Mech Min Sci & Geomech. Abstr 32: 7: 673-697

Kulatilake PHSW and Um J (1999) Requirements for accurate quantification of self-affine roughness using the roughness-length method. Int J Rock Mech Min Sci and Geomech Abstr 36;1:5-18

Kulatilake PHSW, Um J, Panda BB, Nghiem N (1999) Development of new peak shear-strength criterion for anisotropic rock joints. J Eng Mech 125:1010-1017

Kulatilake PHSW, Wang L, Tang H, Liang Y (2011) Evaluation of rock slope stability for Yujian River dam site by kinematic and block theory analyses. Computers and Geotechnics 38:846-860

Lee HS, Ahn KW (2004) A prototype of digital photogrammetric algorithm for estimating roughness of rock surface. Geosciences Journal 8(3): 333-341.

Lee IM, Park JK (2000) Stability analysis of tunnel keyblock: a case study. Tunnelling and Underground Space Technology 15 (4): 453-462

Lee YH, Carr JR, Barr DJ, Haas CJ (1990) The fractal dimension as a measure of the roughness of rock discontinuity profiles. Int J Rock Mech Min Sci Geomech Abstr 27:453-464.

Leine RI, Schweize A, Christen M, Glover J, Bartelt P, Gerber W (2013) Simulation of rockfall trajectories with consideration of rock shape. Multibody Syst Dyn, DOI 10.1007/s11044-013-9393-4

Look BG, Griffiths SG (2001) An engineering assessment of the strength and deformation properties of Brisbane rocks. Australian Geomechanics 36(3):17-30

Lyman GJ (2003) Rock fracture mean trace length estimation and confindence interval calculation using maximum likelihood methods. Int J Rock Mech Min Sci 40:825-832.

Madeira S, Goncalves J, Bastos L (2010) Photogrammetric mapping and measuring application using MATLAB. Computers & Geoscience 36:699-706

Maerz NH, Franklin JA, Bennett CP (1990) Joint roughness measurement using shadow profilometry. Int J Rock Mech Min Sci Geomech 27:329-343.

Mah J, Samson C, McKinnon SD, Thibodeau D (2013) 3D laser imaging for surface roughness analysis. Int J Rock Mech Min Sci;58:111-7.

Malinverno (1990) A simple method to estimate the fractal dimension of a self-affine series. Geophysical Research Letters 17(11): 1953-1956.

Mandelbrot BB (1982) The fractal geometry of nature. W.H.Freeman and Company, New York, 468p.

Marinos V, Marinos P, Hoek E (2005) The geological strength index: applications and limitations. Bull Eng Geol Env 64: 55-65

Markovaara-Koivisto M, Laine E (2012) MATLAB script for analysing and visualizing scanline data. Computers & Geosciences; 40:185-193

Massey CI, Hodgson IF, Petley DN (2006) A rockfall simulation study for housing development in Gibraltar. In: Proceedings of the 10th IAEG International Congress, Nottingham, United Kingdom, paper 377

Matthew NA (2008) Aerial and close-range photogrammetric technology: providing resource documentation, interpretation, and preservation. Technical note 428. U.S. Department of the interior, Bureau of land management, National operation center, Denver, Colorado. 42 pp.

Mauldon M, Dunne WM, Rohrbaugh Jr MB (2001) Circular scanlines and circular windows: new tools for characterizing the geometry of fracture traces. J Struc Geol 23:247-258.

Mauldon M, Goodman RE (1996) Vector analysis of keyblock rotations. J Geotech Engineering 122 (12):976-987

McCarroll D, Nesje A (1996) Rock surface roughness as an indicator of degree of rock surface weathering. Earth Surface Processes and Landforms 21: 963-977

Medapati RS, Kreidl OP, MacLaughlin M, Hudyma N, Harris A (2013) Quantifying surface roughness of weathered rock – examples from granite and limestone. In: Proceedings of Geo-Congress 2013: Stability and performance of slopes and embankments III, San Diego, California, pp. 120-128

Micheletti N, Chandler JH, Lane SN (2015) Structure from Motion (SfM) photogrammetry. Geomorphological Techniques, Chap. 2, Sec. 2.2, ISSN 2047-0371

Milne D, Germain P, Potvin Y (1992) Measurement of rock mass properties for mine design. In: Proceedings of the international symposium on rock support, Sudbury, Ontario.

NGI (2013) Using the Q-system. Handbook for Rock mass classification and support design, Oslo.

Niethammer U, James MR, Rothmund S, Travelletti J, Jowsig M (2012) UAV-based remote sensing of the Super-Sauze landslide: Evaluation and results. Eng Geol 128: 2-11

Nilsson M, Edelbro C, Sharrock G (2012) Small scale joint surface roughness evaluation using digital photogrammetry. In: Proceedings of the Eurock 2012, Stockholm

Oppikofer T (2009) Detection, analysis and monitoring of slope movement by high-resolution digital elevation models. Thése de doctorat, Faculté des Géosciences et de l'Environnement, Université de Lausanne, Switzeland, 201 pp.

Oppikofer T, Jaboyedoff M, Pedrazzini A, Derron M-H, Blikra LH (2011) Detailed DEM analysis of a rockslide scar to characterize the basal sliding surface of active rockslides. Journal of Geophysical Research 116: F02016

Pahl PJ (1981) Estimating the mean length of discontinuity traces. Int J Rock Mech Min Sci & Geomech Abstr;18: 221-228.

Palmström A (2001) In-Situ characterization of rocks. A.A.Balkema Publishers, Lise/Abingdon/Exton(PA)/ Tokio 2001.

Palmström A (1995) RMi – a rock mass characterization system for rock engineering purposes. PhD thesis, University of Oslo, Norway, 409p.

Patton FD (1966) Multiple modes of shear failure in rock. Proc. 1st Int Congr Rock Mech, Lisbon, Portugal, vol. 1:509-516

Peng B (2000) Rockfall trajectory analysis-Parameter determination and application. Thesis of Master of Science in Engineering Geology in the University of Canterbury

Pfeiffer TJ (1989) Rockfall hazard analysis using computer simulation of rockfalls. Engineering Report, Colorado school of Mines, ER-3614

Pinho A, Rodrigues-Carvalho J, Gomes C, Duarte I (2006) Overview of the evaluation of the state of rock weathering by visual inspection. IAEG 2006 Engineering Geology for Tomorrow's Cities, The Geological Society of London, paper 260

Piteau DR (1970) Geological factors significant to the stability of slopes cut in rock. Proc. Symp. on Planning open pit mines, Johannesburg, South Africa :33-53.

Poropat GV (2006) Remote 3D mapping of rock mass structure. In: Proceedings of workshop of "Laser and photogrammetric methods for rock face characterization", Colorado, pp 63-75

Poropat GV (2008) Remote characterization of surface roughness of rock discontinuities. In: Proceedings of the 1st Southern hemisphere international rock mechanics symposium, Perth, pp 447-458

Poropat GV (2009) Measurement of surface roughness of rock discontinuities. In: Proceedings of the 3rd CANUS rock mechanics symposium, Toronto, May 2009 (Ed: M. Diederichs and G. Grasselli), Paper 3976

Priest SD (1985) Hemispherical projection methods in rock mechanics. George Allen & Unwin, London.

Priest SD, Hudson JA (1981) Estimation of discontinuity spacing and trace length using scanline surveys. Int. J. Rock Mech. Min. Sci. & Geomech. Abstr. Vol. 18, pp.183-197

Priest SD (1993) Discontinuity analysis for rock engineering. Chapman & Hall, London

Pötsch M, Schubert W (2006) Kinematic analysis of rock blocks supported by 3D imaging. Proceedings of the 41st U.S. Symposium on Rock Mechanics (USRMS), paper 1079

Qingyan T, Helin F (2011) Block theory rock joint length modifying and slope stability analysis, Geotechnical Special Publication No.216, ASCE:56-64

Rahman Z, Siefko S, Hack R (2006) Deriving roughness characteristics of rock mass discontinuities from terrestrial laser scan data. The Geological Society of London. International Association of Engineering Geology.

Rasouli V, Harrison JP (2010) Assessment of rock fracture surface roughness using Riemannian statistics of linear profiles. . Int J Rock Mech Min Sci 47: 940-948

Rengers N (1970) Influence of surface roughness on the friction properties of rock planes. In: Proc of the 2nd congress of the international society for rock mechanics, Beograd, pp. 229-234.

Rocscience Inc. (2003) RocFall Version 4.0 – Statistical Analysis of Rockfalls, www.rocscience.com, Toronto, Ontario, Canada

Rocscience Inc. (2010) Dips Version 5.0 – Graphical & Statistical Analysis of Orientation Data, www.rocscience.com, Toronto, Ontario, Canada

Rocscience Inc. (2011a) Phase2 – 2D elasto-plastic finite element program for slope and excavation stability analyses, Joint Verification Manual, www.rocscience.com

Rocscience Inc. (2011b) RocData ver.5 web help, www.rocscience.com/help/rocdata/webhelp/RocData.htm

Ryan JC, Hubbard AL, Box JE, Todd J, Christoffersen P, Carr JR, Holt TO, Snooke N (2015) UAV photogrammetry and structure from motion to assess calving dynamics at Store Glacier, a large outlet draining the Greenland ice sheet. The Cryosphere 9: 1-11

Saeidi S, Gratchev I, Kim DH, Chung M (2015) Evaluation of restitution coefficients concerning surface roughness. In: Proc of the 23rd conference on the Mechanics of Structures and Materials (ACMSM23), Byron Bay, Australia, pp. 781-786.

Sharma PK, Khandelwal M, Singh TN (2011) A correlation between Schmidt hammer rebound numbers with impact strength index, slake durability index and P-wave velocity. Int J Ear Sci (Geologische Rundschau) 100: 189-195

Shigui D, Yunjin H, Xiaofei H (2009) Measurement of joint roughness coefficient by using profilograph and roughness ruler. Journal of Earth Science 20:5:890-896

Stevens W (1998) RocFall: A tool for probabilistic analysis, design of remedial measures and prediction of rockfalls . M.A.Sc Thesis, Department of Civil Engineering, University of Toronto, Ontario, Canada

Sturzenegger M, Stead D (2009) Close-range terrestrial digital photogrammetry and terrestrial laser scanning for discontinuity characterization on rock cuts. Eng Geol 106: 163-182

Sturzenegger M (2010) Multi-scale characterization of rock mass discontinuities and rock slope geometry using terrestrial remote sensing techniques. PhD thesis, Simon Fraser university, Burnaby, BC

Strouth A, Eberhardt E (2009) Integrated back and forward analysis of rock slope stability and rockslide runout at Afternoon Creek, Washington. Can Geotech J 46: 1116-1132

Swan G, Zongqi S (1985) Prediction of shear behaviour of joints using profiles. Rock Mech. Rock Engng 18:183-212

Tatone BSA, Grasselli G (2009) A method to evaluate the three-dimensional roughness of fracture surfaces in brittle geomaterials. Rev. Sci. Instrum. 80,125110

Tatone BSA, Grasselli G (2010) A new 2D discontinuity roughness parameter and its correlation with JRC. Int J Rock Mech Min Sci 47: 1391-1400

Terzaghi RD (1965) Sources of error in joint surveys. Geotechnique 15(3): 287-304

Tonon F (1998) Generalization of Mauldon's and Goodman's vector analysis of keyblock rotations. J Geotech Geoenviron Eng 124(10):913-922

Tonon F, Kottenstette JT (2006) Summary paper on the Morrison field exercise. In: Tonon F, Kottenstette JT (eds) Laser and photogrammetric methods for rock face characterization, American Rock Mechanics Association, Alexandria, pp 78-93

Tse R, Cruden DM (1979) Estimating joint roughness coefficients. Int J Rock Mech Min Sci 16: 303-307

Turk N, Dearman WR (1985) Investigation of some rock joint properties: roughness angle determination and joint closure. Proc. Int. Symp. Fundamentals of rock joints. Björkliden:197-204.

Turk N, Greig MJ, Dearman WR, Amin FF (1987) Characterization of rock joint surfaces by fractal dimension. Proc. 28th U.S. Symp. on Rock mechanics, University of Arizona: 1223-1236.

Unal M, Yakar M, Yildiz F (2004) Discontinuity surface roughness measurement techniques and the evaluation of digital photogrammetric method. In: Proceedings of the 20th International congress for photogrammetry and remote sensing, ISPRS, pp 1103-1108

Vasuki Y, Holden EJ, Kovesi P, Micklethwaite S (2014) Semi-automatic mapping of geological structures using UAV-based photogrammetric data: An image analysis approach. Comput Geosci 69: 22-32

Vita PDe, Cevasco A, Cavallo C (2012) Detailed rock failure susceptibility mapping in steep rocky coasts by means of non-contact geostructural surveys: the case study of the Tigullio Gulf (Eastern Liguria, Northern Italy). Nat. Hazards Earth Syst. Sci., 12: 867-880

Wakabayashi N, Fukushige I (1992) Experimental study on the relation between fractal dimension and shear strength. Proc. Fractured and jointed rock masses, Preprints, Lake Tahoe, CA., June 3-5, 1992.

Wang IT, Lee CY (2010) Influence of slope shape and surface roughness on the moving paths of a single rockfall. World Academy of Science, Engineering and Technology 41: 844-850

Wang LG, Yamashita S, Sugimoto F, Pan C, Tan G (2003) A methodology for predicting the in situ size and shape distribution of rock blocks. Rock Mech Rock Eng, 36 (2): 121-142

Weissbach G (1978) A new method for the determination of the roughness of rock joints in the laboratory. Int J Rock Mech Min Sci & Geomech. Abstr. 15: 131-133

Weisstein EW (2002) Point line distance 3 dimensional. MathWorld, A Wolfram web resource. http://mathworld.wolfram.com/Point-LineDistance3-Dimensional.html

Westoby MJ, Brasington J, Glasser NF, Hambrey MJ, Reynolds JM (2012) 'Structure-from-Motion' photogrammetry: A low-cost, effective tool for geoscience applications. Geomorphology 179: 300-314

White K, Bryant R, Drake N (1998) Techniques for measuring rock weathering: application to a dated fan segment sequence in southern Tunisia. Earth Surface Processes and Landforms 23: 1031-1043

Wickens EH, Barton NR (1971) The application of photogrammetry to the stability of excavated rock slopes. Photogrammetric Record 7(37): 46-54

Willmott CJ, Matsuura K (2005) Advantages of the mean absolute error (MAE) over the root mean square error (RMSE) in assessing average model performance. Clim Res 30: 79-82

Willmott WF (2010) Rocks and landscape of the Gold Coast hinterland. Geological society of Australia, Queensland division

Wing MG, Solmie D, Kellogg, L (2004) Comparing digital range finders for forestry applications. Journal of Forestry 102(4):16-20

Wolf PR, Dewitt BA (2000) Elements of photogrammetry with applications in GIS. Third edition, McGraw Hill, Boston, 608 pp.

Wyllie DC, Mah CW (2004) Rock slope engineering. 4th edn, Taylor & Francis

Xia CC, Yue ZQ, Tham LG, Lee CF, Sun ZQ (2003) Quantifying topography and closure deformation of rock joints. Int J Rock Mech & Min Sci 40:197-220

Yang ZY, Lo SC, Di CC (2001) Reassessing the joint roughness coefficient (JRC) estimation using Z2. Rock Mech Rock Eng, 34:243-251.

Yasar E, Erdogan Y (2004) Estimation of rock physiomechanical properties using hardness methods. Eng Geol 71 : 281-288

Yu X, Vayssade B (1991) Joint profiles and their roughness parameters. Int J Rock Mech Min Sci Geomech Abst 28(4): 333-336

Zhang, L (2005) Engineering properties of rocks. Elsevier Ltd.,Oxford, UK

Zhang, L, Einstein HH (2000) Estimating the intensity of rock discontinuities. Int J Rock Mech Min Sci; 37: 819-837.